The
University
Of
Sheffield.

Department of Mechanical Engineering

Strobo-strain: Stroboscopic neutron and X-ray strain measurements in dynamically loaded engineering components

Anthony G.P Reid

December 4, 2019

A thesis submitted for the degree of Doctor of Philosophy.

“*Science knows no country because knowledge belongs to humanity and is the torch which illuminates the world.*”

Louis Pasteur

Abstract

Increasing awareness of the impact that fossil fuel power generation has taken on the environment has driven intensive exploration of low carbon alternatives, such as wind energy. Whilst wind power generation has become a growing resource for meeting the demands of ever-increasing global energy consumption, wind technology has demonstrated reliability issues, mainly due to the stochastic nature of wind conditions. Consequently, downtime associated with unexpected component failure is negatively affecting profit for wind turbine operators. A major contributor towards wind turbine downtime is the premature failure of gearbox bearings, and whilst typically many factors can contribute towards accelerated damage, overloading is believed to be a key driver. Overload events occur due to inertial effects within the drive train, with plastic deformation in the static bearing raceway suggested to be a significant influence on damage propagation, however the mechanism by which this occurs is relatively unknown.

Non-destructive testing approaches, for example synchrotron X-ray and neutron diffraction techniques, have demonstrated the potential for characterising damage in engineering components, and with further development offer the potential for investigating the failure initiation mechanism present in the aforementioned wind turbine bearing and other similar components. This project therefore focuses on the development of such techniques, specifically looking at the advancement of stroboscopic diffraction and neutron imaging methods, taking the wind turbine gearbox bearing as an exemplar component for this study. A novel stroboscopic technique has been incorporated into a custom-built bearing rig, permitting the measurement of time-resolved subsurface strains in dynamic bearings. Prior to testing, bearing samples were exposed to significant overloading, with the aim of reducing experimental times to those appropriate for neutron and X-ray investigations, whilst also creating a specific location to be examined that is more prone to damage. The stroboscopic technique was used to successfully measure dynamic subsurface strain when contact stresses were at a maximum magnitude, whereby the rolling element was in contact with the overloaded region. Additionally, the benefit of using eventmode data acquisition during the neutron diffraction experiment, demonstrated the capability of stroboscopic neutron diffraction for analysing cyclic strains associated with rolling contact fatigue.

Neutron imaging methods for damage characterisation are also being explored, with neutron Bragg edge transmission imaging becoming an increasingly popular technique for measuring through-averaged elastic strains. To aid development of this technique for the purpose of evaluating damage, an in situ fatigue experiment was performed, whereby crack nucleation and propagation in a notched sample was successfully detected. Neutron computed tomography was also applied post-fatigue, successfully permitting visualisation of the crack. Having managed to evaluate elastic strain using this method, Bragg edge transmission imaging was then performed on a bearing sample at increasing load. The Bragg edge broadening parameter presented notable increases beneath the contact, indicative of material yielding, allowing for a qualitative estimation of subsurface plastic zone evolution, as predicted with finite element modelling. The non-destructive neutron imaging results were compared with post-mortem micromechanical characterisation such as scanning electron microscopy to validate the findings.

The combined neutron and X-ray diffraction, neutron imaging, finite element analysis and micromechanical characterisation of damaged bearings resulted in improved understanding of the bearing failure mechanism, which can be exploited in the future to improve bearing performance and reliability.

Acknowledgements

Firstly, I feel exceptionally fortunate to have had such an incredible supervisory team. Thank you to Matt Marshall for supporting me throughout and always being there whenever I have needed guidance. Thank you to Mahmoud Mostafavi, without whom the opportunity to embark on this project would not have been possible. I am eternally grateful to both Matt and Mahmoud for always putting their faith in me, even when I often did not have faith in myself. A big thank you to Saurabh Kabra, not only for all of the guidance and support relating to my project, but also for being a good friend. Moving to Oxford partway through my PhD was difficult, yet the transition was much smoother and an all-round better experience thanks to him. Thank you to Thomas Connolley for all of his support, notably with his outstanding technical knowledge, which helped to improve the overall quality of experimental design.

Thank you to the many technicians who I have had the honour of working with throughout this project. Whilst completing this work, I have come to realise that technicians are the heartbeat of science. In particular, I would like to thank Dave Butcher at the University of Sheffield, for manufacturing the rig that was fundamental to this research, whilst always providing helpful advice and being supportive of my work. Also, Josef Lewis at ISIS for always making himself available to provide technical support. I am extremely grateful to them both, for everything they have done for me.

Along this journey I have had the opportunity to meet many new people, with several becoming friends for life. There is obviously my fellow PhD students in RD12, from the sanity saving tea breaks to the meals out in Sheffield, it has been a great pleasure. I'd like to say a huge thank you to the team at ISIS, in particular Winfried Kockelmann and Tino Minniti, for always having an open door and providing essential guidance whenever I came knocking. Ranggi Ramadhan at Coventry University, whom set off on the Bragg edge exploration at a similar time has provided great support and friendship. Also, a special mention to Ian Martinez, who I have worked closely with for the last 4 years, sharing many highs and lows, remaining a close friend throughout.

Finally, I'd like to thank my family. My mum and dad have always been my closest allies, providing me with love and encouragement in every aspect of my life. In the same way my sister, Fi, and brother-in-law, Jonny, have been a huge support throughout everything. Steph, thank you for your love, patience and for being an amazing mother to our beautiful daughter, Lucia. Everything I strive to achieve is aimed at ensuring our daughter can feel the same love and support that I have been lucky enough to receive.

Contents

CHAPTER 1

INTRODUCTION

In this chapter the growth of wind as a sustainable energy source and the varying issues surrounding commercial wind turbine reliability are discussed. The significant contribution of wind turbine gearbox (WTG) bearing failure is highlighted, leading to an overview of the motivation and targeted objectives of the project. To monitor WTG bearing failure many non-destructive approaches have been established, yet the use of neutron and X-ray diffraction techniques for this application is limited. This chapter introduces the concept of non-destructive testing, with the development of novel diffraction based strain analysis the primary aspiration.

1.1 Wind energy

Wind energy may be considered a form of solar energy, as it originates from irregular heating of the Earth's surface, resulting in a bulk displacement of air from regions of high pressure to regions of low pressure. The moving air particles possess a plethora of kinetic energy, which can be converted into electrical energy using a turbine, forming the basis of wind power technologies. As wind is an example of renewable energy, without any associated greenhouse gas emissions, it is considered a principal technology for mitigating the negative impact of human activity on the Earth's climate.

Based on the concepts of fluid mechanics and the reduction of wind velocity whilst flowing through a turbine, Betz's law states that turbines are incapable of harnessing more than 59.26% of the winds kinetic energy, setting a theoretical efficiency limit [1]. This theoretical limit is expressed using the Betz coefficient, η (16/27 or 0.5926) and is incorporated in the calculation for maximum power output from a turbine, seen in Equation 1.1.

$$P = \frac{\eta \rho v^3 A}{2} \tag{1.1}$$

Where, P is power output, ρ is the air density, v is wind velocity and A is effective cross-sectional area swept by turbine rotation.

In reality, commercially viable turbines operating at the rated speed convert between 44.4% and 47.4% of the wind's kinetic energy [2]. Major issues with wind energy include it's stochastic nature, meaning that power generation is highly dependent on transient weather conditions, making it troublesome to accurately predict the extent of power generation on a long term basis.

Figure 1.1 presents the growth of global wind capacity between 2009 and 2018 [3], demonstrating a steady increase during this time. The UK has seen a sharper rise since 2011, utilising the 'best and most geographically diverse wind resources in Europe' [4]. Remarkably, it has been reported that in 2017, within the 28 European Union member countries, wind power generation exceeded that of coal for the first time [5]. It is suggested that this was the result of significant investment from Germany, Netherlands and UK. This rapid increase may be attributed to the considerable development of innovative wind turbine designs in recent years.

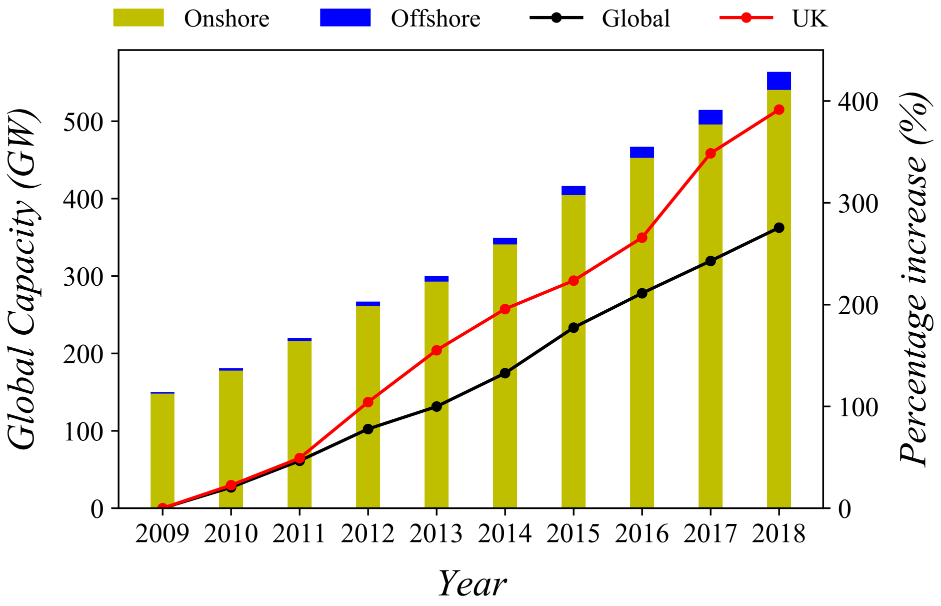

Figure 1.1: Global capacity of onshore and offshore wind turbines between 2009 and 2018. Comparison between the global and UK percentage increase of wind capacity since 2009 [3].

Typically, wind turbines are either a horizontal axis (HAWT) or vertical axis (VAWT) design, with the vast majority of in-service turbines being three-bladed HAWT. A schematic of a HAWT is displayed in Figure 1.2. As can be seen from Betz law (Eq. 1.1), more energy can be harnessed from turbines with a greater swept cross-sectional area. This has proven the most popular approach to developing more powerful turbines. Currently the largest commercially viable turbine, launched as a joint project between Vestas and Mitsubishi Heavy Industries, is an offshore V164 wind turbine of 9.5 MW capacity and boasting a rotor blade area sweeping 23,779 m^2 [6]. Larger rotors have greater speeds at the blade tip, increasing the stresses experienced by the blades and subsequently drivetrain components. This issue provides one example of how research and development (R&D) is of primary importance, with notable scope for aerodynamic design of rotor blades.

Significant expansion of rotor blade length necessitates scaling-up of the remaining system components, accordingly. This involves enlargement of mechanical subassemblies including the hub, generator and gearbox, as well as the tower and nacelle that act as the support and housing for these subsystems, respectively. This proves costly and makes turbines more difficult to install, particularly offshore.

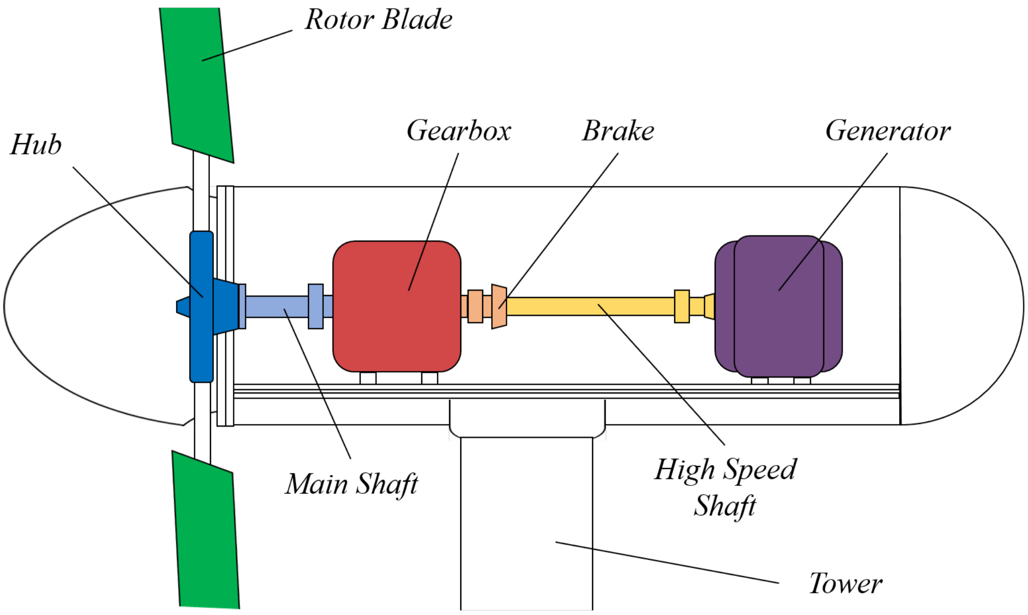

Figure 1.2: Schematic of critical subassemblies in a wind turbine nacelle.

1.2 Wind turbine reliability

In recent years there has been a rapid evolution of wind turbine technologies, yet with the increase of overall system dimensions there has been a negative impact on their in-service reliability [7]; defined as the probability of functioning adequately under operating conditions for a specified period of time. Wind turbine reliability is a significant focus for industry, as operating and maintenance (O&M) costs over their lifetime can reach 95% of the total expense for installation, with wind turbine design life generally accepted to be approximately 20 years [8]. Unscheduled maintenance, as the result of a failure, is particularly problematic, as it may lead to substantial periods of downtime, where the turbine is no longer functional. This issue is exaggerated if the turbine is in a remote location that may be difficult to access, for example offshore.

Wind turbine reliability is frequently presented in terms of the two parameters, annual failure rate, λ_f, and downtime per failure, σ_d [9]:

$$\lambda_f = \frac{1}{t_{bf}} \tag{1.2}$$

$$\sigma_d = \frac{1}{\mu_r} \tag{1.3}$$

Where, t_{bf} is the mean time between failure and μ_r is the repair rate.

The Scientific Measurement and Evaluation Programme (WMEP) was a large monitoring survey conducted between 1989 and 2006, whereby 64,000 maintenance and repair reports from 1,500 onshore wind turbines were analysed [9]. Figure 1.3 demonstrates the percentage contributions of both λ_f and σ_d, associated with different wind turbine subassemblies. This study suggests that electrical subsystems fail more frequently, yet failure of mechanical subassemblies contributes most significantly to the overall downtime of wind turbines, with over 15% attributed solely to the gearbox. It is accepted that annual failure rates and associated corrective time for offshore turbine failures is notably higher than for onshore turbines, with logistical issues and harsh weather conditions influencing accessibility for maintenance and repair [10].

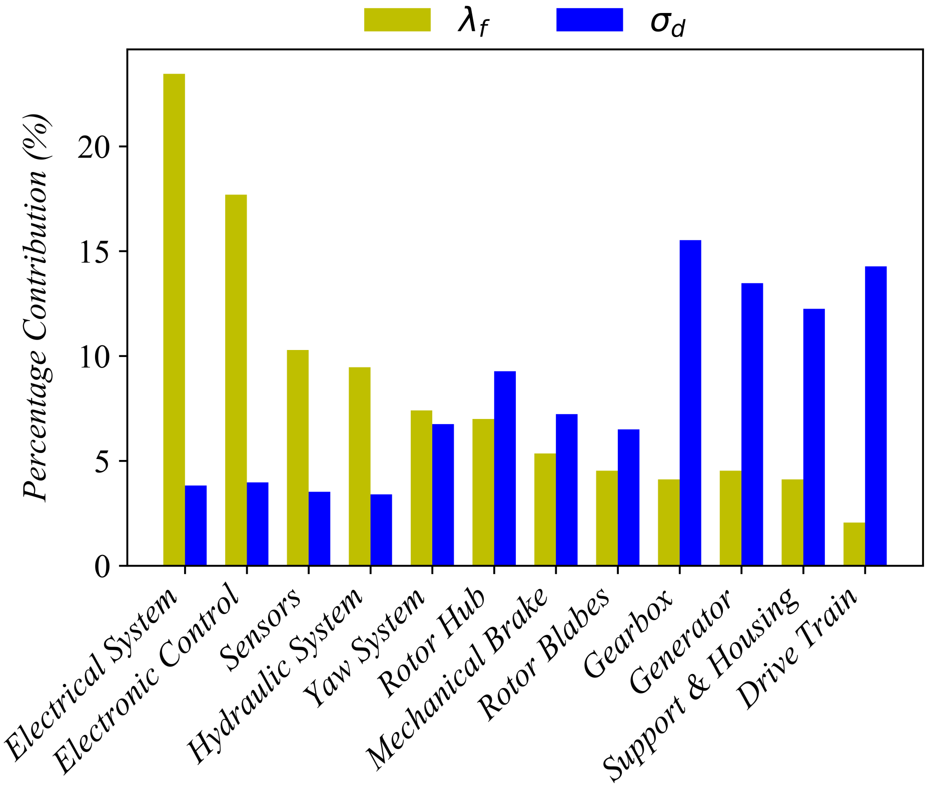

Figure 1.3: Percentage contribution of annual failure rates, λ_f, and the associated downtime per failure, σ_d, for turbine subassemblies. Data obtained from 1500 onshore wind turbine's as part of the WMEP programme (adapted from [9]).

Extensive O&M costs have acted as a driver for research and industry, focusing on advancements to the less expensive preventative and predictive (P&P) techniques, opposed to costly reparative approaches. Reliability can be improved with more robust design of the wind turbine and its constituent subassemblies and components, along with improved industry standards to encourage best practices and implementation of advancing turbine technologies [11]. To accelerate development of these P&P strategies, it becomes of greater importance to understand the root cause of failure, whilst simultaneously enhancing statistical reliability models used to predict when a subsystem may fail [12]. Also, emphasis has been placed on structural health monitoring (SHM) systems, used to monitor the condition of individual components or subsystems and provide early warnings of damage and impending failure. SHM approaches generally incorporate non-destructive techniques such as acoustic emission event detection, thermal imaging, ultrasound probing or modal dynamic monitoring [13].

1.2.1 Wind turbine gearbox bearing failure

As previously discussed, WTG failures contribute significantly to overall downtimes, with 35.1% of insurance claims from UK wind turbine operators being related to gearbox defects [14]. In an attempt to keep WTG's compact, epicyclic stages are regularly employed, with multiple planetary bearings required for this system. Many other bearings are found throughout the gearbox drivetrain, most notably for supporting the low, intermediate and high speed shafts. The schematic of a WTG is displayed in Figure 1.4. Bearing failure is the most prevalent cause of gearbox outage, with damage records from the National Renewable Energy Laboratory suggesting a contribution of 72% [15]. The exact failure locations were:

- High speed shaft (HSS) bearings - 55%
- Intermediate speed shaft (ISS) bearings - 13%
- Planetary bearings - 4%
- Helical gear - 15%
- Planetary gear - 13%.

A proposed contributory mechanism towards premature WTG bearing failure is overloading of the static raceway, defined as any load that generates contact pressures exceeding the material yield strength [16]. Overload events generally occur due to drivetrain inertia resulting in sudden torque spikes, increasing contact stresses in bearings installed to carry load at the affected WTG regions. It has been reported that planetary bearing overloads can occur at wind velocities as low as 12 ms^{-1}, which accounts for roughly 22% of the in-service life of turbines located on a wind farm in Pine Springs, Texas [17]. The large radial forces associated with overloads being related to inertial effects in the drivetrain, suggest their occurrence is the result of adverse operational conditions, for instance transient wind velocities, sudden braking, shaft misalignment, load reversals and the restarting or discontinuance of the generator-grid connection [18, 19, 20].

Most WTG's will convert rotational speeds from between 5 to 60 *rpm* at the rotor main shaft to as high as 1800 *rpm* at the high speed shaft [21, 22]. This allows for generation of electrical power at a suitable frequency, either 50 Hz or 60 Hz, depending on the grid system used at the installed location of the turbine [21]. Innovative technologies, such as direct drive wind turbines (DDWTs), which do not require a gearbox, are currently being proposed as future alternatives, due to the WTG being particularly susceptible to damage. However, at present it is proving difficult to implement the generator subsystems for larger capacity turbines. DDWT's are far less cost-effective as a permanent magnet rotor of substantial size, manufactured using expensive rare earth magnetic materials, is essential to generate adequate electrical power [23]. This makes DDWT's unattractive as a commercially viable option for wind turbine operators, making it unlikely that geared systems will be replaced in the foreseeable future, justifying the requirement for improvement to WTG reliability and upholding the great significance of research for the industry.

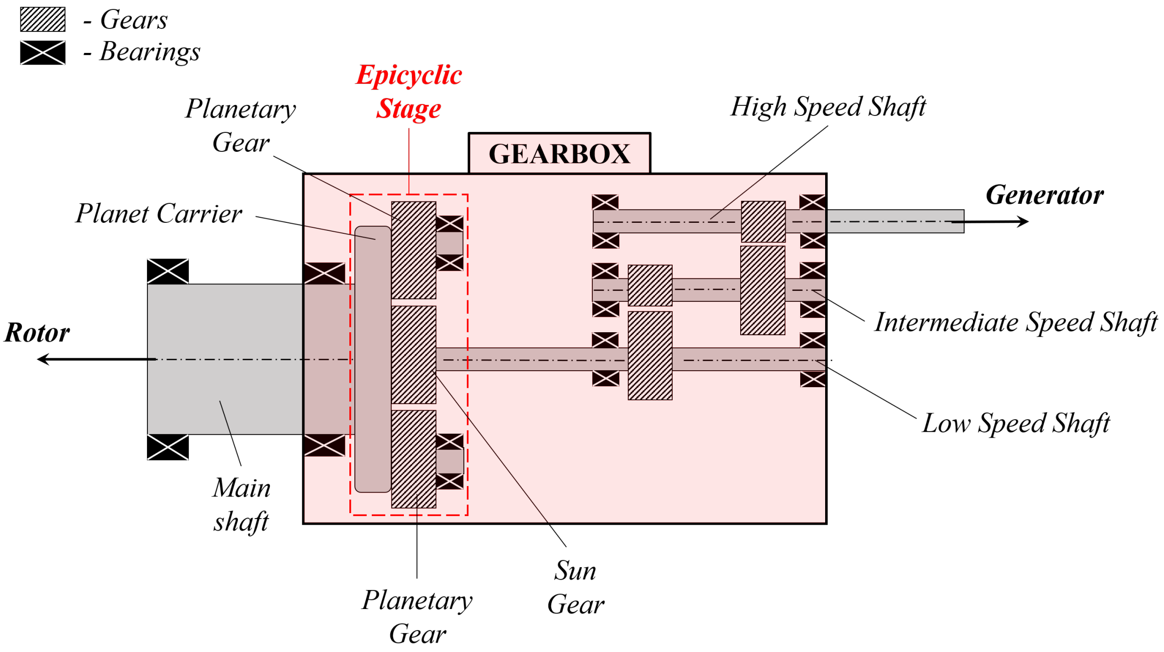

Figure 1.4: Schematic of a WTG. The epicyclic stage consisting of a planetary gear system driven by the main shaft, transmitting rotation to a sun gear that in turn drives the low speed shaft.

1.3 Non-destructive testing

Techniques for measuring material stress and strain can be categorised as destructive, semi-destructive and non-destructive testing. Destructive and semi-destructive methods are generally referred to as stress-relaxing techniques, as they quantify stress released on removing material from the test sample [24]. These methods are perfectly valid, with continuous research and development into numerous techniques taking place worldwide [24, 25]. Non-destructive testing (NDT) may be viewed as complementary to the more established destructive methods, yet has evolved in recent years regarding suitability for industrial applications [26].

NDT allows for the detection of surface and subsurface defects or the monitoring of material condition, whilst maintaining the in-service performance and integrity of a component. As mentioned, commercially viable SHM techniques can non-destructively track alterations in a components operation, ideally pre-empting failure before it happens. Diffraction techniques allow for the non-destructive measurement of atomic planar spacings, permitting the calculation of elastic strains. Due the nature of diffraction investigations, it is not possible to perform experiments on WTG bearings *in situ*, with the equipment required far too large to be fixed to a turbine, and too expensive to have multiple sources. Nonetheless, X-ray and neutron diffraction possess the power to measure strain in the bulk of a bearing sample, and can be used to develop further understanding of the mechanisms responsible for failure.

1.4 Project motivation

As mentioned, there is clearly scope for improving the reliability of commercial wind turbines, with the aim of driving down the associated O&M costs. Failure analysis and determining the root-cause of damage in WTG bearings is a difficult task, as there are many potential failure modes. Nonetheless, a focus of this study is to further understand the influence of overloading on bearing fatigue life using synchrotron X-ray and time-of-flight neutron diffraction techniques. The project has been used as an opportunity to optimise stroboscopic strain measurements on the JEEP (I12) X-ray beamline at the Diamond Light Source and to develop stroboscopic strain measurement capabilities on the ENGIN-X instrument, ISIS Neutron and Muon Source, both based at the Rutherford Appleton Laboratories (RAL) in Oxfordshire, UK. In addition to stroboscopic diffraction experiments, other work completed during an 18-month placement at RAL included; the first energy dispersive neutron imaging experiment to be performed on the IMAT imaging beamline, during its commissioning phase; contribution to development of the IMAT imaging software, BEATRIX; first user to complete *in situ* experiments on ENGIN-X using the IMAT energy selective MCP detector.

This work was half-funded by the Engineering and Physical Sciences Research Council (EPSRC) and half-funded by Science and Technology Facilities Council (STFC), primarily to transfer knowledge of stroboscopic strain measurements already available at I12 to ENGIN-X.

1.4.1 Objectives

The principal aim of the study was to develop the hardware and software required for measuring time-resolved elastic strain in the static outer raceway of a pre-overloaded dynamic roller bearing. This was performed by incorporating a stroboscopic triggering system. Additionally, this project involved work to strengthen the potential of imaging techniques for detecting the presence of fatigue cracking and subsurface yielding. Objectives were as follows:

1. Design a stroboscopic technique for measuring dynamic contact strain in operational roller bearings, using X-ray and neutron diffraction.
2. Establish a method for analysing stroboscopic time-of-flight neutron data.
3. Develop a greater understanding of the effect that overload events have on the rolling contact fatigue life of roller bearings.
4. Identify and observe the evolution of subsurface plastic deformation generated during an overload event, using energy-dispersive neutron transmission imaging.
5. Evaluate the use of neutron imaging techniques for detecting damage, specifically characterising and quantifying fatigue crack nucleation and propagation.

1.4.2 Outline of thesis

The thesis has been submitted as an '*Alternative Format Thesis*', with four sequential chapters having been published, or submitted for publication, whilst also forming a coherent body of work.

Chapter 2 provides technical background on the key concepts included within the presented work. The chapter is divided into two main sections; one covering life rating procedures for roller bearings and the analytical Hertzian contact theory used for predicting surface and subsurface stresses; the second section introduces the fundamentals of X-ray and neutron diffraction, exploring the use of these techniques for engineering applications, such as experimental stress analysis.

Chapter 3 is published work titled 'Application of neutron imaging to detect and quantify fatigue cracking', where neutron computed tomography (CT) and energy-dispersive neutron transmission imaging are evaluated on their ability to detect the presence of a fatigue crack. Additionally, X-ray CT and optical microscopy were used as a benchmark for the neutron results.

Chapter 4 is published work titled 'Mapping of axial plastic zone for roller bearing overloads using neutron transmission imaging', where a unique approach to energy-dispersive neutron transmission imaging has been used to observe subsurface plastic zone evolution during a bearing overload event.

Chapter 5 is published work titled 'Measurement of strain evolution in overloaded roller bearings using energy dispersive X-ray diffraction' where the optimised stroboscopic method, designed as a primary aim of the project, was trialled. The technique exploited superior spatial resolution capabilities available on I12 to measure subsurface time-resolved elastic contact strain.

Chapter 6 contains work that has been submitted for publication, titled 'Measurement of strain evolution in overloaded roller bearings using time-of-flight neutron diffraction'. The chapter contains work that is fundamental to achieving the primary aims of the project, as the technique developed for the prior X-ray experiment was used. More focus is given to the unique approaches used for analysing the stroboscopic neutron data, whilst confirming the advantages and disadvantages of using neutrons for such investigations.

Chapters 7 and 8 contain the discussion and conclusions, respectively. The discussion centres on evaluating the benefits and limitations of the applied techniques, whilst conclusions summarise the novel input of this research project and present recommendations for future work.

1.5 Additional Contributions

1.5.1 Journal Publications

1. Reid, A., et al. "Measurement of Strain Evolution in Overloaded Roller Bearings using Energy Dispersive X-ray Diffraction". *Tribology International*, 140 p.105893.
2. Reid, A., et al., 2019. "Application of neutron imaging to detect and quantify fatigue cracking." *International Journal of Mechanical Sciences*, 159 p.182-194.
3. Reid, A., et al., 2018. "Mapping of axial plastic zone for roller bearing overloads using neutron transmission imaging." *Materials and Design*, 156 p.103-112.
4. Kockelmann, W., et al., 2018. "Time-of-Flight Neutron Imaging on IMAT@ ISIS: A New User Facility for Materials Science." *Journal of Imaging*, 4(**3**) p.47.

Submitted

5. Reid, A., et al. "Measurement of Strain Evolution in Overloaded Roller Bearings using Time-of-Flight Neutron Diffraction." *Materials and Design*
6. Martinez, I., et al. "Acoustic Emission Localisation on Roller Bearing Defects using Time-Delay and Sum Beamforming Technique." *Mechanical Systems and Signal Processing*

Co-authour Contributions

- M. Marshall - PhD supervisor.
- M. Mostafavi - PhD supervisor.
- S. Kabra - PhD supervisor.
- T. Connolley - PhD supervisor.
- T. Minniti - Instrument scientist on IMAT beamline who has provided guidance with analysis of imaging data.
- W. Kockelmann - Instrument scientist on IMAT beamline who has provided guidance with analysis of imaging data.
- A. James - PhD researcher, aiding with completion of experimentation.
- TJ. Marrow - Provided the Duplex steel and proof read paper.
- I. Martinez - Finite element modelling of bearing and aiding with completion of stroboscopic experimentation.
- C. Simpson - developed the pyxe software used for analysing EDXD data.
- O. Magdysyuk - Instrument scientist on I12 who helped with setup for the stroboscopic experiment.
- C. Charlesworth - Electrical engineer who provided guidance regarding setup of the fibre optic triggering system.
- S. Moorby - DAE technician who helped to setup the eventmode data acquisition on ENGIN-X.

1.5.2 Conference Proceedings

1. Reid, A., et al. ‘Qualitative Mapping of Axial Plastic Strain for a Roller Bearing undergoing Overloads using Bragg Edge Parameter Fitting’. *British Society for Strain Measurement (BSSM) 12th International Conference on Advances in Experimental Mechanics, Sheffield, UK* (2017).
2. Martinez, I., et al. ‘A wavelet transform approach for acoustic emission localisation and an examination of PZT sensor self-diagnostics’. *BSSM 12th International Conference on Advances in Experimental Mechanics, Sheffield, UK* (2017).
3. Reid, A., et al. ‘Qualitative Mapping of Axial Plastic Strain for a Roller Bearing undergoing Overloads using Bragg Edge Parameter Fitting’. *The 9th International Conference on Mechanical Stress Evaluation by Neutron and Synchrotron Radiation (MECA SENS), Skukuza, South Africa* (2017).
4. Reid, A., et al. ‘Fatigue Crack Initiation Identification and Quantification with Bragg Edge Strain Tomography’. *14th International Conference on Fracture (ICF), Rhodes, Greece* (2017).

1.5.3 Invited Talks

1. ‘Qualitative Mapping of Subsurface Plasticity in an Overloaded Roller Bearing using Neutron Transmission Imaging’. *Neutron and Muon User Meeting (NMUM), University of Warwick, UK* (2018).

CHAPTER 2

TECHNICAL BACKGROUND

Work presented throughout this research project primarily aims to develop X-ray and neutron strain measurement techniques. Enhancement of neutron diffraction and imaging approaches provides the novel scientific contribution offered by this project. These non-destructive techniques were applied to the context of premature WTG bearing failure, providing some insight into mechanisms that have been proposed to accelerate bearing damage propagation. This technical background chapter opens by introducing important concepts relating to bearing life prediction and analytical Hertzian contact theory. However, greater emphasis is placed on presenting non-destructive neutron and X-ray diffraction, as understanding their use in the characterisation of material strains is paramount for this study.

2.1 Rolling element bearings

Cylindrical roller bearings are uni-directional components, designed to endure mostly radial loads. They are generally employed under heavily loaded conditions and moderate rotation speeds [27, 28]. There are various causes for such bearings to fail prematurely, such as improper installation, unsuitable lubrication, poor maintenance or extreme operating conditions, whilst contamination and improper handling may also lead to a reduction of bearing life [29]. Wear mechanisms that contribute to bearing failures are complex and often occur simultaneously, with some more common causes of bearing damage including brinelling, false brinelling, corrosion and galling [28, 30].

A prominent mechanism associated with the finite nature of bearing life, predominantly occurring in the very high cycle regime (more than 10^7 cycles), is known as rolling contact fatigue (RCF), and contributes towards phenomena known as pitting or spalling [31]. Literature suggests it is difficult to distinguish between the two occurrences, yet some definitions state that pitting occurs closer to the surface (<20 μm) whilst spalling is within the subsurface (20-100 μm) [32]. Pitting and spalling consequently result in the removal of a small amount of surface material, leaving cavities that contribute towards damage. Due to the nature of RCF, failure will eventually arise, regardless of whether the bearing has been installed and operated under ideal design conditions. The contact surface area between roller and surrounding raceway is intentionally small to reduce friction, yet this results in significantly large cyclic stresses, generated as the bearing rotates. Historically, RCF was predominantly caused by unwanted inclusions, incorporated during steel manufacturing processes, acting as significant stress concentrators. In modern roller bearings, where the number of material inclusions have been reduced, the most common form of RCF is known as geometric stress concentration, resulting from high surface pressures that initiate large sub-surface stresses [33]. Notably, maximum principal shear stresses are greatest in the subsurface of dynamically loaded bearing raceways, causing deformation and areas of microplasticity to accumulate, increasing the probability of crack initiation in these regions [34]. Once a subsurface crack has been nucleated, it will eventually propagate towards the surface to produce a spall, or pit. A more comprehensive review of RCF is included in Section 5.1.1.

As one would expect, assessing bearing life must accommodate for statistical techniques, with the probability of subsurface crack initiation dependent on various factors [33]. Several models for predicting bearing life have been developed since 1896, beginning with work from R. Stribeck, along with significant contributions from G. Lundberg and A. Palmgren [31]. The basis for many models, requires Weibull distribution functions that have been developed to help predict the random nature of fatigue failure probabilities. In practice, validating the necessary parameters needs a high number of test specimens. It has been noted that a three-parameter RCF life function using Weibull distribution parameters is most appropriate in this context, as the approach provides greatest accuracy for predicting fatigue life of contemporary industrial materials [31, 33], such as those used in WTG bearings. The three Weibull distribution parameters required are the shape parameter (β), scale parameter (η) and location parameter (γ). Figure 2.1 shows the Weibull probability distributions for different values of β, with a shape parameter of 1.5 generally providing the best fit for cylindrical roller bearings [33].

Most bearing life rating models over-predict lifetimes, as the complex interaction of multiple wear mechanisms and material properties are not consistent, suggesting that with better understanding, more accurate models could be developed in the near future [31]. WTG bearings rarely meet their design life, with the stochastic nature of wind behaviour, along with inertial effects within the drivetrain, contributing significantly to this [35]. Transient overloading causes damage to accumulate at an increased rate, yet it can be difficult to diagnose fatigue damage macroscopically [36]. For analysing bearing life ratings, a frequently adopted method is to predict the length of time it takes for 10% to fail, referred to as L_{10} life and expressed in Equation 2.1 [31].

$$L_{10} = \left(\frac{C}{P_s}\right)^p \tag{2.1}$$

Where, C is the dynamic load capacity, defined as the load at which 10% of bearing are expected to fail after 10^6 revolutions, P_s is the applied load across the entire bearing (combined radial and

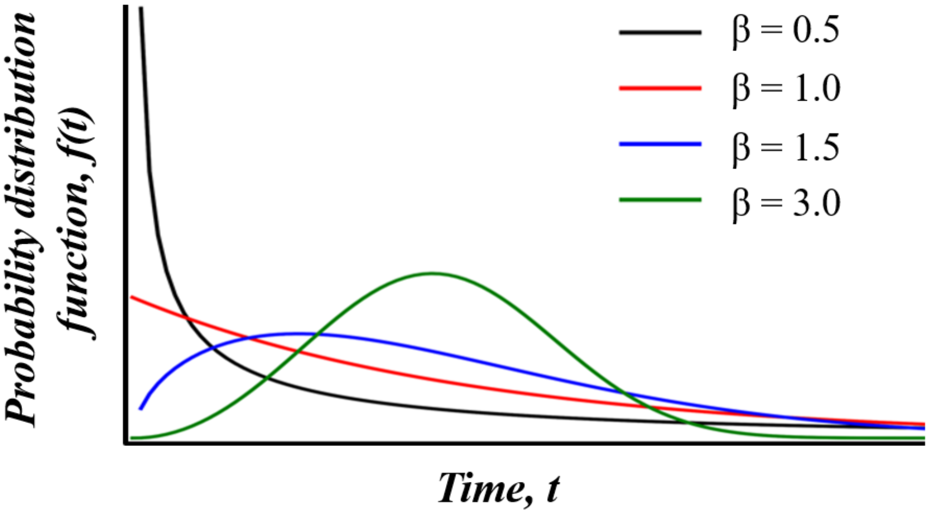

Figure 2.1: Weibull probability distributions, f(t), with varying shape parameters (β).

axial, however for this study samples are assumed to be 100% radially loaded) and p is the load-life exponent, with $p = 10/3$ for roller bearings.

The L_{10} model is still widely reported as it allows for a reasonable statistical approach to bearing life prediction. Nonetheless, since it's introduction the model has been found to be reducing in accuracy, as L_{10} predictions seen in Equation 2.1, may fail to consider the improving quality of bearing steel, whilst also ignoring the effects of lubrication and surface damage initiation. Consequently, that model has been re-developed multiple times, with modification factors included to adjust the predicted L_{10} life by incorporating additional operational parameters. Currently, a newer standardised model has been developed, under ISO281:2007 [37], expressed as a general, modified life rating, as seen in Equation 2.2.

$$L_{nm} = a_1 a_{ISO} \left(\frac{C}{P_s} \right)^p \tag{2.2}$$

Where, L_{nm} is the life rating for a predetermined percentage reliability (nm), a_1 is the life modification factor and allows for probabilities of failure, other than 10%, to be assessed, based on the Weibull distribution of $\beta = 1.5$. The a_{ISO} accommodates for a range of operational parameters, which are influenced by the material and lubrication. The gradual development of these statistical bearing life rating procedures has improved the accuracy of life expectancy predictions, yet they notoriously underpredict failure times for WTG bearings. The modification factors have helped to improve this by incorporating the influence of operational parameters, such as lubrication and percentage reliability, yet, knowledge of the mechanism, or combination of mechanisms, responsible for failure needs to be better understood.

The models presented above, originate from an assumption proposed by Lundberg and Palmgren that RCF failure is mostly the result of subsurface orthogonal shear stresses, based on Hertzian contact theory.

2.1.1 Analytical contact mechanics

When evaluating the stresses associated with bearing contacts, it is important to consider the equivalent load applied by the most heavily loaded rolling element, P_E, and its relationship with the load applied to the entire bearing, P_s, for instance via a shaft. Stribeck proposed a method for calculating the equivalent load, as seen in Equation 2.3, dependent on the number of elements [38].

$$P_E = \frac{5P_s}{Z} \tag{2.3}$$

Currently, the most widely accepted analytical theory for predicting contact stresses is the Hertzian model. According to Hertzian contact theory, when a force is applied between two cylindrical bodies, generating a line contact geometry, the contact half-width can be estimated using Equation 2.4 [39].

$$b = \sqrt{\frac{4P_E R^*}{\pi L E^*}} \tag{2.4}$$

Where, b is the contact half-width, L is the contact length, with R^* and E^* representing the reduced radius and reduced Young's modulus, respectively, as seen in Equations 2.5 [40].

$$\begin{aligned} \frac{1}{R^*} &= \frac{1}{R_1} + \frac{1}{R_2} \\ \frac{1}{E^*} &= \frac{1}{E_1} + \frac{1}{E_2} \end{aligned} \tag{2.5}$$

The pressure distribution generated by a Hertzian contact, has a maximum value, p_0 in the centre of an elliptical profile, reaching zero at the contact edges. The value of p_0 can be calculated using Equation 2.6, with the distribution profile presented in Figure 2.2b. As mentioned, assumptions by Palmgren regarding RCF failure suggested that orthogonal shear stresses were the key driver. It was later demonstrated that induced plastic deformation observed in bearing raceways, corresponded more closely to the depth of greatest maximum principal shear stress, occurring at approximately $y = 0$ and $z = 0.786b$, with a magnitude of $0.3p_0$ [40], whereby y and z represent the tangential and radial co-ordinates, relative to the contact site. It is therefore useful to have approaches available for predicting subsurface stresses associated with Hertzian contacts.

$$p_0 = \frac{2P_E}{\pi b L} \tag{2.6}$$

Where, p_0 is the maximum contact pressure, b is the contact half-width, L is the contact length and P_E is the equivalent load at the most heavily loaded element.

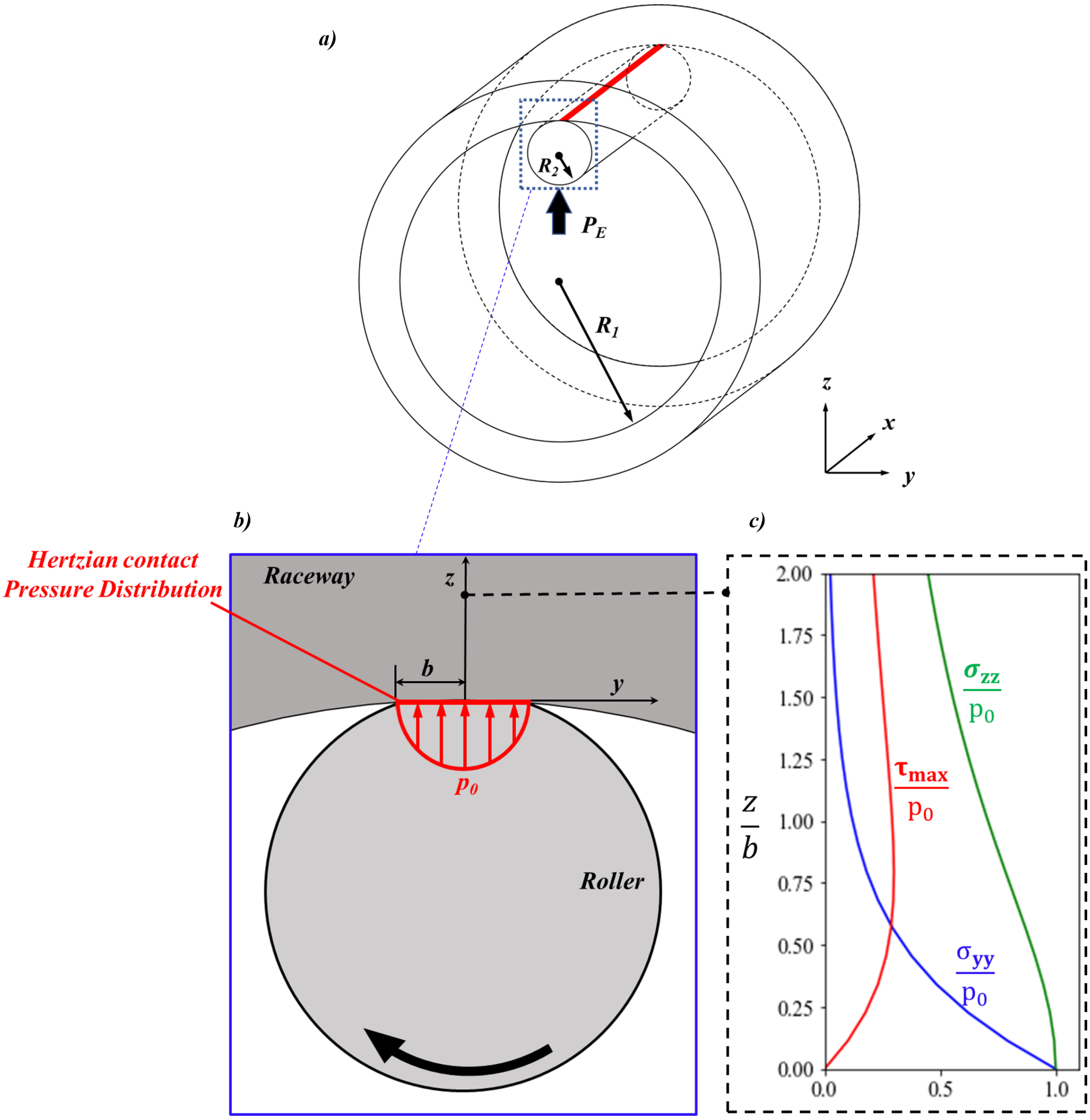

Figure 2.2: (a) Schematic of a bearing outer raceway and roller, forming a line contact geometry. (b) diagram to represent the contact pressure distribution. (c) Plot of subsurface σ_{zz}, σ_{yy} and τ_{max}, directly beneath the contact.

Subsurface stresses

Two-dimensional stress fields for frictionless contacts can be evaluated relative to the axis of symmetry ($y = 0$) with an approach involving complex potentials. In 1948, McEwen demonstrated a suitable method for expressing the Hertzian contact stress at general points in a two-dimensional matrix (y, z) in terms of coefficients m and n, defined using Equations 2.7 [41].

$$\begin{aligned} m^2 &= 0.5\left\{\left[\left(b^2-y^2+z^2\right)+4y^2z^2\right]^{1/2}+\left(b^2-y^2+z^2\right)\right\} \\ n^2 &= 0.5\left\{\left[\left(b^2-y^2+z^2\right)+4y^2z^2\right]^{1/2}-\left(b^2-y^2+z^2\right)\right\} \end{aligned} \tag{2.7}$$

Once the values of m and n have been obtained, the various components of the two-dimensional stress field can be calculated using Equations 2.8.

$$\begin{aligned} \sigma_{yy} &= p_0\, m\left[1+\left(z^2+n^2\right)\Big/\left(m^2+n^2\right)\right]\Big/ b+2z\Big/ b \\ \sigma_{zz} &= -p_0\, m\left[1-\left(z^2-n^2\right)\Big/\left(m^2+n^2\right)\right]\Big/ b \\ \tau_{yz} &= p_0\, n\left[\left(m^2-z^2\right)\Big/\left(m^2+n^2\right)\right]\Big/ b \end{aligned} \tag{2.8}$$

The maximum principal shear stress, which as discussed, is pivotal for understanding subsurface initiated RCF damage, can then calculated using Equation 2.9, with a one-dimensional plot demonstrated in Figure 2.2c. To demonstrate subsurface stress, contour maps for the different stress components, normalised by the maximum Hertzian contact pressure p_0, have been plotted in 2.3.

$$\tau_{max} = \sqrt{\frac{\sigma_{yy}^2-\sigma_{zz}^2}{2}+\tau_{yz}} \tag{2.9}$$

Tangential stresses

The Hertzian model discussed above focusses primarily on normal force application, failing to account for frictional forces, acting tangentially to the contact surface. Consideration of friction certainly increases complexity, however a brief explanation of the impact friction has on the predicted stress fields has been included. Tangential stresses generated by surface traction are related directly to the normal pressure distributions by the coefficient of friction, μ, providing the following relationship, $q_0 = \mu\, p_0$, where q_0 is the maximum frictional pressure. The two-dimensional tangential stress fields can be calculated using Equations 2.10, with distinct similarities between the normal and tangential stress fields, notably for σ_{zz}^q and τ_{yz}^q [39]. The p and q, superscripted to each stress component, corresponds to the normal and tangential forces, respectively.

$$\begin{aligned} \sigma_{yy}^q &= \frac{q_0}{b}\left[n\left(2-\frac{z^2-m^2}{m^2+n^2}\right)-2y\right] \\ \sigma_{zz}^q &= \frac{q_0\ \tau_{yz}^p}{p_0} \\ \tau_{yz}^q &= \frac{q_0\ \sigma_{yy}^p}{p_0} \end{aligned} \tag{2.10}$$

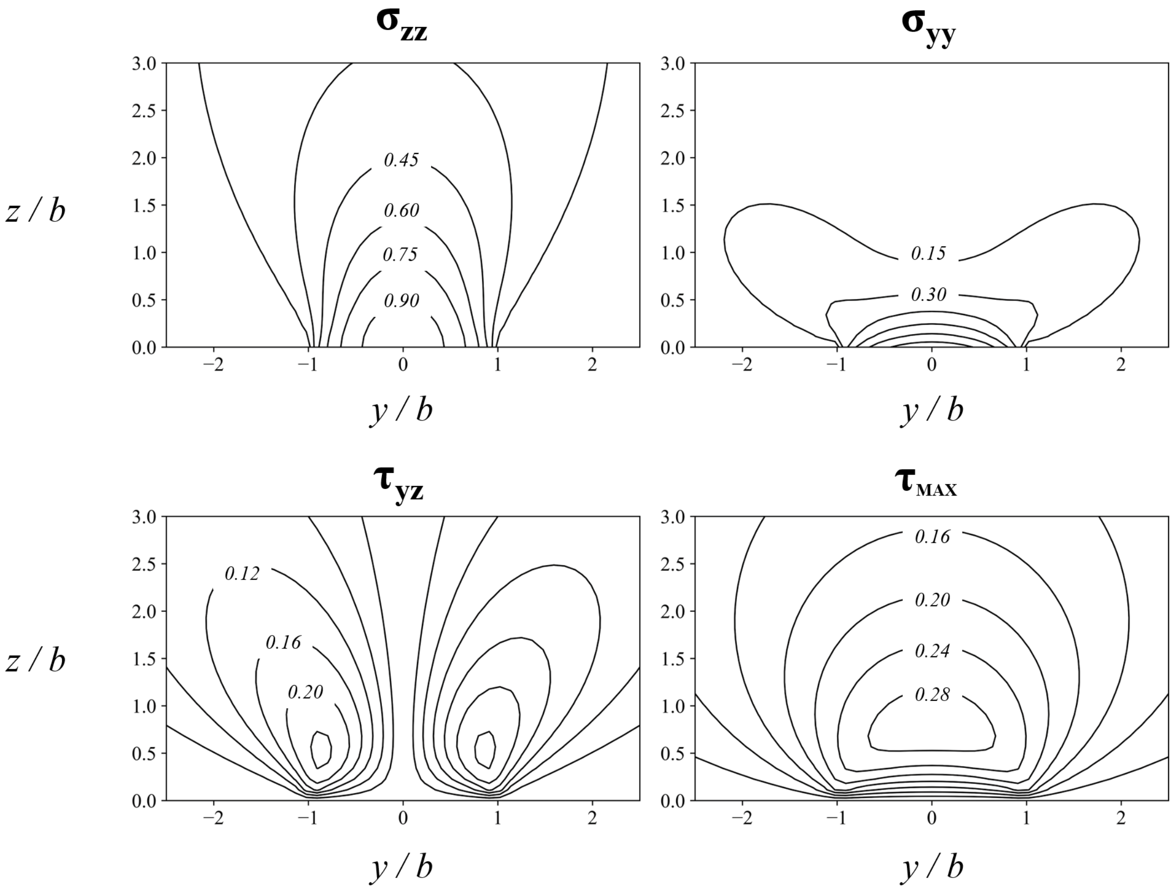

Figure 2.3: Contour maps of the two-dimensional subsurface σ_{zz}, σ_{yy}, τ_{yz} and τ_{max} stress-fields, normalised by p_0.

The subsurface stress approximations from analytical models can be validated using experimental approaches, with the next section focusing on the fundamentals of diffraction techniques, relevant to this study.

2.2 Diffraction techniques

As mentioned, life rating procedures can be relatively poor at predicting WTG bearing failures, with the influence of cyclic subsurface stresses, along with sudden overload events, hypothesised as a principle mechanism for accelerating damage. Non-destructive testing provides the ability to characterise stress during the operation of a component, without inducing damage. Popular non-destructive methods for engineering applications, include the use of radiation, notably X-rays and neutrons, which are capable of penetrating the surface of a sample, permitting bulk material properties to be investigated.

Techniques available at synchrotron X-ray and neutron sources, include imaging, spectroscopy, reflectometry and diffraction. Whilst this work contains novel imaging approaches, the primary focus of this section is to introduce diffraction. It is therefore important to appreciate the fundamentals of elastic coherent scattering, which forms the basis of strain diffractometry. Whilst X-ray diffraction theory is introduced, there is a greater focus on neutron methods, notably data analysis, as neutron experiments contribute most significantly towards the work presented in this thesis.

2.2.1 Basic crystallography

Crystallography is a vast subject, with several textbooks covering the breadth of content within this field [42, 43]. Diffraction heavily relies on the structure of crystalline materials, and it is important to understand how this facilitates the interpretation of results. To simplify, this section only focuses on crystal structures relevant for this work, which are those associated with ferritic and austenitic steel.

Crystal structure of metals

Crystalline materials possess a highly ordered microstructure, where the most basic atomic arrangement is replicated throughout the entire macroscopic structure. Non-crystalline materials, without any structural periodicity, are classed as amorphous and lack clearly defined atomic arrangement. Monocrystalline, or single crystal, materials have a continuous crystal lattice structure throughout the entire volume, without any breaks or variation in orientation. Most metals however are polycrystalline, composed of many crystalline regions with varying size and orientation, referred to as grains. The study of monocrystalline structures is known as single crystal diffraction, whereas the study of polycrystalline materials is powder diffraction [44, 45]. Figure 2.4 demonstrates a basic representation of the atomic arrangement for single crystal, polycrystalline and amorphous materials.

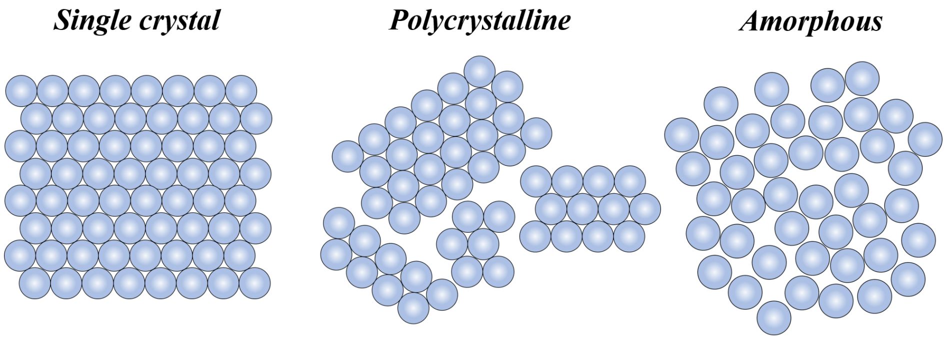

Figure 2.4: Representation of the basic atomic arrangement for structures: (a) single crystal, (b) polycrystalline, (c) amorphous.

For all grains in a single-phase polycrystalline material the lattice structure is identical, yet the grains are aligned differently, relative to each other. This relative distribution of granular orientations dictates the texture of a material, with untextured samples having fully random orientation. Going forward, the bearing steel studied in this work can be assumed as untextured, referred to as demonstrating isotropic behaviour [45].

Unit cell

Crystal structures can be defined by the position of atoms in three-dimensional space, known as a lattice. The unit cell is the smallest repeating pattern of atoms within a crystal lattice, visualised as a three-dimensional shape and characterised by a set of constants describing the unit cell dimensions. The lattice constants, or lattice parameters, consist of the unit cell length dimensions (*a, b, c*) and the angles between them (α, β, γ), as demonstrated in Figure 2.5. The unit cell is constructed of multiple locations, referred to as lattice points, that either consist of an atom or an atomic vacancy [46].

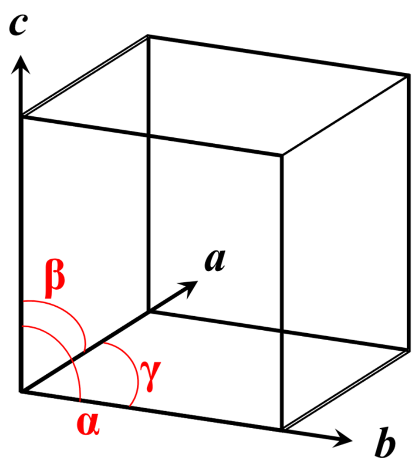

Figure 2.5: Unit cell geometry.

In 1850, Auguste Bravais introduced nomenclature to categorise unit cells, based on their geometry and symmetry properties, which wasn't widely accepted until 1904 when George Friedel validated this through experimental observation [47]. Whilst fourteen potential Bravais lattice configurations exist in three-dimensional space, the purpose of this research is to investigate steel, which primarily constitutes the cubic lattice system, where $a = b = c$. The cubic lattice system consists of three Bravais lattice configurations; primitive, body-centred cubic (*bcc*) and face-centred cubic (*fcc*). It should be noted that martensitic steel has a body-centred tetragonal lattice (*bct*), where $a = b \neq c$ (see Figure2.6d), yet in regard to strain analysis it is generally considered to be *bcc*, as a is approximately equal to c, thus simplifying analytical processing without any significant reduction of accuracy [42, 48].

The simplest cubic structure is known as a primitive unit cell, meaning that it consists of only one lattice point, or atom. Whilst appearing to have eight lattice points in Figure 2.6a, each individual atom is actually shared between another eight adjacent unit cells, therefore only contributing $\frac{1}{8}$ of a lattice point [42]. The *fcc* and *bcc* structures are of most relevance for the steel being used in this research, with ferritic (α-phase) iron possessing a *bcc* structure and austenitic (γ-phase) iron having a *fcc* structure. As mentioned, martensite has a *bct* structure that can be assumed as *bcc* for strain diffractometry experiments [49].

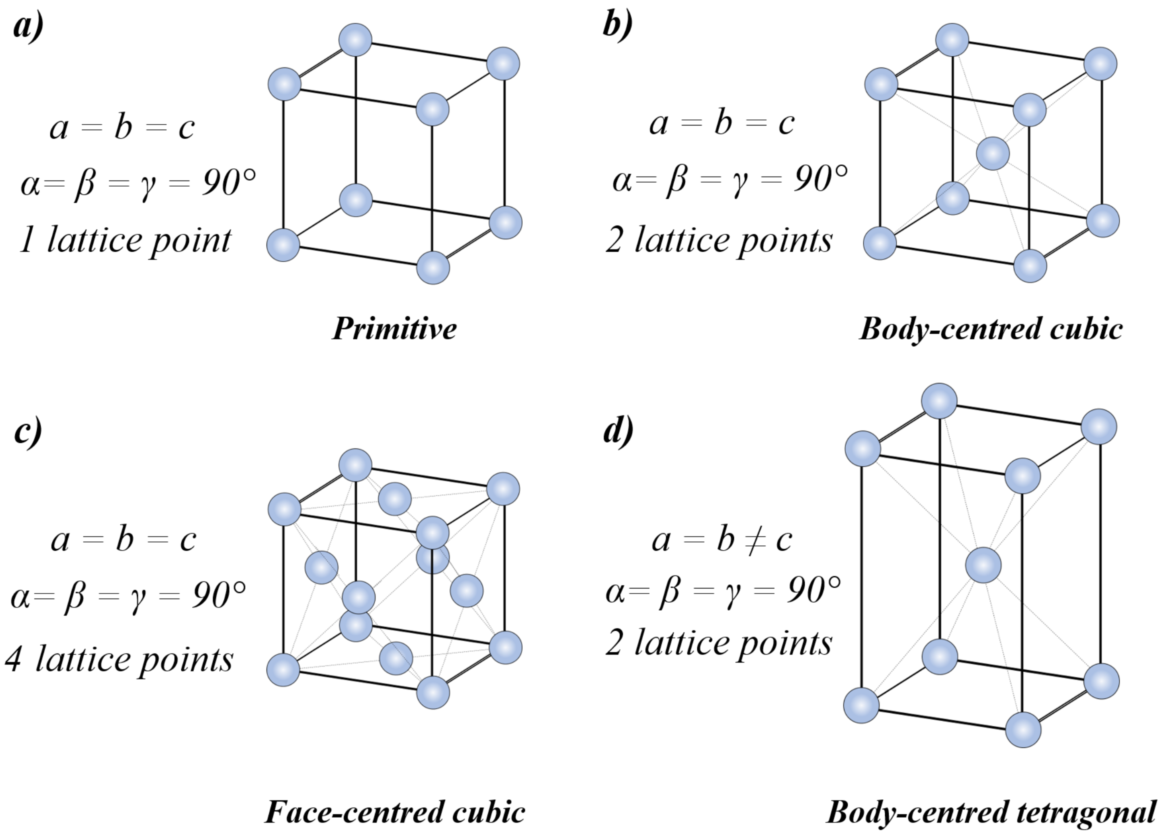

Figure 2.6: Lattice systems associated with steel.

Miller indices

For an entire single crystal, or an individual grain in polycrystalline materials, lattice points can be considered as lying on an imaginary two-dimensional surface, referred to as a lattice plane. In 1839 William Miller introduced, a shorthand notation system providing information about the spacing and orientation of lattice planes within a crystal structure [42]. This indexing system is known as the Miller indices, with lattice planes denoted (*hkl*). The *h*, *k* and *l* are used to represent the points at which a plane intersects the unit cell axis *a*, *b* and *c*, respectively [50]. The *hkl* values signify the smallest permitted integers when a plane intersects the unit cell at *a/h*, *b/k* and *c/l*, as demonstrated in Figure 2.7. It should be noted that if the plane never intersects a specific axis of the unit cell, its intersection point is essentially ∞, meaning its *hkl* value is 0. For example, the plane family (*110*) crosses the unit cell axis at $1a$, $1b$ and never for *c*, whereas the (*211*) intersects at $\frac{1}{2}a$, $1b$ and $1c$.

Due to lattice symmetry, the plane family (*hkl*) will be equivalent to (*khl*) and (*lhk*) etc. Thus, the notation {*hkl*} is used to represent the entire family of planes corresponding to (*hkl*) is being considered. Depending on the crystal structure, only certain *hkl* planes can feasibly exist, with selection rules for cubic structures presented in Table 2.1 [51]. The physical reason for these selection rules is related to the unit cell structure factor, and is discussed further in Section 2.2.4. This is significant, as the distance between *hkl* planes is required for strain calculation. Equation 2.11 gives the general expression for calculating interplanar lattice spacing, frequently referred to as d-spacing or d_{hkl}, for

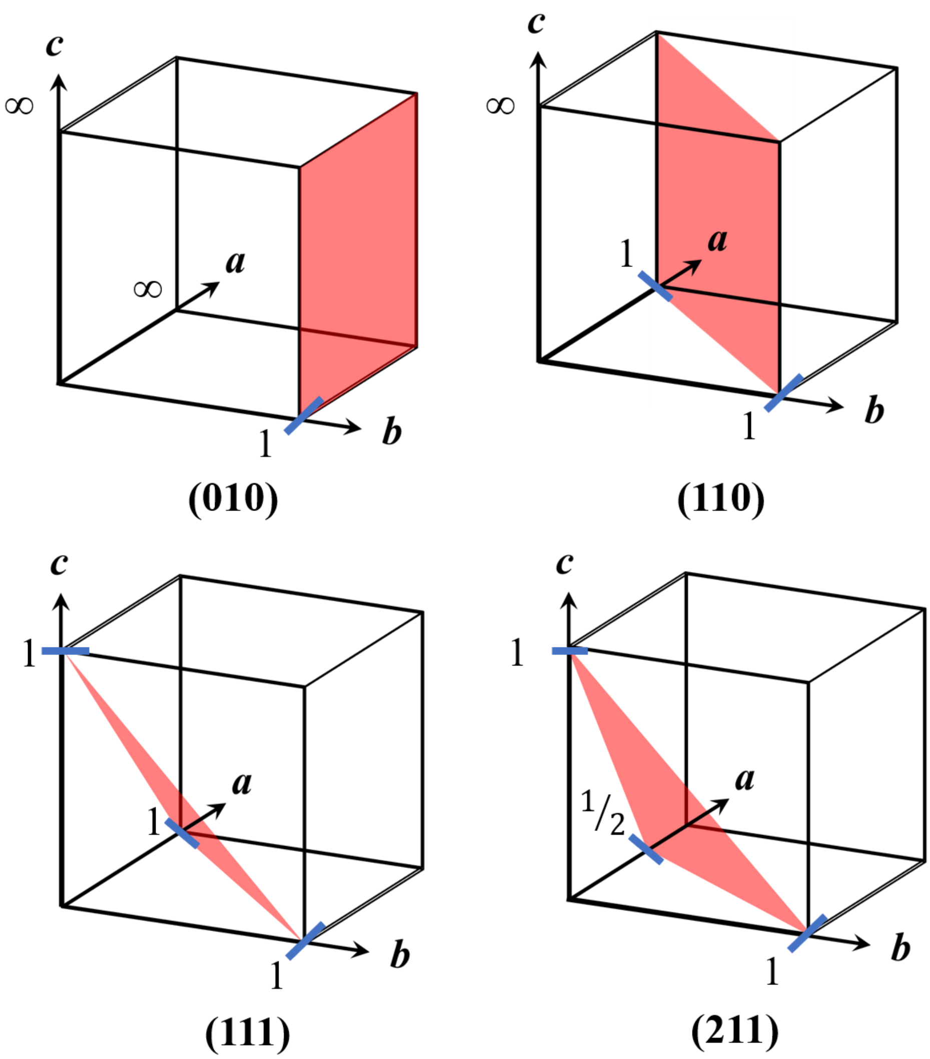

Figure 2.7: Examples of the Miller indices for (010), (110), (111) and (211) planes.

cubic structures.

$$d_{hkl} = \frac{a}{\sqrt{h^2 + k^2 + l^2}} \tag{2.11}$$

Reciprocal lattice

Whilst the Bravais lattice provides a more conventional understanding of how a lattice physically exists in real space, also referred to as direct space, in diffraction theory it is important to understand the concept of reciprocal space. Diffraction is not a conventional microscopy technique, whereby the atomic planar distance can be measured directly. Instead a diffraction pattern provides information about the lattice arrangement in reciprocal space, and needs converting into the more recognisable real space. The majority of work presented throughout the thesis refers to the crystal lattice

Table 2.1: Selection rules for *hkl* families associated with the relevant iron phases [51].

Unit cell structure	Related iron phase	Selection rule	Examples
Primitive	N/A	All *hkl* permitted	*100, 111, 322*
Face-centred cubic (*fcc*)	Austenite (γ-Fe)	*hkl* all odd or all even	*111, 311, 200*
Body-centred cubic (*bcc*)	Ferrite (α-Fe)	$h+k+l=$ even	*110, 211, 200*

in real space, for example d_{hkl}, however a brief explanation of reciprocal space has been included, as it forms the underlying theory of crystallography and diffraction.

Reciprocal space, as the name suggests, is related to real space by reciprocals, for instance the reciprocal lattice vectors a^*, b^* and c^*, are used to describe the unit cell geometry in reciprocal space. The reciprocal lattice vectors are calculated using the real lattice vectors, as seen the Equations 2.12 [46]. The 2π constant is not always found in literature, and depends on the field of study or ones personal preference on how to consider the wave vector, *k*, discussed in Section 2.2.2 [52]. For strain diffraction experiments it is conventional to use 2π, so for consistency it will be used in this work to describe reciprocal space, also referred to as momentum space.

$$a^* = \frac{2\pi\, b\times c}{(a\times b)\cdot c} \quad , \quad b^* = \frac{2\pi\, a\times c}{(a\times b)\cdot c} \quad , \quad c^* = \frac{2\pi\, a\times b}{(a\times b)\cdot c} \tag{2.12}$$

For cubic structures $|a^*| = |b^*| = |c^*|$, and due to the inverse relationship, if a is doubled in real space, a^* is halved in reciprocal space. The *hkl* planes associated with a crystal structure can be characterised using the reciprocal lattice vector, $\mathbf{G}_{hkl}$, which is perpendicular to the associated plane and has a magnitude equal to $\frac{2\pi}{d_{hkl}}$ [51]. As diffraction experiments measure the lattice in reciprocal space, in order to obtain information about the real space lattice parameters, a relationship must be made between the two. Mathematical functions linking reciprocal and direct space are related by the Fourier transform operation. A Fourier transform is a frequently implemented mathematical operation used to convert a function of variables into a new function of their reciprocals. A familiar example is the conversion between time domain and frequency domain, regularly used in signal processing to view the spectral composition of a signal [53]. Fourier transforms are particularly useful as phase information is conserved, meaning that they can be reversed [52].

$$\mathbf{G}_{hkl} = ha^* + kb^* + lc^* \tag{2.13}$$

$$|\mathbf{G}_{hkl}| = \frac{2\pi}{d_{hkl}} = a^*\sqrt{h^2+k^2+l^2} = \frac{2\pi\sqrt{h^2+k^2+l^2}}{a} \tag{2.14}$$

2.2.2 Scattering theory

Now that the basic concepts of crystal structure have been discussed, it is important to understand the intrinsic nature of waves and how this allows for measurement of a crystals interplanar lattice spacing, in turn permitting calculation of elastic strain. Similar to crystallography, scattering theory is a complex subject in its own right, hence this section only focuses on introducing the fundamentals required for understanding X-ray and neutron diffraction experiments.

Wave behaviour

One of the most basic descriptions of a wave is the one-dimensional sinusoidal wave, expressed mathematically in Equation 2.15 [52].

$$\psi(x,t) = A\,\cos(kx - \omega t + \varphi_o) \tag{2.15}$$

Where, ψ is disturbance associated with the specific wave type, A is amplitude, k is the wavenumber, x is linear position in real space, ω is the temporal angular frequency, t is time and φ_o is the phase difference.

The scalar wavenumber is equal to the magnitude of the wave vector, **k**, which as mentioned, can vary in quantity by a factor of 2π, depending on the field of study. The wave vector and wavenumber are important quantities as they describe a wave in reciprocal space, usually in $rad\ m^{-1}$, and can therefore also be referred to as the spatial angular frequency. The wave vector direction is perpendicular to regions of constant phase, known as wave fronts [52, 54].

$$k = |\mathbf{k}| = \frac{2\pi}{\lambda} \tag{2.16}$$

Where, λ is the wavelength.

The characteristic behaviours of a wave are best demonstrated with visible light, for example reflection and refraction, yet the principles of diffraction and interference are the most relevant for this study. Interference relates to the principle of wave superposition, which states that if two or more waves are traversing at the same location in space, the resultant amplitude is at that point is equal to the sum of the incident waves, and related directly to the phase difference, φ_o [55]. For example, if two waves of the same wavelength are in phase and propagate through each other, the resultant amplitude would be double, referred to as constructive interference. If two waves of the same wavelength are π radians out of phase, or in antiphase, the resultant amplitude would be zero, referred to as destructive interference. A simplified diagram is included in Figure 2.8 to demonstrate this effect.

The Huygens-Fresnel principle states that any point on a wave front can be considered as a source of secondary wavelets, described as spherical daughter waves, that sum to produce the subsequent wave front, demonstrated in Figure 2.9a [56]. Diffraction is an important property, occurring as

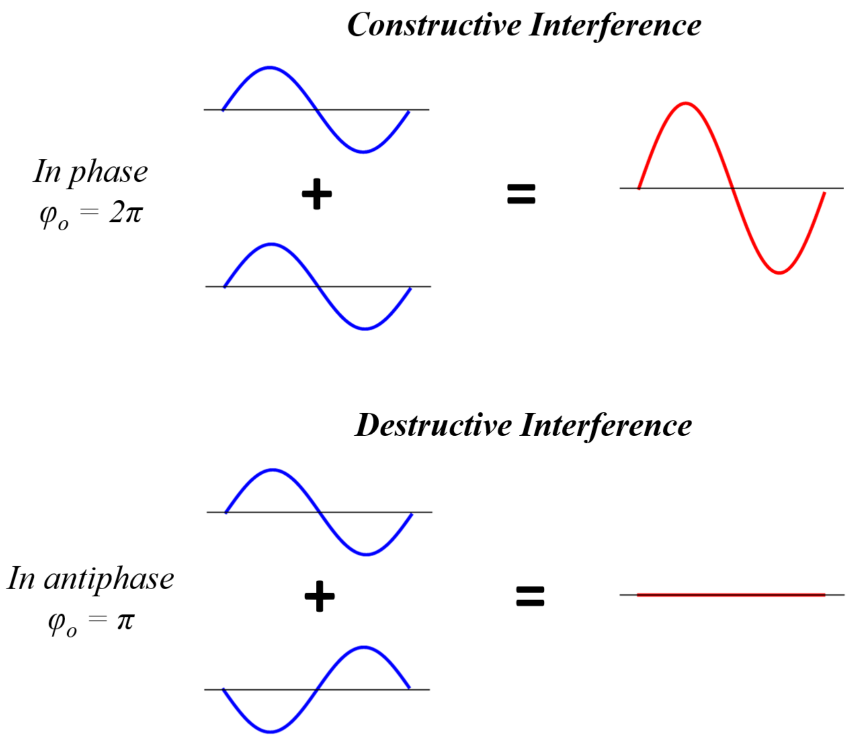

Figure 2.8: Demonstration of constructive and destructive interference for waves in phase ($\varphi_o = 2\pi$) and antiphase ($\varphi_o = \pi$).

waves travel through an aperture or around the edges of an obstacle. Diffraction is observed as a deviation to wave direction, due to wave front modulation, causing a redistribution of energy.

A basic example of the diffraction phenomenon occurs when coherent light passes through an aperture, several times wider than the wavelength of incident light. Along the apertures width, an incident wave front can be considered as a series of individual secondary wavelets. Once through the aperture, inference between these wavelets produces a new wave front, appearing to have spread out, or diffracted [56]. An exaggerated representation is demonstrated in Figure 2.9b, for an aperture of width, W. The effect of diffraction is greatest when the aperture width is equal to the incident wavelength, which is represented by the distance between wave fronts.

Projecting light that has passed through an aperture onto a screen produces a diffraction pattern. The pattern is characterised by a central bright fringe with periodic light and dark fringes either side, with the projected intensity in the bright fringes gradually decreasing (Figure 2.9b). Bright regions are produced by constructive interference and the dark regions are produced by destructive interference, with intensity a function of diffraction angle [52, 56]. If a second aperture is introduced, as Thomas Young demonstrated in 1801, resultant waves passing from both apertures diffract and then interfere with one another. Again, a diffraction pattern is observed, but rather than a single central maxima, it contains several equally dark and bright fringes. Constructive interference at the bright fringes is the result of a path difference, between the two apertures and the screen, being equal to $n\lambda$, where n is an integer value. The central fringe results from waves travelling the same distance ($n = 0$). Dark fringes are the result of destructive interference, with a path difference of $\frac{n\lambda}{2}$

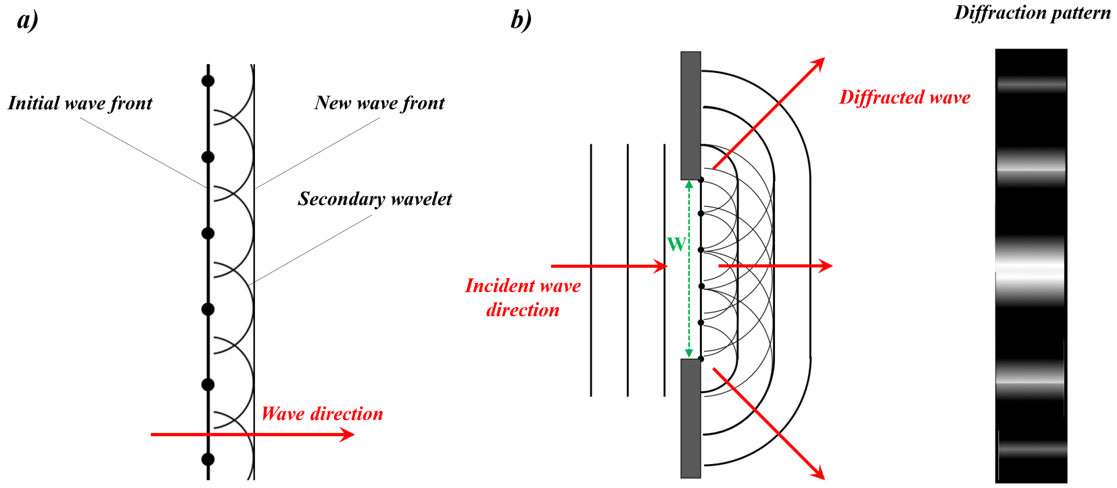

Figure 2.9: (a) Huygens-Fresnel plane wave. (b) Diffraction of a plane wave on passing through an aperture.

[55]. Figure 2.10 presents a schematic of the Young's double slit experiment, including an example of the first order fringe (n=1), with Equation 2.17 showing the simple mathematical relationship between the wavelength, diffraction angle and distance between the slits, d.

$$d \sin\theta = n\lambda \tag{2.17}$$

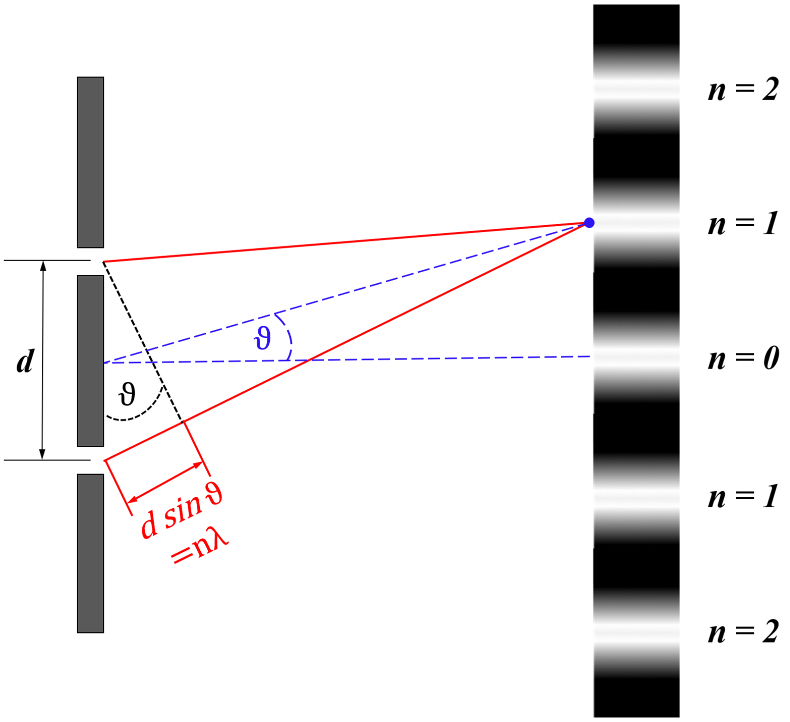

Figure 2.10: Schematic of Young's double slit experiment.

This is a relatively simple experiment, yet it helps to form the basis of strain diffractometry, with distance between the slits being analogous to the interplanar lattice spacings of a crystalline material.

Wave-particle duality

In quantum mechanics, the phenomenon of wave-particle duality states that waves exhibit particle-like behaviour and vice versa. Electromagnetic waves, such as visible light and X-rays, have an associated particle called a photon, described as a quantum of energy generated by an oscillating electromagnetic field. Photons demonstrate particle-like behaviour, as they have finite momentum or positions in space, yet both quantities may not be measured simultaneously [57]. Photon wavelength can be calculated using by Equation 2.18.

$$\lambda = \frac{c}{f} \tag{2.18}$$

Where, c is wave speed and f is photon frequency.

It was determined that the energy of a photon is directly proportional to the frequency, related via a constant of proportionality, the Planck constant, h (6.626 x 10^{-34} J s). Photon energy can therefore be calculated using any of the Equations 2.19 [52].

$$E = hf = \frac{hc}{\lambda} = \hbar\omega = \hbar ck \tag{2.19}$$

Where, $\hbar$ is the reduced Planks constant $(h/2\pi)$, which is considered more useful for calculations that consider angular frequency, such as wave propagation.

Wave-particle duality also describes the wave-like behaviour of particles, such as electrons and neutrons. The corresponding wavelength of a particle, known as the de Broglie wavelength, relates to a particle's momentum (Equation 2.20). The principle of wave-particle duality has been applied for electron microscopy, whereby accelerating electrons using an electric field can result in wavelengths comparable to atomic length scales [52].

$$\lambda_{dB} = \frac{h}{p} = \frac{h}{mv} \tag{2.20}$$

Where λ_{dB} is de Broglie wavelength, and the momentum, p, is the product of particle mass, m, and velocity, v, with a particles kinetic energy, E_k, calculated using Equations 2.21.

Neutrons energies are regularly classified in terms of temperature, with thermal neutrons, considered to be at room temperature, being used for strain measurements because their associated wavelengths most closely resemble interplanar lattice spacings. Table 2.2 contains the energies, velocities and wavelengths that are associated with each classification of neutron temperature.

$$E_k = \frac{1}{2}mv^2 = \frac{h^2}{2m\lambda_{dB}^2} = \frac{|\hbar k|^2}{2m} \tag{2.21}$$

Table 2.2: Temperature classification for neutrons [58].

Classification	Energy (meV)	Wavelength (nm)	Velocity (ms^{-1})
Ultra-cold	0.00025	57	6.9
Cold	1	0.9	437
Thermal	25	0.18	2187
Epithermal	1000	0.029	13,832

Particle Interaction

Atoms are comprised of a dense nucleus, made up of protons and neutrons, surrounded by a diffuse cloud of electrons. Nearly the entire mass of the atom is contained within the nucleus, which has a length scale of femtometres (10^{-15} m), significantly smaller than the atom and therefore can be considered as point-like in comparison. Matter interacts through four fundamental forces, possessing interaction mechanisms and relative strengths that are completely different to one another. The forces are; gravity, weak interaction, electromagnetic and the strong nuclear force, with the latter two being of most significance when probing the structure of matter using particles [52].

As electrons possess a negative charge, repulsive electrostatic forces act between a probing electron and the atomic orbital electrons in matter. Therefore, using electrons to study matter is mostly suitable for surface measurements, as repulsion between the two charges prevents penetration of a sample by more than a few microns. Whilst X-ray photons are uncharged overall, they still interact with orbital electrons via the electromagnetic force, as photons are the result of fluctuating electric and magnetic fields. However, the interaction between X-rays and atomic electrons is much weaker than between two electrons, allowing for greater penetration of matter. Neutrons are not influenced by orbital electrons, instead interacting with atomic nuclei via the strong nuclear force [51]. Of the four fundamental forces, the strong nuclear force is the most powerful, yet only over exceptionally small distances. Also, if comparing the spatial density distribution of the electron cloud and the nucleus, the electrons have a much lower mass over a significantly greater volume. In fact, for simplicity, the spatial distribution of a nucleus may be considered as a Dirac δ-function [52]. It should be noted, neutrons have spin and therefore do in fact interact with magnetic moments, such as those generated in atomic electron clouds. Yet, the impact of magnetic moments is assumed negligible for this research, thus being ignored moving forward.

Elastic scattering

Strain diffractometry experiments rely on a specialised case of particle interaction, known as elastic scattering, whereby there is no transfer of a particles energy on interaction with a sample, i.e. the angular velocity, ω, remains constant. Whilst scattering is responsible for a change in the direction of a particle, for elastic circumstances the magnitude of $\mathbf{k}$ remains constant ($|\mathbf{k}_i| = |\mathbf{k}_f|$) [59]. Figure 2.11 demonstrates the vector diagram of a particle scattering elastically, showing visually the significance of the scattering vector, $\mathbf{q}$ (Equation 2.22). The momentum transfer of the interaction, $\mathbf{p}$, is expressed in Equation 2.23.

$$\mathbf{q} = \mathbf{k}_i - \mathbf{k}_f \tag{2.22}$$

$$\mathbf{p} = \hbar\mathbf{k}_i - \hbar\mathbf{k}_f = \hbar\mathbf{q} \tag{2.23}$$

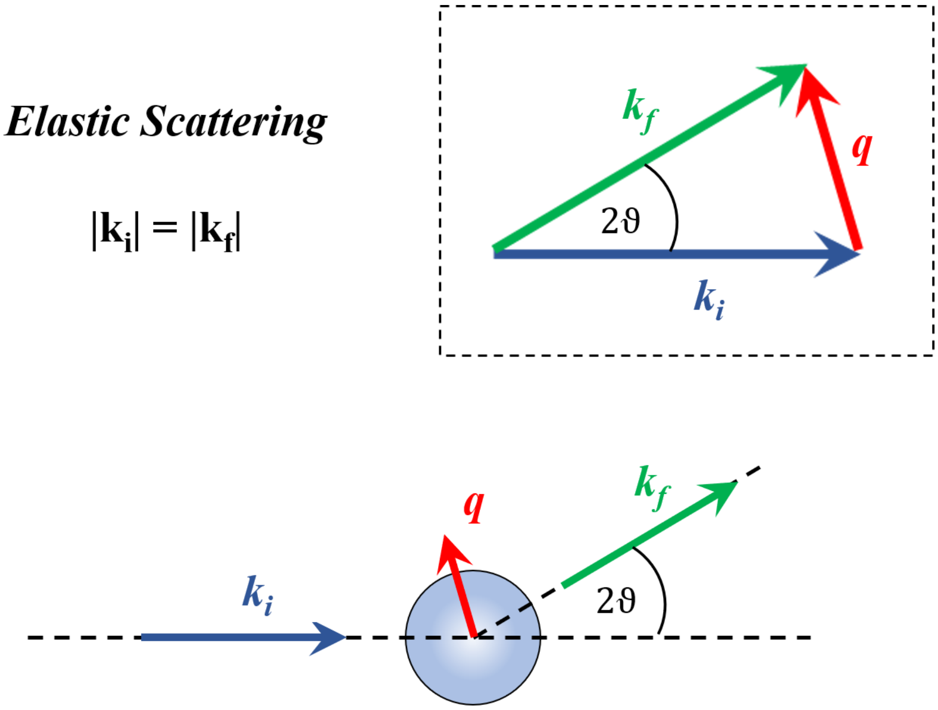

Figure 2.11: Elastic scattering vector diagram.

Note that $q = |\mathbf{q}|$ and is always perpendicular to the interacting *hkl* plane. Conventionally, diffraction spectra are plotted as a function of either d_{hkl} or q. This improves the comparability of separate data sets, acquired using different diffraction techniques or instruments. The measurement of q, or d_{hkl}, is fundamental for this study, as it is required for calculating elastic strain, as discussed later in Section 2.2.3.

$$|\mathbf{q}| = q = 2|\mathbf{k}_i|\sin\theta = \frac{4\pi}{\lambda}\sin\theta \tag{2.24}$$

Bragg's Law

In 1913, a father and son duo, William and Lawrence Bragg, managed to construct a useful yet simple model for explaining diffraction patterns that were observed when examining crystalline materials using X-rays. The Braggs stated that X-rays behaved as if reflecting off individual atomic planes, hence in literature the observation of *hkl* planes in a diffraction pattern is frequently referred to as 'hkl reflections'. In reality, this effect is not radiation being reflected by planes, but instead an interaction followed by a subsequent scattering of wave propagation direction [60].

It was this revelation that led to the formulation of an equation, referred to as Bragg's law, which allows for the calculation of interplanar spacings for specific *hkl* planes, using Equation 2.25. Bragg's law was derived by considering radiation scattered at adjacent planes, with constructive interference only occurring when the path difference, $2d\sin\theta$ is equal to a multiple integer of the wavelength. If Braggs law is satisfied and **q** is perpendicular to the orientation of the specific *hkl* planes, distinct increases of intensity in a diffraction spectrum occur, as the result of interference from many successive planes [61]. Figure 2.12 presents a schematic of scattered waves at two adjacent planes, whereby Bragg's law is satisfied. The aforementioned sharp increases of intensity, when observed in a diffraction pattern, are referred to as Bragg peaks, and provide important information about the crystal structure. Bragg peaks are the result of coherent-elastic scattering, with coherent implying that the diffracted waves must be in phase with each other, thus constructively interfering to produce the peaks.

$$n\lambda = 2d_{hkl}\sin\theta \tag{2.25}$$

The Bragg's law equation can be derived from relationships in reciprocal space, as proposed by Laue, giving appreciation for how diffraction spectra, measured as a function of q, can be used to calculate lattice parameters in real space. Equation 2.26 demonstrates the relationship between d-spacing and the scattering vector.

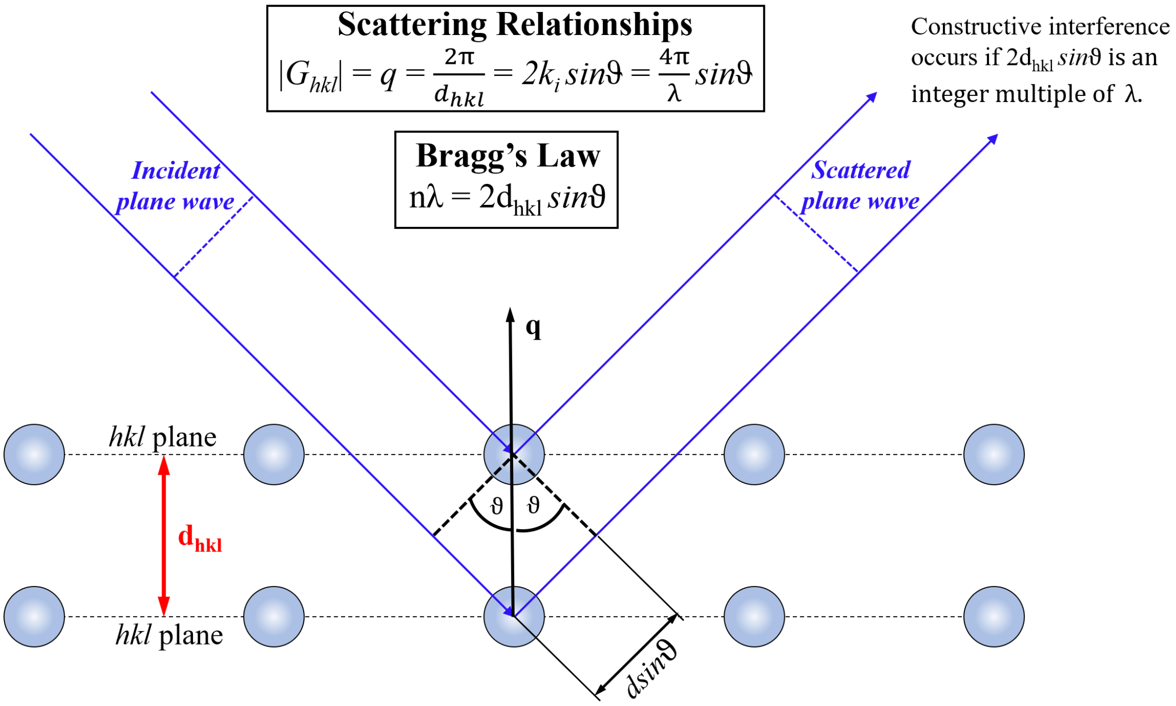

Figure 2.12: Demonstration of Bragg's law, whereby elastic scattering at two adjacent planes results in constructive interference. Some important mathematical relationships are also included.

$$|\mathbf{q}| = q = \frac{2\pi}{d_{hkl}} \tag{2.26}$$

In reciprocal space, variables such as time and distance become frequency and the wavevector, with $\mathbf{q}$, $\mathbf{k}_i$ and $\mathbf{k}_f$ having related directions in real space and reciprocal space. Notice the relationship between q and d_{hkl} for adjacent planes, compared to Equation 2.14, demonstrating that $|\mathbf{q}| = |\mathbf{G}_{hkl}|$ when Bragg's law is satisfied and peaks are produced in a diffraction pattern.

2.2.3 Stress analysis

Ultimately, diffraction spectra provide information about unit cell lattice parameters or the spacing of individual *hkl* planes. For engineering applications this is useful because applied stress will alter the measured dimensions and thus permit the calculation of elastic strain, with the interplanar spacings analogous to a microscopic strain-gauge. Plane specific lattice strains, ε_{hkl}, are calculated from shifts in individual peaks [62]. Applied stress causes induced alterations in d-spacing, which are visualised in diffraction patterns as a shift in peak position. Alternatively, multi-peak refinement of full diffraction spectra allows for changes to the lattice parameter, a, to be analysed, providing strain more representative of the bulk response, ε_{bulk}. A stress-free measurement is usually performed to obtain a reference d-spacing or lattice parameter value, denoted as either d^0_{hkl} or a_0, respectively. Both strain calculations are included in Equations 2.27, with more detail on the different approaches to neutron diffraction data analysis mentioned in Section 2.2.5.

$$\begin{gathered}\varepsilon_{hkl} = \frac{d_{hkl} - d^0_{hkl}}{d^0_{hkl}} = \frac{\Delta d_{hkl}}{d^0_{hkl}} \\ \varepsilon_{bulk} = \frac{a - a_0}{a_0} = \frac{\Delta a}{a_0}\end{gathered} \tag{2.27}$$

Strain diffractometry experiments generally require the following equipment [51]:

- Sources of radiation; whether it is electrons, X-rays or neutrons. This can be monochromatic or polychromatic. To reduce uncertainty in the measured 2θ values, initial strict focusing of the incident beam is important to reduce divergence.
- Sample stage; for rotating the sample. Depending on the type of experiments performed, the stage may rotate on more than one axis.
- Detectors; with the technology used depending on the type of radiation, where gas tubes, scintillators or CCDs are most frequently implemented. Usually collimation is applied to reduce divergence of the diffracted beam. For monochromatic sources, the detector usually moves to acquire data at many values of 2θ, whereas for polychromatic sources the detector position is usually fixed.

Rather than at a single point, strains are measured within a selected volume of the sample material. This volume is located where the incident and diffracted beams intersect, being frequently referred to as the experimental gauge volume [63]. The gauge volume size is dependent on the instrument and determined by precisely controlling the incident and diffracted beam geometries. For polycrystalline materials it is important to consider the crystal grain size, relative to the gauge volume geometry. If grain size is very large, meaning that few grains exist within the gauge volume, orientation of the sample becomes more important as there may not be many *hkl* planes correctly positioned to satisfy Bragg's law. Ideally, a sample will have grains of much smaller dimensions than the gauge volume, and also be assumed as isotropic, meaning that the sample can be orientated in any direction without peak intensity being affected. A perfect single crystal is completely anisotropic and can be assumed as a large individual grain, making consideration of sample orientation essential for measuring the unit cell parameters. As mentioned, for this work AISI 52100 bearing steel is assumed to be isotropic, whilst also possessing suitable grain sizes for diffraction experiments.

There are multiple methods used for measuring the stress-free reference values, with the recommended approach typically depending on the type of experiment being performed. Residual stress characterisation requires a very accurate d^0_{hkl}, or a_0, value which can be obtained by measuring a completely stress-free powder, or by cutting a small sample from the test material, relieving inherent residual stresses [64]. Cutting a small stress-free sample is the preferred option, due to difficulties ensuring that a powder has the same thermo-mechanical properties and composition as the test specimen. However, care must be taken when cutting the sample, with electrical discharge machining preferred for cutting metal specimens, to avoid the introduction of new undesirable residual stresses.

Unlike residual stress characterisation, *in situ* experiments are generally more concerned with the measurement of relative strain, as opposed to an absolute value. This means that a d^0_{hkl}, can be taken from a stress-free region of the test sample without any applied load, or stress. Whilst this method doesn't necessitate an additional stress-free specimen, it does require careful selection of the region to be measured. As this study is mostly interested in the measurement of relative strain, rather than the characterisation of residual stress, no separate stress-free samples were fashioned. However, all components tend to possess varying levels of residual stress and the different types should be considered, along with their influence when interpreting diffraction data.

Types of residual stress

There are two categories of residual stress, known as macrostresses and microstresses. Type-I macrostresses, σ^{RS}_{I}, self-equilibrate over many grains and are representative of the macroscopic behaviour of a sample. Their presence results in observable peak shifts in the diffraction spectra, following continuum models closely, and ignoring the polycrystalline or multiphase nature of a materials [65, 66]. Therefore the multi-peak data fitting procedures are preferred for obtaining information on macrostresses.

Microstresses can be separated into Type-II intergranular stress or Type-III intragranular stress, σ^{RS}_{II} and σ^{RS}_{III}, which equilibrate over the length of an individual grain or on an atomic scale, respectively. Figure 2.13 demonstrates a schematic of the residual stress types across a set of grains. An average of the type Type-II stresses within the gauge volume effects a diffraction pattern in a similar way to Type-I stresses, by shifting the relative peak position, making them difficult evaluate independently. Type-II microstresses are more prominent in multiphase materials, due to variation of elastic or thermal properties between the phases. The effect of Type-II stresses is more obvious when analysing single-peak shifts, opposed to multiple peak shifts, yet they have an influence on the peak shape if they vary wildly within the experimental gauge volume [66]. Type-III microstresses generally result from atomic scale defects such as interstitials, vacancies and dislocations. The presence of intragranular Type-III stresses contributes towards the broadening of peaks, rather than shifts, with the full width at half maximum (FWHM) of Bragg peaks having previously been used to provide information about intragranular stresses, and consequently the presence of plastic deformation [67]. FWHM quantifies the breadth of a Bragg peak at half the maximum intensity, as demonstrated in Figure 2.14.

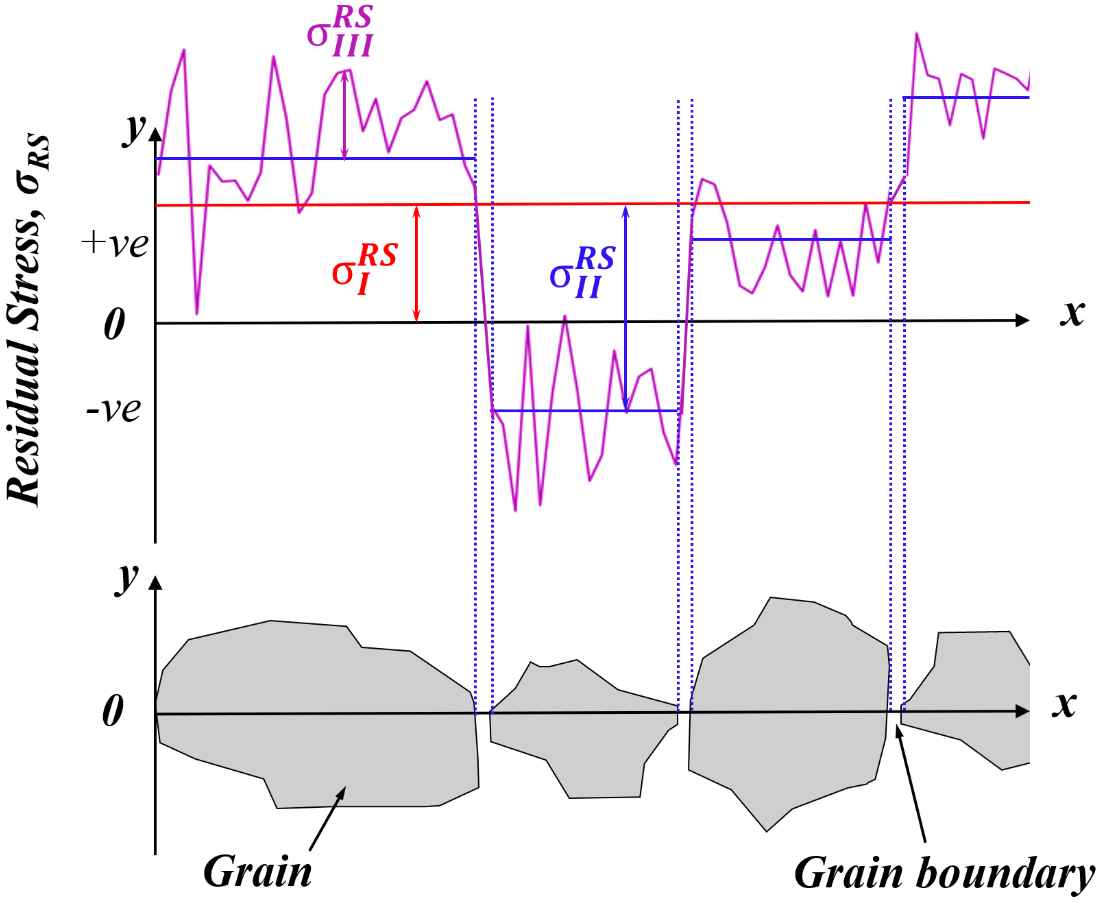

Figure 2.13: Types of residual stress. Macrostress, σ_{I}^{RS}, macrostress self-equilibrating over a significant length scale, whilst microstresses, σ_{II}^{RS} and σ_{III}^{RS}, self equilibrate over a single grain or atomic length scale, respectively.

Typically for homogeneous metallic samples with assumed isotropy, Type-I macrostresses are considered to be the most significant contributors towards peak shifts, yet it is worth considering the potential influence of Type-II microstresses when interpreting results obtained from single-peak fitting [51].

Measurement direction

When planning a diffraction experiment, it is essential to consider the desired strain tensor components to be measured. Sample orientation relative to beam direction determines the measured strain component, which is at the bisector of the incident and diffracted beams in the direction of the scattering vector, q. This effect can be visualised in Figure 2.12, where the direction of q contributing towards constructive interference for a specific *hkl* plane is at an angle of θ from both the incident and diffracted beam. Depending on the exact instrument setup and detector positioning relative to the incident beam, planning which orientations are required is important. For isotropic materials, whereby it is assumed there is no texture and grain orientation is completely random, it is a simpler procedure as the sample orientation is only dependent on the desired components to be measured. Alternatively, for textured samples where peak intensities will vary with sample orientation, more rigorous planning is necessary.

Stress calculation

Whilst diffraction experiment can accurately measure lattice strains, for many applications, engineering stress calculations are necessary. Equation 2.28 demonstrates the relationship between stress and strain. This can be extremely complex, as the elastic stiffness constant, C, has 81 components, with up to 36 being independent. Depending on the instrument, multiple strain components may be measured simultaneously, meaning that stress can be calculated if a suitable proportion of C components are known. Occasionally for engineering applications, where isotropy has been be assumed, C can be described with only two independent elastic constants, Young's modulus, E, and Poisson's ration, v [68]. This results in a generalised Hooke's law equation whereby the measurement of only three strain tensor components is required. This is particularly useful for neutron experiments, assuming the principle stress components are being measured, as data acquisition times are long and generally a maximum of two components can be measured simultaneously.

$$\sigma_{ij} = \sum_{kl} C_{ijkl}\varepsilon_{kl} \tag{2.28}$$

$$\sigma_{ij} = \frac{E}{(1+v)}\left[\varepsilon_{ij} + \frac{v}{(1-2v)}(\varepsilon_{xx}+\varepsilon_{yy}+\varepsilon_{zz})\right] \tag{2.29}$$

Where $i,\ j,\ k,\ l = x,\ y$ or z to represent the component chosen for calculation. Generally, as multiple strain components need to be measured in order to calculate engineering stresses, there are increased magnitudes of propagated uncertainty, associated with statistical and systematic errors of each individual measurement. Consequently, it is more intuitive to compare strain when validating models, such as with Finite Element Analysis [69].

2.2.4 Synchrotron X-ray diffraction

As discussed in Section 2.2.2, X-rays interact with the atom's electron cloud and therefore scattering increases monotonically with atomic number, Z. The atomic form factor, f, is frequently used to quantify the scattering power of X-ray's interacting with individual atoms. The value of f can be calculated as a Fourier Transform of the atoms spatial density distribution, $\rho(r)$, or also referred to as the electron charge density. It should be noted that f decreases with increasing values of 2θ [52]. Equation 2.30 shows the calculation for atomic form factor, with the atom's centre of mass generally represented as $r = 0$. Going forward the dynamic effects of the atom, for example thermal vibrations, will be ignored and the position of the atom in real space is assumed to be stationary.

$$f(q) = \int_0^{\infty} \rho(r) e^{iq\cdot r} \mathrm{d}r \tag{2.30}$$

The atomic form factor provides information associated with the scattering of an individual atom, but for materials with long range order, such as crystals, it is essential to consider how the arrangement of multiple atoms influences diffraction. This is described using the structure factor, $|F_{hkl}|^2$, which is proportional to the detected intensity, $|F_{hkl}|^2 \propto I$. The location of the atom in a unit cell is defined by the vector **R**, which gives x, y, z, positional co-ordinates along the unit cell parameters a, b and c. Equation 2.31 demonstrates how to calculate the structure factor using the form factor and relative positions of unit cells constituent atoms.

$$F_{hkl} = \sum_{j=1}^{N} f_j e^{i\mathbf{G}_{hkl}\cdot\mathbf{R}} = \sum_{j=1}^{N} f_j e^{-2\pi i(hx_j + ky_j + lz_j)} \tag{2.31}$$

This is important because as seen in Table 2.1, for a specific crystal structure, only certain *hkl* planes are present. The value of $|F_{hkl}|^2$ will only be greater than zero for specific *hkl* planes, resulting in the presence of Bragg peaks in the corresponding diffraction pattern. For example, the value of $|F_{hkl}|^2$ is always zero for a *bcc* lattice structure, unless the sum of all *hkl* values is even. Figure 2.14 shows a generic diffraction spectrum of intensity versus d-spacing, however it generally down to convention whether a spectrum is plotted as the function of d-spacing, or scattering vector, q.

Conventional laboratory X-ray diffraction equipment is useful for non-destructively measuring strains, yet is limited to thin surface measurements, as incident energies are usually too low to penetrate the sample sufficiently. In order to generate X-rays with the highest possible energies and flux, and with large energy distributions, a specialised type of radiation is required. Synchrotron radiation is produced when an electron travelling at relativistic speeds is forced to follow a curved trajectory by a perpendicular magnetic field [70]. The Diamond Light Source is a 3 GeV synchrotron facility in Oxfordshire, UK, home to the I12, or JEEP, beamline. The I12 instrument can generate high energy X-rays, in the region of 53 keV to 153 keV, which consequently allows for dense sample materials to be examined, including limited thickness's of steel [71].

Energy-dispersive X-ray diffraction

Traditionally, X-ray experiments have been performed using monochromatic incident radiation and

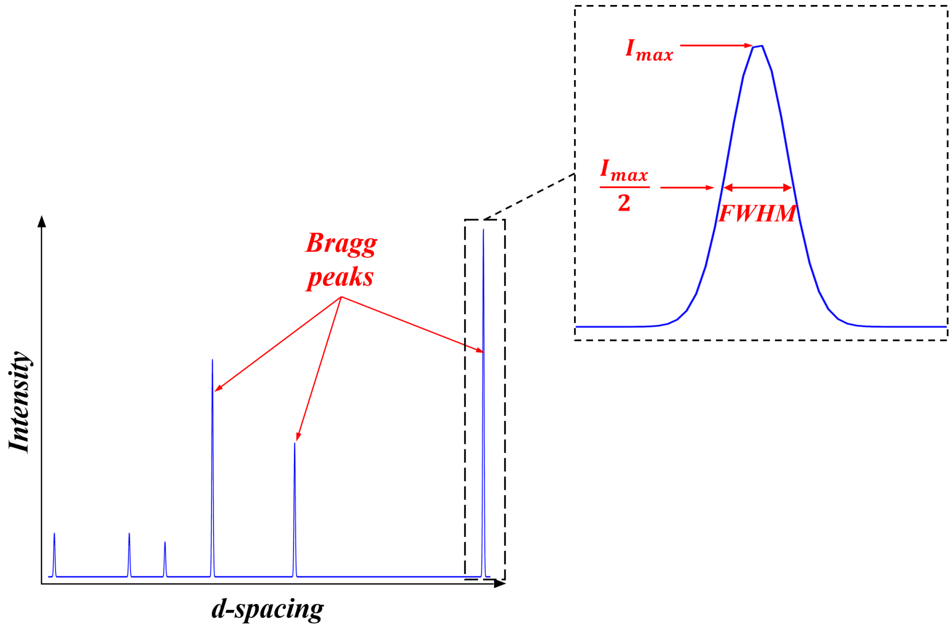

Figure 2.14: A generic diffraction spectrum plotted as intensity versus d-spacing. Inset: a single peak with I_{max} and FWHM demonstrated.

a goniometer to measure precise diffraction angles, plotting intensity as a function of 2θ. Monochromators are usually specifically orientated single crystals that utilise diffraction rules to select the desired wavelength. Energy-dispersive X-ray diffraction (EDXD) uses a continuous spectrum of polychromatic beam and measures diffracted X-rays of different energies at a fixed detector angle [72]. Figure 2.15 demonstrates the main difference between the angle-dispersive and energy-dispersive techniques. The advantages of this process when compared with conventional angle-dispersive methods include; no requirement for a goniometer, a similar quality of data acquired, and also increased sample penetration depths with greater X-ray energy [73, 72]. In terms of this project, the desired property of increased penetration depths is most relevant as strains may be measured deeper within the sample material. The EDXD detector on I12 has 23 individual detecting elements, meaning that 23 components of the strain tensor can be measured simultaneously. As the entire diffraction pattern is acquired, multi-peak analysis allows for accurate determination of the bulk elastic strain, and therefore calculation of the stress tensor if the stiffness constant has been well defined. Greater detail of the EDXD detector and I12 layout is included in Chapter 5.

2.2.5 Neutron diffraction

Whilst X-ray scattering techniques have proven to be a useful tool for measuring residual stress within bulk material, neutron diffraction can be used to provide complimentary strain information. Notable advantages of neutron diffraction include [51]:

- Greater penetration power in most engineering materials, allowing strain measurement deeper within larger components.
- Sample environments, such as furnaces, can be designed using materials with heavier atoms, without a significant loss of neutrons.
- The ability to investigate materials with lower atomic mass, such as hydrogen or lithium.

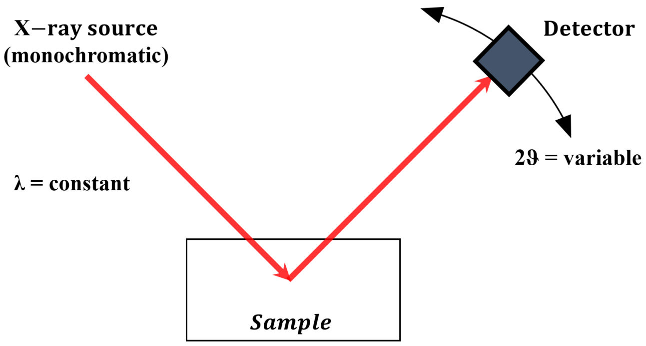

Angle-dispersive diffraction

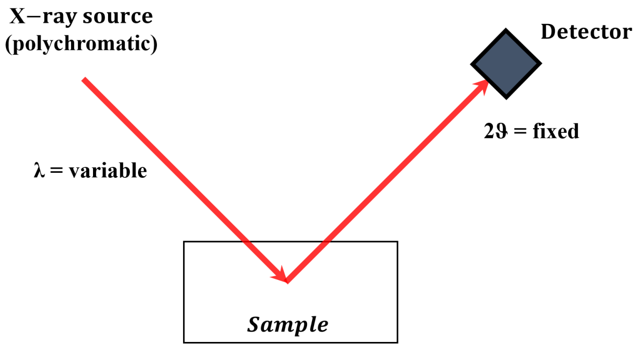

Energy-dispersive diffraction

Figure 2.15: Schematic to demonstrate the difference between angle dispersive and energy dispersive diffraction.

Regarding the work presented in this thesis, reduced flux attenuation by metallic structures, i.e. iron, will be the most significant advantage of using neutron diffraction.

There are two methods of producing neutrons for diffraction experiments. Nuclear reactors, known as steady state neutron sources, generate a continuous beam of varying neutron energies, before a monochromator selects the appropriate wavelengths for the experiment, and is analogous to angle dispersive X-ray diffraction [51]. This method for neutron production is still prominent today, yet various research facilities are focusing their attention on spallation techniques. Spallation, or pulsed, sources use time-of-flight (ToF) neutron diffraction to make the required measurements. The spallation process involves a high energy proton, usually separated from a hydrogen atom, colliding with a heavy metal target. The impact of the proton with the metal nuclei can instantaneously produce roughly 25 neutrons, which predominantly possess higher energies than are necessary. Therefore, the neutrons need to be thermalised using a moderator, which is traditionally water, heavy water or liquid methane, although liquid hydrogen is gradually becoming a more commercially viable option. Each type of moderator provides different energy distributions, meaning that choice of moderator may vary depending on the application of a specific beamline [51].

ToF spallation facilities, such as the ISIS Pulsed Neutron Source in Oxfordshire, are analogous to energy dispersive X-ray diffractometers as the detectors are usually in fixed positions (2θ = constant) and use incident radiation with a range of energies, or wavelengths [74]. Each neutron energy has a corresponding velocity, dictating the time it takes to travel from the spallation target to the detector, which is recorded as ToF. Consequently, Braggs law can be expressed in terms of neutron ToF, derived using the de Broglie wavelength and the linear velocity, as seen in Equation 2.32.

$$d_{hkl} = \frac{h\, ToF}{2mL\sin\theta} \tag{2.32}$$

Where, ToF is the time-of-flight for a neutron to reach the detector and L is the neutron flight path length.

Neutron scattering

Neutrons interact with atomic nuclei via the strong nuclear force, and may be described by their nuclear scattering length, b. The magnitude of neutron scattering lengths for individual nuclei have been measured empirically and may be found in tabulated form, with Sears being cited over 2000 times [75].

The scattering lengths of nuclei are often used to calculate total scattering cross-sections (σ_t), sometimes referred to as "the area of each nucleus as seen by the neutron". For this reason it makes sense that the units may be cm^2, yet in general this is converted to the unit ‘barns’ (1 barn=10^{-24}cm^2). Equation 2.33 demonstrates how this cross-section is calculated [57].

$$\sigma_t = 4\pi b^2 \tag{2.33}$$

Cross-section magnitudes are on a microscopic scale, representing a single nucleus, yet in most cases it is more appropriate to calculate the macroscopic cross-section (Σ), incorporating all atoms within a given volume. Equation 2.34 is used to calculate the macroscopic cross-section, measured in cm^{-1} [51].

$$\Sigma = \sigma_t \rho_a \tag{2.34}$$

Where, ρ_a is atomic density or number of atoms per unit volume.

There are three outcomes for neutron interactions with atomic nuclei, excluding the most frequent event that a neutron is transmitted, meaning that it is unscattered. Neutrons may be coherently scattered, incoherently scattered or absorbed by a nucleus, as demonstrated by Equation 2.35 [75].

$$\sigma_t = \sigma_c + \sigma_i + \sigma_a \tag{2.35}$$

Where, σ_c is coherent scattering cross-section, σ_i is the incoherent cross-section, σ_a is the absorption cross-section.

For strain measurements using neutron diffraction, elastic coherent scattering is of most importance, and as previously mentioned is responsible for Bragg peak intensities, because the diffracted neutrons will be in phase and interfere constructively [52]. Unlike X-rays, where interaction with an electron cloud means that scattering will increase monotonically with atomic number (Z), neutron coherent scattering lengths demonstrate no definitive pattern, appearing irregular in relation to Z [51]. Figure 2.16 plots the coherent scattering length, b_c, for the elements as a function of Z.

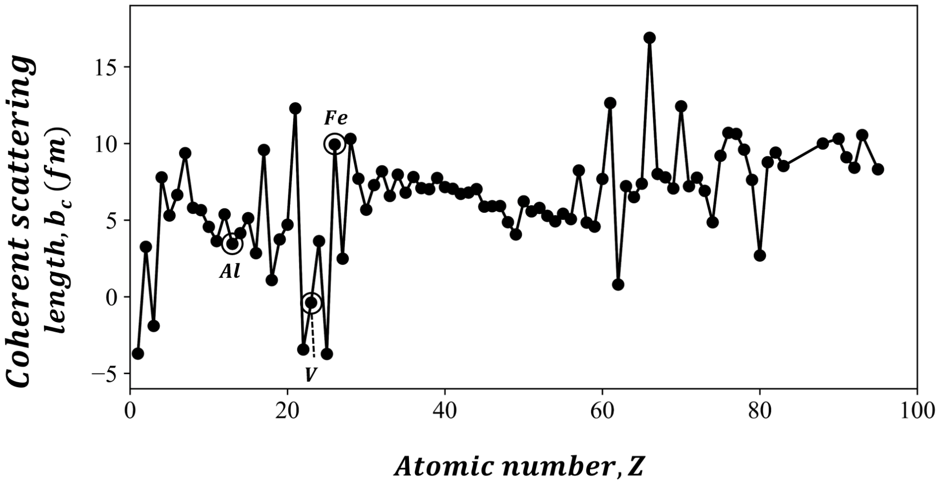

Figure 2.16: Neutron coherent scattering length as a function of atomic number. Values extracted from [75].

The nuclear structure factor, analogous to the X-ray structure factor, is similarly a Fourier transform of the spatial density function, as demonstrated in Equation 2.36, with the nuclear scattering length, b essentially replacing the atomic form factor f. Neutrons interact with the atomic nucleus which is considered to be a Dirac δ-function, or point-like, resulting in the value of b being independent of 2θ, unlike the X-ray atomic form factor.

$$\begin{aligned} F_{hkl} &= \sum_{j=1}^{N} b_j e^{iG_{hkl}\cdot r_j} \\ &= \sum_{j=1}^{N} b_j e^{(-2\pi i(hx_j+ky_j+lz_j))} \end{aligned} \tag{2.36}$$

Where, r_j is the mean lattice position of the nuclei.

Similar to X-rays, neutron Bragg intensity for ToF diffraction is proportional to $|F_{hkl}|^2$. A general expression for intensity, including several wavelength-dependent contributory parameters, is given in Equation 2.37 [76].

$$I_{hkl} = cI_0(\lambda)\varepsilon(\lambda)\lambda^4 V_s A_{hkl}(\lambda)E_{hkl}(\lambda)j|Fhkl|^2\left(\frac{cos\theta\Delta\theta}{4V_c^2\sin^2\theta}\right) \tag{2.37}$$

Where c is the normalisation constant (related to the counting time), $I_0(\lambda)$ is the incident neutron flux at wavelength λ, $\varepsilon(\lambda)$ is the detector efficiency at wavelength λ, $A_{hkl}(\lambda)$ is the attenuation coefficient for the hkl plane, $E_{hkl}(\lambda)$ is the extinction coefficient for the hkl plane, j is the hkl multiplicity factor, V_s is the sample volume, V_c is the unit cell volume, 2θ is the diffraction angle, $\Delta\theta$ is the angular width of the detector.

Time-of-flight strain diffractometry

ENGIN-X, is an optimised ToF neutron strain scanner, and is the instrument where a vast majority of the diffraction experiments discussed throughout this work were performed. A liquid methane moderator is used for thermalising neutrons to energies most suitable for engineering materials, corresponding to a high flux of over 1-3 Å wavelengths. Neutrons are guided from the moderator down the beamline using supermirrors, before apertures are used to control the incident beam geometry. Two detector banks, each composed 1200 ZnS/6Li scintillator elements, sit at 90° to the incident beam and are separated from the sample by a series of collimators, for defining the gauge volume size. The total neutron flight path for ENGIN-X is longer than in most of the instruments at the ISIS research facility, improving the ToF resolution, imperative for making accurate strain measurements [74].

To interpret the data acquired from on a ToF instrument, diffractometer parameters (DIFA, DIFC and ZERO) are required. These experiment dependent constants are refined by performing a scan on a calibration sample, most commonly cerium oxide, as it has well defined lattice parameters. Once the diffractometer parameters have been determined, the exact d-spacing value can be calculated for each ToF, using the quadratic Equation 2.38. Diffraction parameters generally differ depending on the specific instrument and experimental setup [77].

$$ToF = DIFA\, d_{hkl}^2 + DIFC\, d_{hkl} + ZERO \tag{2.38}$$

Where, $DIFA$ produces small ToF corrections for sample absorption, $DIFC$ directly relates the ToF to d-spacing and $ZERO$ is used to correct for delays in moderator emission times [78].

Usually, another scan is performed on a vanadium sample, which is a weak coherent scatterer and strong incoherent scatterer, providing information about incident neutron beam intensity as a function of ToF, allowing for data normalisation [74]. On obtaining the correctly calibrated and normalised diffraction spectra, data analysis can be performed to extract either the individual Bragg peak positions or refined lattice parameters.

Data analysis

Once a scan has been performed, calibration diffractometer parameters have been obtained and the diffraction spectra have been acquired, there are several approaches to analysing the data. Software are available to aid with extracting lattice parameters and d-spacings from the data, such as General

Structure Analysis System (GSAS) for neutrons or Data Analysis WorkbeNch (DAWN) for synchrotron X-rays, yet a fundamental overview of the fitting procedures used for analysis has been included.

The exact nature of fitting a single-peak depends, not only on the radiation being used, but also heavily on the specific instrument. Intensity is related not only to the structure factor for a specific *hkl* plane, but also to the profile peak shape function. Many data sets possess symmetric peaks, where a Gaussian or Lorentzian function is appropriate, such as for EDXD data. The convolution of a Gaussian and Lorentzian function is known as a Voigt profile function and can be useful if the data set requires advantages from both the Gaussian and the Lorentzian approaches. However, asymmetric peaks are pertinent for this work as they are usually associated with ToF neutron spectra.

Moderation of the incident neutrons provides a range of neutron wavelengths, meaning that flux intensity vary depending on wavelength. Due to the asymmetric nature of peak profiles on ENGIN-X, a pseudo-Voigt convoluted with back-to-back exponentials is used [79]. The exponentials govern the rise and decay of the peak, which gives the non-symmetrical shape as there is a sharp rise and slower decay. The profile peak shape function, $H(\Delta T)$, is described in Equation 2.39, where ΔT is the difference between the *hkl* plane ToF profile position, T, and the expected position, T_{ph} [78].

$$H(\Delta T) = \int E(\Delta T - t)\ pV(t) \mathrm{d}t \tag{2.39}$$

Where, $E(\Delta T - t)$ is the back-to-back exponentials (Equation 2.40) and $pV(t)$ is the psuedo-Voight function, a linear combination of a Lorentzian, $L(t,\Gamma)$ and a Gaussian $G(t,\Gamma)$ function (Equations 2.41).

$$\begin{gathered} E(t) = 2Ne^{\alpha t} \quad \text{for} \quad t < 0 \\ \text{and} \\ E(t) = 2Ne^{-\beta t} \quad \text{for} \quad t > 0 \end{gathered} \tag{2.40}$$

Where N is the normalisation factor ($N = \alpha\beta \big/ [2(\alpha+\beta)]$), with α and β the d-spacing-dependent exponential rise and decay coefficients, respectively.

$$\begin{gathered} pV = \eta L(t\Gamma) + (1-\eta)G(t,\Gamma) \\ L(t) = \frac{\Gamma_L}{2\pi} \frac{1}{\left[\left(\frac{\Gamma_L}{2}\right)^2 + t^2\right]} \\ G(t) = \frac{1}{\sqrt{2\pi\Gamma_G^2}} \exp\left[-\frac{t^2}{2\Gamma_G^2}\right] \end{gathered} \tag{2.41}$$

Where, Γ_L and Γ_G are the FWHM for the Lorentzian and Gaussian functions, respectively, whilst η is a parameter referred to as the mixing factor, detailed further in Thompson et al [80].

Fitting single-peaks can provide useful information on elastic anisotropy, texture and plastic deformation, as individual {*hkl*} planes behave differently under stress. However, it is generally accepted that obtaining the averaged lattice parameters, using several peaks, provides better comparison with applied macroscopic strain. Rietveld refinement, is frequently adopted for performing such analysis, as it is a powerful tool for determining information about a crystal's structure, such as atomic coordinates, unit cell geometry and lattice parameters. Rietveld refinement uses a least squares approach to reduce the difference between a calculated and an observed diffraction pattern. Equation 2.42 demonstrates the use of Rietveld method for calculating intensity.

$$Y_{xc} = Y_{xb} + \sum_{p=p_1}^{p=p_2} G_{xp} I_p \tag{2.42}$$

Where Y_{xc} is the calculated intensity at point x in the diffraction pattern, Y_{xb} is the background intensity at point x in the diffraction pattern, G_{xp} is the normalised peak profile function at point x for *hkl* plane p, I_p is the Bragg intensity of *hkl* plane p, whilst p_1 to p_2 are the planes contributing to intensity at point x.

For strain analysis, whereby accuracy of the peak position is essential but peak intensity is considered of less importance, an alternative fitting procedure is frequently utilised. Pawley refinement only constrains peak positions, allowing for calculation of highly accurate lattice cell parameters and concurrently lattice strains. When assuming isotropy the Pawley method is usually applied, as Bragg peak maximum intensity is assumed to be a free parameter [81]. The Rietveld and Pawley methods have been demonstrated to successfully measure lattice strains, representative of the applied macroscopic Youngs Modulus, with very little influence from the Type-II intergranular strains, which is less true for single-peak analysis. Some *hkl* planes demonstrate better agreement with the bulk elastic modulus than others, as they are not as prone to the effect of Type-II stresses.

Figure 2.17 demonstrates elastic strain response of different planes associated with *fcc* austenitic steel, along with Rietveld analysis, the materials Young's modulus and strain gauge measurements [65]. The {200} family is clearly unrepresentative of the strain response within the elastic regime, especially when compared with the {311} family, which demonstrates a similar trend to the Young's modulus and strain gauge, until the elastic limit is reached. The Rietveld method generates strain values, much more closely matching the Young's modulus, but as these diffraction techniques are only capable of measuring elastic strain, they become unreliable above the elastic limit. Table 2.3 contains the planes associated with ferritic and austenitic steel that are most and least influenced by the presence of intergranular stress, helping with selection for single-peak analysis [51]. Note that ToF sources record the entire diffraction pattern, making refinement approaches possible. At a continuous reactor source, it is commonplace to measure just a single-peak, meaning that the choice of peak becomes essential to ensure the measured ε_{hkl} response is representative of the materials

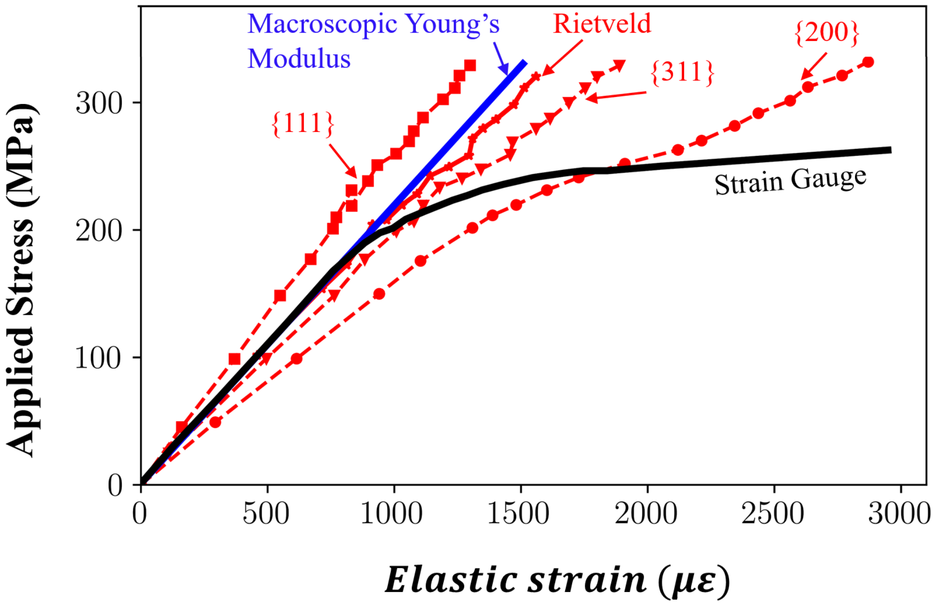

Figure 2.17: Austenitic steel elastic strain response for individual *hkl* planes compared with a Rietveld refinement, Elastic modulus and strain gauge readings. Adapted from [65].

Table 2.3: The recommended and problematic lattice planes associated with in ferritic (*bcc*) and austenitic (*fcc*) steel [51].

Unit cell structure	**Recommended planes (weakly affected by Type II stress)**	**Problematic planes (strongly affected by Type II stress)**
bcc	{211}, {110}	{200}
fcc	{311}, {111}, {422}	{200}

ε_{bulk} response.

2.3 Summary

The key concepts of neutron elastic scattering theory have been introduced, as the use of neutron diffraction and imaging techniques comprise the most novel content in this thesis. Time-of-flight neutron methods offer the unique ability to measure bulk strain deep within large samples, making them incredibly useful tools for engineering applications.

Elastic strain measurements using diffraction techniques, require an understanding of the crystal structure, notably the relevance of Miller indices notation. Each Bragg peak in a diffraction pattern corresponds to a single *hkl* plane, with elastic anisotropy and the influence of intragranular stress becoming of great significance, particularly when considering single peak analysis. Diffraction data provides information about the lattice structure in reciprocal space, i.e. $|G_{hkl}|$, with Fourier transforms being used to obtain the direct lattice parameters, for instance d_{hkl}, which are required to calculate elastic strain. Therefore, the most frequently implemented techniques for fitting single peaks, and for multi-peak refinement, have also presented.

This study aims to demonstrate the development of a technique with the capability to stroboscopically measure time-resolved strains in dynamic engineering components, using both neutron and X-ray diffraction. The specific application of this technique is to perform long term measurements of cyclic contact strains associated with rolling contact fatigue, in the overloaded static raceway of a roller bearing. Consequently, the project allows for useful information to be gathered on the influence of overloading on the fatigue life of WTG bearings. Additionally, the theory introduced in this section helps with understanding the concepts of neutron imaging approaches, which have also been developed for the characterisation of damage in engineering components.

CHAPTER 3

APPLICATION OF NEUTRON IMAGING TO DETECT AND QUANTIFY FATIGUE CRACKING

Authors: A. Reid[1], M. Marshall[1], S. Kabra[2], T. Minniti[2], W. Kockelmann[2], T. Connolley[3], A. James[4], TJ. Marrow[5], M. Mostafavi[4].

[1] *University of Sheffield, Dept. Mechanical Engineering, Sheffield, S1 3JD, UK;*

[2] *STFC-Rutherford Appleton Laboratory, ISIS Facility, Harwell, OX11 0QX, UK;*

[3] *Diamond Light Source Ltd, Harwell Science and Innovation Campus, Didcot, Oxfordshire OX11 0DE, UK;*

[4] *University of Bristol, Dept. Mechanical Engineering, Bristol, BS8 1TR, UK;*

[5] *University of Oxford, Dept. of Materials, Oxford, OX1 3BD, UK;*

Abstract: *Non-destructive imaging techniques provide a unique opportunity to study crack initiation and propagation behaviour in structural materials. To evaluate the applicability of different volumetric imaging techniques, a round bar notched sample of duplex stainless steel was fatigue cracked and studied in situ and ex situ. Neutron and synchrotron X-ray tomography was used along with destructive methods and Bragg edge neutron imaging to evaluate the fatigue crack. Neutron attenuation tomography obtained a three-dimensional image in which the crack was readily identifiable. The neutron tomography, although lower in spatial resolution compared with the X-ray synchrotron tomography and requiring higher acquisition time, is sensitive to the phase chemistry, and has the potential to study engineering size components. Bragg edge neutron transmission imaging allows for the mapping of two-dimensional elastic strains and was used to identify the fatigue crack from the reduction in the strain in the region where the crack propagated. A finite element model of the cracked specimen was used to simulate the average through thickness strain that is measured by the Bragg* *edge neutron imaging technique. The strains measured in the ferritic phase correspond better with the simulation strains than the strain measured in the austenitic phase. It is concluded that this difference is due to strain partitioning, which is influenced by the strong texture present in the duplex steel.*

3.1 Introduction

Structural integrity assessments are important tools when aiming to safely predict the longevity of service components. Many such assessments consider the most common damage mechanisms of engineering components, offering models for fatigue life predictions. Developing a comprehensive understanding of fatigue crack initiation and propagation to inform the models is therefore of great engineering importance. Such predictive models can be used to forecast the fatigue life of service components, with the aim of reducing cost while maintaining safety. Validating fatigue life estimations through comparison with experimental results of non-destructive and destructive techniques is pivotal [82, 83, 84]. However, fatigue failure is microstructurally sensitive [85], and is best described by probabilistic processes. Models for predicting fatigue life are inherently statistical, making their validation difficult. Detecting fatigue cracks is particularly challenging and has been the subject of research for many years.

Destructive micromechanical methods (e.g. serial sectioning [86]) to detect crack initiation sites and propagation paths are well-established. Non-destructive techniques, for example acoustic emission (AE) combined with advanced signal processing [87], offer *in situ* analysis of propagating cracks, though with lower resolution than destructive methods. Optical techniques to identify crack initiation, as well as quantifying associated parameters, such as opening displacement, are widely used in academic studies. One such technique, that is gaining popularity in recent years, is optical or scanning electron microscopy combined with digital image correlation [88]. Digital image correlation (DIC) is now a routine full-field technique for surface displacement measurements and has previously been used, in conjunction with finite element analysis, to calculate crack driving forces [89]. DIC tracks the displacement of a surface speckle pattern before and after material deformation, which makes the calculation of full-field displacement possible. Similar to digital image correlation analysis of surface cracks, digital volume correlation (DVC), applied on laboratory or synchrotron X-ray tomography, has been demonstrated to quantify cracks within the material [90, 91]. While DIC analysis of surface cracks is applicable to all materials, the DVC analysis is only possible on materials which have the appropriate speckle pattern required for image correlation inside them. This prerequisite limits DVC analysis to materials that are composite (e.g. Aluminium Titanium metal matrix composites [92] or nodular cast iron [93]) or heterogeneous materials (e.g. nuclear graphite [94] or wood [95]).

Computed tomographic imaging, performed for DVC, is also useful to study the behaviour of fatigue cracks because of the three-dimensional nature of the crack propagation path [96]. The two widely used techniques are X-ray (laboratory and synchrotron) and neutron tomography. Advances in X-ray imaging are well reported [97, 98, 99], notably as it is developed in parallel with medical research

[100]. Neutron imaging techniques, however, have been less advanced due to the limited number of instruments capable of offering the technique. Both X-ray and neutron tomography have their advantages and disadvantages, for example neutrons can penetrate greater depths in most metallic systems, such as steel, when compared to X-rays, making them more suited for studying engineering components [51]. However, the lower spatial resolution of neutron tomography and often longer acquisition times mean that detailed analysis of smaller features [101], such as cracks, is difficult. The two techniques (X-ray and neutron tomography) provide complementary information, potentially adding more value when used in conjunction with one another for more in-depth analysis. Presently, the UKs dedicated neutron imaging beamline, IMAT, at ISIS Muon and Neutron Source, is advancing time-of-flight (ToF) neutron imaging, energy dispersive radiography, and white-beam tomography for engineering [102] and material science [103] applications.

Duplex Stainless Steels are important for corrosion resistant applications [104]. Duplex stainless steels have two microstructural phases, usually with near equal phase volumes, of ferrite and austenite steel [105]. This complex microstructure, which is often accompanied by internal residual stresses and strong textures, makes predicting the fatigue behaviours of duplex steels complicated [106]. For very high cycle fatigue, it has been suggested that crack nucleation sites generally occur at the phase boundaries on the materials surface [107], yet the presence of non-metallic inclusions has been found to initiate cracking in the material subsurface [108]. Also, much work has focused on low cycle fatigue [109, 110], whilst medium cycle fatigue regime for duplex steel is less understood [111].

The aim of this study is to investigate medium cycle fatigue crack nucleation and propagation in a duplex stainless steel, Alloy 2205, using two neutron imaging techniques: Bragg edge transmission imaging and neutron computed tomography (NCT). While neutron Bragg edge imaging allows measurement of the average elastic strain variation through the thickness of a sample, neutron computed tomography visualises the three-dimensional internal structure. Bragg edge transmission imaging has successfully been used to examine the residual strain developed during additive manufacturing of Inconel 625, via direct metal laser melting [112]. A recent study measured the compressive residual strain beneath the surface of a laser-shock peened plate [113]. The technique has also been employed to map the strain field around a fatigue crack propagating through X70 steel [114]. The neutron imaging techniques were complemented by parallel beam, synchrotron X-ray computed tomography (XCT) and the results of these various non-destructive techniques were validated using destructive, post-mortem scanning electron microscopy. The literature on crack detection using XCT is rich [115] but there are few studies that report crack detection and quantification using Bragg edge transmission imaging or NCT [116, 117]. This is partly due to the novelty of detectors and instruments that are capable of making such techniques more widely available. Future approaches could potentially combine three-dimensional Bragg edge transmission imaging with neutron tomography and DVC to study the elastic and plastic behaviour of materials.

This paper will assess the extent and limitation of neutron imaging techniques to identify and quantify crack nucleation and propagation. In addition, both neutron techniques will be shown to be able to distinguish different phases of the duplex steel as well as quantifying strain partitioning between the phases. In particular, NCT, unlike XCT, allows for different phases in the material to be identified.

3.2 Background

3.2.1 Bragg edge transmission imaging

In Bragg edge neutron transmission imaging, the incident neutron beam is directed at the sample and a neutron counting detector is placed directly behind the sample. The arrangement allows for measurement of Time of Flight (ToF) for individual transmitted neutrons through the sample. The ToF measurements of individual neutrons are used to calculate their wavelength:

$$\lambda = \frac{ht}{mL} \tag{3.1}$$

where λ is the wavelength of the neutron, t its time of flight, h is Plancks constant (6.626 x 10^{-34} Js), m is the mass of the neutron (1.675 x 10^{-27} kg), and L is the path length of the neutron (beamline specific). A spectrum comprising the intensity of neutrons passed through the sample as a function of their wavelength can therefore be created. Transmission spectra contain distinctive increases of intensity, associated with the neutron wavelength at which Braggs law ($2dsin(\theta) = n\lambda$, where θ is the angle between the neutron beam and the lattice plane, d is the lattice spacing and n is an integer) is no longer satisfied for a given family of (*hkl*) lattice planes [114]. At this neutron wavelength, 2θ angle becomes greater than 180° for the given (*hkl*) and neutrons of energies lower (higher wavelength) than this are transmitted and no longer diffracted. An increase of intensity is observed at this wavelength in the transmission spectrum, known as a Bragg edge [118, 119]. A Bragg edge wavelength corresponds to twice the interplanar lattice spacing and is analogous to a Bragg peak, in that shifts in the Bragg edge position can be used to calculate elastic strain:

$$\varepsilon = \frac{d - d_0}{d_0} = \frac{\lambda - \lambda_0}{\lambda_0} = \frac{\Delta\lambda}{\lambda_0} \tag{3.2}$$

Where, d is the lattice spacing, d_0 is the stress free lattice spacing, λ is the wavelength at Bragg edge position and λ_0 is the stress-free Bragg edge position; $\Delta\lambda$ is shown in Figure 3.1 schematically which demonstrates an exaggerated Bragg edge shift, caused by the application of a compressive load.

It has been shown that an analytical function can be used to fit a Bragg edge, giving a wavelength position in the transmission spectrum [112]:

$$\begin{aligned} T(\lambda) = C_1 + C_2 \Bigg[& efrc\left(\frac{\lambda_{hkl} - \lambda}{\sqrt{2}\sigma}\right) \\ & - exp\left(\frac{\lambda_{hkl} - \lambda}{\tau} + \frac{\sigma^2}{2\tau^2}\right) efrc\left(\frac{\lambda_{hkl} - \lambda}{\sqrt{2}\sigma} + \frac{\sigma}{\sqrt{2}\tau}\right)\Bigg] \end{aligned} \tag{3.3}$$

where $T(\lambda)$ is transmission intensity at wavelength λ, λ_{hkl} is the wavelength of the Bragg edge associated with (*hkl*) plane, σ is the edge width, τ is the edge asymmetry, and C_1 and C_2 are constants

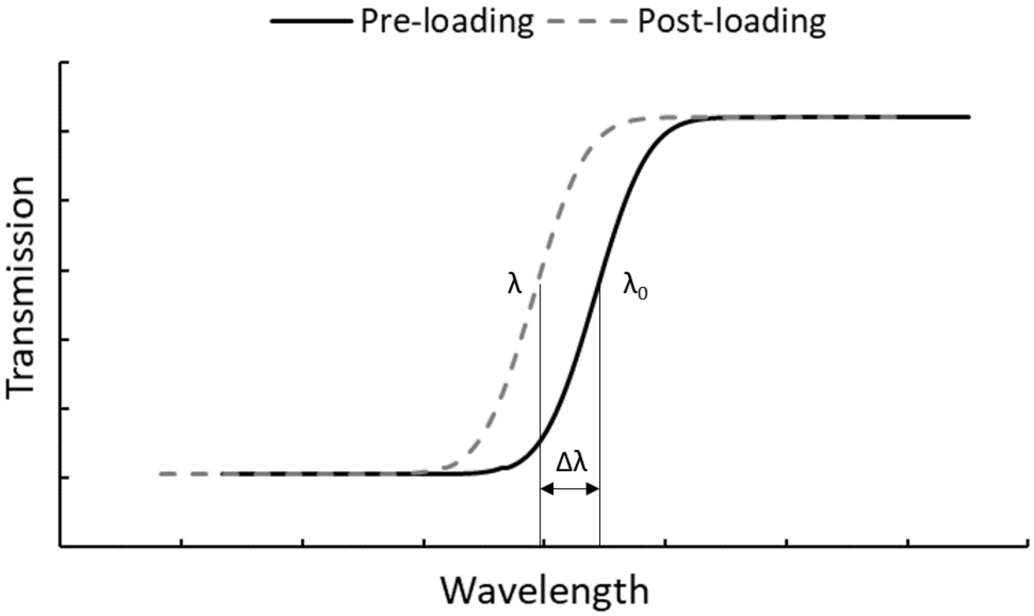

Figure 3.1: A Bragg edge pre-loading and post-loading, with an exaggerated shift to demonstrate the effect used to calculate elastic strain.

related to the offset and height of the edge, respectively. The function was used to plot the Bragg edges in Figure 3.1. Bragg edge imaging has been successfully used to measure through thickness average elastic strain with $\Delta\varepsilon \approx 10^{-5}$ accuracy [120].

The Bragg edge transmission imaging technique generates two-dimensional maps of elastic strain over the entire detector field of view (FoV) in a single scan. The strain map will have a spatial resolution dependent on the detectors pixel size [121]. Producing a strain map with similar spatial resolution using conventional powder diffraction method requires many point measurements with a total acquisition time dependent on the number of points being collected and the chosen gauge volume, which often exceeds the acquisition time of single shot Bragg edge transmission imaging by orders of magnitude [94]. However, it should be noted that in a conventional powder diffraction measurement the combined use of slits and collimators on the incident and diffracted beam allows for a cuboid gauge volume to be defined within the sample. Conversely, a Bragg edge scan measures the elastic strain component parallel to the incident beam direction, averaged through the sample thickness. This may be beneficial or disadvantageous depending on the sample geometry and desired strain component to be measured.

3.2.2 Computed tomography

An alternative three-dimensional technique is attenuation-based computed tomography (CT) in which a volumetric image of the features based on their attenuation coefficient is created. The volumetric image allows for non-destructive interrogation of the features within the sample, including cracks [122]. Methodologically, neutron and X-ray CT are similar, although they are based on different physics laws: whilst X-rays interact with the atoms valence electrons, thermal neutrons interact with the nuclei of the atom [52]. In both techniques, projections of transmitted X-rays or neutrons at multiple angles are captured by an appropriate detector. The projections are then reconstructed into a 3D image using a reconstruction algorithm, depending on the type of CT performed and the data quality [123]. For the attenuation of X-rays and thermal neutrons the Beer-Lambert law is valid [124]. Equation 3.4 demonstrates the simplified Beer-Lambert law of exponential attenuation for monoenergetic incident radiation to allow for a direct comparison of the principles of neutron and X-ray CT.

$$I = I_0 e^{-Bx} \tag{3.4}$$

In this equation I is the transmitted intensity, I_0 is the initial intensity, B is an attenuation coefficient, and x is distance transmitted through the substance.

For X-rays, B is the linear attenuation coefficient, which can be calculated using the product of the mass attenuation coefficient and the material density. This coefficient, for a given energy, will increase for atoms with a greater number of electrons, or higher atomic number [125]. For neutrons, B is often referred to as the total macroscopic cross-section, Σ, and represents the effective interactive area of all nuclei within a certain volume [51]. Values of Σ for a given neutron energy are calculated from the material density, atomic weight and the microscopic cross-section, depending on the type of interaction that has occurred, e.g. absorption or scattering. Equation 3.5 calculates the macroscopic cross-section:

$$\Sigma = \frac{\rho}{A} N_A (\sigma_a + \sigma_s) = \frac{\rho}{A} N_A \sigma_t \tag{3.5}$$

where Σ is the macroscopic cross-section, A is material cross-sectional area, N_A is Avogadros constant, σ_a is the absorption microscopic cross-section, σ_s is the scattering microscopic cross-section, σ_t is the total microscopic cross-section and ρ is the material density.

Synchrotron X-ray micro-CT has become a well-established method for inspecting material damage including cracks, voids and other microstructural inconsistencies with beamlines achieving a voxel size of the order of 1 μm^3, depending on experimental setup, equipment and the size of the sample being investigated [71]. For neutron CT the spatial resolution is heavily influenced by beam divergence and detector characteristics, such as scintillator thickness [126, 127] but the resolution is often of the order of tens of micrometres. However, neutrons have the benefit of deeper penetration in engineering materials compared to X-rays. Hence engineering materials with relatively high atomic numbers, such as steels, are significantly more suited to NCT than XCT. Isotope-specific imaging is another advantage offered by NCT. For example, NCT has been used to observe the distribution of hydrogen, which heavily scatters neutrons, within as-received steel plates, to develop materials resistant to hydrogen embrittlement [128, 129]. Time-of-flight neutron imaging may also be used to identify contrast between phases, if they have differing crystalline structures. For instance, if one phase has a body centred cubic (*bcc*) crystalline structure, and the other has a face centred cubic structure (*fcc*), the transmitted neutron spectra will vary, hence both neutron and X-ray CT have been used in this study.

3.3 Experimental design

3.3.1 Sample material, geometry and initial fatigue study

Alloy 2205 duplex stainless steel was used in this study. It consists of Body Centre Cubic (*bcc*) ferritic α and Face Centre Cubic (*fcc*) austenitic γ phases in roughly equal volume fractions. The typical material properties can be found in Table 3.1, with chemical composition displayed in Table 3.2 [130]. Electron backscatter diffraction was performed on a cross-section of the material, revealing that there was stronger texture in the ferritic phase compared to the austenite (Figure 3.2).

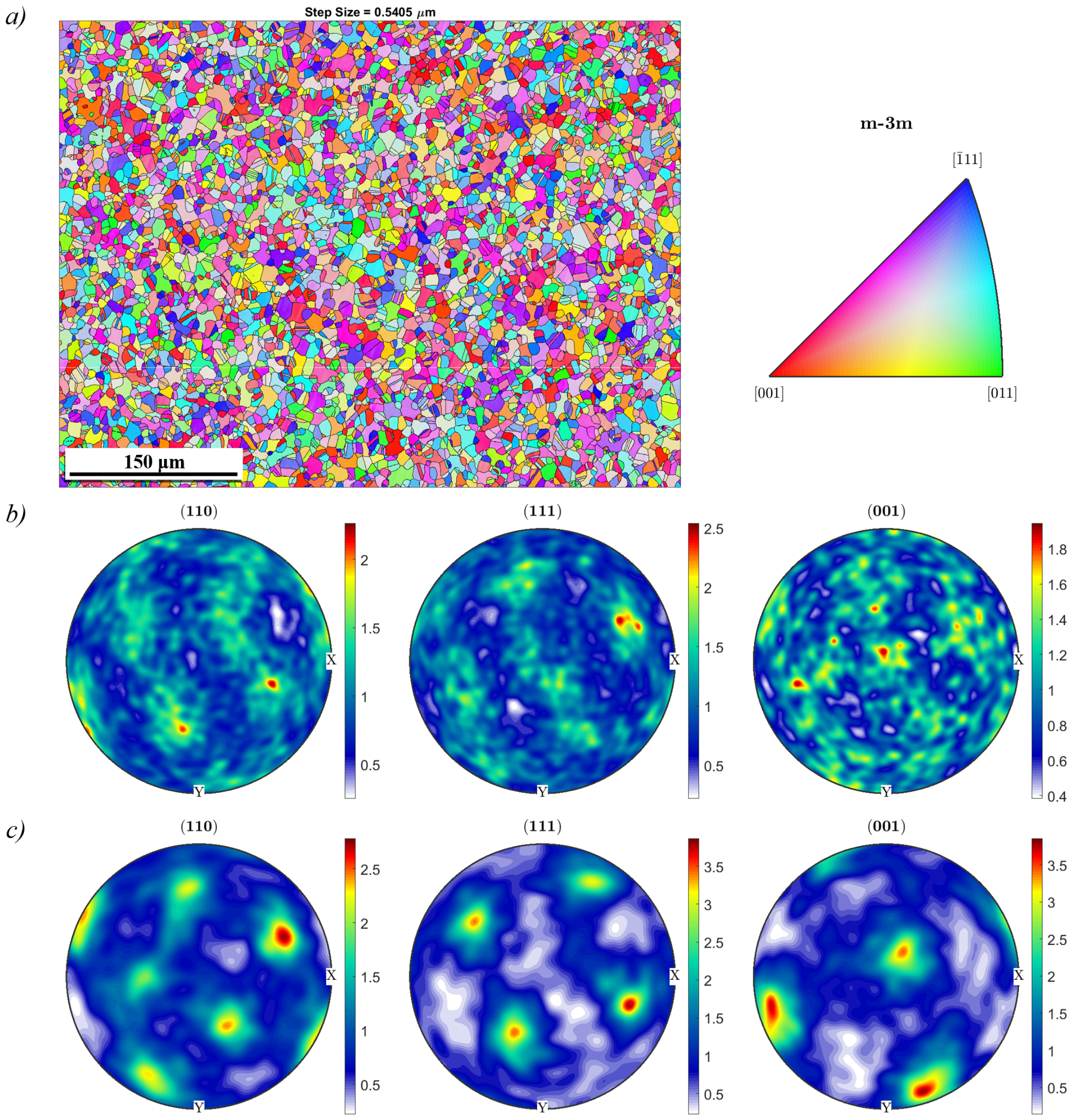

Figure 3.2: EBSD results: (a) The grain-boundary energy distribution (GBED) and corresponding key for Alloy 2205 duplex steel, performed with a step size of 0.5405 μm. The scale bar provides a representation of the material grain sizes. (b) Orientation distribution function for austenite. (c) Orientation distribution function for ferrite.

Table 3.1: Material properties of Alloy 2205 duplex stainless steel [130].

Property	Value
Density $[kg/m^3]$	7700
Young's Modulus $[GPa]$	190
Poisson's Ratio	0.3
Yield Stress $[MPa]$	450

Table 3.2: Alloy 2205 duplex stainless steel chemical composition [130].

C	Cr	Ni	Mo	N	S
0.02	22.1	5.6	3.1	0.18	0.001

A cylindrical sample was used as it has been shown that the 3D elastic stress field in an axisymmetric sample can be back calculated from through thickness average energy dispersive strain measurements [131, 132]. The sample geometry is shown in Figure 3.3; a notch was machined so that the location of the fatigue crack is prescribed to facilitate continuous monitoring using Bragg edge transmission imaging. The notch dimension was a/W = 0.2 (a = 1 mm, W = 5 mm).

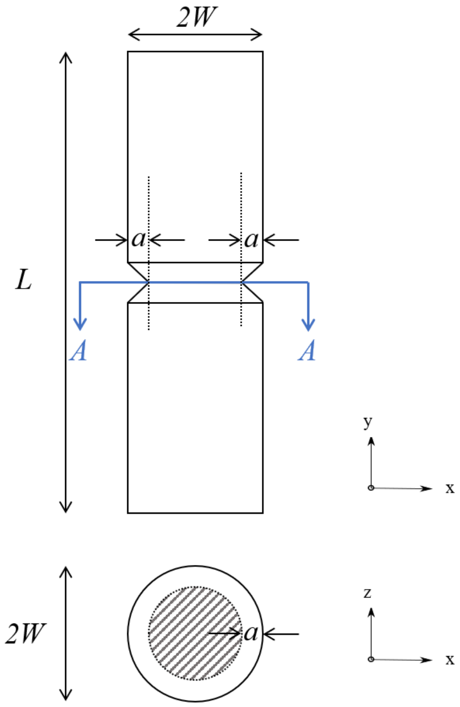

Figure 3.3: Schematic of sample geometry.

It was important to ensure that a crack initiated within a known number of cycles that could fit in the tight schedule of the beamtime. It was therefore essential to select a load that induced failure within the order of several hundred thousand cycles as the test frame could reliably apply fatigue load up to 10 Hz. The total number of test specimens available for preliminary investigations was restricted to seven due to a shortage of material. Whilst ten samples were machined in total, three were retained for the *in situ* experiment, to ensure one test specimen and two spares were available if a sample were to be accidently damaged during setup. In order to identify the appropriate load, a number of specimens were tested before the neutron experiments at different levels of load and their fatigue lives were measured; these can be seen in Figure 3.4. An initial maximum load, P_{max}, for preliminary testing was estimated by applying the Point Method approach to the Theory of Critical Distances [133], which estimated that a maximum load of approximately 11 kN would be required to damage the sample within the medium cycle fatigue regime at roughly 5 x 10^5 cycles. This proved to be conservative and based on the results depicted in Figure 3.4, a maximum applied load of 16 kN would be used for the *in situ* loading experiments. Using assumptions from Linear Elastic Fracture Mechanics, the fatigue life of the sample was estimated to be less than 869,000 cycles, keeping within the dedicated experimental beamtime [134, 111, 135]. In all tests $R = P_{min}/P_{max} = 0.01$ was selected as it often provides the closest agreement with the theory of critical distances and the tests were carried out on an Instron 50 kN servo-hydraulic test frame at 10 Hz.

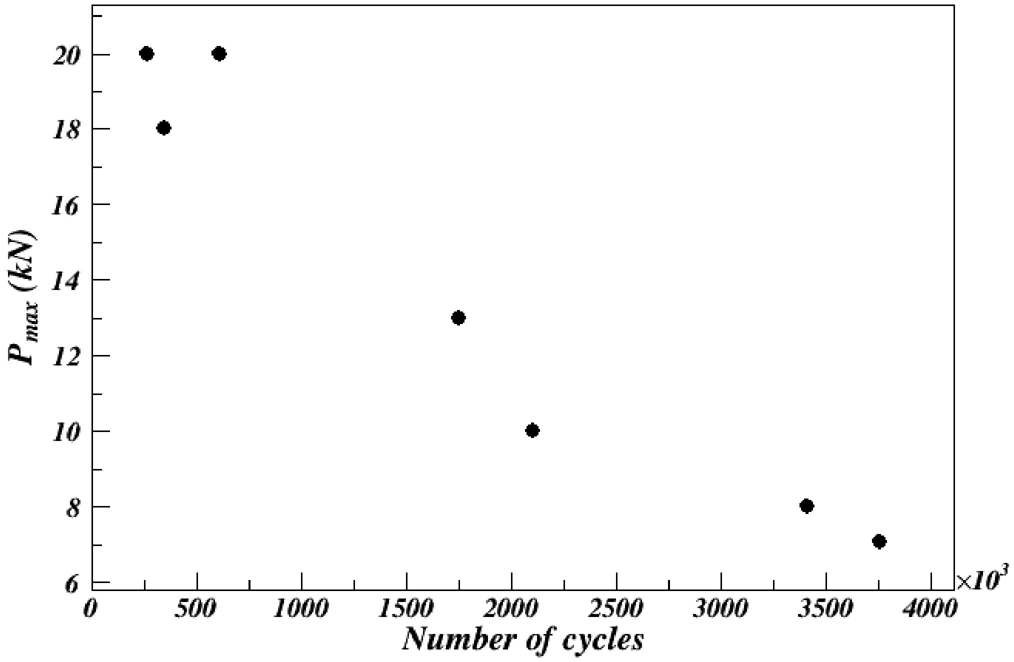

Figure 3.4: Fatigue life of seven samples, preliminarily tested to estimate a load at which the sample could fail in a reasonable number of cycles. R = 0.01.

3.3.2 *In situ* loading Bragg edge transmission neutron imaging

The *in situ* loading neutron transmission imaging experiment was conducted using a 50 kN hydraulic Instron load frame at the ENGIN-X instrument at the ISIS Neutron and Muon Source, Rutherford Appleton Laboratory, UK. The sample was fatigued at maximum load of 16 kN in displacement control, with $R = 0.01$ and frequency of 10 Hz. Local compliance of the sample around the notch was measured before each scan using an extensometer of gauge length 12.5 mm attached to the specimen. Crack nucleation would increase the compliance of the sample thus allowing an independent method to detect the crack. Similarly, peak-to-peak loads were continuously measured and monitored visually as crack nucleation would result in a drop in the load allowing for further validation.

Peak-to-peak load monitoring was achieved using a high frequency load cell with the output signal recorded using a National Instrument data acquisition system at 10 kHz. Load data were concurrently analysed using an in-house python code, providing graphical visualisation of the peak-to-peak load variation every 250 cycles. Cyclic loading of the sample was paused, with the sample held at maximum load, to allow for completion of Bragg edge imaging scans at 0, 2.5 x 10^5, 3.5 x 10^5, 4.5 x 10^5 and 5.145 x 10^5 cycles. A microchannel plate (MCP) neutron counting detector, designed by Nova Scientific and University of California at Berkley, was used to obtain two-dimensional radiographs, details of which can be found elsewhere [117, 136]. The MCP comprised a 2 x 2 array of Timepix readout application specific integrated circuits (ASIC), with 512 x 512 pixels each 55 x 55 μm^2 providing a total field of view (FoV) of 28 x 28 mm^2 [137] On detection of a neutron, an electron avalanche is generated within the MCP pore that is subsequently counted by the ASIC readout CMOS chip, along with the neutron ToF. For the cold and thermal neutron energies, detection efficiency is approximately 50% [138], with a selected time resolution of 4.48 μs [118, 120].

As the MCP has been designed for a different beamline (the IMAT facility) and not for the ENGIN-X beamline, a custom-built mounting arrangement was used to ensure that the distance between sample and detector was minimised, reducing the negative impact of geometrical blurring. The setup, seen in Figure 3.5, enabled a sample to detector distance of 25 mm. The measured ToF range, between 5 ms and 68.3 ms, was chosen to ensure that Bragg edge positions of the most useful *hkl* planes with highest intensities, for example the *110* and *111*, were captured. A flat field scan, without a mounted sample present, was recorded to normalise the scans for varying pixel response and non-uniformity of the beam.

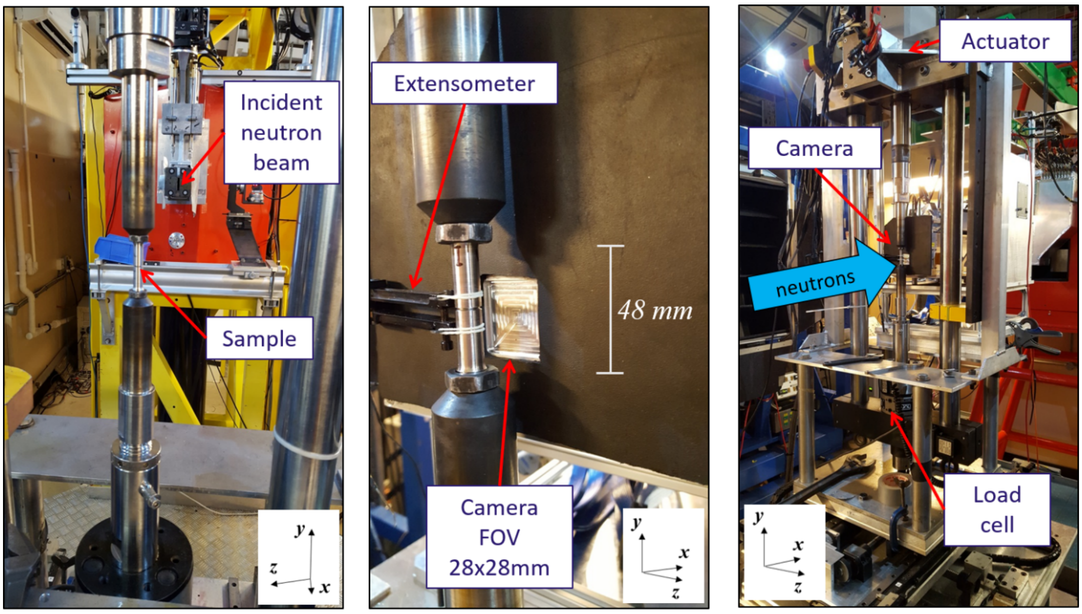

Figure 3.5: Experimental setup, demonstrating the sample position in relation to the incident neutron beam and the MCP detector.

ENGIN-X, a beamline dedicated to strain measurement, is designed for a high ToF resolution which negatively impacts its neutron flux. Conversely, IMAT a dedicated imaging beamline, has much higher flux but at the time of the experiment, was not capable of housing the 50 kN Instron load frame. The experiment, therefore, had to be carried out at ENGINX which meant significantly longer scan times than what is expected from an imaging beamline. A preliminary scan was performed on the sample, with the quality of counting statistics being checked every hour, to ensure that spectral data was satisfactory in all regions of the sample, regardless of the varying material thickness. It was determined that 4-hour scans allowed for adequate acquisition statistics. Figure 3.6 shows an example transmission spectrum for the duplex steel specimen, with certain Bragg edges and their associated crystallographic phases (α or γ) exhibited.

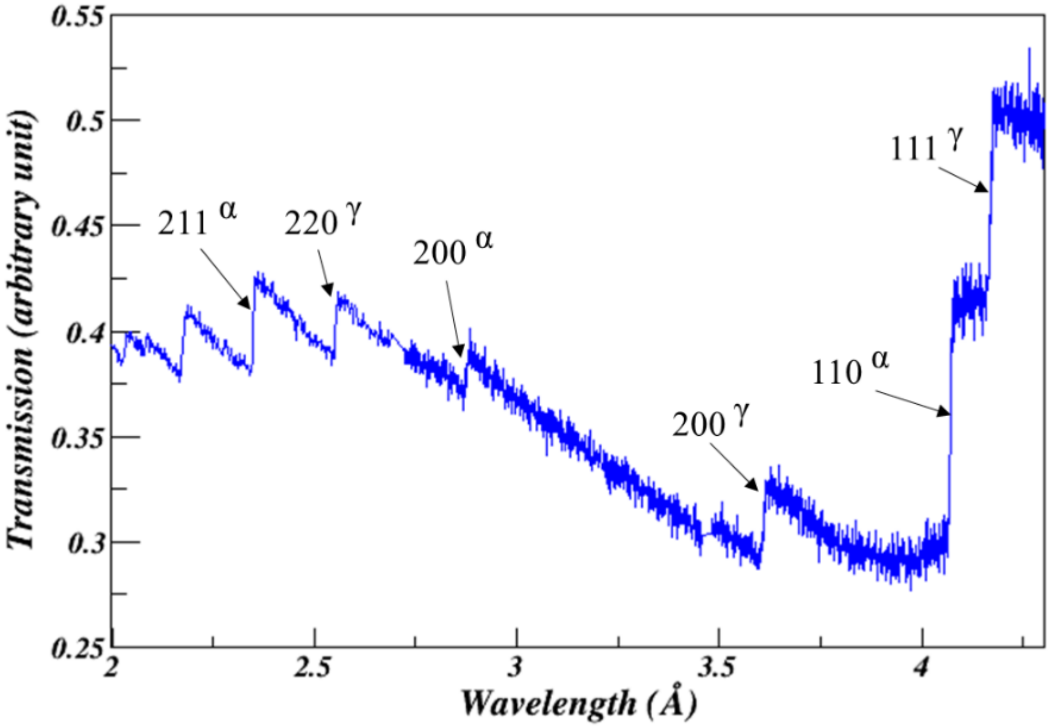

Figure 3.6: Transmission spectrum for Alloy 2205 duplex stainless steel. The individual *hkl* planes have been labelled with reference to their associated allotrope, ferrite α-phase and austenite γ-phase.

The analytical function previously detailed (Equation 3.3) was used to fit Bragg edges and their associated wavelength λ was extracted for each pixel, allowing for generation of two-dimensional maps. The residual stress of the as-manufactured specimen was not the focus of this study thus, a stress free specimen to determine the stress free Bragg edge wavelengths (i.e. d_0) was not examined [51]. The values of λ_0 were obtained at a region away from the notch prior to cycling. Due to the relatively low flux available at neutron facilities, an individual pixel has a low signal-to-noise ratio [139]. Nevertheless, counting statistics were improved substantially by employing a spatial binning technique, at the sacrifice of effective spatial resolution [140, 141]. Analysis was completed pixel by pixel, whilst recursively combining spectral information from a 39 x 39 pixel region, ensuring sufficient statistics were available to fit the Bragg edges.

3.3.3 Neutron tomography

After the *in situ* experiment, a neutron computed tomography (NCT) scan was performed on the sample on the IMAT imaging beamline. The specimen was positioned 11 mm from the 2048 x 2048 pixel ANDOR Zyla CMOS 4.2 Plus detector [126]. The imaging camera does not distinguish between the differing neutron energies, generating white-spectrum radiographies. For neutron CT, spatial resolution is dominated by geometrical blurring because of sample positioning, which is in turn dependent on the instrument specific beam divergence, referred to as the L_B/D_B value. This value is calculated using the equation:

$$\frac{L_B}{D_B} = \frac{l_{max}}{d_B} \tag{3.6}$$

Where, L_B is the distance between the beam focusing aperture and the camera (10 m), D_B is the aperture diameter (40 mm), l_{max} is the maximum distance between the sample and the camera (23 mm), whilst d_B is the geometrical blurring.

The setup for NCT scans equated to geometrical blurring that provided a spatial resolution of approximately $92\mu m$. The Nyquist-Shannon sampling theorem postulates that the minimum number of projections (N) required for a 360° rotation of the samples is calculated for cylindrical samples using the equation [142]:

$$N = \frac{W\pi}{d_B} \tag{3.7}$$

Where, W is the sample radius.

It was calculated that $N = 204$ would be sufficient, each projection count time was thus 30 seconds, with rotations of 1.76° between each scan. Open beam scans (flat field), without the presence of a sample, were taken before and after each tomography to normalise pixel-to-pixel variations in sensitivity and the influence of fluctuations in beam intensity across the detector FoV. Dark scans (dark field), with the shutter closed, were taken before the first and after the final tomography to correct for electronic noise within the detector. Also, scans were performed at 180° and 360° to correct for sample tilting.

Once the projections are recorded, they were reconstructed to produce a three-dimensional representation of the specimen. Neutron tomography data is significantly noisier than X-ray tomography due to a lower signal-to-noise ratio. For such datasets, the simultaneous algebraic reconstruction technique (SART) is preferred to other forms of conventional reconstruction algorithms such as filter back projection (FBP) [143]. SART is an implementation of the frequently applied iterative technique, ART [122, 144], yet only requires one single iteration, significantly reducing the necessity of computational power. The FBP and SART algorithms were both used to reconstruct the NCT datasets to allow for comparison.

3.3.4 X-ray computed tomography

A synchrotron X-ray computed tomography (XCT) scan was also recorded on the sample at Beamline I12 (JEEP), Diamond Light Source, UK [71]. As the X-ray attenuation coefficients for the ferrite and austenite phases are very close (<3%), the scan was not expected to reveal any other microstructural information on the different phases in the duplex steel. The X-ray CT scan used a 90 keV monochromatic parallel beam and the beamlines custom imaging detector, consisting of a 2560 x 2160 pixel PCO.edge sCMOS detector lens-coupled to a LuAG:Ce scintillator. The nominal pixel resolution was 7.91 μm. A total of 1800 projections over 180° were captured with an exposure time of 4.5 ms per projection.

Reconstruction of the X-ray CT data was completed using the Fourier based gridrec algorithm [145]. This method provides significantly higher quality images on well sampled tomographic data sets, when compared to the conventional filtered back projection (FBP) algorithm [145].

3.3.5 Scanning electron microscopy

After the non-destructive methods were used to evaluate the crack initiated in the specimen during *in situ* loading experiments, the sample was destructively tested to validate the non-destructive observations. The sample was cooled in liquid nitrogen below its ferrite phase ductile to brittle transition temperature and pulled in tension using the Instron loading frame at ENGIN-X. This created a final fracture surface that was distinctly different from the fatigue crack surface developed during the *in situ* cyclic loading experiment, therefore allowing the fatigue crack geometry to be studied. The fracture surface was examined using JSM-6610LV low vacuum scanning electron microscope (SEM), at the Research Complex at Harwell (RCAH), UK.

3.3.6 Finite element analysis

Once a fatigue crack nucleates, the stress field in the sample changes to accommodate the reduction in the uncracked ligament as well as the stress concentration around the crack front. To calculate the strain field expected in a cracked sample, ABAQUS version 6.14-2 [146] was used to develop a static three-dimensional elastic-plastic model. The crack geometry as viewed by SEM (see Section 3.4.1) was simulated in the model. A schematic of the model can be seen in Figure 3.7. Mesh refinement was completed in the region of interest, surrounding the crack and the notch, using a mesh size of 0.1 mm, quadratic tetrahedron elements (C3D10). Since there was no unloading simulated, no particular specification on the type of hardening for the plastic behaviour of the material was required, thus isotropic hardening was assumed. The material properties have been obtained from prior work [147]. A quarter of the sample was modelled, taking advantage of the samples symmetry in the z-axis. Symmetry in the y-axis was included to simulate the presence of the crack, through applying symmetry boundary conditions on a partitioned region of corresponding geometry to the crack, as viewed with the SEM. The boundary condition allows for the rotation of the cross-section plane induced by the combined tension and bending of the cracked sample to be simulated. A concentrated load was applied through a single reference point that was distributed across the top of the sample, as it was assumed that this would best simulate the influence of a bending moment induced by a substantial crack whilst under tensile load.

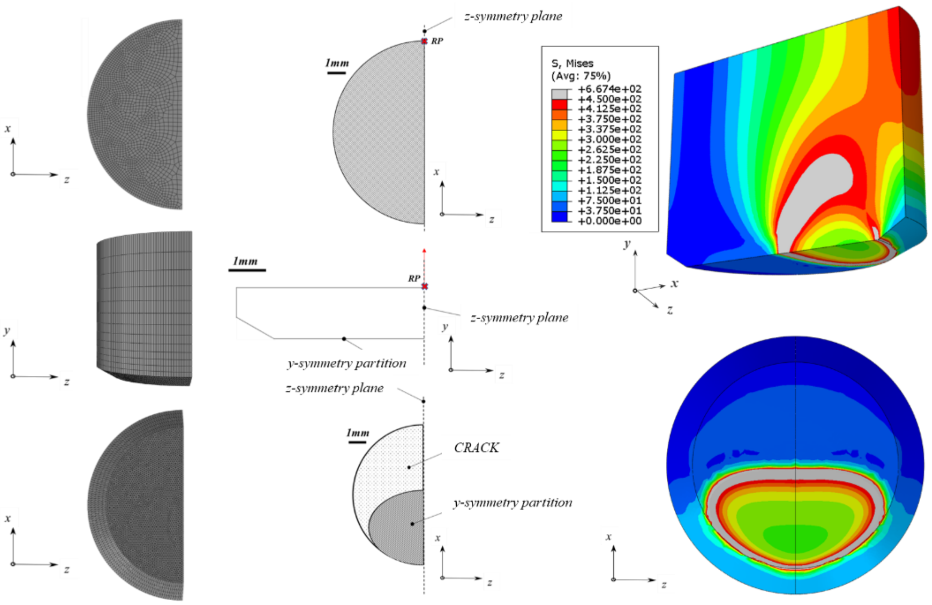

Figure 3.7: Schematic of the finite element model used to examine theoretical elastic strains in the cracked sample, assuming symmetry to simulate the crack geometry, as viewed by SEM. (Left) Mesh, (Middle) symmetry and loading conditions, (Right) examples von-Mises stress distribution from the FEA results in 3D and cross section.

3.4 Results

3.4.1 Fatigue life of test specimen

The cyclic loading was paused during the experiment and scans were performed at 0, 2.5 x 10^5, 3.5 x 10^5, 4.5 x 10^5 and 5.145 x 10^5 cycles. A sudden drop in the peak-to-peak load was observed at roughly 5.0 x 10^5 cycles (see Figure 3.8), with a crack at the notch becoming visible by eye at 5.145 x 10^5 cycles. From the peak-to-peak load, it could be suggested that a crack was nucleated earlier at 1.6 x 10^5 cycles (note the gradual peak-to-peak drop), or possible just before 3.5 x 10^5 cycles (note the significant and visible peak-to-peak drop).

Figure 3.9 shows the SEM images taken from the fracture surface of the sample. The specimen has lost its circular cross section, which indicates some deformation has occurred whilst destructively pulling the sample apart. The fatigue crack growth region is clearly visible as a smooth area typical of ductile fatigue; the final shape of the crack front is obvious in the central image. The large fatigue failure area is accompanied by the rough area (bottom right figure), characteristic of ductile fracture. The interface between these two regions (bottom left) signifies the final crack front during the *in*

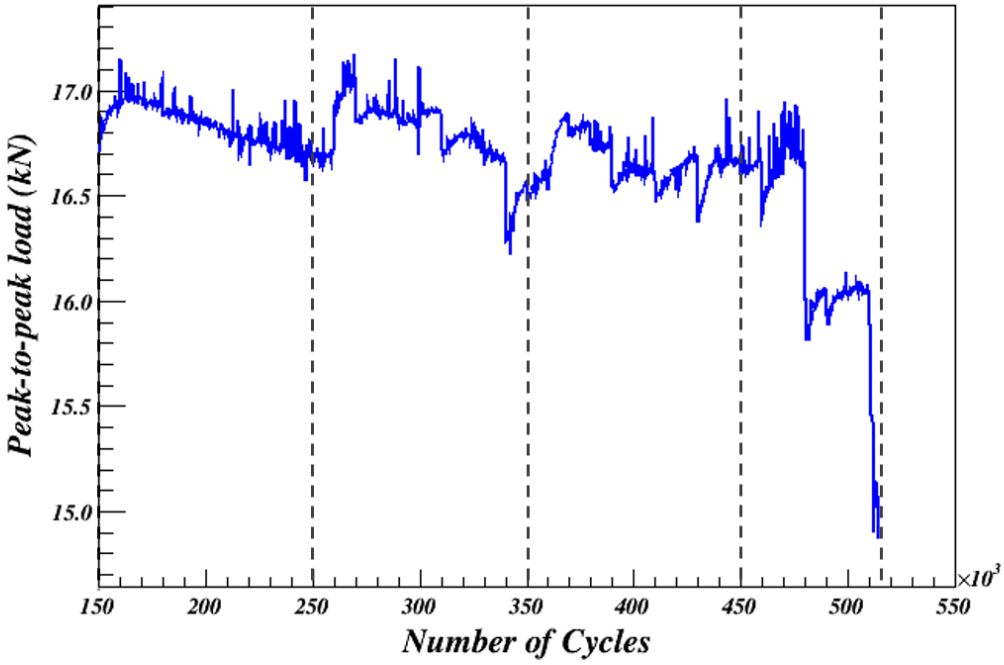

Figure 3.8: Peak-to-peak load versus the number of cycles. The dashed lines indicate when fatigue loading was paused to complete a neutron transmission scan, with the sample held at the maximum load.

situ experiment. The crack has propagated in an asymmetric fashion, which is potentially related to slight misalignment of the Instron loading frame used during the *in situ* experiment.

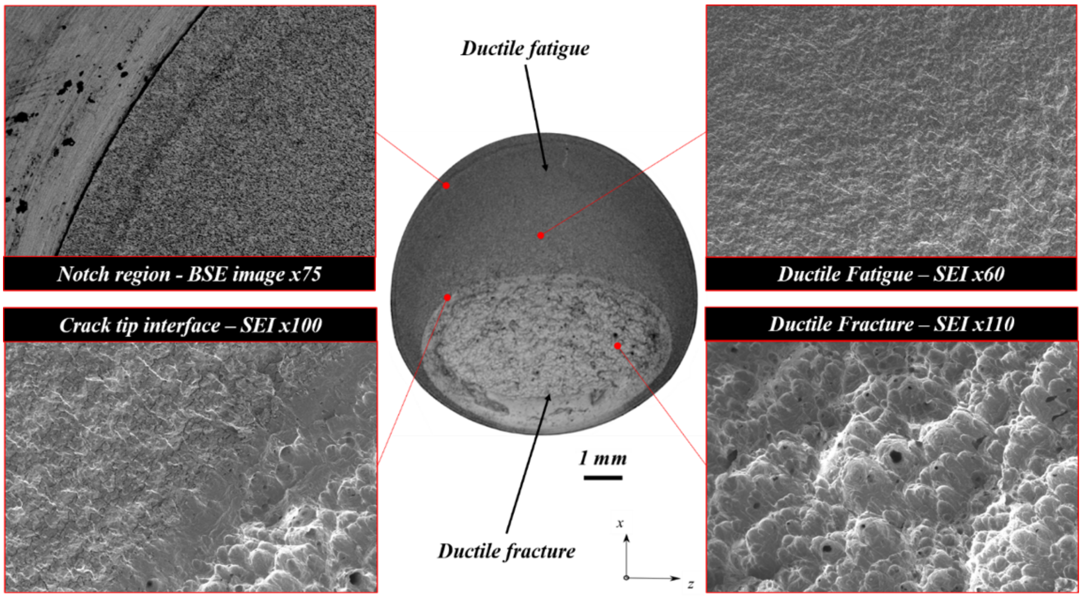

Figure 3.9: (Centre) x13 Image of crack topology, which no longer appears circular due to deformation during the pulling process. (Clockwise from top left) x75 BSE image of proposed crack initiation site; x60 SEI of ductile fatigue region close to the notch; x110 SEI of the ductile fracture region; x100 SEI of crack tip region.

3.4.2 *In situ* energy dispersive neutron imaging

The *bcc* $\{110\}_\alpha$ and *fcc* $\{111\}_\gamma$ lattice planes were used to measure strain in the ferritic and austenitic phases of the duplex steel respectively at peak load. As seen in the materials transmission spectrum (Figure 3.6), the height of both edges are significantly greater than any other Bragg edges in each phase. Most importantly, the $\{110\}_\alpha$ and $\{111\}_\gamma$ plane families have both previously been used successfully to measure strain, demonstrating reasonable agreement with bulk elastic response [114, 148].

Figure 3.10 shows the elastic strain maps and the elastic strain along the notch for both *hkl* planes *bcc* $\{110\}_\alpha$ and *fcc* $\{111\}_\gamma$ at various intervals throughout the cyclic loading. It should be noted that the full field beam measures the average strain through the thickness of the specimen, which varies due to its circular cross section across the map. These results demonstrate the crack may have nucleated prior to 250,000 cycles, as the strain visibly increases relative to pre-loading. Also, there is a distinctive strain redistribution when the fatigue crack has propagated to a significant size at 514,500 cycles. The effect of the fatigue crack can be identified more clearly in the $\{110\}_\alpha$ elastic strain maps compared to the corresponding austenitic $\{111\}_\gamma$ maps. For both maps generated at 514,500 cycles, the region associated with crack tip stresses, which appears to have contributed most significantly to the clear strain redistribution has been labelled, localised crack tip stress. Analysis of ferritic strain partitioning between the ferrite and austenite phases of the duplex steel was not the primary objective of this study. However, it can be seen in the maps that the ferrite phase is carrying more of the strain in the material. This is in agreement with previous studies on duplex stainless steels, which demonstrated stiffness in the ferrite is generally greater than in the austenite [149]. The diffraction elastic moduli of {110} and {111} are 242 GPa and 214 GPa respectively [150] which along with strong texture typically observed in wrought duplex stainless steels [151] can account for the strain partitioning observed in the measurements. The error of measured strain corresponds to uncertainty in determining the Bragg edge position, like strain measured using Bragg peak analysis. The Bragg edge fitting error in the strain map generation is 3.82×10^{-4} for $\{110\}_\alpha$ and 4.29×10^{-4} for $\{111\}_\gamma$. This translates to strain errors of roughly 94 $\mu\varepsilon$ and 103 $\mu\varepsilon$ for $\{110\}_\alpha$ and $\{111\}_\gamma$, respectively.

Small regions of extremely high compressive stress, with some examples labelled non-converging pixels, correspond to areas where it has not been possible to fit the Bragg edge. This occurs more frequently in the $\{111\}_\gamma$ data, particularly at 0 cycles and after the crack has been nucleated at 514,500 cycles. This also suggests that strain in the austenitic material is more difficult to study for duplex steels, as maps for both edges at each number of cycles are generated from the same data set. The presence of plasticity will generate high intergranular strains, known to impact strain measurement accuracy [152]. Yet this effect is assumed to be negligible as the influence of localised plastic strains, associated with crack tip stresses, will have diminished on averaging through the entire material thickness.

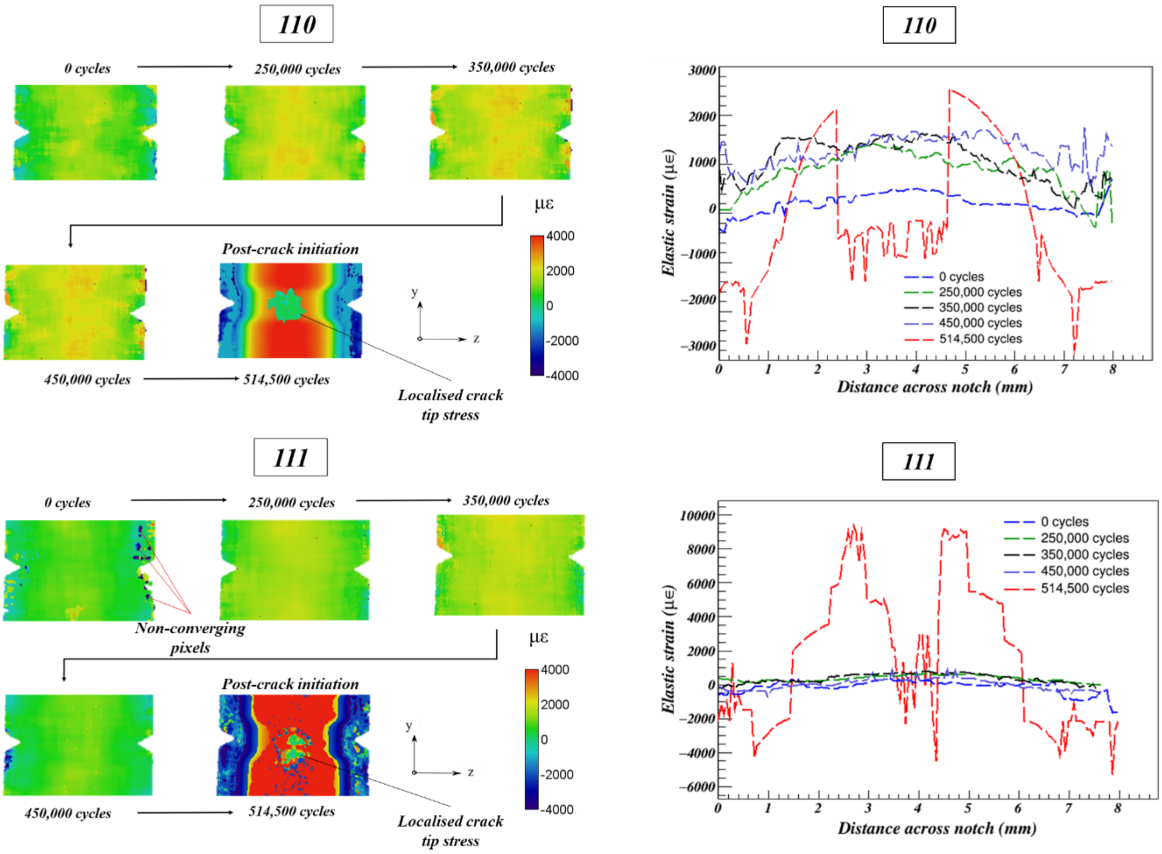

Figure 3.10: (Left) The elastic strain maps generated using the ferritic 110 and austenitic 111 planes, at six points through the samples fatigue life. The strain gradually increases as the crack propagates and the cross section reduces. (Right) Graphical representation of the elastic strain measured along the notch, supporting crack nucleation may have occurred prior to 250,000 cycles. The final scan at 514,500 cycles clearly demonstrates the expected redistribution of stress associated with a crack of significant size. The compressive strain observed in the final stage is due to out of plane bending of the sample as the crack propagates non-symmetrically.

3.4.3 Post-fatigue CT imaging

Figure 3.11 displays reconstructed slices from neutron and X-ray tomography scans. The virtual slices of NCT were obtained using FBP and SART algorithms with and without a median 3 x 3 filter. Figure 3.11 also demonstrates the values of signal to noise ratio (SNR) and contrast to noise ratio (CNR) for each algorithm used for NCT reconstruction. CNR and SNR were calculated using a slice 40 mm from the notch and Equations 3.8 and 3.8 [144, 153]. The visual inspection of the reconstructed slices, presented in the Figure 3.11, appears to demonstrate that SART is the favoured algorithm for the noisy neutron data set. This is confirmed by the CNR and SNR values. Background noise is further reduced on application of the filter, again supported by higher SNR and CNR. For context, the X-ray reconstruction SNR and CNR values were 42940 and 579, respectively.

$$SNR = \frac{\mu_{sig}}{\mu_{bg}} \tag{3.8}$$

$$CNR = \frac{\mu_{sig} - \mu_{bg}}{\sigma_{bg}} \tag{3.9}$$

Where, μ_{sig} and μ_{bg} are mean pixel value for the signal area (inside the sample) and background area (outside the sample), whilst σ_{bg} is the background areas standard deviation.

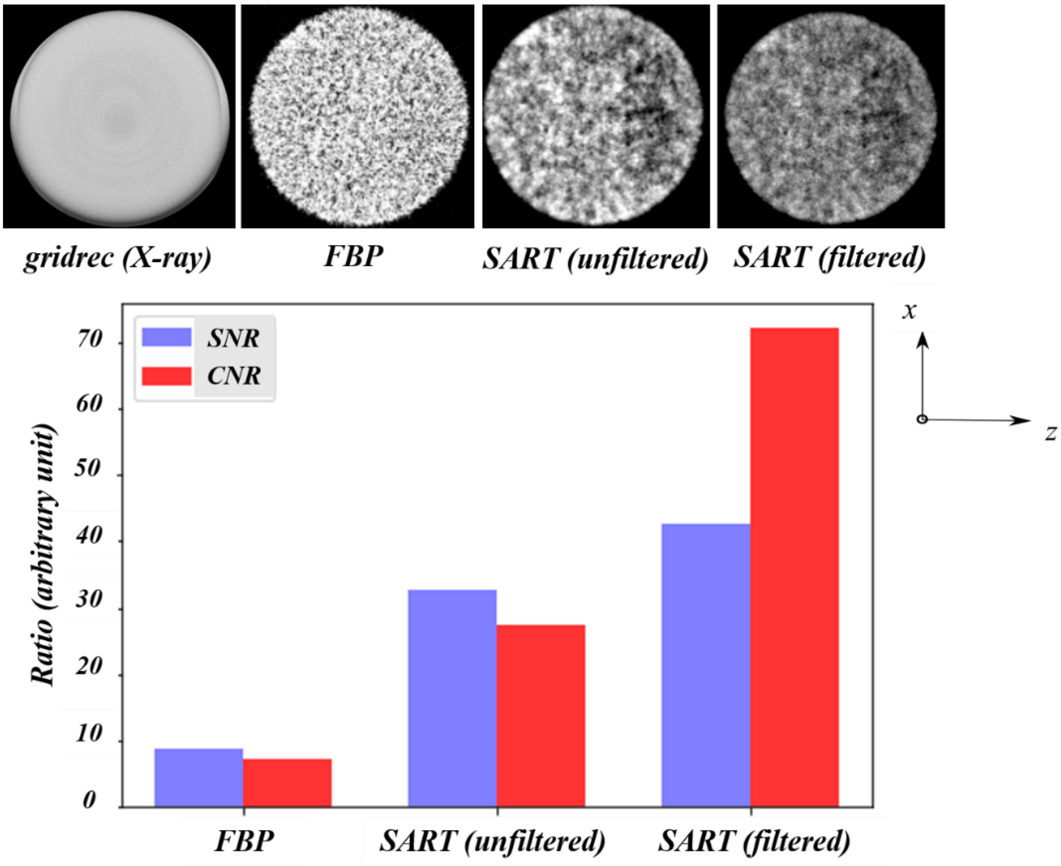

Figure 3.11: (Top) Reconstructed slices of the X-ray data using the gridrec algorithm, with FBP and SART algorithms for neutron data. Slices were all taken 40 mm from the notch, to ensure the crack did not influence results. (Bottom) Quantitative representation of neutron reconstruction qualities using their SNR and CNR.

Volume rendering of both reconstructed data sets was completed in Avizo 9.3.0 software [154]. The better spatial resolution of XCT (~ 7.91 μm) offers a greater opportunity to examine the crack morphology compared to NCT which has poorer spatial resolution (~92.0 μm). It was therefore more difficult to visualise the crack using NCT. Using the filtered SART reconstruction algorithm for NCT reconstruction, however, it was possible to distinguish the crack. The side-by-side comparison of XCT and NCT crack profile in Figure 3.12 confirms this. The X-ray reconstruction shows a clear crack outline, due to the high spatial resolution of X-ray tomography, and with significant attenuation contrast between steel and air, confirming the shadow witnessed in the neutron image is caused by the crack.

The X-ray absorption behaviour is considered the same for both phases but it is apparent that the NCT can provide information on the duplex steel phases, as there is visible contrast as a result of the austenite and ferrite. Whilst localised microstructural features, such as carbides, are certainly present in the material, it is unlikely that they would greatly influence the NCT image quality, as their size is generally much smaller than that of the techniques spatial resolution [155]. Figure 3.12b demonstrates how it is possible to examine the internal variations in phase, and potentially with improved resolution allow for the development of a range of post-processing correlative techniques, to be discussed in Section 3.5. This variation in the greyscale offers a chance to analyse the NCT data using digital volume correlation if the before and after loading volumetric images were available.

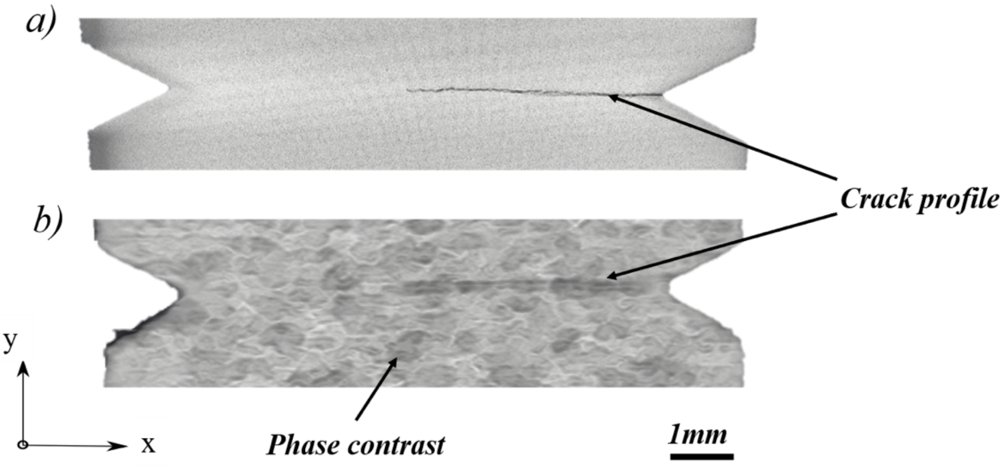

Figure 3.12: Slice from rendered X-ray CT (a) and neutron CT (b) at the same location, allowing for direct comparison of the techniques regarding their ability to visualise the crack profile.

Figure 3.13 compares the fractographical crack topography seen using SEM with the crack morphology observed in a cross-section of the rendered and segmented XCT data. Crack segmentation using the rendered neutron data was not possible as there was insufficient contrast between the crack and surrounding metal. Comparing the segmented XCT and SEM images allows for valuable insight into the limitations in most accurate non-destructive (i.e. XCT) and destructive methods. Whilst the morphology of the crack in both images are very similar, it appears that regions close to the crack tip have been omitted in XCT data as the opening of the crack was less than the spatial resolution of the tomography data.

3.4.4 Finite element analysis

Bragg edge imaging measures average through thickness elastic strain. Therefore, the same through thickness averaging on the elastic component of strain was performed on the FE results. This averaging takes into account the higher stress field around the crack tip as well as the bending stress that is induced in the sample due to the crack invalidating the initial axisymmetric condition of the sample. No differentiation between the phases were considered in the model, and the macromechanical material properties of the duplex steel were considered. Figure 3.14 shows the comparison between the FE results and measurements made on $\{110\}_\alpha$ and $\{111\}_\gamma$ along a profile passing through the

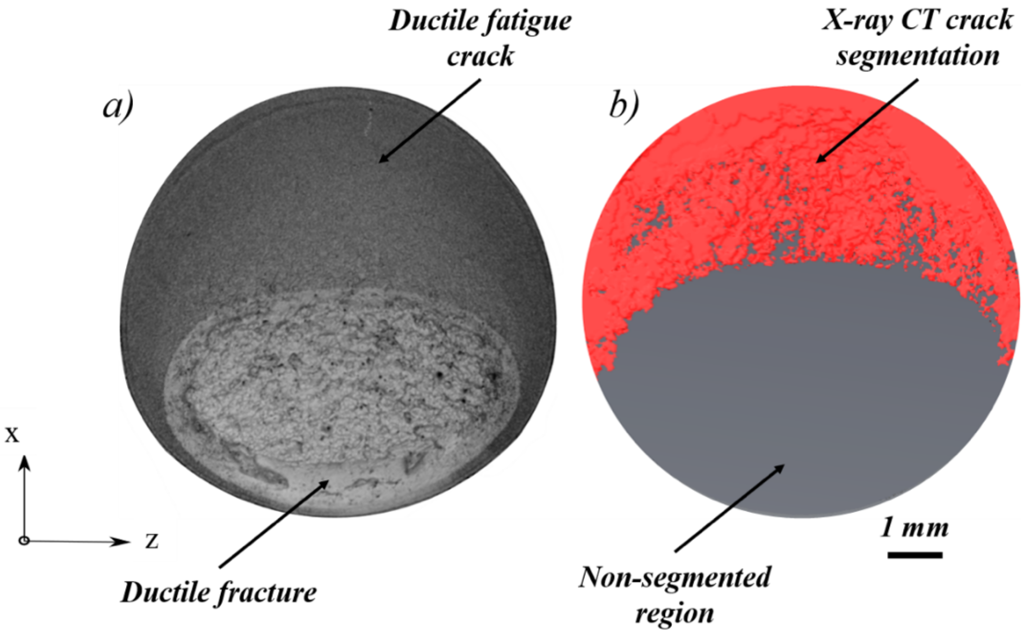

Figure 3.13: The crack as seen using (a) SEM note the distortion that occurred whilst pulling the sample apart; (b) by segmenting the crack using X-ray CT. This is the area over which the neutron Bragg edge tomography measures average strain.

centre line of the notch. Figure 3.14 shows a good agreement between the FE results and the experimental measurements although $\{110\}_\alpha$ measurements are closer to the model than $\{111\}_\gamma$ which could be explained by the significant difference in levels of texture between the two phases.

3.5 Discussion and future work

3.5.1 Discussion

The aim of this investigation was to detect and quantify the effects of a crack using various non-destructive techniques: neutron Bragg edge transmission imaging, neutron computed tomography, X-ray computed tomography. The non-destructive findings were validated against a destructive scanning microscopy analysis. Bragg edge transmission imaging was demonstrated to identify the presence of a crack *in situ*, through the generation of strain maps. Although a quantitative method that measures the average strain through the sample, Bragg edge imaging is incapable of resolving crack morphology. Alternatively, it was shown that neutron tomography can be used to create a three-dimensional representation of the crack in the sample as well as observing contrast in the duplex stainless steel specimen due to its two different phases. X-ray tomography has a much higher spatial resolution, which could be used to segment the crack in a volumetric image more precisely. However, the low penetration depth of X-ray in engineering materials such as steel can be limiting. It is also not possible to resolve different phases of duplex steel in X-ray absorption contrast tomography due to the similarity between their attenuation coefficients. Other techniques such as X-ray propagation phase contrast tomography might be used for this purpose [156].

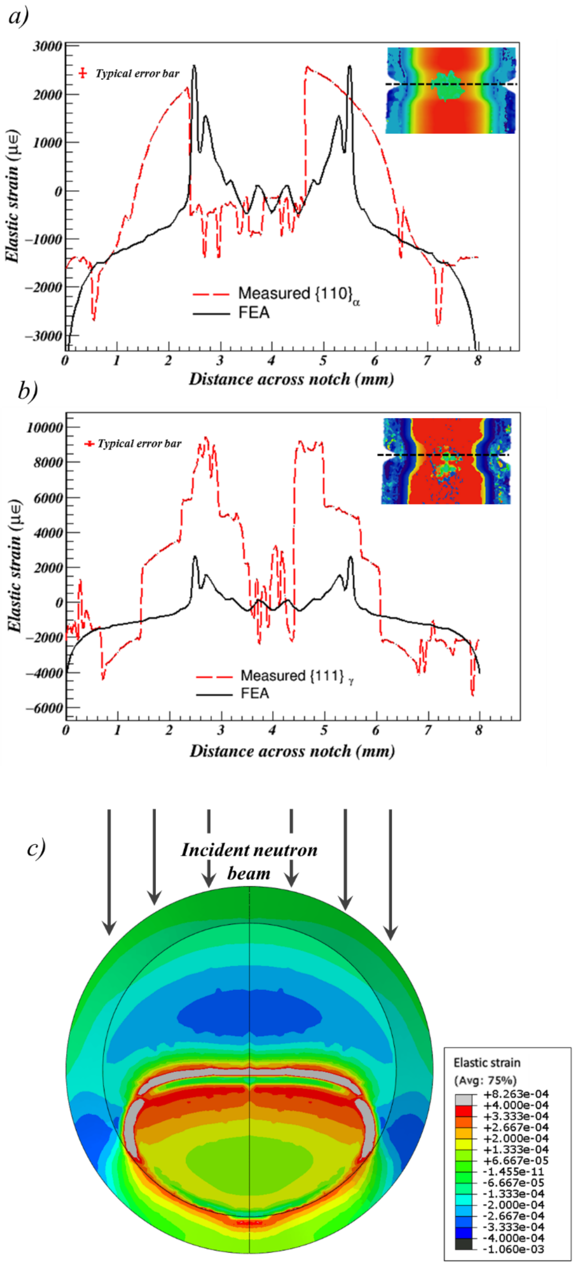

Figure 3.14: (a) Comparison of measured $\{110\}_\alpha$ and FEA elastic strain running parallel to the notch for the cracked sample. (b) Comparison of measured $\{111\}_\gamma$ and FEA elastic strain running parallel to the notch for the cracked sample. Inset on both graphs is the corresponding strain map. Typical $\mu\varepsilon$ error corresponding to the Bragg edge fitting error for the 39 x 39 pixel spatial binning used for strain map generation. (c) Elastic strain from FEA on the cracked cross section of the sample with assumed beam direction relative to the crack.

The specimen was designed to be axisymmetric so that the strain field across its cross-section could be back-calculated from the through thickness average strain measured using the full field beam in the Bragg edge imaging experiment. The crack propagated unsymmetrically through one side of the specimen invalidating its axisymmetric condition. It was therefore not possible to back-calculate the strain variation through the cross-section analytically. Instead, a three-dimensional finite element model was created whose crack geometry was representative of that observed in the scanning electron microscopy study.

It was also concluded that strain accuracy is significantly better for the ferritic $\{110\}_\alpha$ edge, than that of the austenitic $\{111\}_\gamma$ edge. The NCT technique also demonstrates the presence of a crack, yet is restricted by lower spatial resolutions, especially when compared to the more conventional XCT. Both neutron imaging techniques hold great promise, with the potential to be used in conjunction with each other for correlative studies.

Directly compared with X-ray computed tomography, the neutron computed tomography appears to be lower in quality, as seen in Figure 3.12. It was observed that NCT has the ability to distinguish different phases in the duplex steel, potentially providing an opportunity to be used with quantitative three-dimensional strain measurement techniques such as DVC. Despite having a greater spatial resolution, the XCT cannot resolve near-tip crack morphology when the sample is unloaded. This is likely due to the crack closure after unloading. It has been shown that for accurate observation of cracks, *in situ* loading experiments that keeps the crack open are more successful [157].

Finite element analysis of the sample was performed which included information from the crack morphology obtained using SEM analysis. Strain measured in the ferritic $\{110\}_\alpha$ is of a comparable order of magnitude to that of the FEA, with a clear drop when averaging entirely along the crack tip, similar the FEA. The austenitic $\{111\}_\gamma$ edge measures unrealistic magnitudes of strain, and whilst the maps provide evidence of a crack, the strain measurements are less accurate.

The differences between the strains that are measured experimentally and calculated by FEA are likely to be caused by the crack front not being completely perpendicular to the beam direction, which was assumed when modelling. The neutron transmission scan was performed with the crack opening being very nearly perpendicular to the incident beam, yet even small misalignments can cause noticeable shifts in the relative crack position, as seen in the strain cross-section. The scan being averaged through the material thickness, however, only provides useful information because the sample is suitably orientated in a appropriate direction.

3.5.2 Future work

This study demonstrated the potential of Bragg edge transmission imaging for detecting the presence of cracks, through the generation of two-dimensional strain mapping. To improve counting statistics, it would be recommended to scan for longer times, which would eradicate the non-converging regions, whilst also allowing for a reduced spatial binning area and improved effective spatial resolution. The next steps for the Bragg edge technique would be development of a three-dimensional elastic strain field, by completing Bragg edge tomographic scans at many different angles. This is a technique currently under development, with the theoretical and practical issues around it being tackled by others [131, 132]. Also, through the development of microstructurally informed models, for example crystal plasticity finite element modelling, it may be possible to develop a greater understanding of the difference between the strain measured in the ferritic and austenitic phases, assuming that material texture has been measured accurately.

For neutron CT, the practical aspects are current, with dedicated imaging beamlines continuously advancing the technology used to improve spatial resolution. For example, the IMAT beamline has recently introduced a cooled CCD camera, capable of reducing noise and therefore improving the quality of images. Once spatial resolutions improve enough to perform DVC, the ability to measure total three-dimensional strain should become viable using duplex stainless steel. With Bragg-edge strain mapping allowing for analysis of the elastic strain field, and neutron tomography with DVC providing the total strain full field, a combination of both techniques could give a greater understanding on crack tip elastic and plastic strain evolution.

It may also be possible to develop a correlative technique between neutron and X-ray tomography results. The crack morphology is much clearer in the X-ray images, yet it is not possible to visualise grain boundaries. The crack morphology is much less visible in the neutron images, yet the presence of phases may become clear with better spatial resolution. On registration of both volumes, it may be possible to correlate the crack and the presence of grain boundaries, providing important information on crack propagation behaviour in duplex stainless steels.

3.6 Concluding remarks

- Bragg edge transmission imaging can be used for generating two-dimensional maps of the average elastic strain, with spatial resolutions sufficient to see the influence of large fatigue cracks, with ferritic steel delivering better results. Spatial resolution can be improved further to get greater detailed information on localised crack tip stresses.
- Neutron CT allows for visualisation crack profiles, yet with poorer spatial resolution than that of established X-ray absorption CT. Neutron CT images do however provide information on the presence of different phases, and potentially on granular displacements, suggesting DVC is possible.
- Once both techniques reach a certain stage of development, combining results of both may allow for the study of three-dimensional plastic strain. Also, it may be possible to correlate between the information provided in neutron and X-ray tomography to further understand crack growth propagation along grain boundaries.

CHAPTER 4

MAPPING OF AXIAL PLASTIC ZONE FOR ROLLER BEARING OVERLOADS USING NEUTRON TRANSMISSION IMAGING

Authors: A. Reid[1], I. Martinez[1], M. Marshall[1], T. Minniti[2], S. Kabra[2], W. Kockelmann[2], T. Connolley[3], M. Mostafavi[4].

[1] *University of Sheffield, Dept. Mechanical Engineering, Sheffield, S1 3JD, UK;*

[2] *STFC-Rutherford Appleton Laboratory, ISIS Facility, Harwell, OX11 0QX, UK;*

[3] *Diamond Light Source Ltd, Harwell Science and Innovation Campus, Didcot, Oxfordshire OX11 0DE, UK;*

[4] *University of Bristol, Dept. Mechanical Engineering, Bristol, BS8 1TR, UK;*

Abstract: *Premature failure of wind turbine gearbox bearings is an ongoing concern for industry, with sudden overload events potentially contributing towards raceway damage, significantly hindering performance. Subsurface stresses generated along a line contact cause material yielding, and a probable crack initiation site. Currently, the ability to study subsurface plastic zone evolution using non-destructive techniques is limited. Neutron Bragg edge imaging is a novel technique, allowing for two-dimensional mapping of the Bragg edge broadening parameter, indicative of bulk plastic deformation. An experiment on the ENGIN-X strain scanning instrument, at the ISIS neutron source, UK, was setup for Bragg edge transmission imaging, to measure the effect of in situ loading on the raceway of a bearing, scaled-down from a traditional wind turbine gearbox bearing. Results demonstrate a strong correlation between load and the Bragg edge width, and allow for future experimental development in studying, not only the effect of overloads on fatigue life, but also the use of neutron imaging for evaluating plastic deformation in engineering components.*

4.1 Introduction

Wind turbine gearbox bearings, even after decades of engineering optimisation, are still considered to be the root-cause of many failures. Even with the presence of ISO gearbox design standards and specifications [158], bearings continue to fail significantly prematurely, when compared to their design lifetimes [159]. Within the UK, 35.1% of claims processed from wind turbine operators were due to the deterioration of the gearbox [14]. The detrimental impact on installation and operating costs of wind turbines has directed research attention towards further understanding the causes of failure.

Cylindrical roller bearings, such as those found in a wind turbine gearbox, are generally designed to withstand heavy radial loads at moderate rotational speeds [28, 27]. Whilst there are various roller bearing failure mechanisms operating simultaneously, rolling contact fatigue (RCF) contributes substantially. RCF may occur in the subsurface, with many studies indicating cyclic subsurface shear stresses, combined with inherent defects, significantly contribute to damage in the static raceway [160, 161, 162].

Sudden torque spikes associated with transient conditions and inertial effects within the gearbox induce large plastic strain in the subsurface of the static raceway [16]. Along with continued cyclic shear strains caused by RCF, failure within this region is inevitable. Subsurface yielding resulting from sudden overload events is a recognised cause of premature failure, with Hertzian contacts displaying greatest shear stresses in the subsurface [163]. Evaluating the evolution of subsurface plasticity for complex geometries, such as bearing contact sites, is yet to be fully evaluated with non-destructive techniques.

Laboratory destructive techniques such as scanning electron microscopy (SEM) and electron backscatter diffraction (EBSD) have been used to characterise the damage caused by sub-surface plasticity. It has been observed that subsurface plastic deformation damage in bearings is often associated with butterfly cracking at the white etch area (WEA) [164]. WEA is a region associated with nano-recrystallised carbide-free ferrite [165]. EBSD has been used to measure strain associated with fatigue cracks [166]. EBSD has also been successfully used to measure plastic strains in polycrystalline material [167], in combination with SEM. This technique uses the variation in crystal orientation in respect to a reference configuration, along with the analysis of local dislocation density distributions to provide accurate plastic strain measurements. It is however restricted to near surface measurements, typically to depths of 10-50 nm [168], meaning that *in situ* bulk strain measurements are highly impractical.

It is now common practice to non-destructively measure elastic strain in materials using higher energy techniques, such as synchrotron X-ray [169, 170, 171]. X-ray diffraction application to quantify plastic strain is limited however [115]. In X-ray diffraction, lattice spacings for specific *hkl* planes (*hkl* being the miller indices [42]), represented as Bragg peaks are measured. The change in spacing is associated with elastic strain, calculated by measuring the shifts in these interplanar spacings [63]. Attempts have been made to measure plastic strain in diffraction methods by correlating the plastic deformation with the Bragg peak width [172]. Plastically deformed materials exhibit diffraction peak broadening, with this effect becoming more prominent as levels of plasticity increase [172]. Full width at half maximum (FWHM) of the diffraction peaks are often used as measure of plastic strain [173]. However, the ability to use this peak broadening effect to quantify plastic strain is limited since other mechanisms such as stacking faults and/or planar defects also contribute towards peak broadening [174]. Other external factors contributing to peak broadening, impacting the reliability of measurements, include instrumental effects, notably when comparable with dislocation density being correlated with plastic deformation [175].

Similar to X-ray diffraction, neutron strain diffraction has developed significantly in recent decades [74], with advantages and disadvantages over synchrotron X-ray diffraction strain measurement techniques. Neutrons are capable of penetrating greater depths in typical engineering components, such as metals and metal matrix composites [176, 177]. Neutron scattering behaviour permits the investigation of materials possessing low atomic masses, with this benefit being utilised, for example, to directly study hydrogen trapping sites during the hydrogen embrittlement of bearing steel [129]. On the other hand, synchrotron X-rays provide enhanced spatial resolution and incident flux, compared with neutron techniques, greatly reducing the time required for data acquisition [63]. Bragg peak broadening investigations are also used in neutron diffraction [172, 178]. For example Huang et al observed increases in FWHM as a results of increased dislocation density, associated with gross plastic deformation during an *in situ* tensile loading experiment using annealed nickel alloy [179].

In this paper, Bragg edge transmission imaging has been used to identify the presence of plastic strain, through observation of edge broadening. This neutron imaging technique provided the opportunity to measure and generate two-dimensional maps of averaged elastic strains and observe plastic zone evolution in bulk materials with high spatial resolution [136]. FEA was used to compare simulation with experimental plastic zone evolution, allowing for result validation and a reliable method for predicting changes in subsurface plasticity.

4.2 Experimental design

4.2.1 Neutron Bragg edge transmission imaging

Neutron Bragg edge transmission imaging, or energy-dispersive neutron imaging, is a less conventional neutron scattering technique. As with the more established time of flight (ToF) and monochromatic neutron diffraction methods, it can be used to obtain strain information from polycrystalline materials non-destructively. Neutron transmission spectra contain sudden increases of intensity above the critical wavelength at which Braggs law is no longer satisfied, and diffraction no longer occurs for a given family of (*hkl*) lattice planes [114]. These points of sudden change in intensity, known as Bragg edges, occur at wavelengths corresponding to $2d_{hkl}$ (twice the lattice spacing). An exaggerated comparison between a Bragg edge from an unloaded and loaded sample can be seen in Figure 4.1. The shift in edge position, λ, is associated with elastic strain, whilst the broadening effect, σ, is indicative of plastic deformation.

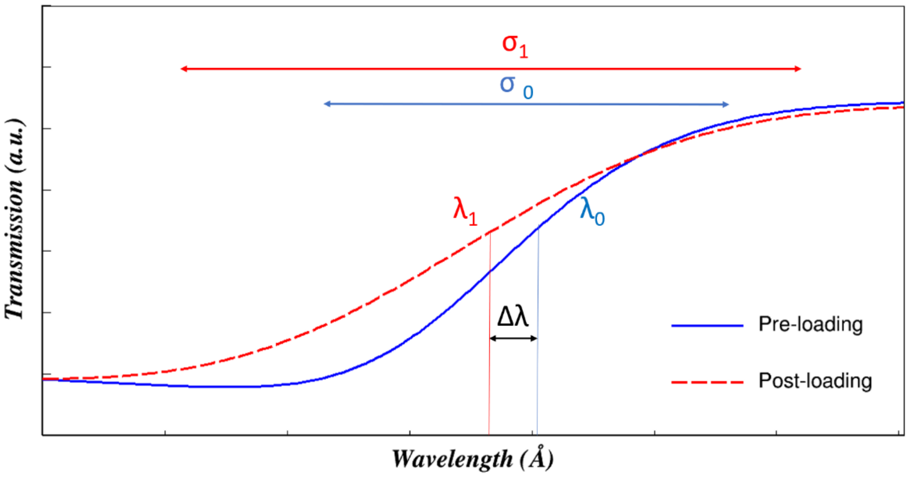

Figure 4.1: Comparison of Bragg edge taken from an unloaded and loaded sample, exaggerated to distinctly demonstrate the shift in edge position, λ, resulting from elastic strain, and edge broadening, σ, caused by plastic deformation.

Measuring strain from shifts in Bragg edges is analogous to more common strain measurements from diffracted Bragg peaks. However, whilst conventional neutron diffraction is a point measurement technique, energy-dispersive neutron imaging allows for the generation of strain maps with spatial resolutions dependent on the individual pixel size of the detector [121]. Due to the increased neutron intensity measured in transmission, compared to that of a diffracted Bragg angle, data acquisition times for Bragg edge transmission imaging are significantly shorter than that required for neutron diffraction. Using neutron diffraction to generate a strain map of the same dimensions as a transmission scan region of interest, multiple individual point scans would need to be acquired. Depending on the diffraction gauge volume and number of point scans this could take several hours [94]. Neutron time of flight information is used to calculate wavelength with Equation 4.1.

$$\lambda_{hkl} = \frac{hToF}{mL} \tag{4.1}$$

Where, λ_{hkl} is the neutron wavelength, h is Plancks constant, ToF is the neutron time of flight, m is the neutron mass, and L is the flight path from source to camera (neutron detector).

The wavelength can then be correlated with the interplanar spacing d_{hkl} using Equation 4.2.

$$\lambda_{hkl} = 2d_{hkl}sin\theta \tag{4.2}$$

Where, λ_{hkl} is the wavelength at which the $\{hkl\}$ plane diffracts the neutron beam, d_{hkl} is the lattice spacing of the $\{hkl\}$ plane. 2θ is the angle between the incident and the diffracted beam. Therefore, in the case of neutron transmission, $2\theta = \pi$.

The average strain component in the beam direction may be calculated using the definition of strain expressed in Equation 4.3.

$$\varepsilon = \frac{d_{hkl} - d^0_{hkl}}{d^0_{hkl}} \tag{4.3}$$

Where, d^0_{hkl} is the interplanar spacing of the unstrained material. The strain accuracy of the method has been previously estimated as $\Delta\varepsilon \approx 10^{-5}$ [120].

In a neutron Bragg edge transmission experiment, if counting times are long enough to gather data with sufficient statistics, the shape of the edges may be fitted using the analytical function, expressed in Equation 4.4 [120]:

$$B(d_{hkl}, t) = \frac{1}{2}\left[erfc\left(-\frac{t - t_{hkl}}{\sqrt{2}\sigma}\right) - exp\left(-\frac{t - t_{hkl}}{\tau} + \frac{\sigma^2}{2\tau^2}\right) erfc\left(-\frac{t - t_{hkl}}{\sqrt{2}\sigma} + \frac{\sigma}{\tau}\right)\right] \tag{4.4}$$

In which t is time, t_{hkl} is the time of flight associated with $\{hkl\}$ plane, τ is a constant associated with the instrumental pulse width (pre-determined experimentally [120]), and σ defines the width of the Bragg edge.

The σ parameter is increased by the presence of higher intragranular strain caused by dislocations, and fluctuating intergranular strain within a specific region [180], analogous to FHWM in a diffraction peak. As Bragg edge broadening, and increases in the σ parameter, are indicative of plastic deformation, experimental results focus on this relationship. The ability to map this broadening parameter offers the unique opportunity to qualitatively image the evolution of subsurface yielding in an overloaded roller bearing.

4.2.2 Test bearing

Wind turbine gearbox bearings are large components, unsuitable for neutron strain measurement techniques due to their high attenuation. A SKF, NU1010 ECP bearing was used in this research as it provides the opportunity to scale-down the sample size whilst maintaining the contact conditions experienced in a wind turbine gearbox bearing. It was ensured that the selected sample bearing has the same average contact pressure through the contact area as the wind turbine bearing. The selected bearing has an outer diameter of 80 mm and bore diameter of 50 mm, with a thickness of 16 mm (along x-direction see Figure 4.2) being of notable importance for this experiment, as this allows sufficient neutron penetration within the neutron wavelength range of interest (0.5 – 6 Å). Material properties for AISI 52100 bearing steel can be found in Table 4.1, whilst chemical composition is detailed in Table 4.2.

Experimental work using the same bearing has demonstrated that there is reasonable agreement between the stress measured experimentally by X-ray diffraction and that predicted by Hertzian contact mechanics [183]. Therefore, the elastic limit load of the bearing can be calculated by using theoretical Hertzian equations. The elastic limit load is based on the following rearrangement

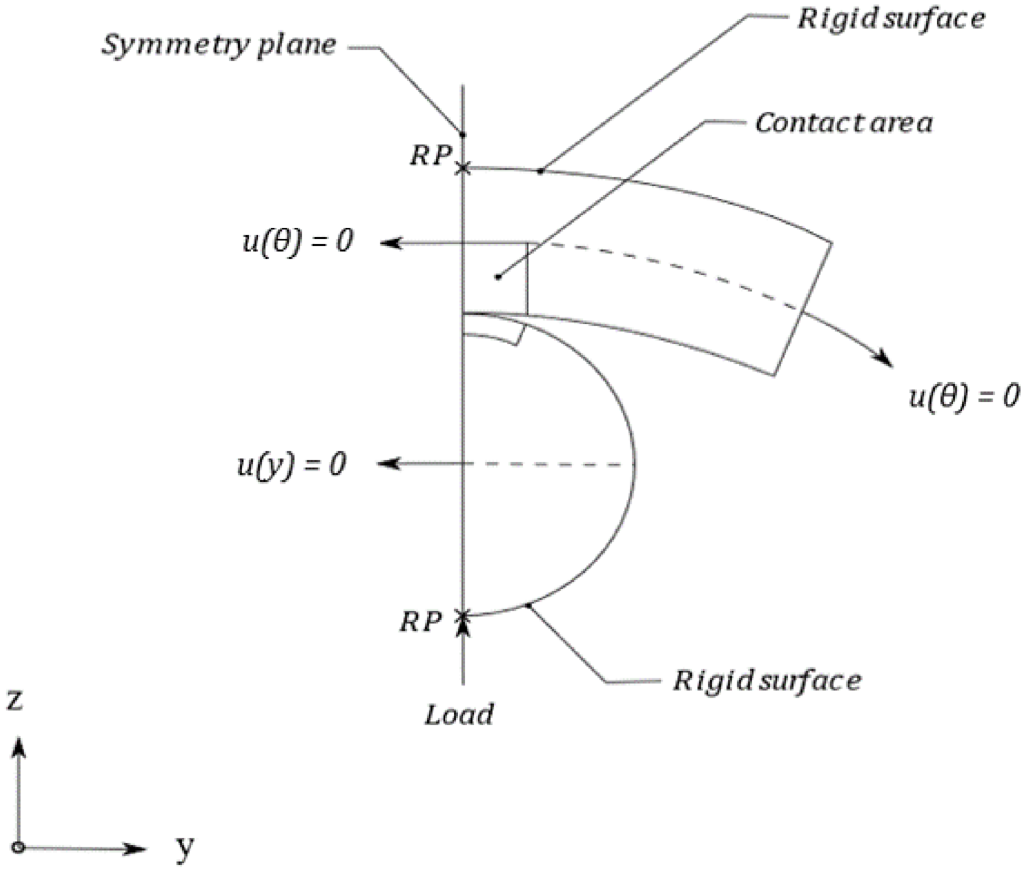

Figure 4.2: Finite Element Model Boundary Conditions.

of Hertzian contact equation, assuming that the bearing elastic limit load is reached once the maximum von-Mises stress in the contact stress field reaches the materials yield stress.

$$F^Y = \frac{L\pi R^*}{E^*}\left(p^Y\right)^2 \tag{4.5}$$

$$p^Y = 1.67\sigma_Y \tag{4.6}$$

Where, p^Y, F^Y, L, R^* and E^* are the limit contact pressure, limit load, line contact length, equivalent radius, and equivalent Youngs Modulus, respectively. σ_Y is materials yield stress. The equivalent Youngs modulus and the equivalent radius are calculated using Equations 4.7 and 4.8, respectively.

$$\frac{1}{E^*} = \frac{2(1-\upsilon^2)}{E} \tag{4.7}$$

Table 4.1: AISI 52100 Properties [181].

Property	Symbol	Value
Density $[kg/m^3]$	ρ	7830
Young's Modulus $[GPa]$	E	201
Poisson's Ratio	υ	0.3
Yield Stress $[MPa]$	σ_Y	1410

Table 4.2: AISI 52100 Chemical Composition [182].

C	Mn	Si	Cr	Cu	S
0.95 - 1.10	0.20 - 0.50	≤0.35	1.30 - 1.60	≤0.025	≤0.025

$$\frac{1}{R^*} = \frac{1}{R_1} + \frac{1}{R_2} \tag{4.8}$$

To assess the effects of plastic overload on the life of the selected bearing, its life in normal conditions is to be calculated and compared with the overloaded reduced life measured experimentally. As the bearing life expectancy is largely statistical, it is standard practice to use the basic rating life, L_{10}, defined as the length of time in which 10% of bearings fail, stated in millions of cycles [37]. Basic rating life is calculated using the following equation [184]:

$$L_{10} = \left(\frac{C}{P}\right)^p \tag{4.9}$$

Where, C is the bearing dynamic load rating, P is the applied pressure and p is the load-life exponent ($\frac{10}{3}$ for roller bearings [184]). Adjustment factors may be used to predict life times with varying probabilities of failure [185], for example to calculate the expected time for 50% (L_{50}) or 90% (L_{90}) of bearings to fail.

4.2.3 Finite element analysis

It was critical to have an estimation of the bearing sub-surface plastic zone size as a function of applied load before the experiment. This is to determine an appropriate load, whereby the plastic zone can be identified using a neutron Bragg edge imaging detector with certain pixel size. A three dimensional finite element model was developed using ABAQUS version 6.14-2 [146] to estimate subsurface plastic zone evolution in the outer raceway. Schematic of the model can be seen in Figure 4.2. The raceway and the rolling elements were modelled using quadratic elements (C3D20R). Deformation of the rest of the component, i.e. the case of the shaft and the rigs cage, was ignored by modelling it as a rigid body; bilinear rigid quadrilateral elements (R3D4) were used. As the region of interest (i.e. the outer raceway area close to the raceway-roller contact site) has high stress gradient profiles, a mesh refinement was performed in that zone. The contact area at the outer raceway was modelled using a mesh size of 0.02 x 0.02 mm, the elements in the contact area (indicated in Figure 4.2) on the roller bearing were doubled in size, where its corresponding contact surface was defined as a master surface to prevent penetrations on the roller contact surface. This assumption was made as the roller surfaces are normally harder than the surface on outer raceway. The contact interaction was assumed to be frictionless for all the contact interactions in the model, also the contact between the roller and the outer raceway was modelled as a line contact, no effects on logarithmic profile were included. Assuming symmetry in the x-axis and θ-axis, a quarter of the bearing was modelled.

The model simulates the elastic-plastic behaviour of overloading, where initial yielding is governed by the distortion energy hypothesis (i.e. von-Mises stress). An isotropic hardening rule was used in the FE model derived from the stress-strain curve for AISI 52100 [186]. The model was solved in quasi-static conditions. Density values should be included in the analysis even though the inertial effects are going to be neglected, solving convergence issues during contact initiation between bodies in load-controlled problems. The active yielding zone, defined as the region where the material von Mises stress reached the materials yield stress, was of most importance for this analysis. The elements in the model where this condition is reached are flagged and their volume were added together by an in-house MATLAB code. Figure 4.3 demonstrates the evolution of the expected plastic area from initiation at 10.3 kN to 34 kN, where plasticity has propagated to the raceway surface. Validation was completed by comparing the FEA predicted values of p^Y and F^Y, with those calculated using Hertzian contact stress theory. The results, reported in Table 4.3 shows excellent agreement validating the model.

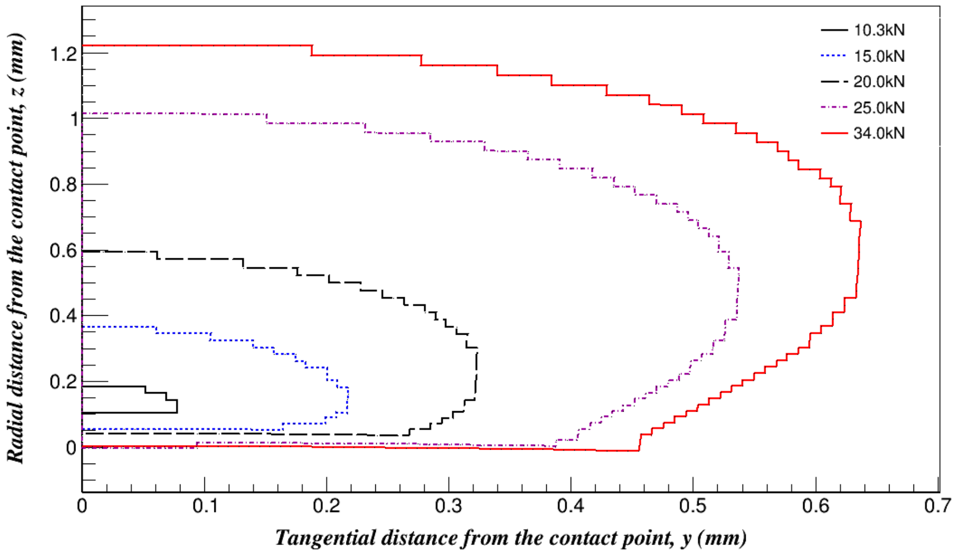

Figure 4.3: Subsurface plastic zone as predicted FEA, from initiation (10.3 kN) to the load at which yielding reaches the raceway surface (34 kN).

Table 4.3: Contact pressure and load yield limits.

	FE Model	Theoretical Prediction	Absolute Error (%)
p^Y [MPa]	2894.92	2805.6	3.18
F^Y [N]	9894.92	9285	3.90

4.3 Experiments and results

4.3.1 Bearing fatigue

To study the influence of overload events on the bearing life, a fixed raceway loading frame (FRLF) was designed to recreate an overload event within an isolated outer raceway, using a single rolling element. Fatigue tests were completed offline at University of Sheffield, UK, as neutrons were only required for the static overload experiment. The FRLF was mounted in an ESH servo hydraulic dynamic test machine (capacity 150 kN) with a Moog closed loop controller. Figure 4.4 shows the setup of the overload experiment and details of the designed overloading frame. The test frame allowed static overloads to be applied on the bearing in displacement control at a rate of 0.2 mm/min and fatigue loads to be applied at 15 Hz.

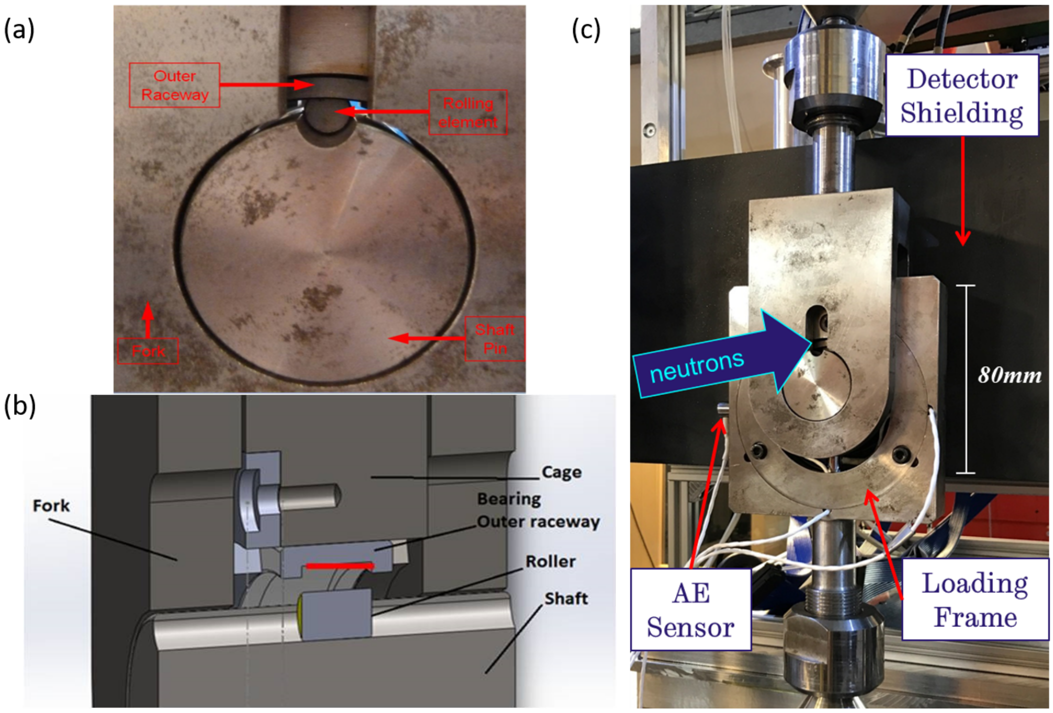

Figure 4.4: (a) Roller bearing and FLRF assembly. (b) CAD cross-section of the assembled FRLF visualising contact site (red line). (c) Experimental setup on ENGIN-X instrument, with MCP detector.

The most extreme loading condition where yielding reaches the raceway surface, as shown by FE simulation (see section 4.2.3), was overloading at $p^{overload}$ = 34 kN. A static overload at 34 kN was followed by a fatigue load of p^{max} = 10 kN (maximum load below initiation of subsurface yielding, according to FE) and p^{min} = 100 N. Sinusoidal loading was applied on the sample. The R ratio (p^{min}/p^{max}) of 0.001 intended to recreate the effect of roller passage, imitating pressure being removed from the raceway without repeated impact. After 5 million cycles (equivalent of approximately 2.78 x 10^5 revolutions), a well-defined crack was observed propagating axially along the line contact position. This signifies an approximated 64% reduction in the dynamic load rating, as a result of damage induced by the overload.

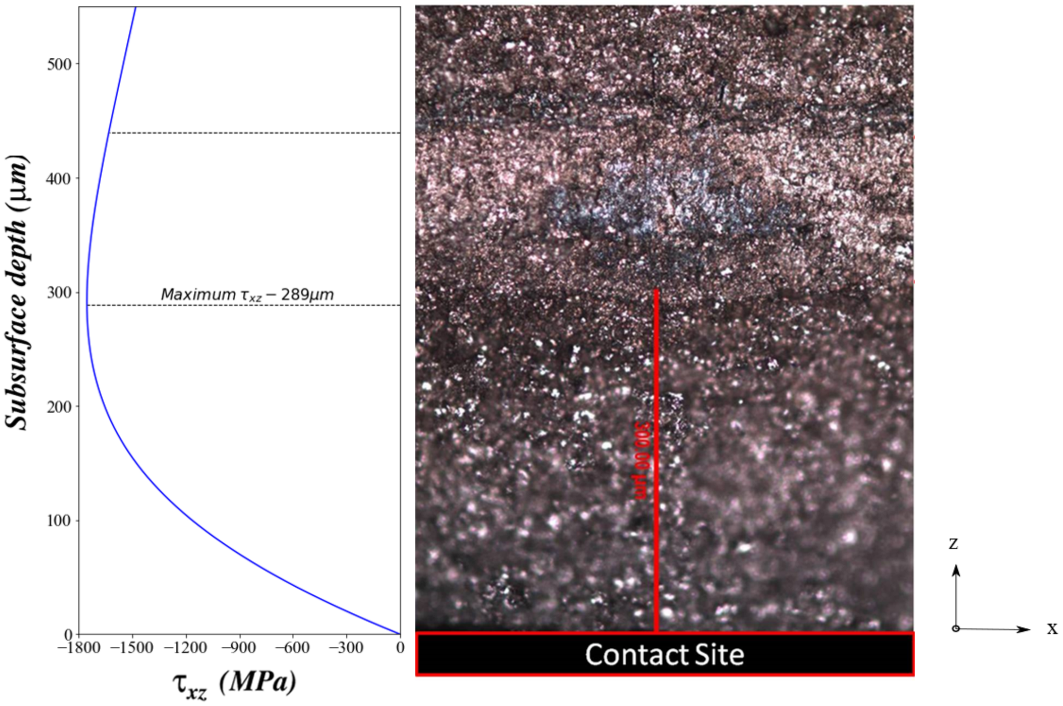

Figure 4.5: Optical microscope image of the fracture surface under x20 magnification, with graphical representation of the subsurface shear stress at 34 kN, calculated using Hertzian contact mechanics.

Figure 4.5 shows the fracture surface of the bearing midway through its width (xz-plane) taken by an optical microscope with x20 magnification. The theoretical variation of the shear stress radially through the thickness of the bearing is included in this image with the point of maximum shear stress also being indicated. It can be seen that a region of significant microstructural alteration is present at depths between roughly 300 μm and 450 μm. A SEM image of this area is shown in Figure 4.6, which shows a transition between the regions of highest shear stress caused by overload and the fatigue cracking region. The smoother surface, in the overload affected zone, is characteristic of ductile fatigue, whilst the region closest to the surface is rougher with spherical voids visible, indicative of ductile fracture. This experiment confirmed that an overload of 34 kN reduced the life of the selected bearing. The shape and magnitude of the plastic zone was then investigated in depth using neutron transmission Bragg edge imaging.

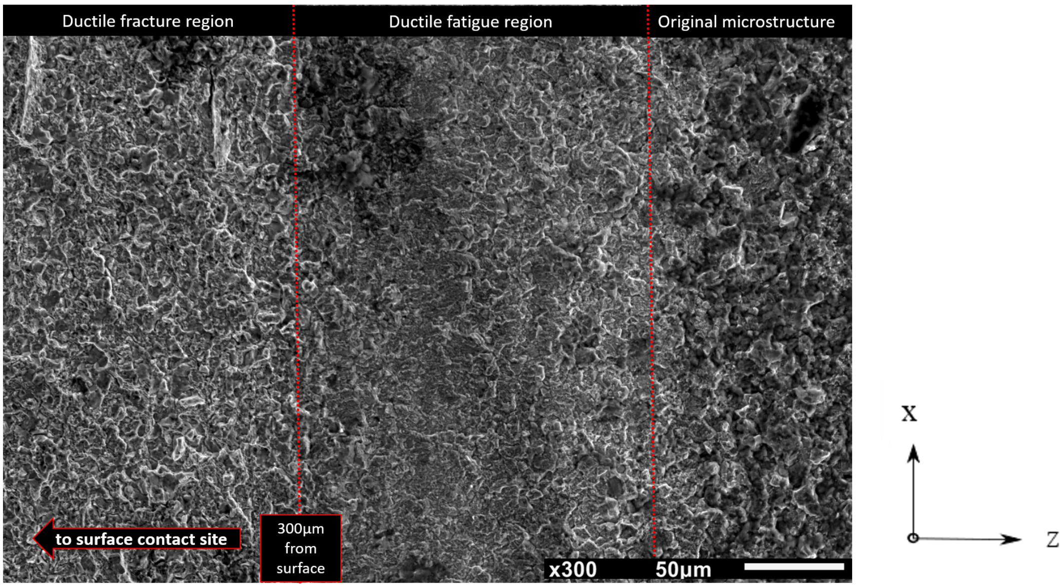

Figure 4.6: SEM image (x300 magnification) of the transition between the region of highest shear during fatigue loading, the altered microstructure in the region of maximum shear from overloading, and the coarse pearlitic microstructure present in the unaffected zone.

4.3.2 Bragg edge imaging

This experiment was conducted on the ENGIN-X instrument at the ISIS pulsed neutron spallation source, located at the Rutherford Appleton Laboratory, UK. The FLRF was mounted on a 50 kN hydraulic Instron load frame, to overload an outer raceway using a single rolling element *in situ* (as in Section 4.3.1).

Bragg edge neutron transmission imaging was undertaken using a ToF neutron camera, based on a microchannel plate (MCP) detector, designed by Nova Scientific and University of California at Berkley, for the IMAT imaging beamline at ISIS neutron source [136, 119]. The MCP consists of a 2 x 2 array of Timepix readout application specific integrated circuits (ASICS), with a total field of view of 28 x 28 mm^2 (512 x 512 pixels with individual pixel sizes of 55 x 55 μm^2) [137]. Within a pixel, a detected neutron generates an electron avalanche which is registered by the ASIC (CMOS) readout chip, whilst the neutron arrival time is also registered. For this experiment, a time resolution of 4.48 μs was set. The MCP has a detection efficiency of approximately 50% for neutron energy ranges relevant for to this study [138]. Details of the detector and its specifications can be found elsewhere [139, 137].

The MCP was positioned using a specially designed mounting arrangement, unique for this experiment (see Figure 4.4c). Due to the non-uniform divergent nature of the neutron beam, it is preferable to minimise the distance between the sample and the detector in an imaging experiment. The camera was positioned at 48 mm from the furthest edge of the bearing raceway, as the FRLF geometry restricted the minimum distance. The scans were taken whilst the sample was held at any specified load, with the Instron in displacement control. The measured range of neutron time of flights for each scan was 18 ms to 55.7 ms.

ENGIN-X beamline is a strain diffractometer, and therefore not optimised for imaging experiments. Although flux on ENGIN-X is significantly lower than a dedicated imaging beamline, such as IMAT, ENGIN-X has the 2^{nd} best resolution of any neutron beamline at ISIS. ENGIN-X was chosen for this experiment as it does provide the opportunity to carry out *in situ* testing using a 50 kN hydraulic loading frame. Material thickness will also influence the necessary scan times, with an optimum being found where the thickness allows for averaging over significant grain numbers without being overly attenuating. After trial experiments, it was concluded that the sample of 16 mm thickness required scan times of 2 hours. This provides sufficient statistics for Bragg edge analysis, and completion of scans at several different loads within the allocated timeframe.

As each individual pixel records a separate transmission spectrum, any non-uniformity in the beam or variations in pixel response need to be accounted for. A flat field scan, where no sample is mounted, is used to normalise these neutron beam and detector effects. Flat field scans were taken prior to mounting and after removing the sample to improve statistics. Bragg edge transmission images were then taken at 0.4 (reference), 10 (elastic limit), 15, 25, and 34 (plasticity reaching surface) kN.

Bragg Edge Analysis for Transmission and Imaging Experiment (BEATRIX) software, was used to analyse the data recorded in this experiment, through the fitting procedure described by Santisteban *et al* [120] to extract the individual fitting parameters for a specified edge [187]. A pixel situated in a region away from the contact site at an applied load of 400 N was chosen to measure the position of the stress-free Bragg edge associated with {110} plane and A Bragg edge position of 4.06510 Å, corresponding to d^0_{hkl}= 2.03255 Å was measured. This method for acquiring a stress-free measurement was chosen because the focus of this study is on Bragg edge broadening and elastic residual strain measurement was not a priority. Residual stress experiments require a highly accurate stress-free, or d^0_{hkl}, value [51] which requires non-negligible acquisition time. It was decided to spend more time acquiring data related to material yielding and use a far-field stress-free area of the sample while unloaded as a representative of a stress-free lattice spacing. BEATRIX software accounts for variation of Bragg edge position in calculating broadening, therefore, the lack of an exact stress-free Bragg edge position does not reduce the accuracy of broadening measurement. An example of the transmission spectra at 400N load is given in Figure 4.7, along with a BEATRIX fitted {110} Bragg edge with statistics corresponding to 31 x 31 pixel spatial binning.

The software uses the flat-field scan for normalisation and accounts for detector deadtime by means of an event overlap correction algorithm [188], outputting two-dimensional maps with pixel size spatial resolution for each individual fitting parameter, along with a map of strain. Parameters extracted using this technique are averaged through the thickness of the sample, giving the averaged axial (ε_{xx}) strain (see Figure 4.8 for coordinate system). Low signal-to-noise ratios (SNR) within each individual pixel required spatial binning to gather sufficient data statistics for fitting edges with the required precision, visualised as a smoothing effect in the two-dimensional maps. Spatial binning of 31 x 31 pixels was used in the analysis for this experiment to improve counting statistics. The analysis is completed pixel by pixel, whilst recursively running an average mask of 31 x 31 neighbouring pixels, centred to that specific pixel under analysis, to ensure the statistics are sufficient to fit the Bragg edges [112].

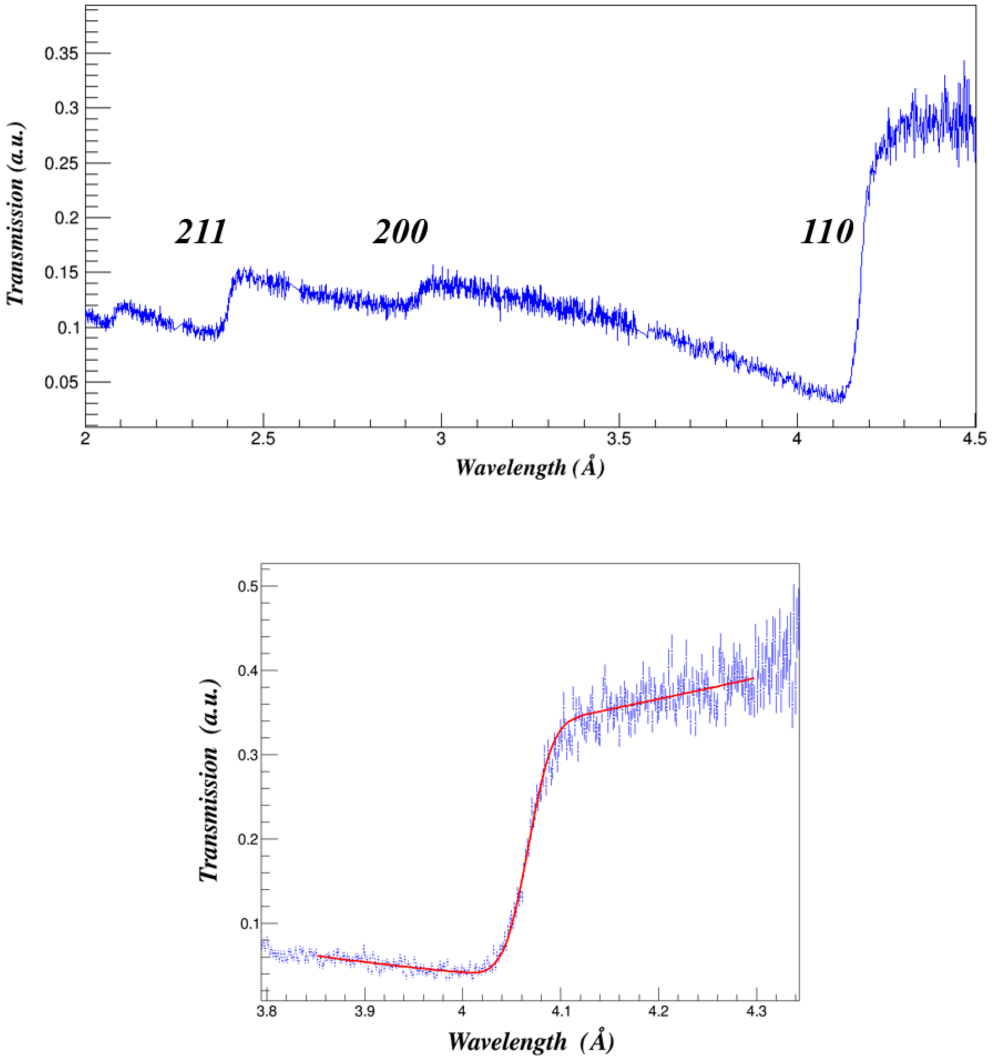

Figure 4.7: Neutron transmission spectrum through a bainitic SKF NU1010 ECP bearing outer raceway indicating Bragg edges associated with {110}, {200}, and {211}. Bottom: BEATRIX fit for a {110} edge using 31 x 31 pixel spatial binning statistics.

The *bcc* {110} lattice plane was used to calculate strain as it has significantly greater intensity than the other available edges. The aim of this research was to evaluate Bragg edge broadening effects, which can be observed with greater confidence in edges of largest intensity. For *bcc* crystal structures the {211} lattice planes exhibit the most favourable relationship with the macroscopic strain, yet the {110} Bragg edge suitably demonstrates the bulk elastic response [189]. In this study, elastic strain was not a primary focus, as the aim was to generate the shape of the plastic area. Material yielding generates substantial intergranular residual stress, therefore reducing the accuracy in elastic strain measurements when compared to the macroscopic applied stress field [190, 152].

Two-dimensional maps of Bragg edge broadening, quantified by σ in BEATRIX, were generated for two loads prior to yielding and three loads post plastic initiation, according to FEA. Figure 4.8 displays the maps of the σ parameter, showing clear increases in the contact region as a function of increased load, indicative of subsurface yielding. Once 10 kN elastic limit is exceeded, the contact

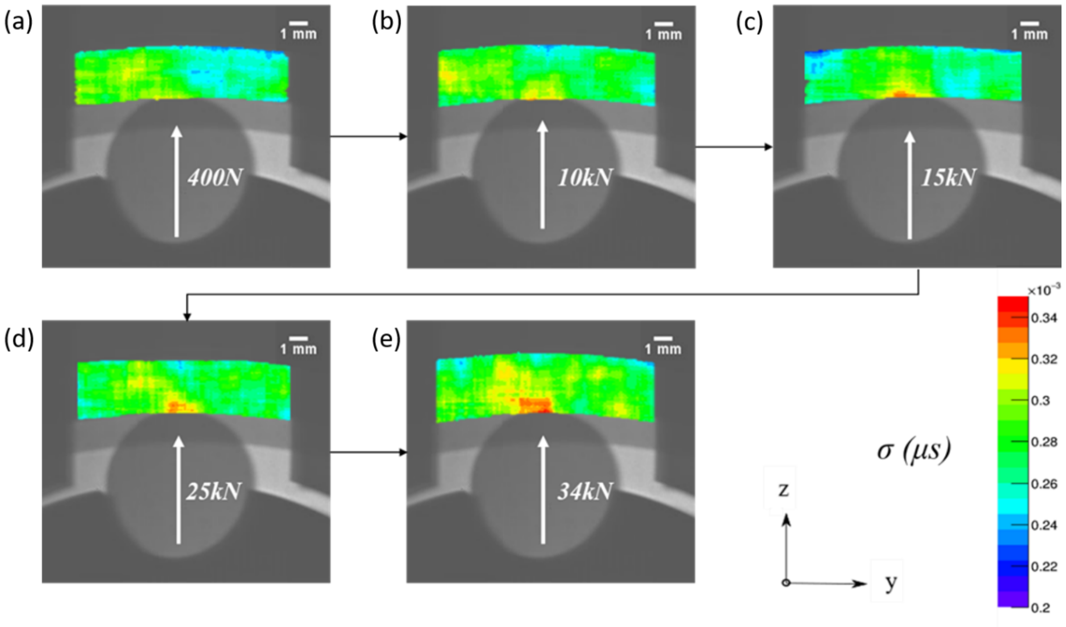

Figure 4.8: 2D maps of the Bragg edge broadening parameter, σ, at various loads: (a) 0.4 kN (b) 10 kN (c) 15 kN (d) 25 kN (e) 34 kN.

region demonstrates greater broadening, with this evolving until 34 kN load is reached. Due to the complexity of the mechanisms involved with plastic deformation, quantitative analysis of plastic strains is not yet possible using this technique. However, when comparing the increase of σ radially from the contact site, the greatest fluctuations post-yielding occur in the subsurface. Figure 4.9 displays increases in the subsurface line profile extracted by the σ parameter maps, relative to the 400 N load, with values averaged across the Hertzian contact width, 400 μm, corresponding to 7 pixels (385 μm). The cause of unexpected subsurface fluctuations in σ can only be speculated at this current time. For instance, bearing manufacturing and post-manufacturing treatment, such as shot peening may well cause variations in microstructure, resulting in differing response to load at different subsurface depths.

4.4 Discussion

4.4.1 Bragg edge imaging

Onset of yielding above 10 kN inherently makes measured elastic strain difficult to compare with FEA accurately, as plastic deformation generates substantial intergranular residual stress. Averaging through 16 mm of steel with such significant presence of plastic deformation would not allow for accurate elastic strain comparisons. Nevertheless, this study demonstrates reasonable correlation between measured elastic strains and those predicted by the model at 10 kN, averaged through thickness the same way that the measurement in the ε_{xx} was carried out. Figure 4.10 shows the variation of elastic ε_{xx} strains measured by BEATRIX through the width of the bearing compared with that predicted by finite element simulation. As the distance from the contact site, and highest strain

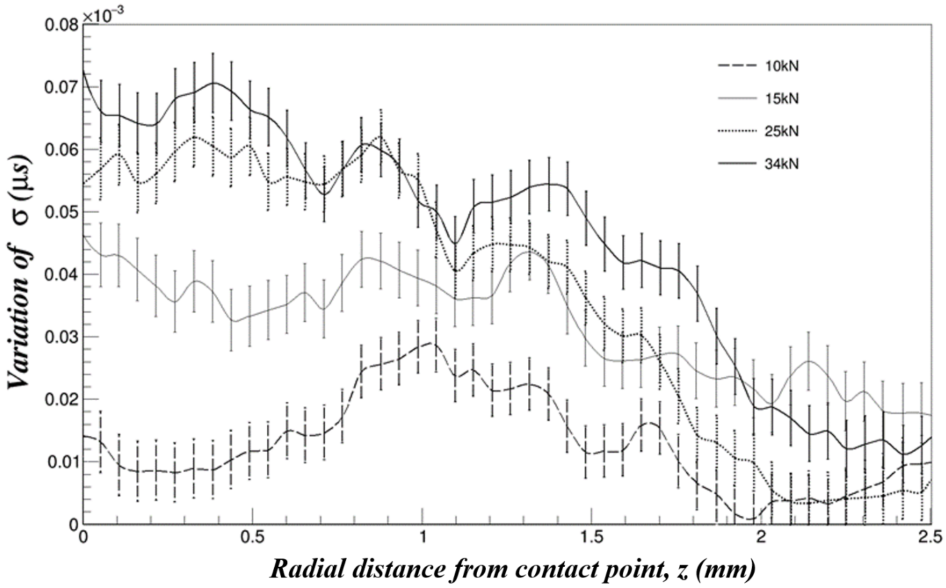

Figure 4.9: Increase in sigma value from the contact site into the subsurface for several each loads, relative to the reference 400N load.

gradients, increases the agreement between the FEA and experiential measurement of elastic strain increases.

Mapping of the Bragg edge broadening parameter, σ, gives an indication of subsurface yielding in bulk engineering components, with a wide range of applications. It may be noted that a detail of the materials manufacturing and post-manufacturing treatment history, if available, could be used to determine microstructural variations, which may influence result accuracy. The active yield area that was generated from FEA corresponds well with the σ maps of the contact area generated by

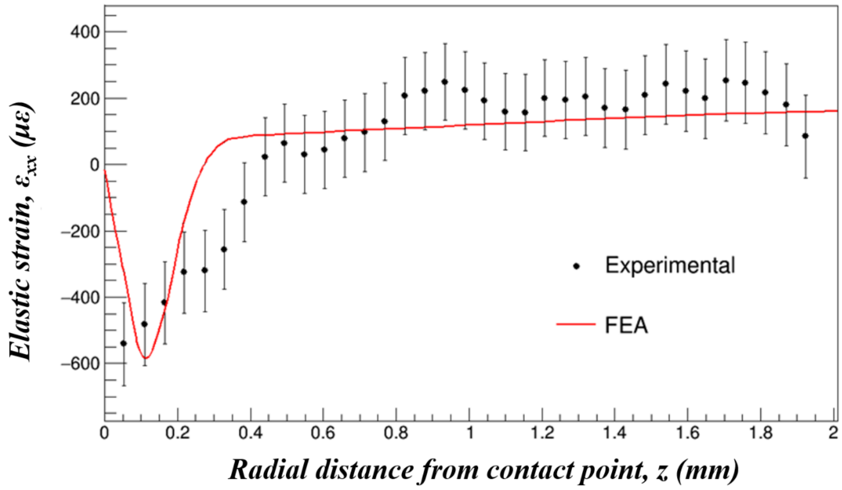

Figure 4.10: Subsurface axial (ε_{xx}) strain averaged through the sample, as a function of distance from the contact site, compared to the same component of average FEA strain.

the experiment (see Figure 4.11). It was observed that using a threshold σ value of 0.3175 μs, calibrated at 34 kN and then applied to the remaining loads, allowed for reasonable comparisons with predicted plasticity. However, the spatial resolution was not adequate for distinguishing the small elastic region at the contact for 15 kN and 25 kN. There are some discrepancies between experimental data and FEA, notably at 34 kN, where spots above the threshold appear. Without access to repeatable data it is difficult to give an exact explanation, yet it could be speculated that either experimental error or significant microstructural changes at greater loads cause this effect. Whilst an encouraging result, this suggests that future studies will need to be completed in order to quantify plastic strains with Bragg edge imaging, although the σ threshold will vary depending on the sample geometry and material used. For quantitative plastic analysis using energy-dispersive transmission imaging, simpler and well understood sample geometries would be required.

4.4.2 Future work

Whilst energy-dispersive imaging is a unique method for studying the evolution of subsurface yielding, and Bragg edge broadening is indicative of plasticity, it has yet to be demonstrated as a technique capable of measuring plastic strains quantitatively. Due to the complexity of plastic deformation, and its influence on neutron scattering, the ability to quantitatively study subsurface yielding using such ToF techniques remains a problematic task. Future development of this technique may not only allow for quantitative plastic strain analysis, but also for a more automated approach to FEA and experimental analysis. For instance, it may be possible to develop software capable of cross-correlating experimental data with FEA results to extract the most suitable σ threshold.

Time restrictions for completing this experiment resulted in scan times limited to 2 hours per load. Increasing exposure time improves counting statistics, which reduces the size of spatial binning areas, refining the effective spatial resolution. Carrying out the experiment at an imaging beamline, such as IMAT, designed for such high flux experiments ensures that counting statistics are improved. IMAT also uses pinhole collimator capabilities, allowing for greater control over beam divergence, which is responsible for geometrical blurring effects that can negatively impact spatial resolution. Whilst ENGIN-X has better pulse width (τ parameter), due to using a methane moderator, compared to a hydrogen moderator used at IMAT, this parameter has been fixed for the analysis of results in this work. Future studies will use multi-Bragg edge approaches, requiring well-characterised ToF dependencies and correlations between τ and σ parameters, which will lead to gains in spatial accuracy and spatial resolution of mapped parameters.

Fractography results suggest that subsurface yielding may seed defects, impairing bearing performance, yet the tests completed using the FRLF were not fully representative of operational bearing conditions. This experiment will need to be complemented in future work with time-resolved strain measurement in the overloaded region of an *in situ* dynamic bearing (i.e. a rotary test rig) to give greater confidence that bearing overload events are detrimental to predicted life.

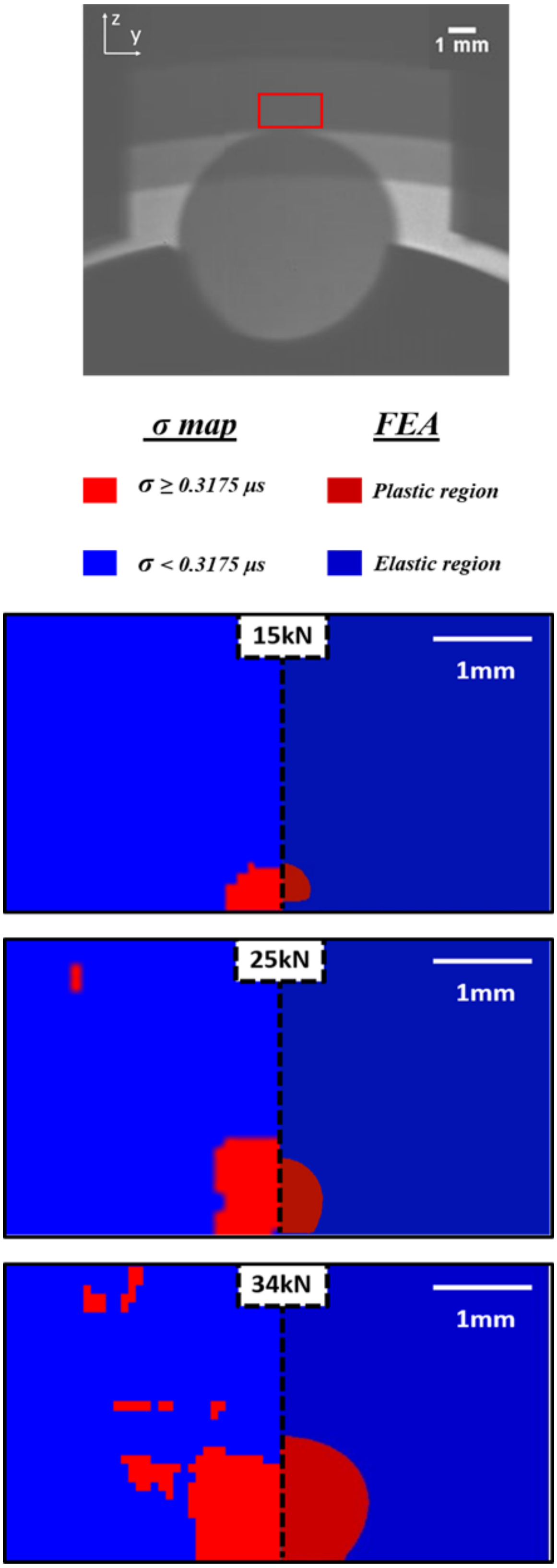

Figure 4.11: (Top) Radiograph indicating the region of interest, beneath the contact. (Bottom) Comparison of σ broadening parameter and the active yield region at the contact site, with applied loads of 15 kN, 25 kN and 34 kN load.

4.5 Conclusions

- Neutron Bragg edge transmission imaging can be used to visualise the evolution of material yielding non-destructively in bulk engineering components. Quantitative analysis of plastic strains is yet to be demonstrated. It may be possible to determine a σ threshold capable of indicating the presence of plastic deformation in materials of certain sample geometries.
- To gain sufficient counting statistics, long exposure times are required for each scan. Spatial binning techniques may be used to overcome this at the expense of spatial resolution. Alternatively, the use of a dedicated imaging beamline equipped with *in situ* loading rig, can improve counting statistics.
- Overload events reduce the fatigue life of bearings, with high subsurface shear stresses and the presence of yielding is likely to induce defects that act as a site for crack initiation. Future work on the time-resolved strain in dynamic overloaded bearings, may potentially give greater confidence of the extent of damage caused.

CHAPTER 5

MEASUREMENT OF STRAIN EVOLUTION IN OVERLOADED ROLLER BEARINGS USING ENERGY DISPERSIVE X-RAY DIFFRACTION

Authors: A. Reid[1], C. Simpson[2], I. Martinez[1], S. Kabra[3], T. Connolley[4], O. Magdysyuk[4], C. Charlesworth[4], M. Marshall[1], M. Mostafavi[2].

[1] *University of Sheffield, Dept. Mechanical Engineering, Sheffield, S1 3JD, UK;*

[2] *University of Bristol, Dept. Mechanical Engineering, Bristol, BS8 1TR, UK;*

[3] *STFC-Rutherford Appleton Laboratory, ISIS Facility, Harwell, OX11 0QX, UK;*

[4] *Diamond Light Source Ltd, Harwell Science and Innovation Campus, Didcot, Oxfordshire OX11 0DE, UK;*

Abstract: *There are several mechanisms contributing towards detrimental damage in wind turbine gearbox bearings, with sudden overload events believed to reduce their expected operational life. The generation of subsurface plasticity, followed by rolling contact fatigue, may lead to the initiation of either surface or subsurface cracking. This study presents a novel technique capable of measuring subsurface strain evolution in a rotating roller bearing, using energy dispersive X-ray diffraction. A pre-overloaded bearing was tested dynamically and consequently failed prematurely, supporting the hypothesis that overloads accelerate bearing failure. Throughout the test, an increase in compressive radial strain was observed, indicative of material softening, generally associated with the unstable stage of rolling contact fatigue, which occurs prior to definitive bearing failure.*

5.1 Introduction

5.1.1 Background

Premature failure of wind turbine gearbox (WTG) bearings is an area of great importance for industry due to significant interruptions to regular operating conditions [191]. The downtime for a single WTG failure is generally reported to be longer than for other constituent systems, with bearing failure suspending regular operation for up to 562 hours [192, 193]. Damage reports completed by the National Renewable Energy Laboratory in USA found that as much as 70% of gearbox component failure was related to bearings [15]. Research and development of condition monitoring systems, such as acoustic emission measurement and vibration analysis, is currently crucial for saving time and money for wind turbine operators, as these techniques may offer the opportunity to identify a faulty bearing prior to a failure [194]. The cause of WTG bearing failures has conventionally been diagnosed post mortem, with *in situ* techniques now becoming important for real-time validation.

The drivetrain of a wind turbine conventionally consists of several large cylindrical or tapered roller bearings, capable of withstanding the substantial loads exerted during normal operation. One of the most prominent locations for failure is at a bearing that supports the high-speed shaft (HSS), operating with rotational frequencies of up to 1800 revolutions per minute (*rpm*) [195, 22]. Even when installed and maintained carefully, it is established that bearings have a finite lifetime, as tribological effects will eventually lead to failure [184]. Cyclic contact stresses generated during the passage of a rolling element, known as rolling contact fatigue (RCF), will result in either surface or subsurface damage. These highly localised stresses, exerted between the bearing raceway and the rolling elements, can be estimated using Hertzian contact theory, assuming there are negligible effects from lubrication [20]. Due to the assumptions of Hertzian contact theory, RCF failure is regarded as a multiaxial fatigue condition, which is much more complicated to study than uniaxial fatigue problems [34].

Failure due to RCF is known to occur in three-phases; (I) shakedown, (II) the steady-state elastic response and (III) instability [196]. It has been established that during shakedown, both the transformation of retained austenite into martensite and work hardening generate small regions of microplasticity, which in turn influence the localised residual stress field [182]. The hardening increases the time spent in steady-state Stage II, where only elastic deformation occurs, without any fatigue damage or accumulation of plastic strain [161]. The duration of Stage II is also influenced by loading conditions, material properties and operating temperature, whilst residual stresses in the material may either reduce or increase during the steady-state stage [197]. Therefore, it can be deduced that increasing the time spent in Stage II will be fundamental to improving the fatigue life of bearings [196]. Gradual material softening causes a reduction of yield strength, eventually triggering the onset of Stage III instability and drastically increasing the size of the plastically deformed region which occurs at the subsurface [198]. The subsurface plasticity causes tensile residual stress to accumulate in the radial direction, perpendicular to the contact surface, increasing the opening force experienced by cracks growing parallel to the surface [199].

Failure arising from RCF has two prominent mechanisms; either subsurface-initiated spalling or surface-initiated pitting [200]. The nucleation and coalescence of subsurface microcracks, most frequently originating at depths corresponding to the maximum shear stress, result in the creation of a spall by detachment of material [201]. In addition to the growth of subsurface plastic deformation, it is hypothesised that RCF subsurface spalling is more prevalent in areas containing non-metallic inclusions, large carbides, voids or other material inhomogeneities [160, 202, 203]. On the other hand, surface-initiated pitting is most likely to occur in the presence of surface defects such as dents, which generate regions of substantial stress concentration, nucleating surface cracks that eventually remove small amounts of material [204]. Increased pitting rates have been demonstrated to correlate with higher applied loads, and therefore contact pressures, whilst lubricant conditions were also reported to have a significant influence [205]. It was reported that depth of damage accumulation may also be greatly affected by surface roughness, with spalling becoming notably more prominent as roughness decreased for steel gear systems [206]. It has been demonstrated that bearing life may be enhanced by increasing the probability of damage initiating in the subsurface, opposed to the surface, with approaches such as reducing steel impurities, innovative filtration techniques and improved sealing being researched to lower RCF failure [207].

Whilst RCF explains the finite nature of bearing life, other mechanisms are responsible for the high rates of premature failure in WTG bearings, as their operational life is significantly shorter than the predicted design life based on RCF. Overload events have been proposed as a root cause of the reduced life of WTG bearings [165]. Overloads in WTG bearings can occur due to sudden torque spikes or oscillations through the drivetrain, as a result of exposure to transient wind conditions or shutdowns in normal operation [16]. A wind turbine shut-down can be an emergency measure or a normal operational procedure. Normal shut-downs occur when wind speeds exceed or drop below the most efficient levels for power generation [23]. It has been demonstrated that a cylindrical roller bearing on the HSS can exceed recommended contact stresses by 18% in the event of a manual shut-down [16]. Poor handling and installation can also be responsible for WTG overloads [208]. An overload event can induce subsurface stresses that significantly exceed the yield criterion, producing a region of subsurface plasticity. The extent of subsurface yielding has been evaluated using non-destructive methods such as neutron imaging, indicating that overloads generate more severe plastic deformation than would be expected with typical Stage I RCF [141]. It has been shown that bearing life is significantly reduced by the overload, with failure originating in the subsurface within the plastically deformed region [141]. This suggests that the plasticity induced by overloads decreases the time spent in steady-state Stage II, promoting the early onset of Stage III instability, which results in accelerated damage. An overload could either lead to subsurface originated failure due to gross plastic deformation and the material softening associated with the latter stages of RCF, or surface originated failure, if there were a surface irregularity causing great enough stress concentration effects.

As there are multiple mechanisms contributing to early onset failure, an inherently statistical approach to bearing life prediction models is taken, particularly as knowledge of the components load history is rarely recorded. Equation 5.1 is the preferred model for calculating the basic life rating, L_{10}, is an estimate for the number of revolutions (in millions) it would take for 10% of bearings to fail under a specified load [209].

$$L_{10} = \left(\frac{C}{P_s}\right)^p \tag{5.1}$$

Where C is the dynamic load rating, P_s is the radial load applied to the bearing and p is the load-life exponent ($p = \frac{10}{3}$ for cylindrical roller bearings [184]).

This paper will focus on the radial bearing load, as it is most relevant, but where necessary, will also refer to the equivalent load applied to the most heavily loaded individual rolling element (P_E), calculated using Equation 5.2 [38].

$$P_E = \frac{5\,P_s}{Z} \tag{5.2}$$

In which Z is the total number of rolling elements.

5.1.2 Strain characterisation using EDXD

Various synchrotron X-ray diffraction methods have become a powerful tool in determining microscopic elastic strain by measuring the changes in interplanar lattice spacings deep within the materials. Energy dispersive X-ray diffraction (EDXD) uses photons of a wide ranging wavelength spectrum, to measure lattice spacing with a fixed angle detector [71]. Collimation of the incident and diffracted X-rays creates a gauge volume, which is the region where the incident and diffracted beams intersect, such that only diffracted X-rays from within the gauge volume reach the detector [63]. Thus, the EDXD technique can be used to probe inside samples or components. The collimation of the beam, and use of penetrating high energy photons, offers the opportunity to examine subsurface strain in engineering materials, such as steel and aluminium. EDXD experiments regularly involve the characterisation of material residual stress distributions [210] or the mapping of evolving quasi-static strains [211]. In a previous study, Sato et al. used EDXD to analyse residual stress in the ferritic phase of a pearlitic steel wire, whilst simultaneously studying its relationship with dislocation densities [212]. Similarly, Lopez-Crespo et al. performed an *in situ* experiment using EDXD with digital image correlation (DIC) to map the bulk elastic strain field and surface total strain field, surrounding the crack tip in a bainitic compact tension fatigue specimen [213].

Stroboscopic diffraction techniques allow for live strain measurements, recorded *in situ* on moving machinery, specifically when the motion is cyclic. The technique requires gating on the EDXD detectors acquisition system. The detector only counts detected X-rays when a digital signal received from an external sensor opens the gate and captures the diffracted beam. The gating sensor is set up so that the gate is only open during a specific point in the motion of the component under investigation. The X-ray counts for one cycle may not be sufficient for forming a full diffraction pattern, but by summing up the collected gated data associated with the same point in the cycle over many cycles, an analysable diffraction pattern is acquired. Baimpas et al. performed such a study, using stroboscopic EDXD to measure strain in the connecting rod of a four-stroke internal combustion engine [214]. A proximity sensor on the engines output shaft was used to detect when the connecting rod was at the top dead centre position of a stroke, generating a pulsed signal that controlled the X-ray detectors gate, initiating photon counting for a period of time pre-determined by the pulse width. In this case, the width of each pulse from the sensor allowed for 0.289 ms of data collection, resulting in a total of 24 s of data acquisition throughout an 80-minute run, which means that 99.5% of incident X-rays were discarded throughout the entire experiment. Mostafavi et al. also used stroboscopic strain measurement techniques, measuring the dynamic strain in the raceway of a rotating ball bearing [171]. A dynamically loaded bearing rig was used to run a bearing. The bearing was fitted with a Hall sensor to provide a triggering system, generating a signal for the detector to collect data for every bearing rotation. With a pulse width of 2 ms and rotational frequency of 150 *rpm*, the accumulative time required to collect sufficient fitting statistics was 20 s. The experiments demonstrated that reducing the pulse width improved the time-resolution of the dynamic strain measurements, yet it increases the total time required to gather statistically sufficient data, necessary to perform strain analysis. It is also important to reduce the total acquisition time for a single strain measurement when studying the evolution of strain, as it is not possible to distinguish exactly whether a change, such as crack initiation, has occurred in the material. These experiments also highlighted that reducing vibrations in the experimental equipment is essential for improving the accuracy of these techniques, as stroboscopic strain measurements should be collected from a single point within a moving component.

5.1.3 Aims and structure

The purpose of this work is to (i) develop a stroboscopic technique capable of measuring time-resolved contact strain using EDXD, with optimised time resolution, (ii) map subsurface contact strain distributions for a statically loaded bearing raceway with EDXD, (iii) stroboscopically measure dynamic strain in a pre-overloaded roller bearing. The results of this experiment aim to provide a deeper understanding of the considerable impact severe overload events have on the fatigue life of roller bearings. As developing a technique with the ability to measure *in situ* strain evolution of a dynamically loaded bearing accurately during a long-term experiment was the primary objective experimental design, a custom-made loading rig was designed for integration with existing hardware and software available on the I12 X-ray beamline at Diamond Light Source [71].

The results include static strain maps and dynamic subsurface strain measurements of an overloaded bearing. Also included are observations of the bearing post-test by destructive sectioning and optical microscopy.

5.2 Experimental design

5.2.1 Test bearing

An SKF, NU1010 ECP cylindrical roller bearing was selected for the experiment as it can represent the contact conditions experienced by commercial WTG bearing, yet its geometry is suitably scaled-down to permit adequate X-ray transmission through its raceway. The NU1010 ECP bearing has an outer diameter of 80 mm, a bore diameter of 50 mm and 20 rolling elements. The outer raceway thickness of 16 mm, in the x-direction, permits up to 9% transmission within the 50 keV to 150 keV usable X-ray range available on I12. Table 5.1 provides the chemical composition and of AISI 52100 of which the bearing steel is made [182]. A cylindrical roller bearing was selected as they are frequently found in WTGs. Hertzian contact theory predicts the generation of uniform subsurface stresses along the line of contact, reducing the complexity of the localised strain conditions and allowing for more robust assumptions during data analysis, particularly as experimental setup prevented measurements of the strain component parallel to the line contact.

Table 5.1: AISI 52100 Chemical Composition [182].

C	Mn	Si	Cr	Cu	S
0.95 - 1.10	0.20 - 0.50	≤0.35	1.30 - 1.60	≤0.025	≤0.025

5.2.2 Dynamic *in situ* loading rig

A compact mechanical rig was designed specifically for measuring time-resolved strain in the bearing outer raceway (5.1a and b). The rig was purpose built to allow for measurements in both X-ray and neutron diffraction experiments, taking into consideration the differences in beamline geometry. Neutron data is not reported within this body of work. The load is applied through a threaded bar screw mechanism and cantilever arm. The OMEGA LCM20-20kN load cell with SGA/A load cell amplifier provided load values as a 0-10 V analogue signal.

To ensure the load is continuously applied along the radial axis, directly on to the region of interest, a line contact was introduced between the cantilever arm and direct loading piece (DLP), as seen in Figure 5.1c. The displacement of the DLP was constrained using linear ball bearings, ensuring the load is constantly applied along the radial axis. The shaft diameter (50 mm) is greater where the test bearing is positioned, compared to the main body of the shaft (30 mm) where support bearings are positioned. This prevents obstruction of the X-ray line-of-sight. The custom-made pulley system had the lowest permittable outer diameter for the shaft dimensions, also maintaining a clear line of sight to the region of interest. A 0.75 kW 4 pole single phase motor and WEG CFW-10 inverter were selected, capable of producing the required 2 Nm for a bearing at maximum experimental load. A gear ratio of 1.05:1, provided the greatest transfer of torque possible considering that both the bearing shaft and motor shaft were fitted with pulleys of the lowest feasible pitch diameters. The

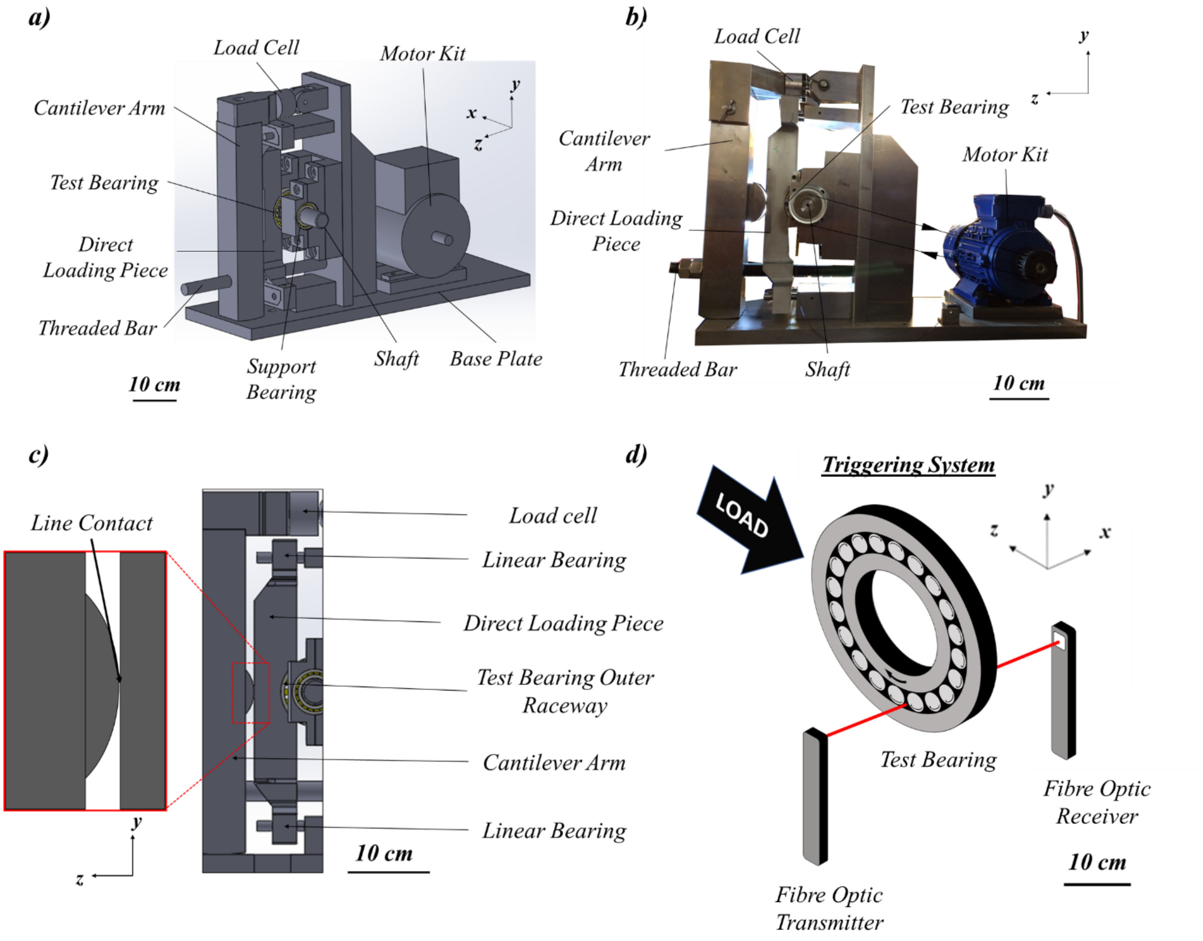

Figure 5.1: (a) Schematic of the custom-made loading rig. (b) Photograph of the custom-made loading rig. (c) The loading mechanism used to ensure that loads were applied entirely in the radial direction (z-direction). (d) Fibre optic sensors generated a signal for every roller passage, optimising the data acquisition process.

test bearing was lubricated through the application of KRYTOX GPL 203 grease, operating under mixed-film lubrication regime with a viscosity ratio of 1.79 for dynamic test conditions [215].

5.2.3 Stroboscopic triggering system

The experiment consisted of two measurement types; static and dynamic. The dynamic measurements required a method to ascertain the position of the rolling elements as a function of time. A stroboscopic triggering system was developed to determine when a roller was in contact with the region of interest. Keyence FU-18M thru-beam fibre optics were mounted to the rig within a fitted groove in the support bearing housing (Figure 5.1d), situated so the transmitted beam passes between the inner and outer raceway. When the bearing rotates the transmitted beam is cut as a passing roller obstructs the line-of-sight between the transmitter and receiver. The Keyence FS-N10 Series digital amplifier with PNP output and in-house signal processing box were used for converting into the required 0-10 V analogue signal. The digital amplifier was calibrated to determine a suitable light intensity threshold, based on the obstructed and unobstructed light intensity. This fibre optic system generated a pulse when the light intensity fell below a specified threshold value, i.e. when the transmitted beam was blocked by a roller.

To assist initial setup of the gating system, a high-speed camera was positioned close to the bearing region of interest and synchronised with the rising edge of pulses emitted from the fibre optic triggering system. This provided a still image each time a pulse was produced, allowing for verification of the time lag required to ensure the roller was in position for X-ray diffraction measurements. To verify the roller position, Phantom 7.3 and MIRO 310M cameras were used for visible light and X-rays, respectively. Figure 5.2 shows a visible light (left) and X-ray (right) image taken using the high-speed camera, synchronised using the trigger pulse and delay to ensure acquisition occurs only when the roller was generating maximum subsurface stress. During dynamic tests the I12 beamlines combined digital signal hardware and field programmable gate array (FPGA), known as ZEBRA, was used to detect the rising edge of the stroboscopic trigger pulse. The ZEBRA was programmed to output a transistor-transistor logic (TTL) pulse with the specified time delay and pulse width to the EDXD detector gate, with data collected only during the width of these pulses.

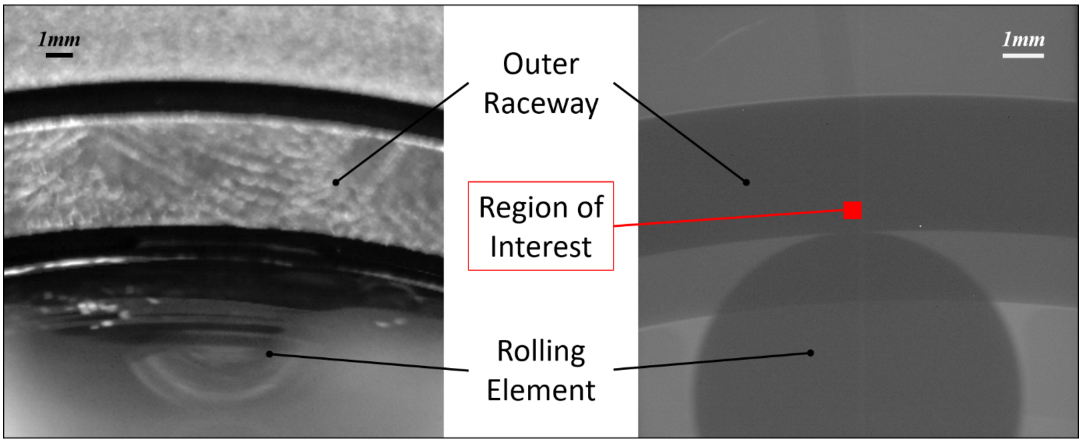

Figure 5.2: Images obtained dynamically when the pulse was synchronised with the roller position. (Left) Visible light image. (Right) X-ray radiograph.

5.2.4 EDXD strain measurements

Prior to the experiment, the EDXD detector and collimators were aligned with the X-ray beam, and a calibration of intensity versus the reciprocal lattice vector, q, was obtained using a National Institute of Standards (NIST) 674b cerium oxide reference sample. A straight forward relationship between q and the atomic lattice spacing, d_{hkl}, in a material is expressed in Equation 5.3.

$$q = \frac{2\pi}{d_{hkl}} \tag{5.3}$$

The test rig was mounted on the I12 sample stage that is used to accurately position the bearing region of interest within the X-ray beam line-of-sight. The sample stage can be translated in the x-, y- and z- directions, with a resolution on 10 μm [71]. To align the test sample and detector, the rig was positioned so that the incident beam was parallel to the axial direction, through the test bearing (x-axis). An approximate alignment of the X-ray beam and outer raceway region of interest was initially completed using a laser. Refinement of the necessary y- and z- sample stage positions was then performed using the high-speed MIRO 310M (CMOS) camera with transmitted X-rays being converted to visible light using a scintillator. For static tests a script translated the stage to a set point required to generate a map around the localised contact stresses. Mapping of the subsurface strain in the contact region under static conditions was performed by scanning a 1.5 x 0.9 mm^2 region directly beneath the contact, with point intervals every 150 μm. The scan time for all 77 points was 120 s each. For the dynamic tests the camera was used to determine the y- and z- positions so that the centre of the gauge volume was located at 250 μm radially from the contact surface (see Figure 5.3a and b). For dynamic scans the incident beam geometry was 150 x 150 μm with a gauge volume length of approximately 5 mm along the line of contact. To align the gauge volume in the x-direction, a scan was taken whereby the stage was translated parallel to the incident beam. The intensity of diffracted X-rays was plotted as a function of displacement in the x-direction, with intensity dropping when the gauge volume was no longer entirely located within the sample. By noting the stage positions, where the gauge volume had entered and exited the bearing, it was possible to determine the location corresponding to the centre of the sample. All experimental loads were applied radially along the z-direction.

The I12 EDXD detector has 23 detecting elements set at $2\theta = 4.5°$, equally spaced through azimuthal angles of 0° to 180°, with 8.18° between each element. To determine the dynamic fatigue load, it was decided that maps would be taken of the statically loaded bearing, and the load was chosen where the Hertzian contact stresses were clearly visible in the map. By ensuring that subsurface stress was significant enough to be visualised in static conditions, it was deemed suitable for dynamic experiments. See Results Section 5.3.1 for static stress maps. Static measurements were performed with a rolling element positioned at the region of interest, applying pressure to the raceway in the area covered by the scan.

The stroboscopic tests completed on I12 measured strain at a single location, whereas static tests were used to generate 2D maps of the subsurface strain profile. Three dynamic scans were performed for the same loads performed for static scans and it was determined that a cumulative 60 s data acquisition time provided sufficient fitting statistics. It took approximately 13 minutes to collect each 60 s data point, with a pulse width of 500 μs and a rotational frequency of 854 *rpm*, typical of a WTG intermediate-speed shaft (ISS) bearing with a HSS gear ratio of 2:1 [216, 217]. Figure 5.4 compares the diffraction spectra for a static scan and a dynamic scan, demonstrating the quality of data is not compromised by using the stroboscopic technique. Analysis of the diffraction data was carried out using the pyXe strain analysis software [218], with a Rietveld type (Pawley) refinement being used to determine the lattice parameter for each of the 23 detectors. While the focus was on radial strain, leveraging the measurements from each detector to calculate the in-plane strain tensor improves the overall measurement accuracy. In this case, the uncertainty (standard deviation) in strain from the in-plane strain tensor fit was $\pm 7 \times 10^{-5}$, which is associated with an error in stress of approximately ±14 MPa.

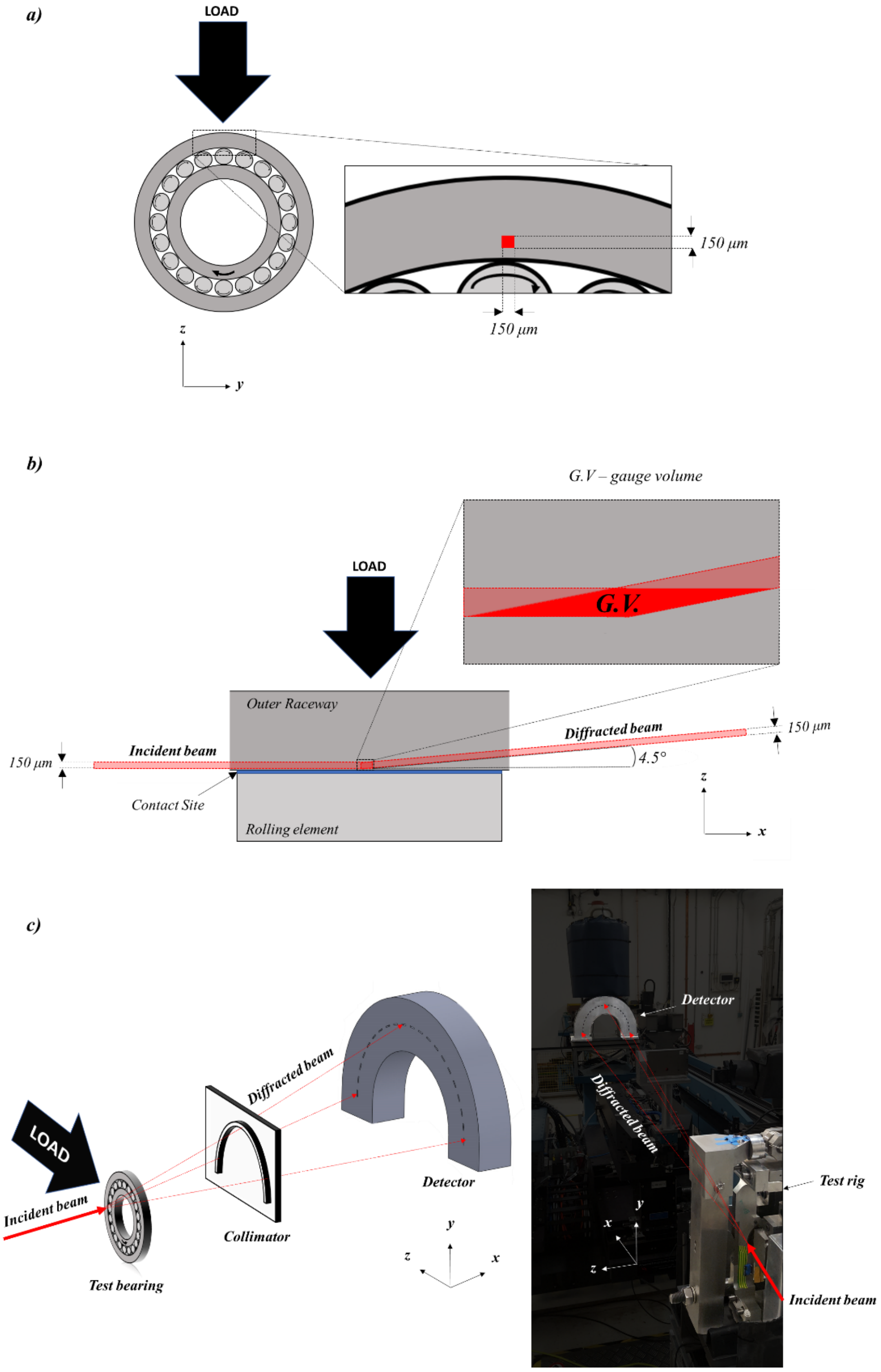

Figure 5.3: a) Projection of the gauge volume in the yz-plane position of the outer raceway, relative to the rolling element and radial load application. The centre of the gauge volume was 250 μm into the subsurface, within a region plastically deformed from pre-overloading. b) Projection of the gauge volume in the xz-plane. c) (Left) Schematic of EDXD experimental setup, with applied load direction (z-direction), collimator, and 23-element detector. (Right) Photograph of experimental setup prior to alignment of the collimator. The image has been darkened where auxiliary equipment is positioned, making the detector and test rig more visible.

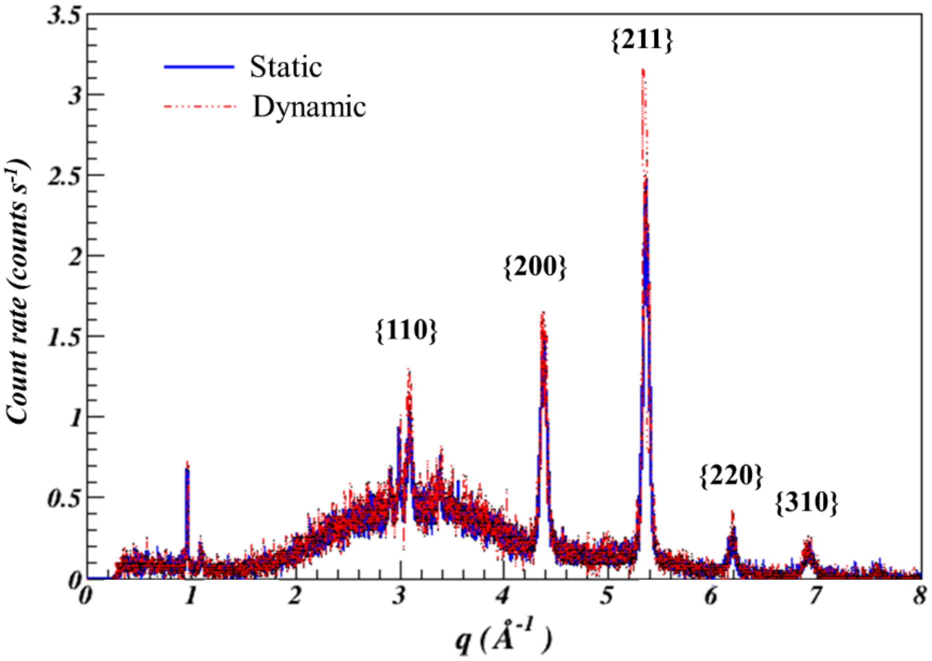

Figure 5.4: Diffraction spectra for a static and dynamic scan, with labelled {*hkl*} planes.

5.2.5 Finite Element Analysis

A three-dimensional elastic-plastic finite element model, developed in ABAQUS version 6.14-2 [146] and validated in previous work [141], was used to simulate static loading conditions for comparison with those measured using EDXD. Figure 5.5 shows a schematic of the model and boundary conditions. The bearing raceway and rolling element used quadratic elements (C3D20R), whilst the other components were rigid bodies, modelled using bilinear rigid quadrilateral elements (R3D4). Mesh refinement in the contact region was performed to give elements with dimensions 150 x 150 μm in the yz-plane, matching the dimensions as the X-ray gauge volume. A quarter of the bearing was modelled as the x-axis and θ-axis (accounting for bearing curvature) were assumed to be symmetric, whilst friction in the contact site was ignored. Quasi-static conditions were used in the simulations, with an assumption of isotropic hardening using the stress-strain curve for AISI 52100 [186]. The model was used to predict subsurface elastic strains in static loading conditions, with material properties found in Table 5.2.

Table 5.2: AISI 52100 Properties [181].

Property	Symbol	Value
Density $[kg/m^3]$	ρ	7830
Young's Modulus $[GPa]$	E	201
Poisson's Ratio	ν	0.3
Yield Stress $[MPa]$	σ_Y	1410

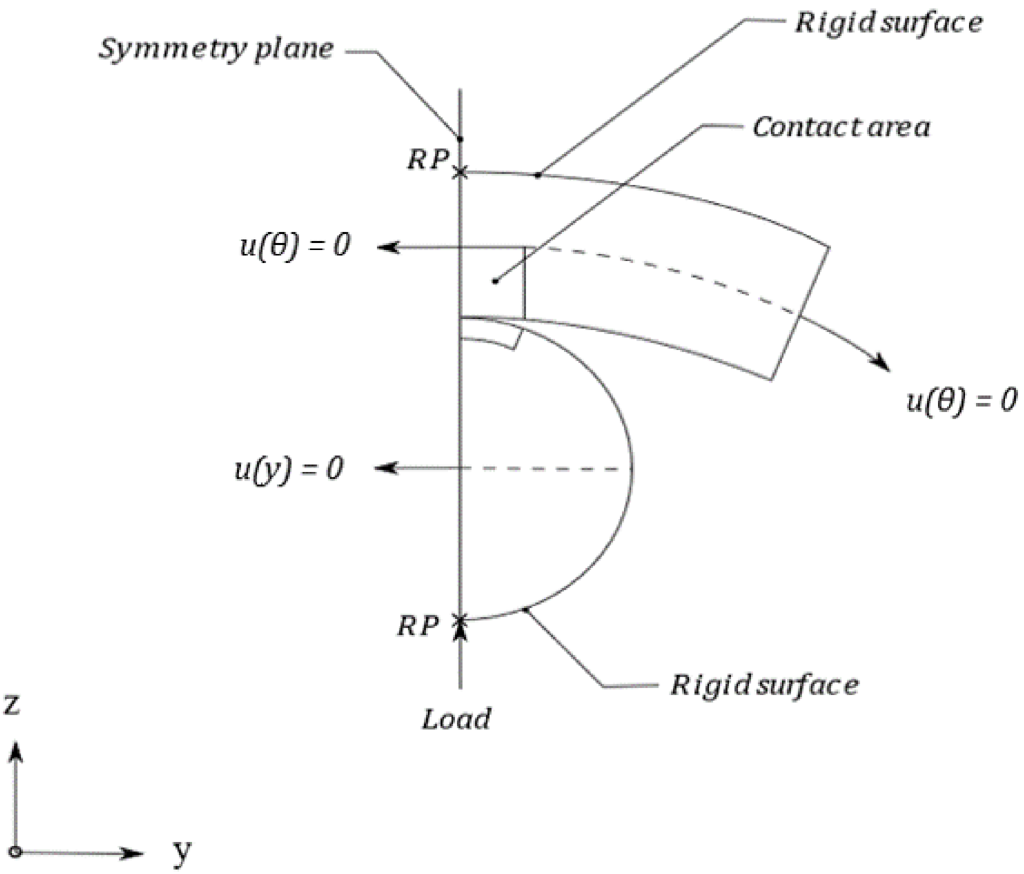

Figure 5.5: Schematic of finite element model, with labelled boundary conditions.

5.3 Results

5.3.1 Static strain mapping

Strain was mapped under static conditions with the roller placed directly beneath the contact site. The load was progressively increased from 3.6 kN to 9.0 kN in increments of 1.8 kN, with elastic strain maps being generated concurrently, to allow for visualisation of localised subsurface radial strain distributions. Figure 5.6 demonstrates the subsurface radial strain distributions measured using EDXD. Above 5.4 kN the strain distributions resembled those expected by Hertzian contact theory, yet below it was not possible to distinguish any recognisable strain distributions. A load of approximately 9.0 kN was deemed as suitable for running the dynamic tests on an overloaded bearing, as the map demonstrated that at this load the subsurface strain distributions are great enough to be detected within a dynamic gauge volume of 150 x 150 μm, at 250 μm beneath the contact subsurface. This corresponds to a maximum contact pressure of approximately 1350 MPa, in between the maximum allowable stresses of 1300 MPa for HSS bearings and 1500 MPa for low speed planetary bearings, as reported in wind turbine design standards [16].

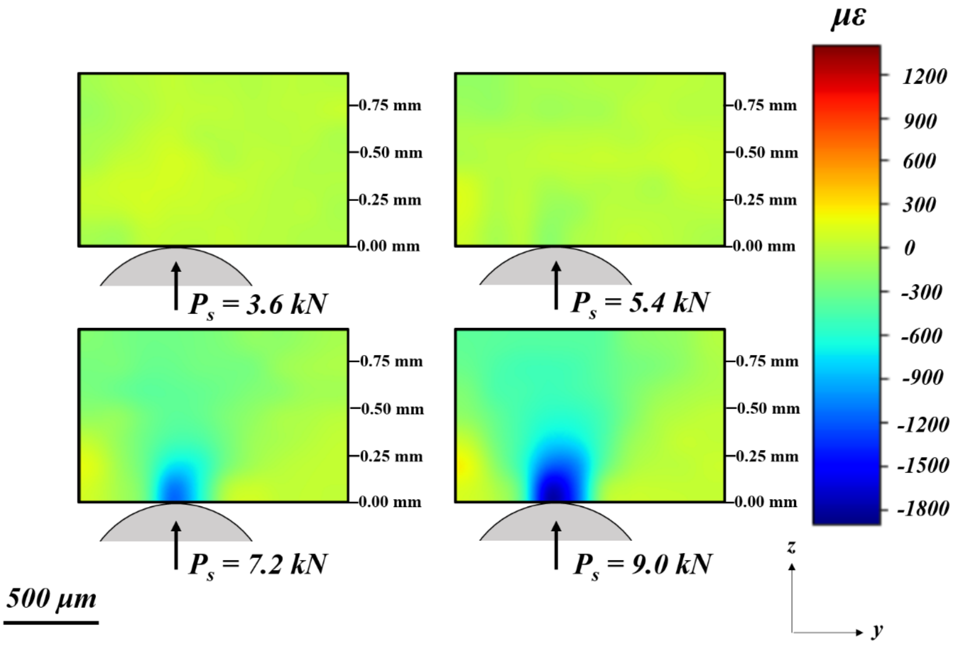

Figure 5.6: Measured two-dimensional subsurface radial strain maps (ε_{zz}) at loads of P_s = 3.6 kN, 5.4 kN, 7.2 kN and 9.0 kN. The subsurface depth axis has been included.

The experimentally measured subsurface radial strain at 9.0 kN demonstrates a similar trend to the FEA at the same load, although measured strain values are of lower magnitude. Figure 5.7 shows a comparison of the FEA and experimental radial strain, with a plot of values from the contact into the subsurface. Although spatial alignment errors are small when using the precise positioning equipment on I12, the nature of the localised contact strains suggests that the apparent shift in strain could be caused by a small misalignment, with the dashed lines showing the minimum and maximum FEA values if a misalignment as small as the height of the gauge volume, 150 μm, had occurred in either direction along the z-axis.

5.3.2 Time-resolved subsurface elastic strain measurements

Prior to beginning the 24-hour time-resolved test, individual data points were measured dynamically at different loads. Each scan cumulatively acquired one minute of data, with three scans performed at each load. Figure 5.8 demonstrates the measured elastic strain for three scans at each loading condition, confirming the techniques capability to measure time-resolved strain and that approximately 9.0 kN was a suitable load for the long-term dynamic test. It was not possible to run a dynamic test at 0.0 kN as a load is required to ensure the outer raceway remains static, nonetheless results show that below roughly 5.0 kN it is difficult to differentiate the strain from the noise of the detector. This was equally demonstrated in the static maps, suggesting that below a threshold load, strain cannot be measured. The d^0_{hkl} value used for the dynamic test was the same as that of the static maps.

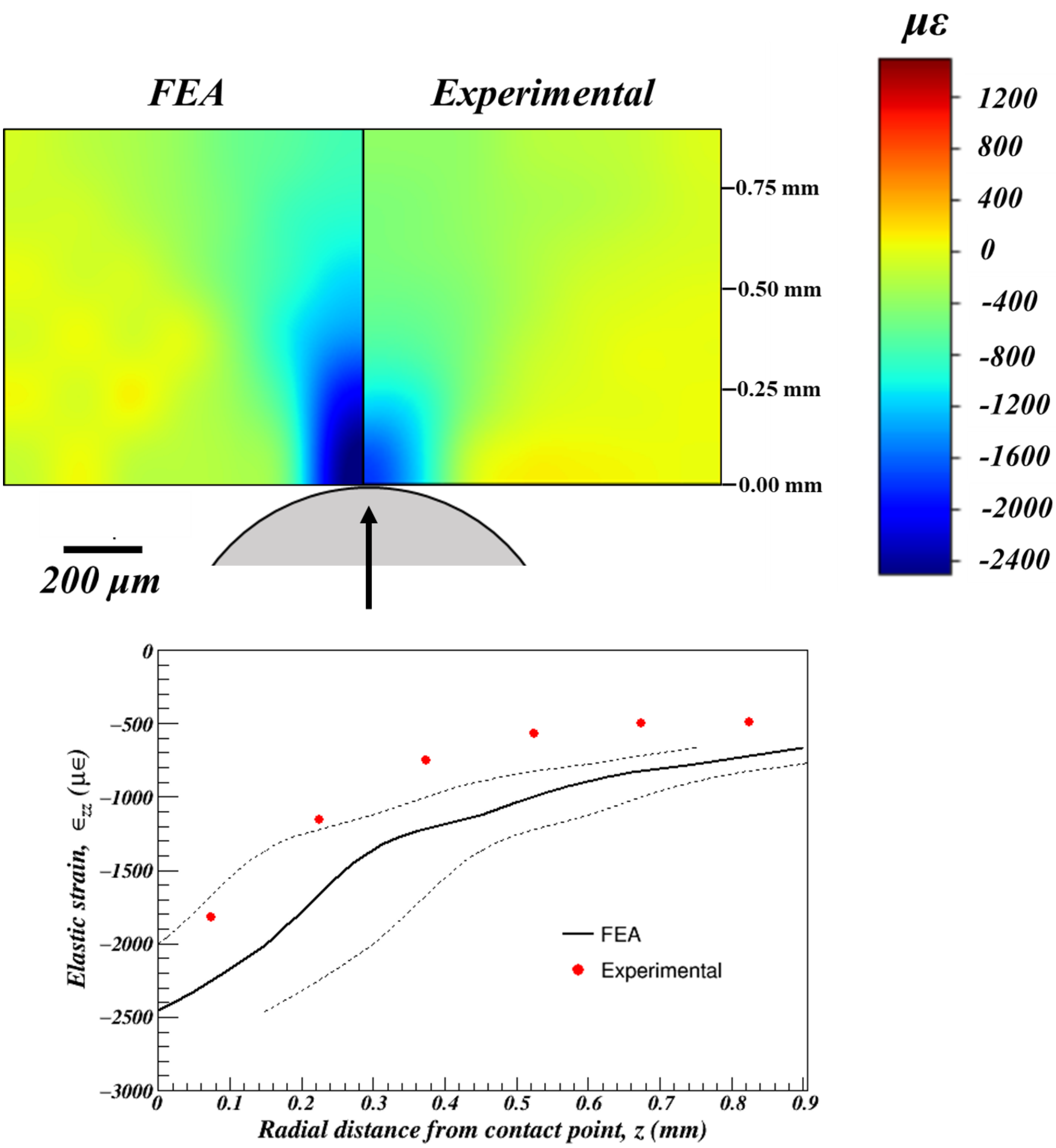

Figure 5.7: (Top) Radial elastic strain map at 9.0 kN compared with FEA results at the same load. (Bottom) Radial elastic strain as a function of distance from the contact site. The dashed lines represent the minimum and maximum values when taking into consideration a misalignment of up to 150 μm.

As a principal aim of the project is to explore the influence of yield inducing overloads on subsurface fatigue strains, the dynamic test specimen was subject to an overload event prior to cycling. The details of the apparatus with which the overload is applied is given elsewhere [141]. However, to ensure the current work is self-contained, a brief description of the apparatus and overload procedure is given here. The overload was performed using a purpose-built loading frame, applying a load to the bearing outer raceway using a single rolling element. A cage was designed to hold an isolated bearing outer raceway, whilst a fork was used to carry a static shaft for holding the individual rolling element through the middle of the raceway. The rolling element was positioned at the region of interest and an Instron loading frame was used to pull the fork in tension, applying the designated load to the contact site. The rolling element was discarded after the overload was performed, with

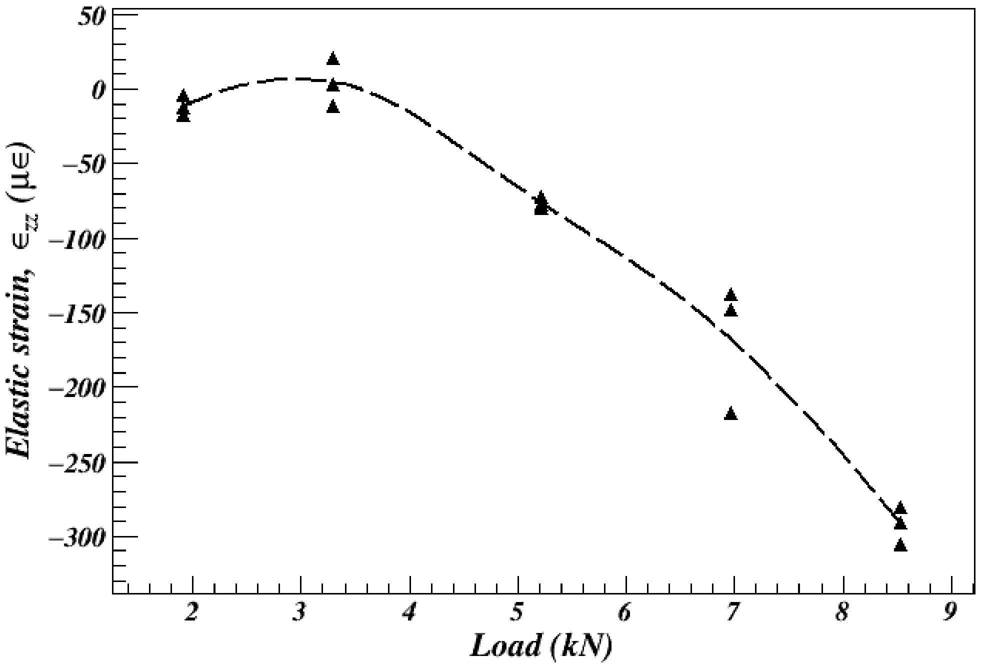

Figure 5.8: Radial elastic strain (ε_{zz}) measured stroboscopically for three scans performed at each load. The dashed line is a fit of the average strain for each load.

only unloaded elements being used for the dynamic X-ray experiment. Previous work indicated that the elastic limit being reached at 40 kN, with a 136 kN overload (P_E = 34 kN) seeding a plastic zone that initiates in the subsurface and propagates to the contact surface [141]. As the long-term test was being run at a fatigue load of 8.8 kN, a more significant pre-fatigue overload event of 180 kN was used (P_E = 45 kN). This load was chosen to increase the probability of damage initiation within the available experimental timeframe at a lower cyclic load than had been presented in previous studies, whilst also increasing the likelihood that dynamic measurements were taken from a plastically deformed region. The test was run for 23 hours and 35 minutes, equating to approximately 1.21 million bearing revolutions at 854 *rpm*, approximately 0.5% of the L_{10} life, as predicted using Equation 5.1. A beam loss in the synchrotron storage ring between 12 and 14 hours left a gap in data acquisition.

Figure 5.9 shows the plot of subsurface radial strain averaged within the gauge volume, at a depth of 250 μm beneath the contact. Over the duration of the experiment, the strain became increasingly compressive throughout cycling, possibly due to continual material softening in the region being measured as a result of early onset Stage III RCF caused by the significant pre-cycling overload event. Scatter in the strain measurements predominantly fits within the experimental uncertainty of ± 70 $\mu\varepsilon$. Additionally, small amounts of scatter may be attributed to the continual variation of subsurface strain, including whilst data was being collected during the gating pulse width. The compressive radial strain in this region increases by approximately 19% during bearing operation. This is of interest as the elastic properties of the localised subsurface and surface region appear to continually alter when cycling is nested within a plastically deformed region. The induced subsurface residual stress field clearly influences the cyclic elastic strains as they are more than double

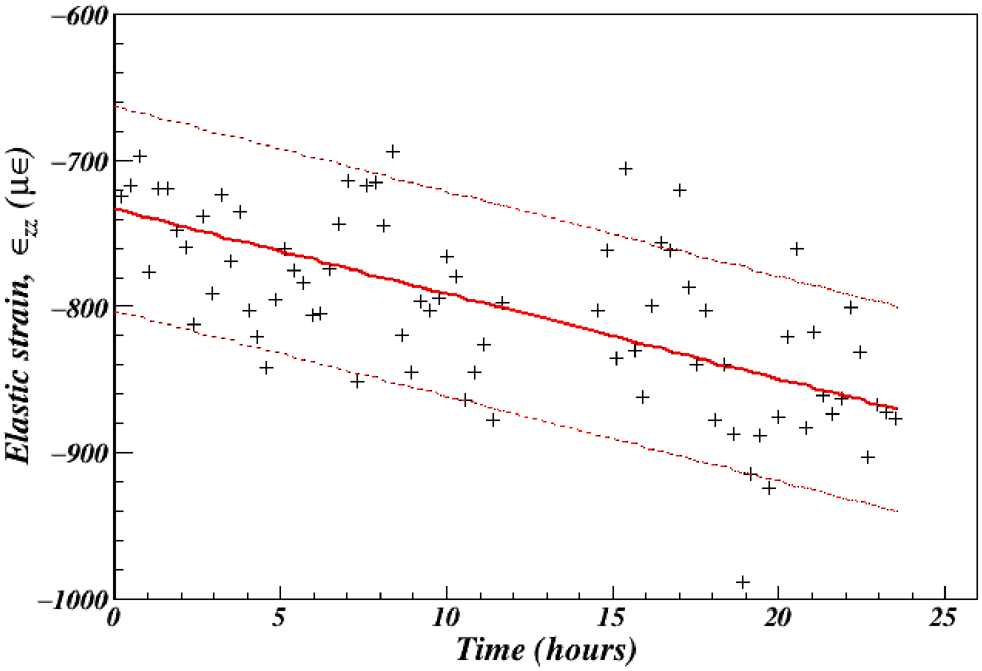

Figure 5.9: Time-resolved subsurface radial elastic strain (ε_{zz}) measured during the long-term dynamic test at 8.8 kN having been exposed to overload equivalent to P_s = 180 kN. The experimental uncertainty of ±70 $\mu\epsilon$ has been represented using a line of best fit (solid red line), with minimum and maximum errors (dashed red lines). A gap in the data between 12 and 14 hours was due to loss of stored beam in the synchrotron.

those for the static scans when the specimen had not been subjected to an overload. In many cases the purposeful induction of residual stresses has been utilised to improve component life, yet the severity of the plastic deformation appears to accelerate damage, as discussed in Section 5.3.3.

5.3.3 Post-fatigue interrogation

A final static map was performed on the bearing post-cycling, with the dynamic load applied and a roller positioned beneath the surface. The map shows a significant tensile region in the subsurface, slightly offset from the contact zone. Figure 5.10 shows a comparable subsurface tensile region that is also apparent in the FEA, implying that the overload is inducing a significant residual stress field in the material. A profile of radial elastic strain into the subsurface provides reasonable agreement between the FEA and experimental data. The FEA map suggest a compressive region should be present at the surface, which is not visible in the experimental map. This could be an effect of the previously mentioned possibility of misalignment, or that the self-equilibrating residual stress field generated during the overload varies from the FEA at the surface due to the inherent stresses that were already present in the bearing prior to the influence of any experimental loading.

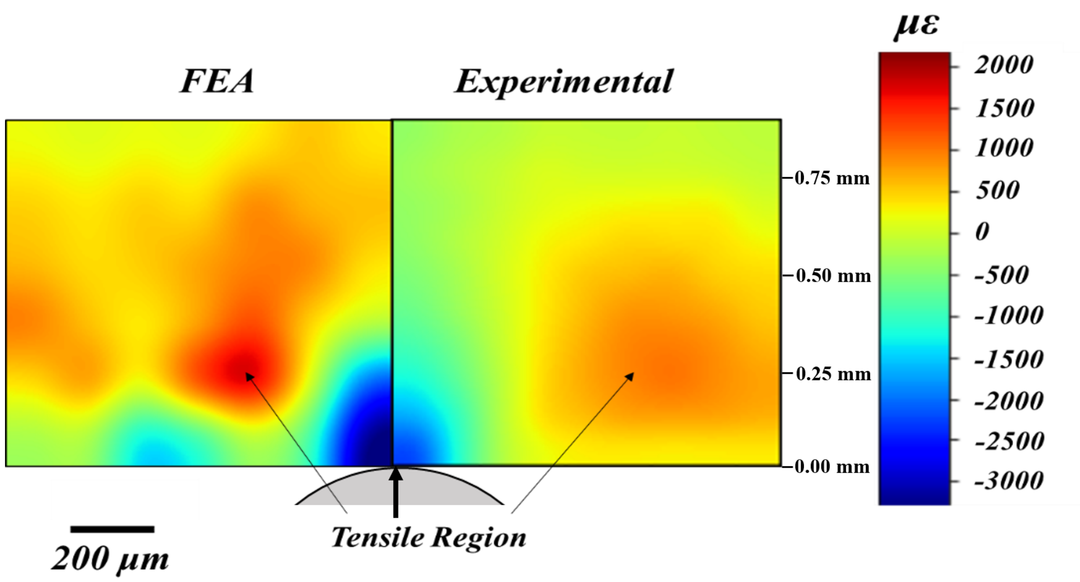

Figure 5.10: Radial elastic strain FEA results for bearing a bearing exposed to a bearing pre-overloaded at P_E and static load of P_s = 8.8 kN, compared with the experimental radial elastic strain map of a bearing pre-overloaded at P_E = 45 kN and fatigued for approximately 531,000 cycles at P_s = 8.8 kN.

5.3.4 Post-fatigue optical microscopy

The bearing was sectioned circumferentially to verify whether a failure had occurred. A bearing is considered to have failed is when it no longer functions as intended, as opposed to being completely non-operational [219]. At the end of the fatigue test, the bearing appeared to be fully operational, without presenting obvious indications of failure, yet optical microscopy of the sectioned raceway revealed the presence of cracking, and the appearance of severe deformation in the contact region, as seen in Figure 5.11. Cracks were observed beneath the contact zone, most notably a crack running roughly 4 μm into the subsurface, classified as a surface failure. The observed cracks are indicative of fatigue pitting and occurred within a highly deformed region with width and maximum depth of roughly 210 μm and 20 μm, respectively. As suggested in the literature, surface irregularities introduced by a substantial overload generate regions of high stress concentration resulting in surface initiated cracking, which may have contributed towards the observed surface damage in this sample [204].

5.4 Discussion

Using the hardware and software developed as part of this project, the ability to measure time-resolved strain has been successfully demonstrated. The custom-designed rig and experimental setup allowed for high quality data acquisition, and long-term dynamic testing allows for the measurement of *in situ* subsurface strain evolution. Fibre optic sensors to detect the passage of every rolling element in the bearing has proven effective, optimising the data acquisition time for a single

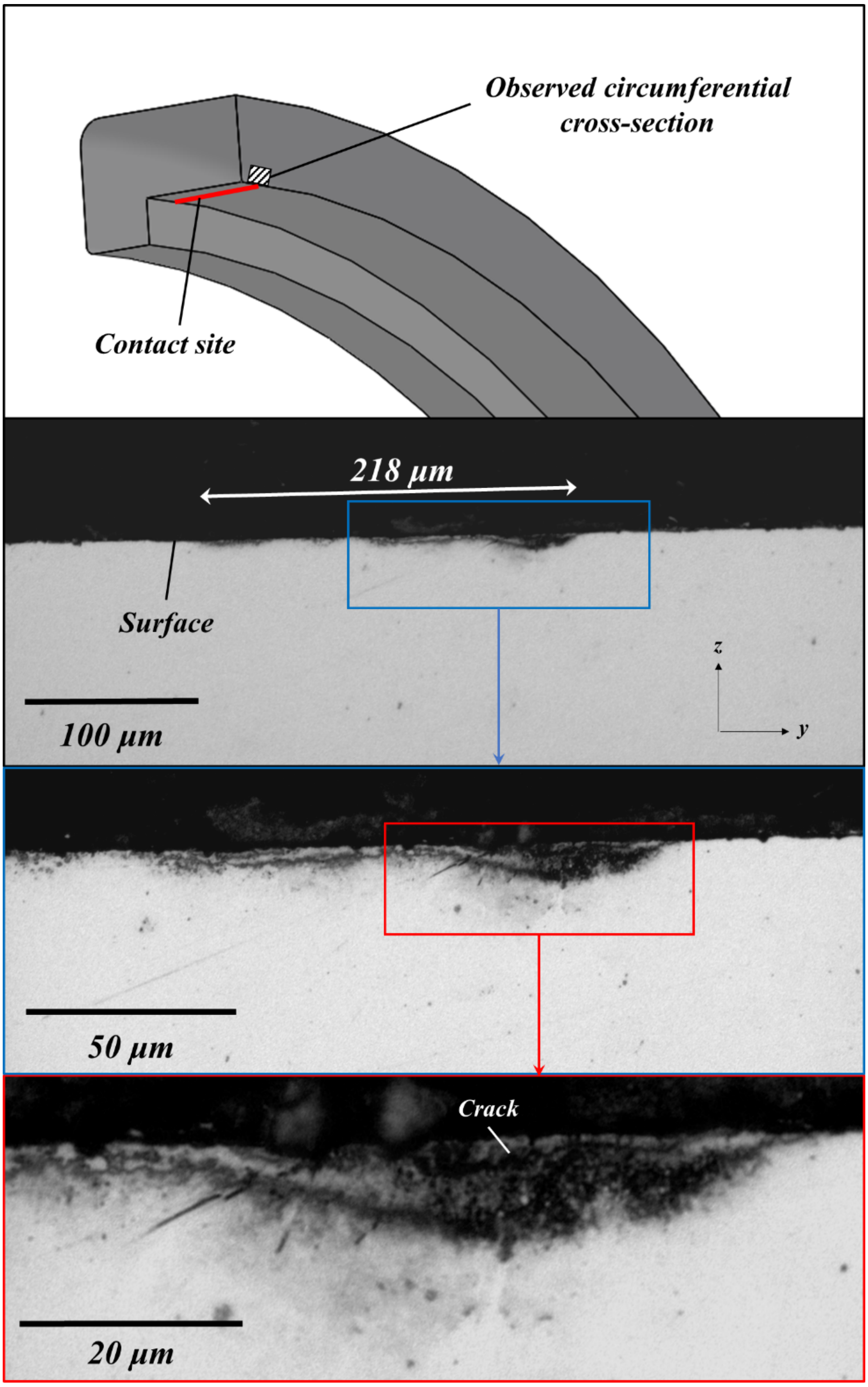

Figure 5.11: Schematic to demonstrate the circumferential cross-section surface being observed, with visible light micrographs taken from the contact site at x20, x50 and x100 magnification.

strain measurement when compared to previous studies [171]. Static maps provide a useful validation in that contact stress distributions correspond closely those predicted by Hertzian contact theory. The long-term dynamic tests demonstrate increase radial strain with time, suggesting that when cycling occurs nested within the yield zone, material softening causes accelerated failure.

Experimental results provide further evidence that overloads that seed subsurface plastic regions contribute towards premature failure of wind turbine gearbox bearings. The comparison of FEA and experimental radial elastic strain mapping have clearly demonstrated that substantial overloading generates a residual stress field in the region in the location of fatigue loading occurs during bearing operation. The tensile residual stress gradients are positioned where the highly localised cyclic fatigue stresses occur, reducing the expected time for failure by driving crack growth parallel to the surface. This work supports literature suggesting that, although the effect of subsurface residual stress and plastic deformation contribute towards failure, the presence of tensile residual stress in the radial direction increases the force driving crack growth [199]. The observed crack appears to be a precursor to fatigue pitting, which eventually lead to more severe surface failures, as described by in other work by Muro et al [204]. Without an overload event, the bearing would still be expected to fail due to rolling contact fatigue once the steady-state Stage II has progressed to Stage III instability, yet the results support the hypothesis that a gross plastic overload effectively accelerates the onset of Stage III instability and material softening, resulting in premature failure.

It appears that the damage arises from fatigue cycling within a region of severe plastic deformation, caused by the overload event. The width of the damaged region was experimentally measured at 218 μm (See Figure 5.11), similar to the predicted Hertzian contact width of 210 μm at the dynamic load of 8.8 kN. Nonetheless, failure has occurred significantly premature of the L_{10}, suggesting that the combined influence of gross plastic overload and rolling contact fatigue have been key contributory factors.

Additionally, dynamic loads used during the experiment generate a maximum subsurface shear stress at 83 μm from the contact site, based on the Hertzian contact model. The overload carried out before the experiment at 180 kN, induces subsurface plastic deformation with a significantly larger geometry and a maximum shear stress at 370 μm deep from the contact point. The observed damage, as can be seen in Figure 5.11, occurred between the surface and a subsurface depth of 20 μm which is more comparable with the effect expected from the dynamics load than the overload. Figure 5.12 demonstrates the comparative sizes of the surface defect, subsurface maximum principal shear stresses at the dynamic load, as predicted by Hertzian contact theory, and a section of the subsurface plastic zone induced through overloading, as predicted by FEA. It should be noted that the contours and plastic zone has been cropped to allow for suitable comparison with the surface defect. The previous study by Reid et al. [141] demonstrated premature bearing failure within a region of gross plastic deformation generated by a severe overload event. This work supports the hypothesis that a yield inducing overload may significantly reduce bearing life expectancy.

It is apparent that the overload plastic zones size should encompass the localised region of maximum dynamic stress, yet it can also be postulated that the location of damage is dependent on the magnitude of fatigue loading rather than the overload, assuming the dynamic stresses fall within the yielded region. This implies, such as for this experiment, that an overload generating surface and subsurface plasticity followed by relatively low fatigue loads fail at the surface. For future experiments, it would be beneficial to perform thorough characterisation of the surface condition

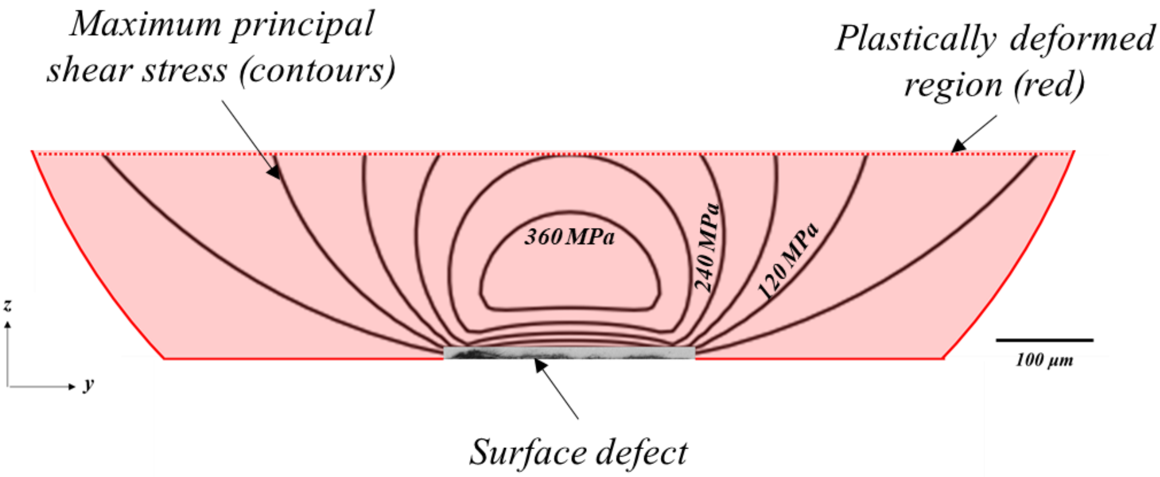

Figure 5.12: Comparative sizes of the surface defect, subsurface shear stress contours as predicted by Hertzian contact theory for the dynamic load, and subsurface plasticity caused by the overload. The optical micrograph is at x20 magnification. The shear stress contours and plastically deformed region has been cropped to allow for reasonable comparison with the defect, as its dimensions are significantly smaller than the other features.

post-overload, but prior to dynamic testing. This would provide greater understanding of the extent of surface damage from the overload event, potentially supporting the proposal of an exact failure mode. Also, the presence of inherent material defects and impurities will also impact mechanisms responsible for failure, yet their role in life reduction has not been considered for this research.

With the development of this novel and effective technique for measuring subsurface strain, future experiments can be planned to further understand the influence of subsurface stresses on rolling contact fatigue failure. For example, the completion of tests with varying overloads and operational loading conditions would allow for further validation of the hypothesis that surface and subsurface failure is determined solely by fatigue load, rather than the extent of subsurface plastic deformation. This would also provide more understanding of precisely how overload events impact bearing life. Having extended experimental times would allow for longer dynamic experiments to be completed, yet beamtime access on synchrotron sources is usually limited to a few days. Improved knowledge about the effect of overloads and extent of life reduction has the potential to be scaled up and theoretically could be used to predict the life of in-service wind turbine gearbox bearings, if their load history has been recorded. The rig could be optimised for future experiments, for example, although load variation throughout the dynamic test was below 4%, a feedback loop could be installed to ensure the applied load is constant.

5.4.1 Future work: Stroboscopic neutron diffraction

The rig has been specifically designed for the completion of X-ray and neutron diffraction experiments. Now that this technique has been successfully demonstrated using energy dispersive X-ray diffraction, the main aim is to perform this experiment using neutron diffraction. This experiment is part of a wider project to develop the capability for time-resolved strain measurements on the world-renowned strain diffractometer, ENGIN-X at the ISIS neutron source, UK. The instrumentation on I12, whilst demonstrating unrivalled spatial resolution and rapid data acquisition times, only allows for stroboscopic data acquisition at times that coincide with the pulses, i.e. at only one point within a single fatigue cycle. It is therefore not possible to study the cyclic stress induced by rolling contact fatigue. ENGIN-X can collect all incident neutrons and therefore offers the unique opportunity to measure the strain evolution throughout the entire fatigue cycle. Also, neutrons can penetrate much greater depths of engineering material, such as steel, meaning that if it were possible to transition this technique to ENGIN-X, much larger tests samples could be studied, including commercial wind turbine gear box bearings. There are currently obstacles to this transition due to much slower data acquisition times and worse spatial resolution. The next phase in assisting transition of the presented technique is to ensure that data acquisition hardware and analysis software are capable of delivering accurate strain measurements.

5.5 Conclusions

- The use of a custom-made rig and fibre optic triggering system allows for measurement of time-resolved elastic strain using energy dispersive X-ray diffraction. The data acquired during both static and dynamic scans is of similar quality.
- A long-term 24-hour stroboscopic scan demonstrated a gradual increase of compressive radial strains in an overloaded region of the bearing outer raceway.
- Overloading accelerates the onset of Stage III instability, reducing bearing life and increasing the probability of cracking due to rolling contact fatigue.

CHAPTER 6

MEASUREMENT OF STRAIN EVOLUTION IN OVERLOADED ROLLER BEARINGS USING TIME-OF-FLIGHT NEUTRON DIFFRACTION

Authors: A. Reid[1], M. Marshall[1], I. Martinez[1], S.Moorby[2], T. Connolley[3], M. Mostafavi[4], S. Kabra[2].

[1] *University of Sheffield, Dept. Mechanical Engineering, Sheffield, S1 3JD, UK;*

[2] *STFC-Rutherford Appleton Laboratory, ISIS Facility, Harwell, OX11 0QX, UK;*

[3] *Diamond Light Source Ltd, Harwell Science and Innovation Campus, Didcot, Oxfordshire OX11 0DE, UK;*

[4] *University of Bristol, Dept. Mechanical Engineering, Bristol, BS8 1TR, UK;*

Abstract: *Neutron diffraction is an established method for non-destructively characterising residual stress or observing in situ strain during external stimuli. Neutron based stroboscopic techniques have previously been introduced for measuring strains undergoing cyclic processes but have not been used for tribological applications. This work presents a novel approach for measuring the evolution of radial strain in a rotating bearing through part of the components lifetime. A cylindrical roller bearing was pre-overloaded to increase the probability of damage within a reasonable experimental time and to help develop further understanding of the influence such events have on bearing life, notably for the application of wind turbine gearbox bearing failure. The stroboscopic neutron diffraction technique was successful in measuring time-resolved contact strain, with a significant increase in compressive radial strain being observed after a suspected failure had been detected using condition monitoring techniques, implemented for validating damage propagation. Cyclic contact strains associated with rolling contact fatigue were also evaluated using neutron diffraction.*

6.1 Introduction

6.1.1 Background

Power generation from sustainable sources is of extreme importance, with global renewable energy capacity increasing by roughly 257% between 2008 and 2017 [3]. Wind power has played a significant role in the growth of renewable energy generation, yet premature failure of wind turbine components is proving to be an issue for the industry [194]. Operation and maintenance of wind turbines is challenging and costly, as the unexpected failure of a critical drivetrain components normally leads to significant downtime. The failure of a wind turbine gearbox (WTG) bearing can suspend operation for up to 23 days [193], suggesting that a deeper understanding of WTG bearing failure mechanisms is essential for improving wind turbine reliability [220].

The mechanisms responsible for premature WTG bearing failure vary and more appreciation for the influence of non-torque loading may be required for future gearbox design, as this effect can lead to highly transient contact pressures [195]. Recently several test rigs have been designed to study the effect of non-torque loading on WTGs, with the aim of understanding and optimising commercial gearbox lifetime [221]. The impact of WTG bearing overloads, in which contact pressures exceed the materials yield strength, has been highlighted as one potential cause of accelerated failure in these components [17]. It has been suggested that wind conditions associated with underloading, whereby surface damage developing through excessive skidding and wear, are more prevalent than overload events. In reality, one or a combination of both phenomena may contribute towards damage [165]. Overloads are the result of inertial effects along the WTG drivetrain caused by instantaneous impulses from transient wind conditions, torque reversals when engaging and disengaging from the grid or misaligned drivetrain components [165]. Previous work has demonstrated that overloading generates regions of subsurface plasticity, which may significantly reduce bearing life expectancy [141].

Gross plastic deformation in bearings is strongly linked with severe distortion of microstructure, potentially accelerating the formation of subsurface failure processes, for example white etching cracks (WECs) [30]. WECs are associated with rolling contact fatigue (RCF) and have been intensely researched [222, 223]. Whilst a definitive cause for this phenomenon remains unknown, WECs are frequently observed encompassed by a white etching area (WEA). ‘White etching’ refers to a white appearance of localised microstructure when observed under an optical microscope post-etching. It has been proposed that WEAs generate as the result of carbide dissolution through exposure to cyclic stresses during RCF, leaving a region of nano-ferrite grains supersaturated with carbon, 30-50% harder and more brittle than the surrounding steel matrix [20, 224]. It is common for bearing applications that WEA and WECs occur near to material inclusions, referred to as butterflies due to their appearance [18]. Dark etching regions (DER), named due to the dark appearance of the deformed microstructure, are more uniform subsurface features and have low hardness when compared to the surrounding matrix [225]. Previous studies have suggested that DERs occur prior to WEC nucleation and are indicative of the early stages of RCF initiated failure [226, 34]. It was demonstrated that the size of DERs generated during RCF resembled the plastic zone geometries predicted using elastoplastic modelling [227]. This implies that significant overload events can create a large subsurface region that is susceptible to RCF damage, with subsequent cyclic contact stresses occurring within the deformed area.

6.1.2 Engineering neutron diffraction

Neutron diffraction provides the unique opportunity to non-destructively probe materials, measuring internal elastic strains and thus allowing for calculation of stresses. Strain diffractometry involves measurement of the interplanar lattice spacings within crystalline materials, with the planes effectively acting as atomic-scale strain gauges. A significant advantage of neutron diffraction techniques, particularly when compared to X-ray diffraction, is that neutrons have higher penetration powers in engineering materials, such as steel [51].

A time-of-flight (ToF) neutron source produces a pulse of polychromatic neutrons through a spallation process. Incident neutrons are guided towards the sample, interact with the material and diffract at an angle dependent on their energy [25]. For a neutron ToF strain diffractometer the detectors are generally at a fixed location, usually measuring diffraction angles of ±90° to the incident beam [228]. The experimental gauge volume is defined as the region situated at the incident and diffracted beam intersection [25]. The incident beam geometry is selected using aperture slits and diffracted beam geometry determined through collimation [63]. Neutron flight paths, from the spallation target/moderator assembly to the instrument detectors, via the sample gauge volume, are fixed and well-defined, with the ToF entirely dependent on individual neutron energies. Wave-particle duality states that the neutrons will have a wavelength associated with energy, meaning that Braggs law can be used to calculate the average interplanar lattice spacing within the experimental gauge volume. Equation 6.1 demonstrates the calculation for interplanar lattice spacing, or d-spacing (d_{hkl}), using neutron ToF information [74]. For a value of $2\theta = 90°$, the neutron scattering vector direction, q, and therefore measured strain component will be at 45° to the incident and diffracted beams.

$$d_{hkl} = \frac{h\,ToF}{2\,m\,L\,sin(\theta)} \tag{6.1}$$

Where, h is Plancks constant, m is the neutron mass, L is the flight path from moderator to detector and θ is the angle between the incident beam and the scattering vector. The detected spectrum, or diffraction pattern, is a plot of neutron intensity as a function of ToF or d-spacing, and usually consists of several peaks, each corresponding to a specific family of $\{hkl\}$ lattice planes. Elastic strain can be calculated using changes to the interplanar spacing, observed as a shift in peak position, relative to a stress-free value, d^0_{hkl} (Equation 6.2) [228]. Figure 6.1 demonstrates the exaggerated peak shift expected during compressive loading. Once a diffraction pattern has been acquired, there are two approaches for obtaining macroscopic strains, namely single peak fitting or full pattern fitting. Using single peak fitting, provides the strains relating to a specific crystallographic plane, d_{hkl}, whilst full pattern fitting gives strains relating to changes in the overall lattice parameter, a. The latter being an average, make it more representative of the macroscopic strain state. The least-squares procedures, Rietveld and Pawley refinement, are the preferred techniques for full pattern fitting [81, 229]. The resulting value of a can be then used to calculate strain using a stress-free reference lattice parameter, a_0, analogous to d^0_{hkl} for single peak fitting, as seen in Equation 6.2.

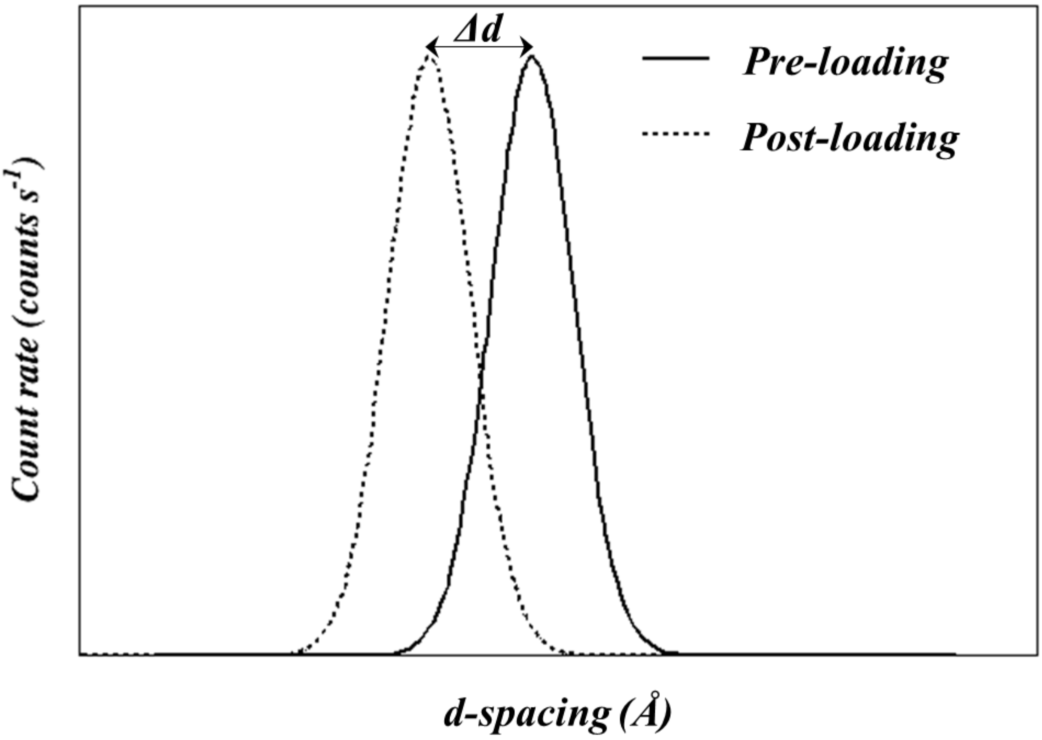

Figure 6.1: Exaggerated peak shift in a generic Bragg peak, demonstrating the effect of compressive loading.

$$\varepsilon_{hkl} = \frac{d_{hkl} - d^0_{hkl}}{d^0_{hkl}} = \frac{\Delta d_{hkl}}{d^0_{hkl}} \quad , \quad \varepsilon_{bulk} = \frac{a - a_0}{a_0} = \frac{\Delta a}{a_0} \tag{6.2}$$

Traditionally, engineering neutron diffraction experiments involve the characterisation of residual or *in situ* strain. Common residual stress measurements include those performed on welded or cladded specimens [230, 231]. Narayanan et al. successfully measured residual stresses in a laser cladded rail, demonstrating the benefits in reducing the effect of ratcheting under fatigue loading and consequent wear mechanisms [232]. The study additionally highlights the benefits of neutron diffraction as a complementary technique for measuring residual stress, potentially being used in parallel with semi-destructive procedures, such as incremental hole drilling. *In situ* neutron experiments generally involve the measurement of strains within a sample under varying load, occasionally during exposure to harsh high-temperature or cryogenic conditions [233, 234]. For example, *in situ* neutron diffraction has been used to characterise the stress relaxation of Inconel 625 nickel-base superalloy at temperatures of 700°C, comparing behaviour of conventionally processed and additively manufactured specimens [235]. It is common practice to apply neutron diffraction results for validating computational models, such as Finite Element Analysis (FEA) [236].

A disadvantage of neutron diffraction is the relatively long data acquisition times that are required to collect suitable statistics for performing the peak fitting procedures, particularly compared to rapid X-ray data acquisition rates. Depending on the gauge volume geometry, it can take between a few minutes and a few hours to obtain sufficient neutron counts for steel, with smaller gauge volumes requiring longer scan times [74]. Nonetheless, if the stress state within the specified gauge volume remains constant throughout the measurement, for example during residual stress characterisation, this does not pose much of a problem. However, if stress conditions are continually altering throughout data acquisition then the accuracy of measurements will be compromised, making time-resolved studies more difficult. As a result, the development of stroboscopic techniques has been used as a method for measuring the time dependent variation of strain in cyclic processes [237].

Stroboscopic measurements are useful for measuring cyclical processes where the strain state varies within each cycle but every cycle is nearly the same. Even though the neutron statistics within each section of the cycle is insufficient for a full analysis, if the same section of the cycle is added up over multiple cycles, enough statistics can be obtained for the data to be analysable. Stroboscopic strain measurements using neutron diffraction were introduced in 1996, to study the behaviour of a metal matrix composite exposed to thermal cycling [237]. The composite was rapidly cycled between 175-400°C, with a reference signal being sent from the furnace to the data acquisition system at the beginning of each cycle. There have since been several stroboscopic neutron experiments, including a study by Feuchtwanger et al. which used a reference pulse generated from an Instron loading frame to synchronise neutron data acquisition with the applied strain, allowing for the study of stress-strain behaviour in polymeric matrix composites [238]. The loading frequency for this experiment was 0.5 Hz, using 100 time segments for every individual cycle, with each segment being 20 ms. Furthermore, a recent study also successfully measured time-resolved strain in a piezoelectric actuator, exposed to an alternating electric field of frequency 0.5 Hz and magnitude of 0-130 V [239]. Neutron detection events were divided into 26 segments each with a width of 10 V, allowing for the evaluation of cyclic strains. It is apparent from these previous studies that to successfully measure time-resolved strain a suitable triggering system is required, in order to provide a reference for data acquisition processes.

Stroboscopic X-ray experiments are more commonplace due to rapid data acquisition rates, with Baimpas et al. using the technique to measure dynamic strain in the connecting rod of an operational internal combustion engine [214]. Time-resolved X-rays were also used for tribological applications, to measure dynamic contact strain in a ball bearing, using a Hall sensor to trigger whenever a ball passed the region of interest [171]. A more recent study used a fibre optic triggering system to detect every individual roller passage in a rotating bearing. This method was capable of performing dynamic strain measurements in under 13 minutes, with a contact loading frequency of 125 Hz associated with bearing operation at 854 *rpm* [240]. The equipment from the mentioned X-ray experiment has been adapted for stroboscopic neutron diffraction experiments, forming the basis of the present study.

6.1.3 Aims and structure

The aims of this study are to (i) develop hardware and software for measuring dynamic contact strain using ToF neutron diffraction, (ii) stroboscopically measure dynamic *in situ* elastic strain in an overloaded roller bearing, (iii) develop a method for processing stroboscopic data to obtain cyclic strain associated with rolling contact fatigue, (iv) develop further understanding of the influence overloading has on bearing failure.

Using a novel stroboscopic triggering technique and utilising the benefits of eventmode neutron data acquisition systems, it has been demonstrated that there is potential for measuring dynamic strain, even at the high rates of strain variation experienced at the contact of an operational roller bearing. A loading rig was designed for the purpose of conducting dynamic strain measurements on a running bearing using the ENGIN-X neutron diffractometer. Stroboscopic neutron diffraction has successfully been used to study the evolution of strain at the maximum stress state, as well as characterising cyclic strain variation associated with rolling contact fatigue. This work offers a novel approach in the field of tribology to further understand RCF using time dependent strain measurements, whilst results support the hypothesis that overloads accelerate raceway damage, lowering bearing life expectancy, with post-test interrogation confirming the occurrence of surface and subsurface damage.

6.2 Experimental design

6.2.1 Test bearing

The experiment was designed to be performed using both energy dispersive X-ray diffraction and ToF neutron diffraction, however this body of work focuses on results obtained during the neutron investigation. The test bearing was selected with major consideration given to the sample geometry, optimising radiation attenuation, particularly for X-rays, as neutrons penetrate AISI 52100 bearing steel more easily. The SKF NU1010 ECP cylindrical roller bearing was selected, as a raceway thickness of 16 mm ensured up to 9% transmission for high energy X-rays, allowing for penetration that provides suitable data acquisition [240]. The bearing has 20 rolling elements with an outer diameter, D, and bore diameter, d, of 80 mm and 50 mm, respectively (see Figure 6.2b). As WTG bearings are very large components, they would be unsuitable for diffraction experiments due to attenuation issues, nonetheless the test bearing recreates similar operational contact pressures to those generated in a commercial WTG, whilst being scaled down appropriately in size. A cylindrical roller bearing creates a line contact between roller and raceway, generating subsurface stress fields that are inherently less complex that those associated with point contacts found with spherical rolling elements. This allows for the assumption that stresses are uniform in the axial direction (x-axis), along the contact. Table 6.1 contains the chemical composition, whilst Table 6.2 shows the material properties of AISI 52100 bearing steel.

Table 6.1: AISI 52100 Chemical Composition [182].

C	Mn	Si	Cr	Cu	S
0.95 - 1.10	0.20 - 0.50	≤0.35	1.30 - 1.60	≤0.025	≤0.025

Table 6.2: AISI 52100 Properties [181].

Property	Symbol	Value
Density $[kg/m^3]$	ρ	7830
Young's Modulus $[GPa]$	E	201
Poisson's Ratio	υ	0.3
Yield Stress $[MPa]$	σ_Y	1410

6.2.2 Dynamic loading rig

A purpose-built rig was designed with essential features, taking into consideration that experimentation was to be performed using both the I12 X-ray beamline and the ENGIN-X neutron strain diffractometer, each with unique setup requirements and scattering geometries [71, 74]. Further details on the features that are specific to the X-ray experiment are included in previous work [240]. Detector geometry (fixed ±90°) at ENGIN-X allows for a maximum of two orthogonal strain components to be measured simultaneously. Since the radial component (z-axis) was of primary interest, only that component was measured in the presented work. The rig was designed to apply loads and perform neutron measurements along a direction of 90° from the top of the rig, ensuring that the neutron scattering vector was aligned with the bearing radial loading direction. Figure 6.2a, shows a photograph of the rig.

The rig was fitted with an OMEGA LCM20-20kN load cell and SGA/A load cell amplifier, with loads applied using a cantilever arm and threaded bar screw mechanism. A direct loading piece (DLP), between the cantilever arm and the test bearing, was guided by linear ball bearings to ensure that load application was radially aligned. Care was taken to ensure that rig components did not obstruct the incident and diffracted neutron beam line-of-sight, yet this could not be avoided with the DLP. Therefore, the DLP was constructed with aluminium, which has a very low neutron absorption cross-section (0.23 barns for aluminium compared to 2.56 barns for iron with neutrons at 2200 ms^{-1}), thus making it effectively transparent at this material thickness [75]. There were also access points made available for the mounting of acoustic emission sensors (AE) and accelerometers, as part of a condition monitoring project running in parallel with this study [241].

6.2.3 Neutron diffraction strain measurements

The experiment was completed on the ENGIN-X neutron strain diffractometer at ISIS Neutron and Muon Source, UK [74]. The ENGIN-X beamline is a designated engineering strain scanning instrument, with a neutron flight path of approximately 50 m and high flux over a wavelength range of 1-3

Å, suitable for most polycrystalline engineering materials. A neutron pulse rate of 25 Hz was used, providing a ToF window for each individual pulse of approximately 40 ms. The rig was positioned on the sample stage with the bearing z-axis at 45° to both the incident neutron beam and north detector bank, allowing for measurement of the radial strain component. Figure 6.2c shows a schematic of the sample in relation to the neutron beam and scattering vectors. The slits were opened to allow for an incoming beam with a cross-section of 2 x 2 mm^2, whilst the 2 mm collimators were positioned in front of the detectors to limit the diffracting volume in that direction. This resulted in a 2 x 2 x 2 mm^3 gauge volume, aligned with the overloaded region of interest in the raceway subsurface, as represented in Figure 6.2d, where it should be noted that the cubic gauge volume sits 45° to the bearing coordinates. Scans were also performed on standard calibration samples; vanadium and NIST standard cerium oxide. Cerium oxide is a very strong coherent neutron scatterer, with well-defined lattice parameters, allowing for ToF information to be accurately calibrated. The vanadium sample is a very poor coherent neutron scatterer but a strong incoherent scatterer, used to determine the incoming incident neutron spectra. This is then used to normalise the collected experimental data.

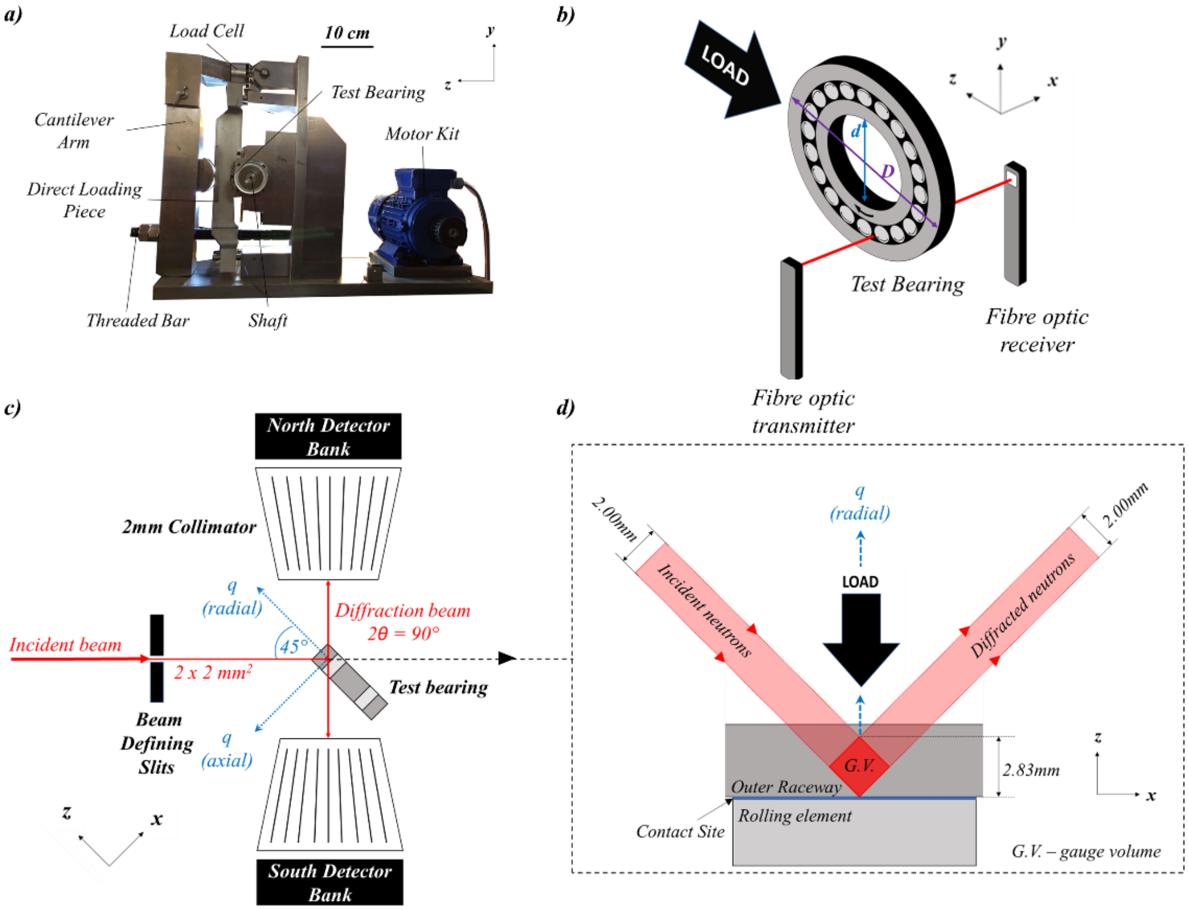

Figure 6.2: (a) Photograph of the dynamic loading rig. (b) Fibre optic system used for the stroboscopic strain measurement technique. (c) Schematic of ENGIN-X experimental setup. (d) Projection of the cubic gauge volume in the xz-plane.

The experiment included static scans (stationary bearing), typical of those performed during ENGIN-X experiments, and dynamic scans, which required a stroboscopic method for synchronising the bearing rotations with the ENGIN-X data acquisition electronics (DAE). Static scans were performed without shaft rotation and with a roller placed in contact with the outer raceway location being measured. The gauge volume was positioned in the outer raceway, directly beneath the contact, to measure the elastic radial strain under different loads, P_s. Static scans were performed at increasing increments of P_s = 10 kN up to 40 kN, with the stress-free a_0 lattice parameter measured at 0 kN, allowing for calculation of relative elastic strain. A maximum load of 40 kN was selected because it had previously been demonstrated as being slightly within the elastic limit, according to FEA, described in Section 6.2.5.

Dynamic scans were performed, measuring strain in an overloaded region of the static outer raceway, while the bearing was running at 927 *rpm* under a constant radial load of P_s = 40 kN. Overloads were performed using a fixed raceway loading frame (FRLF), described in previous work [141]. The frame uses a single isolated rolling element mounted in a static shaft, with a fork mechanism used to apply the designated load to a fixed outer raceway. Loads are applied using an Instron loading frame, meaning that the FRLF can also be used for 'static' fatigue investigations, with such results presented in Section 6.3.2. An overload equivalent to P_s = 136 kN was applied prior to the dynamic test, with subsurface plasticity propagation reaching the contact surface, as predicted by FEA. The substantial overload maximises acceleration of damage and increases the likelihood that failure will be observed during the experiment.

For dynamic strain measurements, a stroboscopic triggering technique was used, as previously described in the stroboscopic X-ray study [240]. This made use of a Keyence FU-18M thru-beam fibre optic system to detect the passage of individual rolling elements (Figure 6.2b). For every roller passage the Keyence FS-N10 Series digital amplifier generated a PNP output signal, which was converted to a TTL pulse using a Stanford Research Digital Delay/Pulse Generator. The TTL pulse triggered a Phantom 7.3 high speed camera, used to capture a still image of the region of interest, ensuring that the roller was in contact with the overloaded zone on the rising edge of the pulse, after correcting for a time delay. The high speed camera was used to determine the delay.

The delayed TTL pulse was used to provide a time-reference, indicating where the rollers were positioned throughout the experiment. The delay/pulse generator was used to specify a pulse width (Δt), which determines the size of the time-bins used for filtering neutrons. The reference pulse was fed into the DAE to synchronise roller position with the detection of the ToF neutrons. The DAE consisted of a Digital Data Interface Board, which fed into the Sample Environment Breakout Board (SEBB) and the detector card. The DAE was operated in eventmode for dynamic tests. The fibre optic pulse metadata from the sample environment, could be logged using an analogue-to-digital converter (ADC) channel in the SEBB, along with neutron detector acquisition running in synchronisation. Whilst running in eventmode, every neutron detection is stored with the time of collection, allowing for filtration of these events into discrete time-bins during post-processing. Each eventmode data file consisted of roughly 28 minutes of data acquisition, rather than storing data in one continuous file, which would be too large for post-processing. Figure 6.3 provides an example of an ADC sample log recording, indicating a time period of 7.56 ms, or BPF_o of 132 Hz, validating the predicted outer raceway BPF_o of approximately 136 Hz for a shaft speed of 927 *rpm*, using Equation

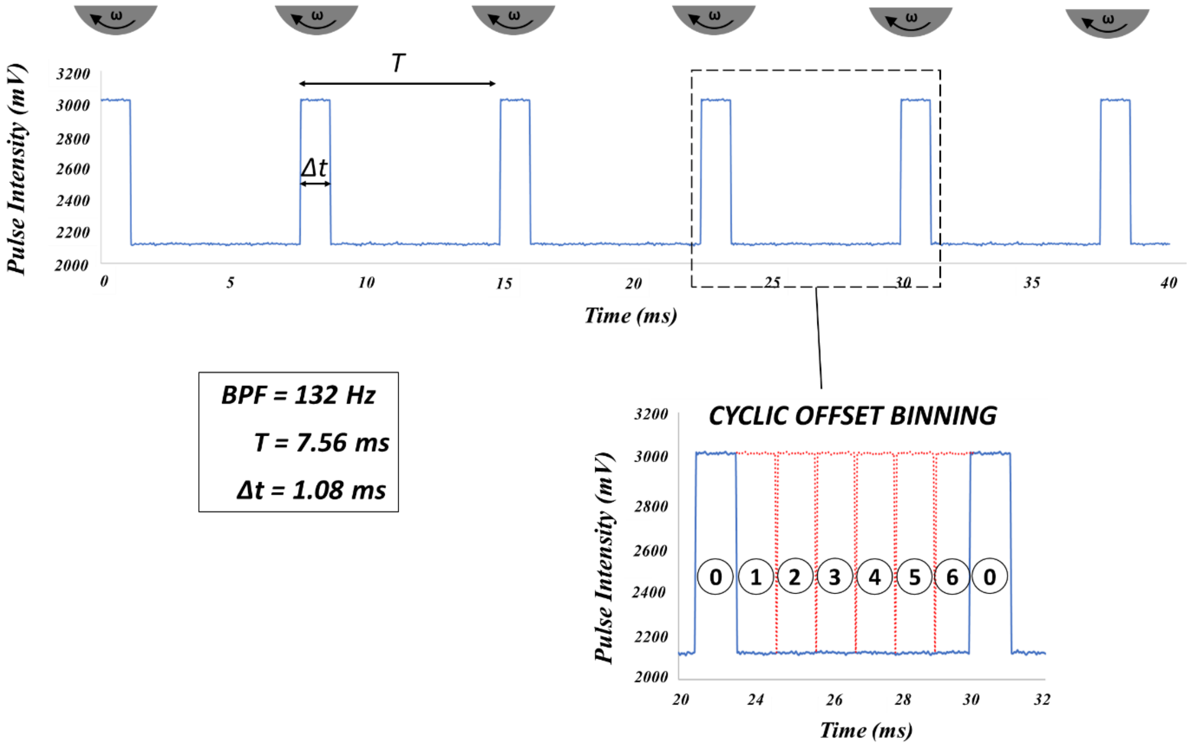

Figure 6.3: ADC sample log reading demonstrating the generation of pulses over 40 ms, the ToF range recorded for each pulse of neutrons. INSET -visualisation of the seven time-bins (numbered with an index starting at zero) generated by shifting the original pulse by an integer multiple of the pulse width.

6.3 [242].

$$BPF_o = \frac{\omega_s Z}{120}\left(1-\left(\frac{d}{D}\right)cos(\alpha)\right) \tag{6.3}$$

Where, ω_s is the shaft speed in rpm, Z is the number of rolling elements, d is the rolling element diameter, D is the bearing pitch diameter and α is the contact angle between the roller and the raceway.

6.2.4 Stroboscopic data analysis Dynamic scans

Eventmode data was analysed using python scripting, which incorporated pre-programmed algorithms within the Mantid Project Application Programming Interface [243]. In order to analyse data collected whilst the DAE was operating in eventmode, the ADC sample log is required to generate a filter workspace, consisting of a sequence of start and stop times corresponding to the beginning (t_0) and end of an individual pulse ($t_f = t_0 + \Delta t$). All filter times are determined using a threshold value in the sample log, in this case the threshold was set to 2200 mV, capturing the rising edge of each pulse (see Figure 6.3).

The neutron detection events and the filter workspace events generated from the roller passage are all synchronised with the same clock, relative to the start of the individual scan. A separate algorithm then collates all the neutron events that occurred at times between the t_0 and t_f, for each roller passage throughout the entire scan. These neutrons are then re-collated to generate a diffraction spectrum, like those generated by the DAE during static scans. The ToF resolution for both static and dynamic data was set to 4.67 μs.

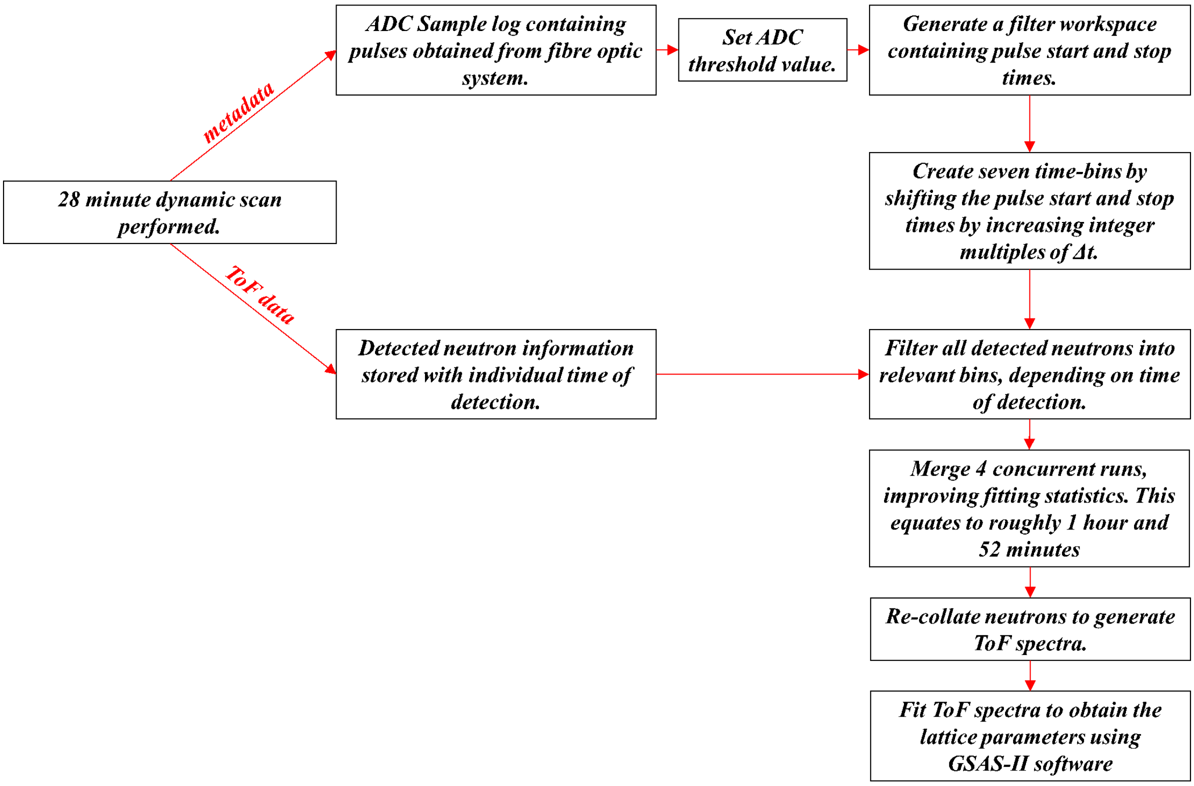

Figure 6.4: Summary of the processing steps for dynamic scans.

As every neutron acquisition is recorded, with their individual ToF information, the reference pulse generated as a roller passes the region of interest can be shifted to evaluate the cyclic variation of strain during bearing operation, demonstrated by the inset of Figure 6.3. As the pulse width was one-seventh of the time period, neutrons were segmented into seven time-bins, each equal to the pulse width. Therefore, every recorded neutron incident was used to generate a spectrum for fitting strain data. Consequently, the statistical quality of data associated with a single scan was compromised by splitting the neutron counts, but to minimise this effect four scans were merged together during post-processing, providing suitable quality of statistics for fitting. Merging was performed using a running average with successive overlaps, so as not to significantly reduce the number of strain values generated over the entire experiment. This resulted in nearly 2 hours of data collection to produce each fitted strain measurements.

In order to obtain the lattice parameters, all spectra, static and dynamic, were fitted using the GSAS-II crystallography software [244], with Pawley refinement in the ToF range of 20 ms and 40 ms (d-spacing range of 1.09 Å to 2.17 Å), incorporating the most prominent {110}, {200} and {211} Bragg peaks. Figure 6.4 presents a graphic, summarising the individual processing steps for dynamic scans. Figure 6.5 shows a comparison between the static and dynamic data. The peak intensities and signal-to-noise ratio is greater for the static scans, as would be expected due to dynamic data post-processing techniques reducing the effective data acquisition time. The average strain uncertainty for static scans was ±93 $\mu\varepsilon$, whereas for dynamic scans the average uncertainty was ±117 $\mu\varepsilon$, signifying that data is of better quality for static data collection.

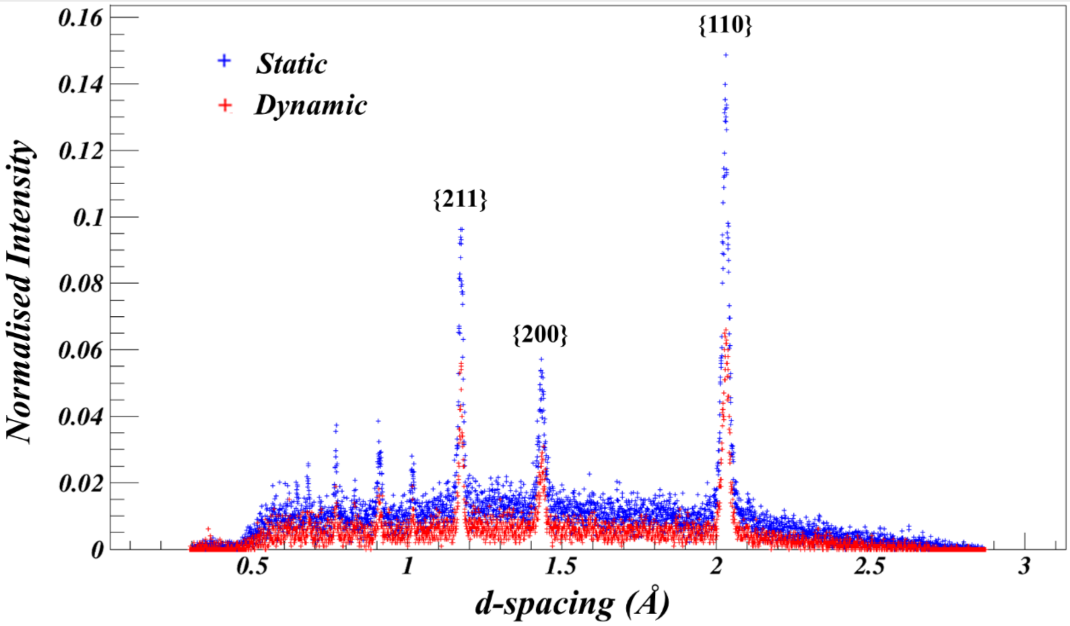

Figure 6.5: Comparison of static and processed dynamic spectra normalised using a vanadium standard sample.

6.2.5 Modelling

Finite Element Analysis

In a previous study, FEA simulated in ABAQUS version 6.14-2 [146], was used to predict the elastic and plastic behaviour of the sample. The primary aim of the model was to provide the loading conditions whereby the elastic limit was exceeded and the extent of subsurface yielding that occurs during overload. The model was validated using Hertzian contact theory, showing excellent agreement with the calculated theoretical predictions of contact pressure and elastic load limit [141]. A schematic of the three-dimensional elastic-plastic model, with boundary conditions, is demonstrated in Figure 6.6. Quadratic elements (C3D20R) were used for modelling the bearing raceway and roller element, whilst the remaining components were bilinear rigid quadrilateral elements (R3D4). Contact friction was assumed to be negligible as static loading conditions were being simulated, whilst only one-quarter of the bearing was modelled to reduce computational expense, with symmetry assumed in the x-axis and θ-axis. Additionally, isotropic hardening was assumed using derivations from the AISI 52100 stress-strain curve [186]. Table 6.2 provides the AISI 52100 material properties used for the model.

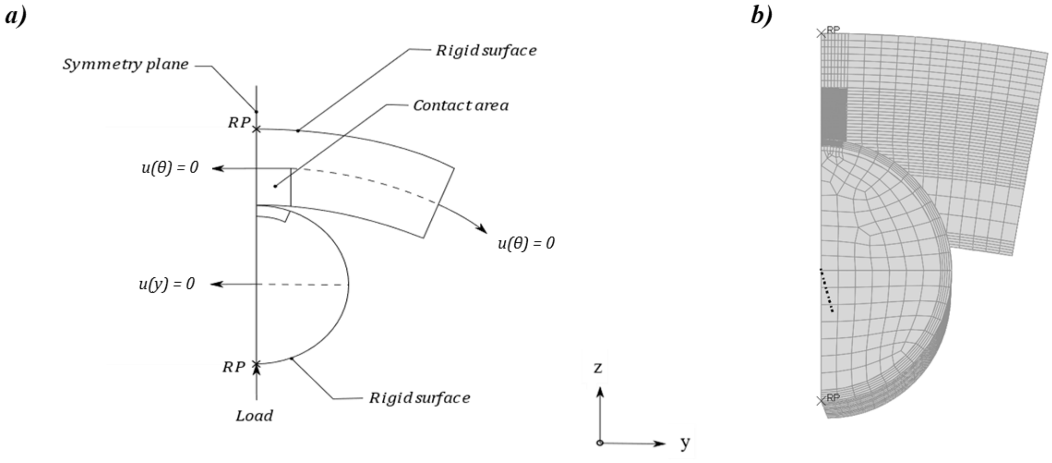

Figure 6.6: (a) Finite Element Model boundary conditions. (b) Mesh.

Analytical raceway model

Hertzian contact theory was utilised for comparison of the subsurface elastic strains being generated in the raceway at different static and dynamic loads [40]. For comparison with static scans, two-dimensional subsurface strain fields were calculated, in the yz-plane, for each experimental load. As a line contact was generated between the roller and the raceway, strains were assumed to be uniform along the contact (x-axis). This assumption allows for averaged strains within a theoretical three-dimensional gauge volume to be obtained by weighting the calculated two-dimensional strain field. The experimental gauge volume extended to a depth of 2.83 mm into the subsurface, due to detector geometry and beam alignment with the sample, as demonstrated in Figure 6.2d.

For dynamic strains, traction between the roller and the raceway surface was incorporated by the model, assuming that Amontons law holds [39, 41]. A coefficient of friction of 0.05 was assumed, which is relatively high for most roller bearing applications, yet has been demonstrated to be reasonable for very high loads, such as those being used in dynamic test (P_s = 40 kN) [54]. The model simulated a static bearing raceway, with subsurface radial strains generated as rollers moved throughout the period of a single roller passage, T, relative to when a roller was in contact with the contact site beneath the gauge volume, where $t = 0$. Figure 6.7 demonstrates the model at $t = 0$, $t = T/3$ and $t = 2T/3$, with the 2 x 2.83 mm^2 cross-section of the gauge volume represented with a black box.

6.2.6 Novelty Detection

A novelty detection strategy was implemented to determine whether bearing damage was produced during operation. A common strategy includes comparing the vibrational spectral data obtained from the acceleration signal to identify the occurrence of any peaks at the characteristic defect frequency, relating to a specific bearing component. In practice, this type of analysis may not always be possible and thus more sophisticated methods are needed to provide a reliable diagnosis.

The vibrational data was measured with a tri-axial acceleration sensor (PCB 356B21), bonded on the top of the rigs DLP using a cyanoacrylate. The output was connected to a NI cDAQ 9223 Module

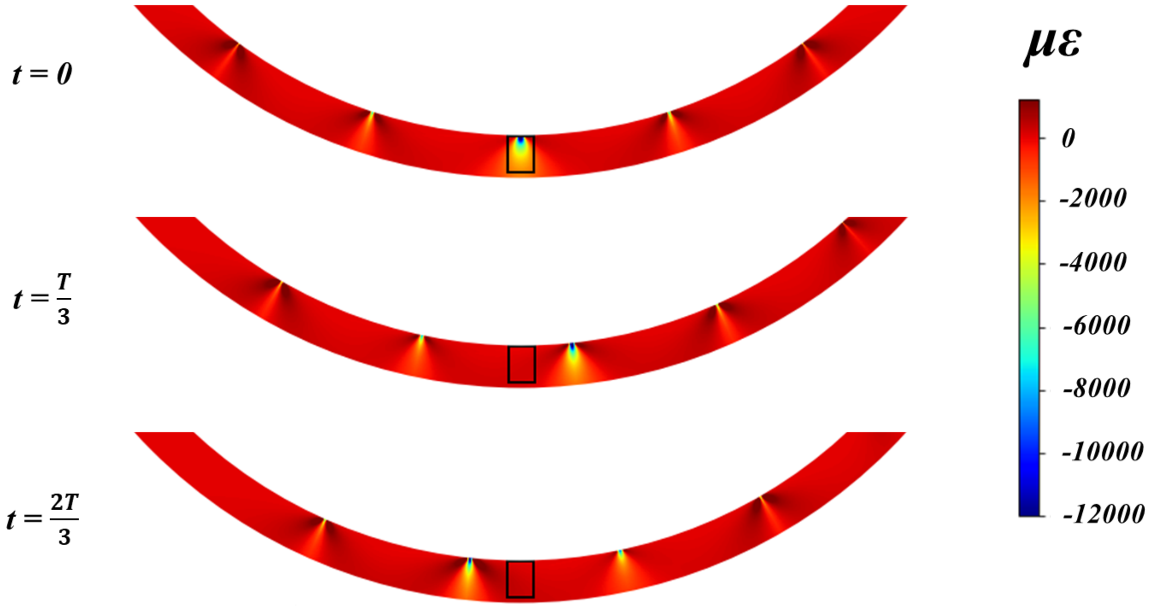

Figure 6.7: Analytical model of dynamic strain in the bearing raceway at t = 0, t = T/3 and t = 2T/3. The black box symbolises the theoretical gauge volume.

coupled to a NI cDAQ 9184 chassis for signal acquisition. The rig was monitored via a LabVIEW interface that allowed visualisation of the captured signal in real time and to perform basic storage operations. The recorded signal was periodically stored by segmenting 10 seconds streams of data every 15 minutes at a sampling rate of 51.2 kHz.

In order to find any deviation from the bearings standard operational behaviour, a novelty detection method based on the Squared Mahalanobis Distance (SMD) was used. This method quantifies the extent that a measured point differs from the standard conditions in terms of standard deviations with respect to a specific distribution. Therefore, if a measured multidimensional feature shows a greater separation between a specific distribution representing the normal (undamaged) state of the machine, then a novelty can be inferred. The SMD can be defined using Equation 6.4.

$$D_{\zeta} = \sqrt{(x-\mu)\Sigma^{-1}(x-\mu)'} \tag{6.4}$$

Where x, μ and Σ^{-1} represent the n-dimensional sample point, the mean and the inverted covariance matrix respectively. The analysed features were vectors containing spectral data obtained from the vertical axis of the acceleration signal. These features were obtained by transforming the time domain acceleration signal, using the Fast Fourier Transform algorithm, and then reduced to a frequency range of 25 to 150 Hz. This method requires a baseline feature, used as a reference for the undamaged state, and obtained by calculating the mean and covariance matrix for a pristine bearing sample. Findings from the novelty detection approach for condition monitoring are detailed in further work completed by Martinez et al [241].

6.3 Results

6.3.1 Static strain measurements

Strains measured during static scans are presented in Figure 6.8, alongside values predicted by Hertzian contact theory. The elastic compressive strain increased with load application, yet at lower loads there was lesser agreement with the analytically strains. This is possibly due to the region of localised subsurface contact stress being significantly smaller than the overall experimental gauge volume, with even a minor misalignment of the gauge volume position impacting the result. As the stress increases and the size of the localised stress field increases, results become more comparable with predicted values. This result was useful for determining the suitability of the applied load and selected gauge volume geometry for dynamic testing.

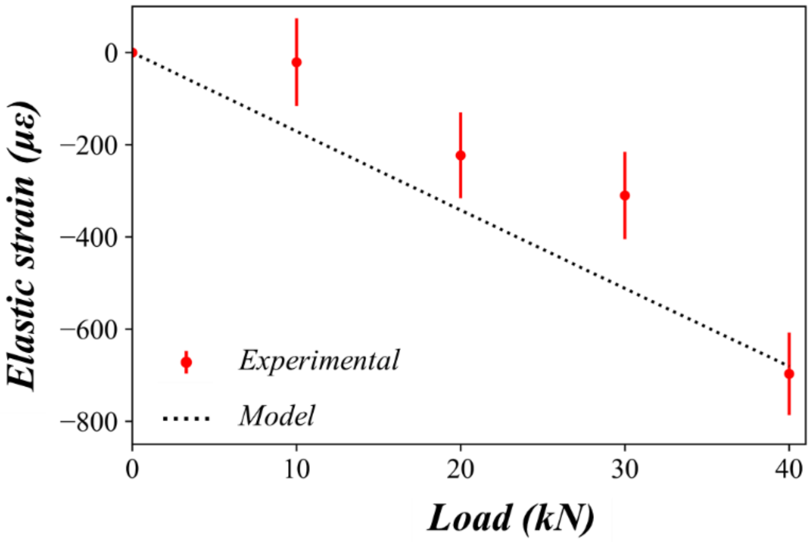

Figure 6.8: Static radial elastic strain for increasing load, compared to the values predicted using Hertzian contact theory.

6.3.2 Time-resolved subsurface elastic strain

A long-term dynamic test was performed, with the aim of running a bearing to failure, using ‘worst case’ pre-overload and dynamic load conditions, as determined using FEA. An overload of P_s = 136 kN and a dynamic load of P_s = 40 kN was applied. Overall, the dynamic experiment lasted for more than 29 hours, performing approximately 1.5 million bearing revolutions. The elastic radial strain at maximum stress, when the roller is positioned beneath the gauge volume, are presented in Figure 6.9, alongside the measured SMD values. It should be noted that between 13 and 17 hours there is a gap in data acquisition, as a result of the rig stalling. This resulted in the motor and support bearings being replaced as they would be the components to experience the greatest duty if the test bearing had failed. The rig was restarted and then operated for a further 12 hours, until it stalled for a second time and the test was ended.

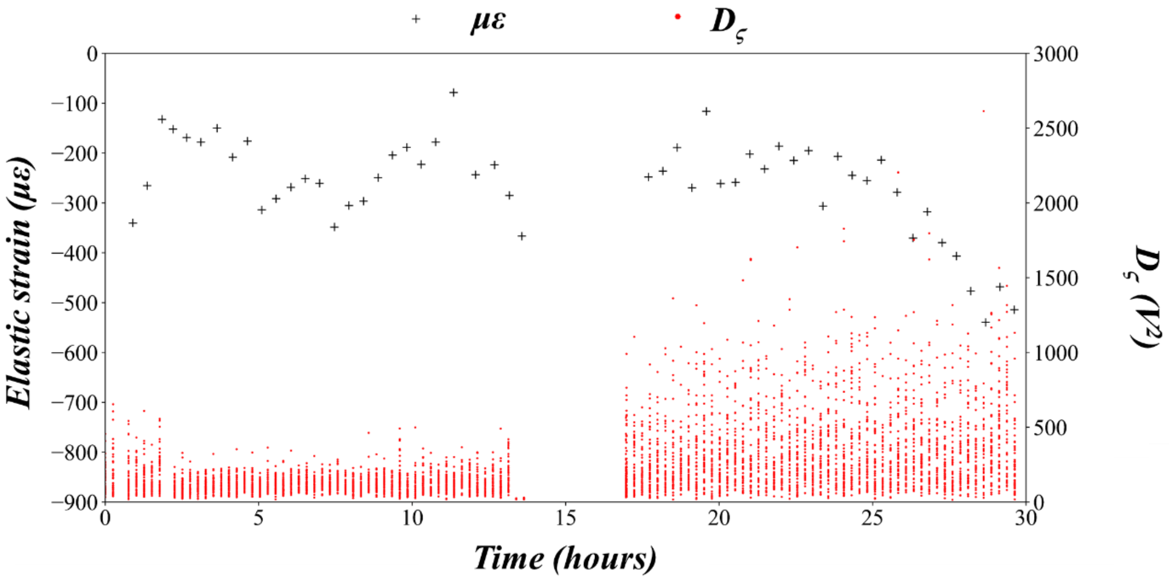

Figure 6.9: Measured elastic radial strain and the Squared Mahalanobis Distance recorded over the long-term dynamic experiment.

As all neutrons are detected throughout the entire experiment with the triggering signal simply acting as a time reference, cyclic strain was evaluated by segmenting the data, as described in Section 6.2.4. The neutron data were sorted into seven discrete time-bins, corresponding to a different point within the rollers passage, relative to bin-0, which is the point when maximum compressive strain is expected as the roller is in contact with the region of interest. Figure 6.10a presents all 53 strain cycles measured over the long-term test. Each cycle has 7 data points, with the scan merging process offering a time resolution of slightly under 2 hours per measurement.

The data is inherently noisy, as would be expected with such high frequency cyclic strain, the nature of ToF neutron data acquisition, and the time resolution being compromised by post-processing procedures. The sampling time for each cycle was intermittent relative to the absolute experimental time, yet the sample rate is constant and each cycle represents the same physical phenomena, i.e. a roller passage. Therefore, a Discrete Fourier Transform (DFT) was implemented to examine the frequency domain, in order to assess whether any periodicity existed within the strain variation [245, 246]. The sample rate, f_s, was equal to the pulse width (Δt = 1.08 ms, so f_s = 926 Hz). This demonstrated noteworthy spikes at the BPF of 132 Hz, followed by harmonics belonging to that fundamental frequency. This gives confidence that although the data is noisy, there is an expected cyclic trend and that strain variation is consistent with the applied RCF stresses. Figure 6.10b shows frequency domain from the original signal. The DFT confirming that the most prevalent frequency component related to the BPF_o, indicates that strain could be averaged for each time-bin over the entire experiment, to evaluate the overall cyclic strain variation. Figure 6.11a shows the measured cyclic strain for a single roller passage as measured by neutron diffraction, compared to those predicted using the analytical raceway model, with error bars representing the standard deviation of the 53 values.

Averaging the raw signal provides strain magnitudes that are slightly lower than those predicted

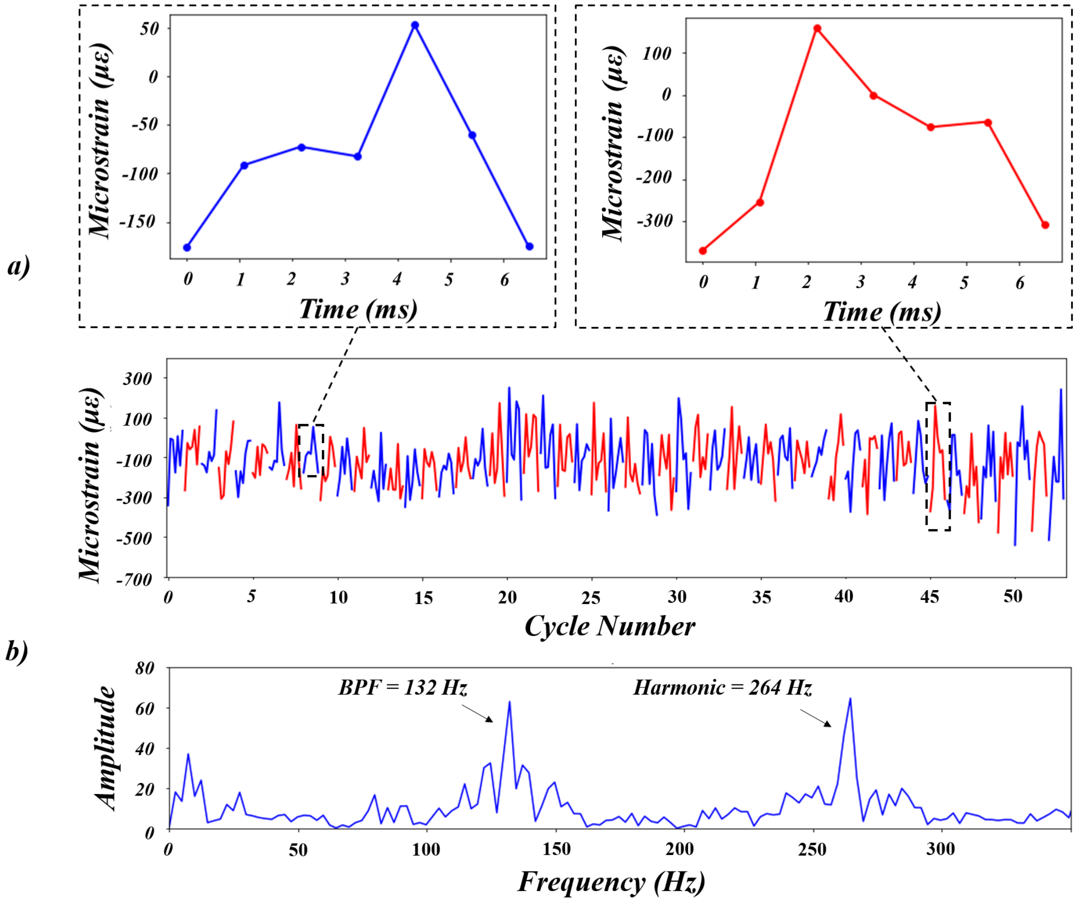

Figure 6.10: (a) Calculated strain for the seven time-bins within each of the 53 dynamic cycles. Alternating colours used to provide clarity on where each cycle begins and ends. INSET -two examples of individual cycles represented on the time axis. (b) Frequency domain of the 53 cycles, under the assumption the data is continuous.

by modelling, and the presence of a small unexpected bump in the cyclic data. For future stroboscopic neutron experiments, it may be useful to integrate signal processing approaches for removing noise from stroboscopic data. Initially for this study, a multi-band finite impulse response filter was adopted for trialling denoising approaches, as this technique is frequently adopted in signal processing for improving signal-to-noise ratios [247, 248]. The filter was used to attenuate frequencies outside of the bands; 120 - 150 Hz and 5 - 20 Hz, incorporating the BPF_o and the shaft rotational frequency, respectively. Figure 6.11b shows cyclic strain results obtained from the filtered signal, demonstrating a trend more comparable to the model.

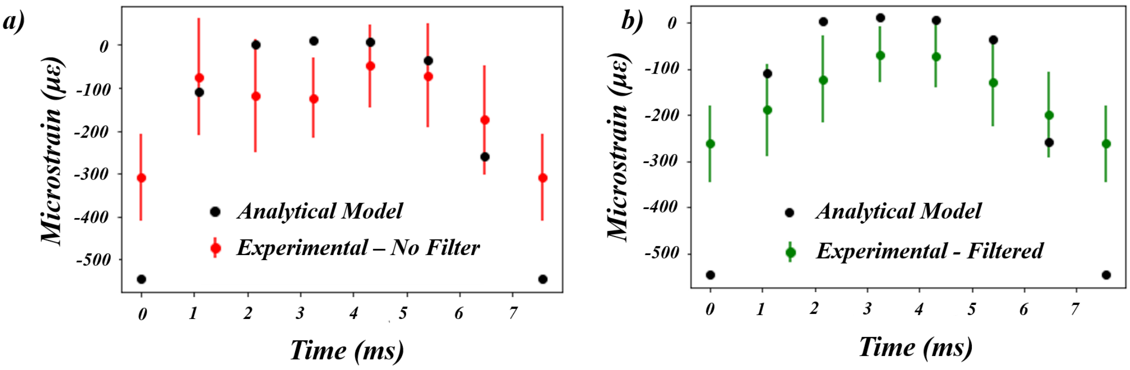

Figure 6.11: (a) The average experimental radial strain at each time within the 53 recorded cycles, compared to the radial strain predicted by the analytical raceway model. (b) The average experimental radial strain, post filtering, at each time within the 53 recorded cycles, compared to the model. Error bars represent the standard deviation. Please note that the final point for both (a) and (b) is a repeat of t = 0 s, completing an entire cycle.

6.3.3 Post-mortem interrogation

Confocal scanning microscopy

Global plastic deformation at the contact site was visible by eye in the form of a dent, with more prominent damage close to the contact edges. To determine the extent of surface deformation a Leica DCM 3D confocal microscope with a pitch of 1.66 μm was used to examine the surface morphology in an approximately 1.86 by 8.30 mm^2 area, around the contact site. Due to limitations in the microscopes field of view, the area was divided in 24 individual scans, stitched together to produce the final 3D image, as seen in Figure 6.12a. The scan confirmed that significant plastic deformation was formed, with evidence of pitting having occurred on both edges of the contact indentation.

Reference scans were also completed at a location away from the contact region, to correct for curvature of the bearing surface, allowing for examination of 2D profiles of the contact area. A profile along the x-direction, demonstrates the indentation depth along the length of the contact, shown in Figure 6.12b. It appears that pitting has occurred at the contact edges, which is almost certainly due to stress concentration effects in those regions. Figure 6.12c shows a profile along the y-direction taken from the edge and the middle of the contact. This also demonstrates the extent of pitting at the contact edge, with roughly a 4-times increase in depth when compared to the dent observed from the middle of the contact. Width at the centre of the contact was measured at roughly 1 mm, whilst the width during overload was 0.83 mm, as predicted using Hertzian contact theory.

6.3.4 Post-mortem interrogation

The sample was circumferentially sectioned to observe subsurface microstructure, with a 2% nital solution used for etching. Figure 6.13b demonstrates an alteration to the microstructure surrounding the contact, with WEAs close to the surface and a substantial DER that gradually brightens as it

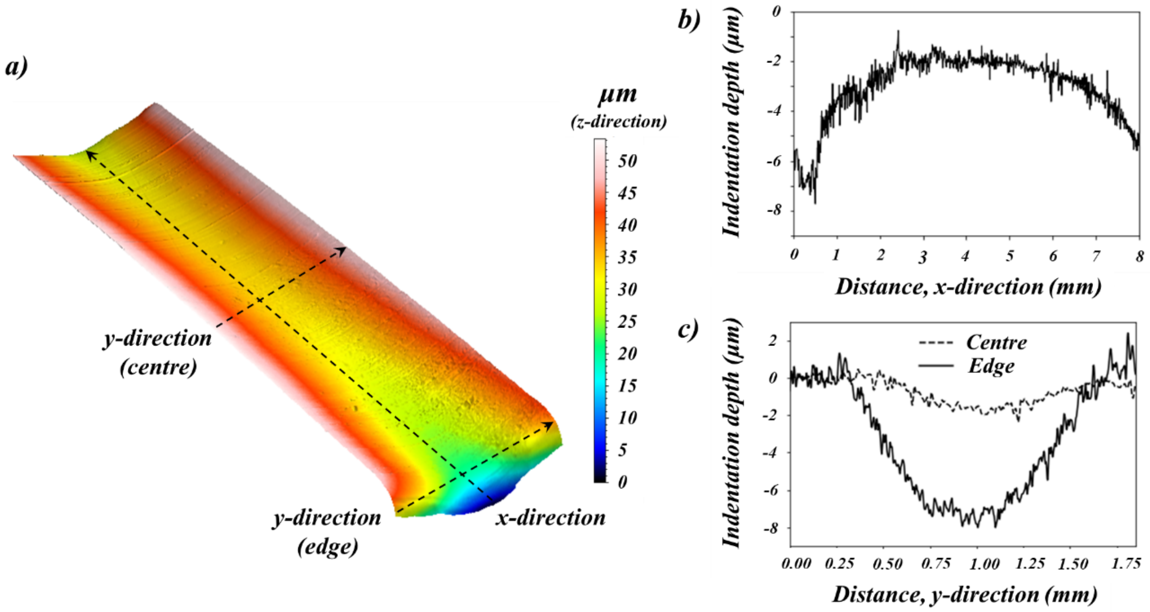

Figure 6.12: (a) Three-dimensional representation of the contact site generated using a confocal scanning microscopy. (b) Profile of the contact depth along the x-direction. (c) Profile of the contact depth along the y-direction, for both the centre and edge of the contact.

fades into the original microstructure with increasing subsurface depth. The darkest DER appears as a band, running between the surface and a depth of roughly 170 μm, closely associated with a maximum shear stress at the depth of 175 μm, predicted using Hertzian contact theory and indicated using a dashed red line. Figure 6.13c demonstrates a subsurface region that contained a WEC, surrounded by WEA, appearing to initiate at an inclusion, typical of WECs [20]. The crack was observed at a depth of 120 μm into the subsurface. Figure 6.13d shows a section whereby there was evidence of DER, close to several WEA formations around potential cracks or material voids.

6.3.5 Offline bearing fatigue

A separate offline fatigue experiment, where no diffraction was used, was performed with the FRLF and an Instron loading frame, under the same overload (P_s = 136 kN) and dynamic loading (P_s = 40 kN) conditions, for an equivalent of approximately 0.28 million revolutions. Considering the statistical nature of bearing failure, this is judged to be within reasonable range of the failure observed during the neutron experiment. A large axial crack had formed, with most severe damage appearing in the subsurface beneath the contact edges. The microstructure, observed using a scanning electron microscope (SEM), appears typical of ductile fatigue, with striations occurring perpendicular to the subsurface crack, in the same region where clear severe microstructural alterations have formed, as seen with the optical microscope. Figure 6.14 shows the axial cross sections, observed using SEM and optical microscopy from the FRLF test.

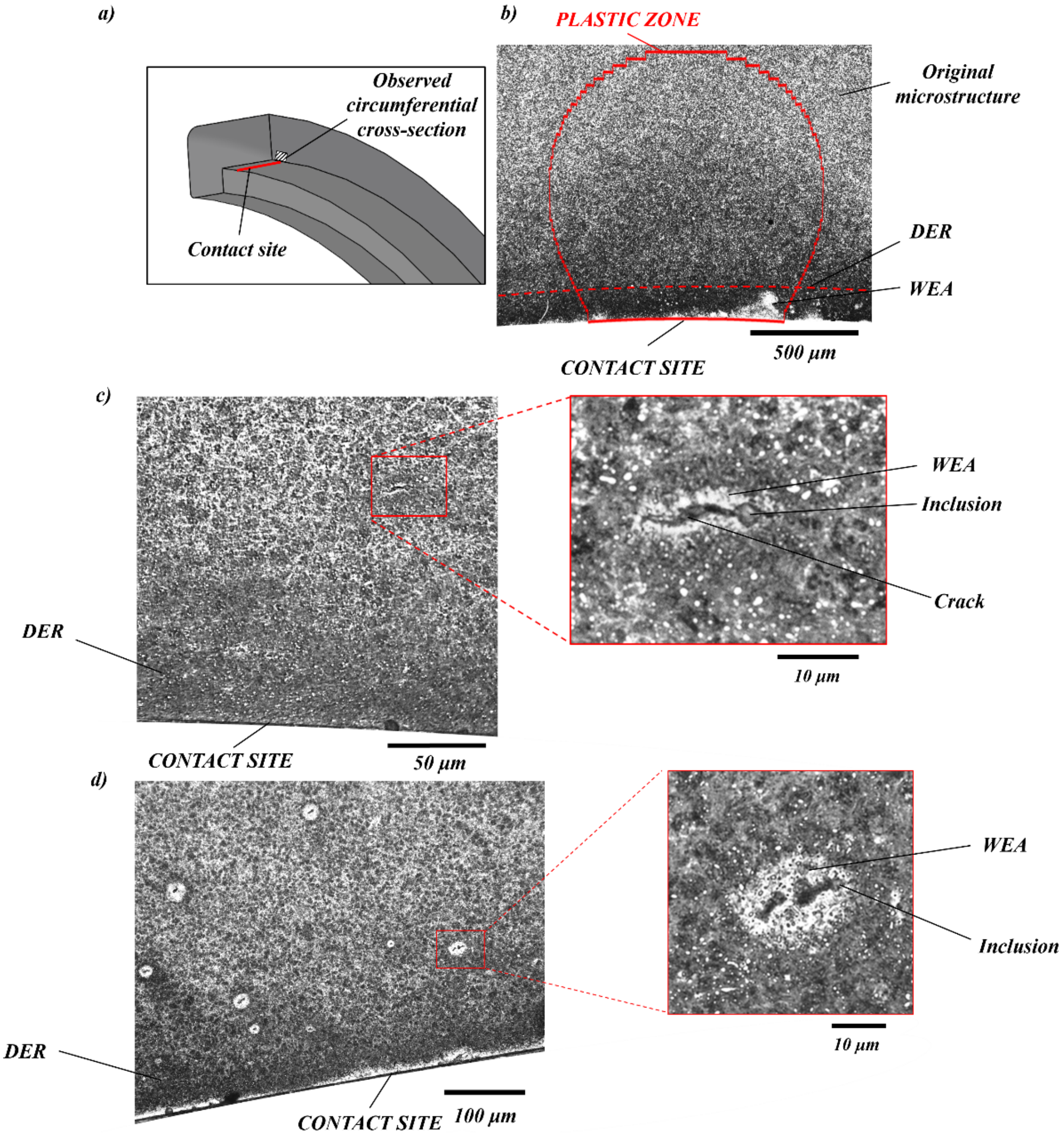

Figure 6.13: (a) Schematic to demonstrate the circumferential cross-section being observed. (b) Subsurface image in the overloaded region. (c) Subsurface crack initiated at a material inclusion, with associated WEA. (d) Subsurface damage and WEA, adjacent to a material inclusion.

6.4 Discussion

During the dynamic test, a significant increase in the measured compressive strain begins shortly after the initial interruption to rig operation at 13 hours, suggesting that test bearing failure might have prevented the rig from functioning correctly. The proposed test bearing failure, along with support bearing degradation, would have increased the coefficient of friction, resulting in the required torque exceeding that being provided by the motor. Assuming that bearing failure had occurred when the rig initially stalled at 13 hours, this corresponds to a 59% reduction of life, compared to the expected L_{10} prediction for that applied load.

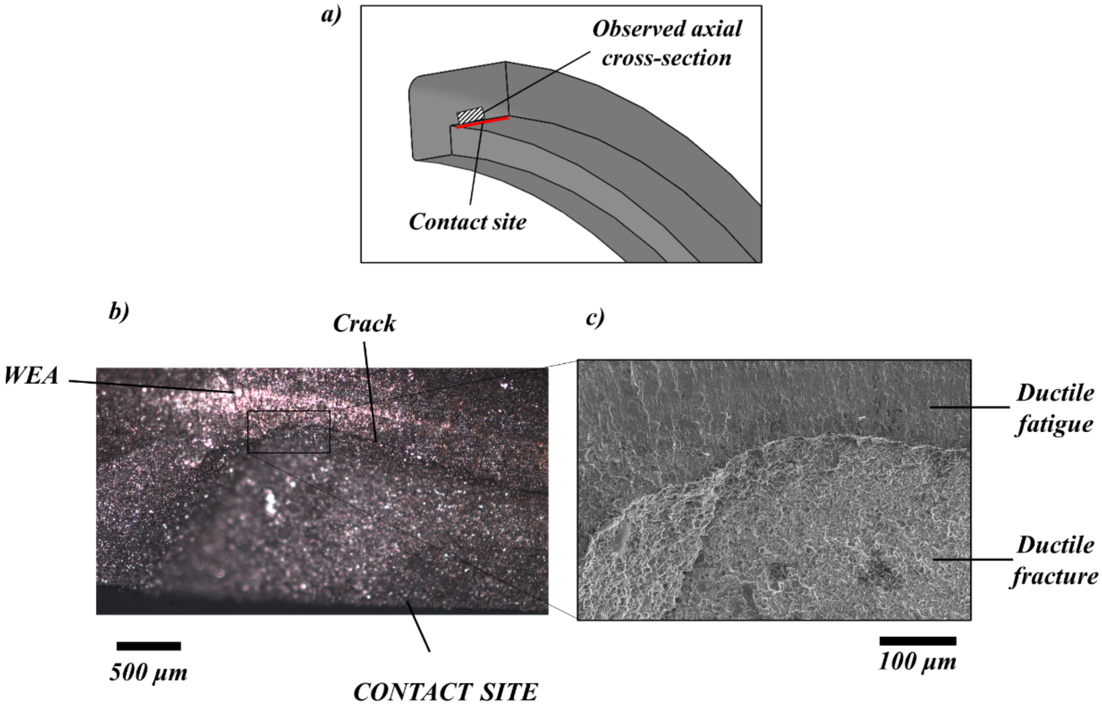

Figure 6.14: (a) Schematic to demonstrate the axial cross-section being observed. (b) Optical microscope image of the contact edge subsurface. (c) SEM image of the contact edge subsurface.

For the first time, a stroboscopic diffraction procedure has been used, simultaneously with condition monitoring techniques, and has successfully identified an approximate time of failure. Multivariate analysis using the novelty detection method on vibration levels, revealed a statistically significant increase in SMD values after recommencing rig operation, relative to standard operating conditions, suggesting damage had been initiated (as seen in Figure 6.9). A further investigation on damage localisation was performed in parallel by Martinez et al. [241], where a localisation approach used time-delay and sum beamforming methods with three AE sensors. This indicated that the detected abnormality originated from the overloaded site, with standard deviation uncertainty of 45.2°. Nonetheless, bearing failure is defined as the point at which it no longer operates as intended, which is certainly implied by these non-destructive techniques [219].

The proposed stroboscopic technique offers a novel method for further understanding tribological mechanisms, such as rolling contact fatigue, with its ability to non-destructively measure dynamic strain using neutron diffraction. This is comparable with other diffraction techniques, for example using synchrotron X-rays. A previous experiment, performed with energy dispersive X-ray diffraction, using the same rig and test bearing, had previously measured radial strain stroboscopically in a dynamically loaded sample [240]. A benefit of using X-ray diffraction is the improved spatial and temporal resolution, with the mentioned experiment obtaining strain values within 13 minutes, in addition to a gauge volume cross-sectional area of only 150 x 150 μm^2. The results indicated similar effects on elastic strain, with gradually increasing compressive strain prior to an observed failure. It was also proposed that this effect was the result of a reduction in yield strength due to material softening, induced during severe plastic deformation. The consequence of this damage is accelerated onset of rolling contact fatigue associated instability (Phase III), supporting the hypothesis that overloads significantly reduce bearing life expectancy.

Whilst spatial and temporal resolution are better for synchrotron X-ray diffraction, neutron diffraction holds the unique capability for characterising cyclic strains, as every detected neutron can be utilised. Additionally, neutron diffraction is better suited for probing engineering materials of larger geometries, more representative of commercial components. For neutron diffraction, strain measurement uncertainties were greater for dynamic scans compared to static scans, although this was not the case for X-ray experiments, where signal-to-noise was similar for both static and dynamic measurements. Prior to this study, data analysis procedures for stroboscopic neutron techniques were not practical, however significant developments in the post-processing of eventmode data have been demonstrated by this work.

Examining the bearing post-mortem offers the proposal that failure could either be related to surface damage, subsurface damage or a combination of both. Pre-overloading certainly appears to have accelerated bearing failure via surface denting prior to the dynamic test, yet there is also evidence to suggest subsurface failure as a failure mode. The overload seems to be have contributed towards surface indentation exaggerated at the contact edges by stress concentration of cyclic loading. In addition, the subsurface plastic deformation appears to have generated a region prone to subsurface cracking. The DER appears to resemble the shape associated with a Hertzian contact, of similar size to the predicted plastic zone generated during pre-overloading, as seen in Figure 6.13b. It has been demonstrated in previous studies that DERs resemble the size and shape of plastically deformed microstructure, as predicted by elastoplastic modelling [227]. It has been proposed that DER occurs prior to the formation of WEC and WEA, with Figure 6.13 demonstrating WEA growth in the region closest to the subsurface, within the DER [249]. It is not within the scope of this work to characterise the exact cause of failure, yet condition monitoring approaches confirmed damage propagation at the contact site, stimulated during RCF cycling. The offline experiment performed using the FRLF supports the confocal microscopy results described in Section 6.3.4, as the most detrimental pitting depths were greatest at the contact edges and acting as a location of higher failure probability. Stress concentration effects are proposed as the probable cause for increased damage at the contact edges.

Now that first experiments using stroboscopic strain measurements with roller bearings have been successfully conducted on the ENGIN-X neutron diffractometer, the technique could be scaled-up to study full-size commercial WTG bearings. The high penetration power of neutrons can pass through up to 60 mm of steel, with high speed shaft bearings having raceway thicknesses of approximately 48 mm [74, 250]. Using larger test bearings would generate localised stress fields with significantly larger dimensions, improving accuracy as the gauge volume size would be more suitable and allow for characterisation of greater strain magnitudes. Additionally, reducing the bearing rotational speed would allow for either a greater number of time-bins per cycle, or increased pulse widths, reducing the number revolutions necessary to acquire sufficient fitting statistics. However, slowing the bearing would require longer experimental times to complete a similar number of revolutions, which is not always possible for neutron diffraction experiments, as the designated beam-time is usually no longer than a few days. This work demonstrated the potential of stroboscopic techniques to measure cyclic strain at loading frequencies of approximately 132 Hz, whereas in previous studies cycling rates have generally been much slower, for example 0.5 Hz [234, 235]. It was apparent that accuracy can be hindered at such high frequencies, which is to be expected for ToF techniques. Therefore, it is proposed that there is considerable scope for the future development of more advanced digital signal processing techniques for analysing stroboscopic data, collected under rapidly varying cyclic stress conditions.

6.5 Conclusions

- A custom-built rig and fibre optic triggering system permitted measurement of time-resolved strain using a novel approach to stroboscopic neutron diffraction.
- Static measurements demonstrated closest agreement with Hertzian contact predictions at high loads.
- During a long-term dynamic scan, a condition monitoring novelty detection technique was able to identify bearing failure. Subsequently, a significant increase in subsurface compressive radial strain was observed, as measured using stroboscopic neutron diffraction.
- Cyclic strain associated with rolling contact fatigue was measured using every detected neutron. This was possible due to stroboscopic pulses from the rig and neutron detection events being synchronised.
- Post-mortem surface scans and mechanical cross-sectioning show that the contact edge is the most probable failure location yet were unable to confirm whether failure occurred at the surface or in the subsurface.

CHAPTER 7

DISCUSSION

This chapter assesses the advantages and limitations of the implemented non-destructive techniques. As discussed in Chapter 1, an important aim of this work was to provide insight into WTG bearing reliability issues, specifically relating to overload events and rolling contact fatigue. However, the design and implementation of a technique capable of performing time-resolved strain measurements in dynamic engineering components was the principle motivation. Innovative use of neutron instrumentation has indicated the benefit of incorporating multi-technique approaches, whilst also highlighting the scope for adapting stroboscopic strain measurements to investigate other dynamic engineering systems. Furthermore, an overview of how this work may contribute to improving WTG bearing reliability has been discussed.

7.1 Diffraction techniques

As with any other strain measurement technique, each diffraction method that was applied throughout this study possesses unique advantages and limitations. It is important to consider that, whilst not always directly comparable with one another, multiple technique approaches can be used to obtain complementary information. This can be particularly useful for the validation of analytical theories and numerical techniques. In this study, a custom-built loading rig acquired dynamic radial strain measurements using neutron and X-ray diffraction. The difference in gauge volume geometry and instrument setup prevented a definitive comparison between the results obtained from these techniques, yet numerical modelling and analytical Hertzian contact theory consistently demonstrated reasonable agreement. Regardless of the difficulties associated with comparing X-ray and neutron results directly, appreciation for advantages and limitations of each approach, allows for a holistic evaluation of the experimental outcomes, and demonstrates how technique development throughout this study has contributed towards bridging the knowledge gaps.

It is clear from the experiments performed that EDXD boasts superior spatial and temporal resolutions. The high flux generated at a synchrotron X-ray source allows for rapid data acquisition, even with experimental gauge volumes that are significantly smaller than those conventionally used for neutron strain scanning. For EDXD experiments, spatial resolutions of 150 μm permitted the mapping of localised subsurface contact strains under static loading conditions, showing agreement with finite element analysis and with radial strain field profiles clearly resembling those expected by Hertzian contact theory. The EDXD experimental setup allowed for 23 strain directions to be measured simultaneously, with measurement uncertainty reducing as the radial strain component was extracted from the calculated strain tensor. Additionally, dynamic time-resolved strain measurements were highly optimised in this work. A pioneering study in adapting stroboscopic techniques for tribological applications was successfully performed by Mostafavi et al. using a Hall effect sensor to detect the passage of a single rolling element per revolution [171]. However, the stroboscopic approach developed in this work utilised a purpose built loading rig, whilst demonstrating the use of a novel fibre optic triggering system to accurately detect every individual roller passage. This resulted in significantly reduced data acquisition times, and therefore the ability to track elastic strain evolution with relatively high time resolutions.

Neutron diffraction experiments appear to be better suited for stress and strain characterisation in larger components, with neutron attenuation significantly lower for most engineering materials. The NU1010 ECP test bearing selected for this study was chosen based on it's thickness, permitting suitable transmission of steel and consequently sufficient counting statistics for both X-ray and neutron scanning. Therefore, experimental design for neutron diffraction only, would offer the opportunity to scale-up the rig and test bearing, enabling examination of contact geometries representative of bearings used in the wind industry. The eventmode data acquisition procedures, used during dynamic neutron diffraction experiments, collected ToF information for each neutron detection event, whilst simultaneously recording triggers generated by passage of the rolling elements. This provides the unique opportunity to measure strain continually during fatigue cycling, under the assumption that load variations are the same for every cycle. This has been explored during this study, as presented in Chapter 6, with experimentally determined cyclic strain being compared with analytical theories.

Stroboscopic results

High data acquisition rates, associated with X-ray experiments, provide better time resolution for tracking dynamic strain evolution when using stroboscopic techniques. For instance, the X-ray experiment required 13 minutes for each measurement, whereas each eventmode neutron scan equated to approximately 2 hours, including the influence of post-processing procedures. As mentioned, data acquisition using the stroboscopic technique was optimised, when compared to those previously used for similar applications. This has demonstrated significant advancements in time-resolved X-ray diffraction approaches, by developing the capability to track strain evolution continually throughout long term testing. Additionally, the development of this novel technique has demonstrated the ability of neutron diffraction methods for measuring strains in dynamic engineering components with high cyclic strain rates. Other stroboscopic neutron studies, such as that performed by Feutchtwanger et al., have successfully managed to characterise cyclic stains, yet with significantly reduced strain rates, demonstrating the extent to which this work has progressed time resolved neutron techniques [238].

As previously mentioned, it is difficult to directly compare stroboscopic strain results obtained during both long term experiments, notably as the gauge volumes vary significantly. Nevertheless, both experiments demonstrated the same trend, which was a notable increase in compressive strain, indicating that failure had occurred during the experiment. On each occasion, failure was premature for that specific load, suggesting that overloading had accelerated the onset of damage. During the steady state (Stage II) of rolling contact fatigue failure, regions of microplasticity coalesce, eventually resulting in material softening and the onset of instability [197, 198]. The results from both experiments show increasing radial strains, which appear to suggest that material softening had occurred earlier than expected, supporting the proposed failure mechanism. Statistically, the number of experiments that have been performed during this study is not sufficient enough to definitively claim that overloads reduce bearing life, yet failure times were consistently premature. As mentioned in the literature, rolling contact fatigue initiated subsurface damage, as the result of geometric stress concentration, is more prevalent in heavily loaded bearings [33]. This was evident from the dynamic neutron experiment, where higher surface pressures were generated, as subsurface features typically associated with failure were observed post-mortem.

7.2 Imaging

This work contributed significantly towards the development of two neutron imaging techniques; energy dispersive transmission imaging and neutron computed tomography. When compared to diffraction approaches, these imaging techniques are relatively less well established within the field of engineering. Their development for the purpose of damage characterisation has been undertaken as a substantial contribution of this study, presented in Chapter's 3 and 4. Adapting the MCP detector setup, from the IMAT beamline, made imaging experiments possible on the ENGIN-X strain diffractometer, offering a unique opportunity to perform *in situ* loading scans using neutron transmission imaging. Significant enhancements have been made, not only in the detection of damage through characterisation of elastic strains, but also by using qualitative analysis of a Bragg edge fitting parameter, indicative of material yielding.

Neutron transmission imaging was successfully used to detect crack nucleation in a notched cylindrical duplex steel specimen, providing reasonably accurate strain measurements, particularly for ferritic steel, when compared with finite element analysis. Effective spatial resolutions of 55 μm can be achieved due to the MCP camera's pixel size, yet relatively poor counting statistics per pixel required the use of spatial binning to ensure that Bragg edge's were appropriately fitted. Connolly et al. have previously detected cracks using Bragg edge strain mapping at the NIST Center for Neutron Research [114]. However, the study undertaken as part of this project quantitatively investigated crack induced stress profiles, whilst additionally utilising multiple experimental and numerical techniques for further comparative characterisation.

In Chapter 4, the Bragg edge σ broadening parameter was monitored at regular increasing intervals during a bearing overload event, permitting observation of subsurface plastic zone evolution. When a threshold value was applied to maps of the σ broadening parameter, good agreement was found with the levels of yielding predicted by finite element modelling. Other work has previously demonstrated the ability of Bragg peak broadening for estimating plastic deformation [172], yet the Bragg edge broadening approach demonstrates an original use for energy dispersive imaging. These novel results demonstrated that the technique can be adapted for other engineering studies, where material yielding is of interest.

The recently introduced IMAT beamline [103], specifically designed for performing imaging experiments, offers improved flux within the relevant wavelength range, along with optimised neutron optics and a flight path of 56 m to enhance ToF resolution. The planned introduction of an Instron loading frame, means that the improved ToF resolution can be utilised to perform other such damage initiation studies, whilst lowering the extent to which spatial binning will be required. IMAT's Bragg edge fitting software, BEATRIX [187], has been continually developed using data obtained during these experiments, helping to improve the user friendly interface. This further demonstrates how the investigations undertaken have advanced energy dispersive imaging.

The opportunity for neutron attenuation computed tomography on the IMAT beamline was also utilised, for inspecting the propagated fatigue crack profile within the duplex steel specimen. Crack opening was marginally within the techniques resolution capabilities, resulting in a faint observation of the crack, particularly when compared to a corresponding X-ray computed tomography scan. Nonetheless, such small features have rarely been witnessed using neutron tomography, supporting technique advancements in relation to previous comparable studies [251]. Furthermore, the different neutron attenuation properties of ferritic and austenitic steel provided visible contrast, indicating that the different phases may be distinguished. It has been suggested that with improved resolution, this could be used for digital volume correlation (DVC), whereby the total three-dimensional strain field can be calculated. DVC has been demonstrated using X-ray tomography [92], but trackable features throughout the bulk material were necessary. Contrast between the phases of duplex steel have been proposed as a method to develop DVC for neutrons, with this study supporting that claim.

7.3 Limitations of the applied techniques

A drawback to each of the diffraction and imaging techniques used during this study was the limited experimental times, with allocated beamtime denying the opportunity for repetition, consequently reducing reliability. Whilst offline tests remain a possibility, the chance to obtain X-ray and neutron data is ultimately constrained. Nonetheless, each technique presented it's own individual limitations that are worthy of discussion. Similarly, Hertzian analytical theories have been demonstrated throughout the work, yet the Hertzian contact is considered to be a simplification of the real pressure distributions. When using these theories, assumptions about contact conditions and environment are being made, indicating that subsurface stress fields are more complex than those being predicted, most notably for dynamic cases [41].

X-ray diffraction

It was clear that the greatest hindrance when designing X-ray diffraction experiments, was the levels of attenuation associated with steel. The selected bearing specimen was close to the maximum thickness permissible for obtaining reasonable counting statistics, making it difficult to scale-up the test rig for use with larger bearings, more representative of those installed in commercial WTG's. Nevertheless, the contact pressure distributions created in the dynamic tests, were comparable with operational WTG bearings, predicted using Hertzian contact theory. A further limitation is that the data acquisition system does not have any capability for collecting data continuously throughout the entire experiment, therefore preventing the analysis of cyclic strain associated with rolling contact fatigue. If this ability were implemented it would be a significant advancement, however the sheer quantity of data being collected and computational processing power required may make it a difficult procedure to incorporate within the already established I12 data acquisition electronics.

Neutron diffraction

The most prominent disadvantage of using neutron diffraction is the lower spatial and temporal resolutions. For static scans, neutron gaugue volumes were significantly larger than for X-ray scans, with sufficient statistics obtained in 20 minutes, compared to 1 minute for X-rays. Due to the gauge volume size in relation to the localised stress field, it was also not possible to generate maps of the subsurface contact strain. Most ToF neutron diffractometers, including ENGIN-X, permit a maximum of two simultaneous strain measurement directions, compared to 23 on the I12 EDXD detector. This requires several assumptions about the directions of principal stresses, in order to mitigate the requirement for multiple scans to be performed at different sample orientations when characterising material stresses. Generally, this can be a relatively sound assumption for uniaxial loading experiments, however for this work, rolling contact fatigue is considered a complex multiaxial fatigue problem making stress calculations immensely difficult. Even under static loading conditions, relatively high loads were required for greatest accuracy, suggesting that larger localised strain field dimensions could result in more accurate results. The spatial resolution of X-ray scans allowed for dynamic loads, whereby maximum contact pressures were representative of those generated in operational WTG bearings. However, dynamic loads for neutron diffraction experiments were significantly greater, with maximum contact pressures similar to the compressive yield stress of AISI 52100 [165]. Larger contact geometries, and therefore test bearings, would be beneficial for measuring dynamic strain using the stroboscopic neutron diffraction technique.

Neutron imaging

Neutron energy dispersive transmission imaging is used to measure the averaged strain through a material, suggesting that the most appropriate specimens should have constant thickness, particularly at the region of interest, positioned within the camera's field of view. This will lead to the counting statistic being homogeneous for all pixels, which was the case for the bearing sample used in this study. However, this was not true for the cylindrical duplex steel sample. In this case, a cylindrical geometry was intentionally selected, although compromising statistics away from the centre, an axisymmetric sample is required to perform three-dimensional Bragg edge tomography. The Bragg edge tomography technique is currently under development [131, 132], so as part of future investigations, the data obtained during the experiment could be used for calculating an estimation of the three-dimensional elastic strain field. Therefore, if the total strain field were to be successfully obtained using neutron tomography with DVC, plastic strain within the sample could be predicted. Nonetheless, sample geometry should be carefully considered for future Bragg edge imaging experiments.

It is also worth noting that transmission imaging demonstrates greater accuracy when elastic strain in the measured direction is relatively uniform throughout the entire material thickness, as demonstrated by Ramadhan et al. for a laser shock peened aluminium alloy sample [113]. This was not the case for either of the specimens examined in this study, however as the bearing generates a line contact spanning along a significant width of the sample thickness, it was deemed to be a reasonable assumption in this specific case. Furthermore, in the majority of *in situ* uniaxial loading experiments, Bragg edge imaging may not actually provide the best approach, as the strain component in the applied load direction is usually of most interest, particularly if only one strain direction is required for measurement. As a result of experimental setup, it is inherently difficult to measure this strain component. However, the use of transmission imaging simultaneously with diffraction could be an alternative and provide complementary information. Fortunately, the ability to use both techniques is due to become available on the IMAT instrument in the near future, potentially opening exciting new research opportunities.

As previously mentioned, neutron attenuation computed tomography allowed for visualisation of a fatigue crack nucleated in a duplex steel specimen, yet spatial resolutions were relatively poor, particularly when being compared to the X-ray computed tomography. Additionally, beam divergence as the result of using a pinhole to define the incident beam geometry, reduces the effective spatial resolution of scans. To improve the issues surrounding resolution with neutron tomography, the CMOS camera on IMAT is due to be replaced with a cooled CCD camera, which will notably improve signal-to-noise ratios.

7.4 Wind turbine gearbox reliability

Research has a significant influence on the way that industry approaches problems. Gathering a more fundamental understanding of the mechanisms that result in operational issues, motivates the development of innovative methods to pre-empt or eradicate these problems. It is difficult to quantitatively characterise the impact of overload events on fatigue life, particularly due to the statistical nature of failure requiring substantially more tests to be performed. However, the results intuitively provide insight, supporting the hypothesis that overloads reduce bearing life expectancy [165]. Although there are many contributing factors leading to premature failure, for instance misalignments, inherent defects and poor lubrication, reducing the influence of overloading can help to improve WTG bearing reliability.

The induction of plastic deformation, appears to increase the probability of defects and damage in the overloaded region, with all conducted experiments demonstrating failure prior to the predicted L_{10} life. Results presented throughout this work have failed to determine whether damage initiation is more prevalent in the raceway surface or subsurface. Nevertheless, it is suggested that high dynamic loading, whereby the maximum principle shear stress occurs at greater depths, is more likely to result in subsurface failure. During the stroboscopic X-ray experiment, when the dynamic loads were more representative of operational contact pressure distributions, surface failure was observed when the bearing was inspected post-mortem, whereas offline 'static fatigue' and higher dynamic loads both presented evidence of subsurface damage.

Rolling contact fatigue is certainly considered to be a key driver in bearing failures, ultimately instigating failure even if installation and operation is considered to be under ideal conditions. As previously mentioned, it has been proposed that the rolling contact fatigue phenomenon occurs after a steady state period of stability, during which microplasticity accumulates and coalesces in the contact region, leading to material softening, which in turn causes instability and failure [196]. Throughout dynamic tests for both X-ray and neutron, the measured elastic strain in the overloaded region of the raceway became increasingly compressive throughout bearing life, indicative of material softening. It is proposed that during extreme overload events, such as those performed prior to dynamic testing, significant subsurface plasticity is induced, essentially shortening the steady state stage, accelerating onset of failure. This was observed using Bragg edge imaging with the utilisation of such findings potentially leading to progression in approaches, either by wind turbine design engineers or WTG bearing manufactures, in the development of techniques implemented within the gearbox to reduce the impact of damage initiation and propagation or to improve material properties and quality.

Strategies to reduce this effect and extend bearing life on a commercial scale are welcomed by industry, with development of innovative technologies required to negate the effect of overloads on WTG bearing raceways. It is known that the static raceway is the most susceptible to failure, as a single location will experience the highest contact stresses and therefore damage will be more prevalent in that region. The Ricardo MultiLife bearing system was designed to reduce this effect in bearings with static inner raceways, for example WTG planetary bearings [23]. The mechanism uses hydraulics to drive actuating pistons that periodically rotates the static raceway, distributing the effect of wear and reducing the accumulation of localised damage.

7.5 Summary

Development of this optimised stroboscopic diffraction technique may now lead to an expansion in it's use for other potential engineering applications, meaning that *in situ* time-resolved studies may become more widely accessible. Additionally, results support the use of non-destructive diffraction testing in adding to the already extensive inventory of techniques available to engineers, particularly for characterising material stress and strain. In many cases, the individual investigation being conducted or the application of a specific study, may explicitly advocate the use of a particular technique. As discussed, each approach possess advantage and limitations, depending on the application or the experimental design. For this reason, use of multi-technique analysis is becoming generally accepted, particularly in tandem with ever advancing analytical theories and numerical methods.

CHAPTER 8

CONCLUSIONS AND RECOMMENDATIONS

The project has been successful in developing a novel stroboscopic technique for measuring time-resolved strain in dynamic engineering components, whilst also enhancing neutron imaging approaches and contributing knowledge regarding the influence of overloads on bearing life expectancy. This chapter covers the most significant novel findings from the research project, along with recommendations on future work opportunities that can continue with technique development and with understanding of the concepts covered.

8.1 Conclusions

Stroboscopic strain measurement technique

A principle aim was the development of hardware and software required to measure time-resolved strain in dynamic engineering components, using X-ray and neutron diffraction. A purpose built loading rig was specifically designed for conducting such investigations, incorporating a fibre optic triggering system that optimised data acquisition rates. Additionally, experimental design was used to incorporate features of the rig that required careful consideration of the different diffraction instrument setup's, ensuring that radial strain measurements were possible. Stroboscopic diffraction experiments performed during this work were successful and permitted the measurement of time-resolved strain in a dynamically loaded roller bearing. Also, eventmode neutron data acquisition held the additional benefit of permitting the analysis of cyclic strains, as ToF information was recorded continually. The proposed technique, whilst designed specifically for tribological components, can now be adapted for the analysis of time-resolved strain in other dynamic engineering applications.

Neutron time-resolved data processing

A software package capable of stroboscopic X-ray data analysis had previously been established, yet currently a user friendly approach for analysing stroboscopic neutron data is not available. Although sample environment metadata is recorded simultaneously with neutron ToF information, exhaustive post-processing was required in order to perform satisfactory data analysis. The unique experimental design and data acquisition arrangement used, required the compilation of multiple algorithms to perform the necessary data manipulation. As part of this project, a code has now been developed to filter neutrons depending on their measured ToF, relative to a recorded external stimulus, permitting analysis of stroboscopically acquired data.

Influence of overloads on fatigue life

Statistically, accurate calculation of fatigue life estimations without a significant number of test samples is problematic. However, this study has suggested that extreme overloading does reduce bearing life, with notable premature failure observed during each of the individual investigations. It is difficult to determine the root cause of failure, with surface and subsurface initiated damage apparent, yet only two different loading conditions were used. Nonetheless, it is proposed that subsurface plasticity generated as a result of overloading causes increased instability in the contact region. Both X-ray and neutron experiments demonstrated increases in radial compressive contact strains prior to failure, proposed to be the result of material softening, a phenomena witnessed in the final stages of rolling contact fatigue failure. Furthermore, a static X-ray scan performed after dynamic testing on a bearing that had been pre-overloaded, demonstrated a tensile region in the subsurface, away from the plane of symmetry. This tensile region was also observed with finite element analysis, potentially acting as a driver for subsurface crack propagation.

Observing subsurface plastic deformation

Significant developments in the potential applications of neutron transmission imaging have resulted from this study. A bearing was overloaded using a custom-built fixed raceway loading frame, with energy dispersive transmission scans being performed in the contact region at regular load intervals. Maps of the Bragg edge broadening parameter, σ, were then generated demonstrating increased broadening in the contact subsurface, as the applied load was increased. A threshold σ value was introduced, more clearly highlighting plastic zone geometries, which strongly agreed with yielding predicted by finite element analysis. The Bragg edge broadening parameter provides information on intragranular Type III stresses, analogous to the Bragg peak FWHM, and this investigation provided the first demonstration of the σ parameter being used to study material yielding. Results support the hypothesis that overloads induce subsurface plasticity, potentially detrimental to bearing life expectancy.

Crack detection using neutron imaging

Bragg edge transmission imaging was used to track the evolution of averaged elastic strain in a cylindrical notched duplex steel sample at different stages during fatigue life. Elastic strain maps successfully detected significant stress redistribution at 5.14 x 10^5 cycles, associated with significant crack propagation. It was found that the elastic strain measured in the ferritic phase was much more accurate than in the austenitic phase, when compared with finite element analysis.

Neutron computed tomography was also performed on the cracked sample, permitting observation of the crack profile, as well as visible contrast in the three-dimensional reconstruction, due to differences in the ferrite and austenite neutron attenuation properties. Further validation of the fatigue crack was performed using X-ray computed tomography and post-mortem fractography. This study evaluated several imaging techniques, presenting the advantages and limitations associated with each, whilst ultimately developing an understanding of how these approaches can be utilised for characterising crack propagation.

8.2 Recommendations for future work

This work has positively contributed toward development of stroboscopic diffraction and imaging techniques, notably in enhancing the capabilities of each approach for characterising damage. This section indicates scope for future investigations, continuing the presented research.

In regard to experimental design, further stroboscopic X-ray and neutron tests could be performed now that the hardware and software has been successfully demonstrated. This would permit the investigation of time-resolved strain under different overload and dynamic loading conditions, potentially providing additional information about the influence of overloading on bearing life expectancy. However, as mentioned in Chapter 7, this may not be suitable for future neutron experiments, due to the small contact geometries associated with the current test bearing, relative to the experimental gauge volume size. It is suggested that a scaled-up version of the rig could be used to investigate larger test bearings, whereby contact geometries are increased, with the potential for using commercial WTG bearings. This would give a more representative approach to studying the effects of overloading using stroboscopic neutron diffraction. Additionally, integrating structural health monitoring techniques on the neutron and X-ray instruments, for example vibrational data acquisition or acoustic emission equipment, would allow for a standardised, complementary damage detection method. This could indicate an appropriate time to halt dynamic testing and perform detailed examination of the damaged region under static conditions, for example localised strain mapping.

The stroboscopic technique could also be incorporated onto the IMAT imaging beamline, permitting the measurement of averaged axial strains and for the σ fitting parameter to be continually monitored. This would be of significant interest for determining whether the coalescing of microplasticity associated with rolling contact fatigue could be observed, particularly as the use of a threshold σ value has been verified for highlighting the presence of plastic deformation.

As mentioned, there are inherent difficulties associated with the application of analytical theories, particularly for predicting dynamic contact stresses. Following on from the successful use of finite element analysis for static load estimations, a dynamic model could be developed to simulate stress and strain in a bearing after overloading, which could then be validated using the presented stroboscopic technique. This would provide a more in depth understanding of how overloading effects operational contact stress, and potentially strengthen theories used to predict the exact mechanism responsible for failure.

Further work is also suggested in making the stroboscopic neutron data processing more user friendly. However, streamlining the current method would require several other data sets, necessitating collaboration with other users of the technique. Preferably additional data would be obtained from experiments performed using a variety of different applications, and would certainly be beneficial in promoting this stroboscopic technique for dynamic strain measurements. Also, Chapter 6 advocates signal processing as a means for smoothing the inherently noisy stroboscopic neutron data. Signal processing is an active field with a huge number of techniques available, suggesting the potential for enhancing data de-noising methods, making time-resolved neutron studies a more attractive research engineering approach. The use of these techniques could allow for rapid data analysis to be performed continuously throughout an experiment, aiding with the detection of damage close to the time of initiation.

BIBLIOGRAPHY

[1] A W Manyonge et al. “Mathematical modelling of wind turbine in a wind energy conversion system: Power coefficient analysis”. In: *Applied Mathematical Sciences* 6.91 (2012), pp. 4527–4536.

[2] A K Gupta. “Efficient wind energy conversion: evolution to modern design”. In: *Journal of Energy Resources Technology* 137.5 (2015), p. 051201.

[3] International Renewable Energy Agency (IRENA). *Renewable Capacity Statistics 2019*. Tech. rep. IRENA, 2019. URL: `https://www.irena.org/publications/2019/Mar/Renewable-Capacity-Statistics-2019`.

[4] Sustainable Development Commission. (UK). *Wind Power in the UK*. Tech. rep. London: HMSO, 2005.

[5] A Energiewende. “Sandbag (2018): The European Power Sector in 2017”. In: *State of Affairs and Review of Current Developments* (2018).

[6] MHI Vestas Offshore Wind. *Leading edge technology: Turbines and innovations*. `www.mhivestasoffshore.com/innovations/`. Accessed: 4/7/2019.

[7] PJ Tavner, J Xiang, and F Spinato. “Reliability analysis for wind turbines”. In: *Wind Energy: An International Journal for Progress and Applications in Wind Power Conversion Technology* 10.1 (2007), pp. 1–18.

[8] C A Walford. *Wind turbine reliability: understanding and minimizing wind turbine operation and maintenance costs*. Tech. rep. Sandia National Laboratories, 2006.

[9] S Faulstich, B Hahn, and P J Tavner. “Wind turbine downtime and its importance for offshore deployment”. In: *Wind energy* 14.3 (2011), pp. 327–337.

[10] L Huang et al. “Modeling of operational availability of offshore wind turbines”. In: *2016 International Conference on Probabilistic Methods Applied to Power Systems (PMAPS)*. IEEE. 2016, pp. 1–6.

[11] D Vučina, I Marinić-Kragić, and Z Milas. “Numerical models for robust shape optimization of wind turbine blades”. In: *Renewable energy* 87 (2016), pp. 849–862.

[12] M D Reder, E Gonzalez, and J J Melero. “Wind turbine failures-tackling current problems in failure data analysis”. In: *Journal of Physics: Conference Series*. Vol. 753. 7. IOP Publishing. 2016, p. 072027.

[13] C C Ciang, J-R Lee, and H-J Bang. “Structural health monitoring for a wind turbine system: a review of damage detection methods”. In: *Measurement science and technology* 19.12 (2008), p. 122001.

[14] G Marsh. “Offshore reliability”. In: *Renewable Energy Focus* 13.3 (2012), pp. 62–65.

[15] S Sheng. *Gearbox reliability database: yesterday, today, and tomorrow.* NREL, National Renewable Energy Laboratory, 2014.

[16] T Bruce, H Long, and R S Dwyer-Joyce. “Dynamic modelling of wind turbine gearbox bearing loading during transient events”. In: *IET Renewable Power Generation* 9.7 (2015), pp. 821–830.

[17] N T Garabedian et al. “The Cause of Premature Wind Turbine Bearing Failures: Overloading or Underloading?” In: *Tribology Transactions* 61.5 (2018), pp. 850–860.

[18] A Greco et al. “Material wear and fatigue in wind turbine systems”. In: *Wear* 302.1-2 (2013), pp. 1583–1591.

[19] F Rasmussen, K Thomsen, and T J Larsen. “The gearbox problem revisited”. In: (2005).

[20] M-H Evans. “An updated review: white etching cracks (WECs) and axial cracks in wind turbine gearbox bearings”. In: *Materials Science and Technology* 32.11 (2016), pp. 1133–1169.

[21] A Ragheb and M Ragheb. “Wind turbine gearbox technologies”. In: *2010 1st International Nuclear & Renewable Energy Conference (INREC).* IEEE. 2010, pp. 1–8.

[22] G Mandic et al. “Active torque control for gearbox load reduction in a variable-speed wind turbine”. In: *IEEE Transactions on Industry Applications* 48.6 (2012), pp. 2424–2432.

[23] T P Howard. “Development of a novel bearing concept for improved wind turbine gearbox reliability”. PhD thesis. University of Sheffield, 2016.

[24] NS Rossini et al. “Methods of measuring residual stresses in components”. In: *Materials & Design* 35 (2012), pp. 572–588.

[25] P J Withers and HKDH Bhadeshia. “Residual stress. Part 1–measurement techniques”. In: *Materials science and Technology* 17.4 (2001), pp. 355–365.

[26] M Willcox and G Downes. “A brief description of NDT techniques”. In: *Toronto: NDT Equipment Limited* (2003).

[27] Z Ye and L Wang. “Optimization analysis on assembly interference of cylindrical roller bearings”. In: *Advances in Mechanical Engineering* 7.7 (2015), p. 1687814015593868.

[28] RK Upadhyay, LA Kumaraswamidhas, and M S Azam. “Rolling element bearing failure analysis: A case study”. In: *Case studies in engineering failure analysis* 1.1 (2013), pp. 15–17.

[29] RL Widner and WE Littmann. “Bearing damage analysis”. In: *Proceeding of the 20th Meeting of the Mechanical Failures Prevention Group.* Vol. 423. NBS Special Publication. 1976, pp. 67–83.

[30] C R Gagg and P R Lewis. “Wear as a product failure mechanism–overview and case studies”. In: *Engineering Failure Analysis* 14.8 (2007), pp. 1618–1640.

[31] E V Zaretsky. “Rolling bearing life prediction, theory, and application”. In: *NASA STI Program* (2013).

[32] Y Ding and N F Rieger. “Spalling formation mechanism for gears”. In: *Wear* 254.12 (2003), pp. 1307–1317.

[33] R W Bruce. *Handbook of lubrication and tribology, volume II: Theory and design.* CRC press, 2012.

[34] J Gegner. “Tribological aspects of rolling bearing failures”. In: *Tribology-lubricants and lubrication.* IntechOpen, 2011.

[35] S Sankar, M Nataraj, and Prabhu V Raja. “Failure analysis of bearing in wind turbine generator gearbox”. In: *Journal of Information Systems and Communication* 3.1 (2012), p. 302.

[36] C G Santos and C Laird. “Fractography of induction-hardened steel fractured in fatigue and overload”. In: *Materials characterization* 39.1 (1997), pp. 25–41.

[37] Organización Internacional de Normalización. *Rolling Bearings: Dynamic Load Ratings and Rating Life*. ISO, 2007.

[38] B Jacobson. “The Stribeck memorial lecture”. In: *Tribology International* 36.11 (2003), pp. 781–789.

[39] K L Johnson and K L Johnson. *Contact mechanics*. Cambridge university press, 1987.

[40] J Williams. *Engineering tribology*. Cambridge University Press, 2005.

[41] J A Williams and R S Dwyer-Joyce. “Contact between solid surfaces”. In: *Modern tribology handbook* 1 (2001), pp. 121–162.

[42] C Hammond. *The Basics of Crystallography and Diffraction*. fourth. New York: Oxford University Press, 2015.

[43] D Mc Kie and C Mc Kie. “Essentials of crystallography”. In: (1986).

[44] H P Klug and L E Alexander. “X-ray diffraction procedures: for polycrystalline and amorphous materials”. In: *X-Ray Diffraction Procedures: For Polycrystalline and Amorphous Materials, 2nd Edition, by Harold P. Klug, Leroy E. Alexander, pp. 992. ISBN 0-471-49369-4. Wiley-VCH, May 1974.* (1974), p. 992.

[45] T Mak and G Zhou. “Crystallography in modern chemistry. A resource book of crystal structures”. In: *Acta Cryst* 49 (1993), pp. 576–578.

[46] A M Kosevich. *The crystal lattice*. Wiley Online Library, 1999.

[47] J Donnay and D Harker. “A new law of crystal morphology extending the law of Bravais”. In: *American Mineralogist: Journal of Earth and Planetary Materials* 22.5 (1937), pp. 446–467.

[48] J H Jang, HKDH Bhadeshia, and D Suh. “Solubility of carbon in tetragonal ferrite in equilibrium with austenite”. In: *Scripta Materialia* 68.3-4 (2013), pp. 195–198.

[49] GB Olson and M Cohen. “A general mechanism of martensitic nucleation: Part II. FCC BCC and other martensitic transformations”. In: *Metallurgical transactions A* 7.12 (1976), pp. 1905–1914.

[50] FC Frank. “On Miller–Bravais indices and four-dimensional vectors”. In: *Acta Crystallographica* 18.5 (1965), pp. 862–866.

[51] M T Hutchings et al. *Introduction to the characterization of residual stress by neutron diffraction*. CRC press, 2005.

[52] D S Sivia. *Elementary scattering theory: for X-ray and neutron users*. Oxford University Press, 2011.

[53] S Parsons, A M Boonman, and M K Obrist. “Advantages and disadvantages of techniques for transforming and analyzing chiropteran echolocation calls”. In: *Journal of Mammalogy* 81.4 (2000), pp. 927–938.

[54] J A Ogilvy and H M Merklinger. *Theory of wave scattering from random rough surfaces*. 1991.

[55] L B Felsen and N Marcuvitz. *Radiation and scattering of waves*. Vol. 31. John Wiley & Sons, 1994.

[56] M Born and E Wolf. *Principles of optics: electromagnetic theory of propagation, interference and diffraction of light.* Elsevier, 2013.

[57] M Utsuro and V K Ignatovich. *Handbook of neutron optics.* John Wiley & Sons, 2010.

[58] K W Herwig. “Introduction to the Neutron”. In: *Neutron Imaging and Applications.* Springer, 2009, pp. 3–12.

[59] R Pynn. “Neutron scatteringa non-destructive microscope for seeing inside matter”. In: *Neutron applications in earth, energy and environmental sciences.* Springer, 2009, pp. 15–36.

[60] B E Warren. *X-ray Diffraction.* Courier Corporation, 1990.

[61] GEM Jauncey. “The scattering of x-rays and Bragg’s law”. In: *Proceedings of the National Academy of Sciences of the United States of America* 10.2 (1924), p. 57.

[62] M T Hutchings. “Neutron diffraction measurement of residual stress fields: overview and points for discussion”. In: *Measurement of Residual and Applied Stress Using Neutron Diffraction.* Springer, 1992, pp. 3–18.

[63] PJ Withers and PJ Webster. “Neutron and synchrotron x-ray strain scanning”. In: *Strain* 37.1 (2001), pp. 19–33.

[64] RA Winholtz. “Characterization of macrostresses”. In: *Analysis of Residual Stress by Diffraction using Neutron and Synchrotron Radiation (Ed. ME Fitzpatrick, A. Lodini)* (2003), pp. 60–77.

[65] MR Daymond et al. “Use of Rietveld refinement for elastic macrostrain determination and for evaluation of plastic strain history from diffraction spectra”. In: *Journal of Applied Physics* 82.4 (1997), pp. 1554–1562.

[66] P J Withers and HKDH Bhadeshia. “Residual stress. Part 2–Nature and origins”. In: *Materials science and technology* 17.4 (2001), pp. 366–375.

[67] R Fernández, G Bruno, and G González-Doncel. “Residual stress evolution with compressive plastic deformation in 6061Al–15 vol.% SiCw composites as studied by neutron diffraction”. In: *Materials Science and Engineering: A* 403.1-2 (2005), pp. 260–268.

[68] HE Coules et al. “Neutron diffraction analysis of complete residual stress tensors in conventional and rolled gas metal arc welds”. In: *Experimental Mechanics* 53.2 (2013), pp. 195–204.

[69] X Song et al. “Finite element modelling and diffraction measurement of elastic strains during tensile deformation of HCP polycrystals”. In: *Computational Materials Science* 44.1 (2008), pp. 131–137.

[70] A Balerna and S Mobilio. “Introduction to synchrotron radiation”. In: *Synchrotron radiation.* Springer, 2015, pp. 3–28.

[71] M Drakopoulos et al. “I12: the joint engineering, environment and processing (JEEP) beamline at diamond light source”. In: *Journal of synchrotron radiation* 22.3 (2015), pp. 828–838.

[72] B Kämpfe, F Luczak, and B Michel. “Energy Dispersive X-Ray Diffraction”. In: *Particle & Particle Systems Characterization* 22.6 (2005), pp. 391–396.

[73] B B He. *Two-dimensional X-ray diffraction.* Vol. 2. Wiley Online Library, 2009.

[74] JR Santisteban et al. “ENGIN-X: a third-generation neutron strain scanner”. In: *Journal of Applied Crystallography* 39.6 (2006), pp. 812–825.

[75] V F Sears. “Neutron scattering lengths and cross sections”. In: *Neutron news* 3.3 (1992), pp. 26–37.

[76] AC Hannon, SM Bennington, and S Langridge. “Neutron Training Course Booklet”. In: *ISIS* (2003).

[77] HEA Brand et al. “The thermal expansion and crystal structure of mirabilite (Na 2 SO 4· 10D 2 O) from 4.2 to 300 K, determined by time-of-flight neutron powder diffraction”. In: *Physics and Chemistry of Minerals* 36.1 (2009), pp. 29–46.

[78] A C Larson and R B Von Dreele. “Gsas”. In: *Report lAUR* (1994), pp. 86–748.

[79] K Fan et al. “Residual stress and diffraction line-broadening analysis of Al2O3/Y-TZP ceramic composites by neutron diffraction measurement”. In: *International Journal of Refractory Metals and Hard Materials* 64 (2017), pp. 122–134.

[80] P Thompson, DE Cox, and JB Hastings. “Rietveld refinement of Debye–Scherrer synchrotron X-ray data from Al2O3”. In: *Journal of Applied Crystallography* 20.2 (1987), pp. 79–83.

[81] GS Pawley. “Unit-cell refinement from powder diffraction scans”. In: *Journal of Applied Crystallography* 14.6 (1981), pp. 357–361.

[82] J B Chang and C M Hudson. *Methods and models for predicting fatigue crack growth under random loading*. Vol. 748. ASTM International, 1981.

[83] C Lan et al. “Weibull modeling of the fatigue life for steel rebar considering corrosion effects”. In: *International Journal of Fatigue* 111 (2018), pp. 134–143.

[84] T Svensson et al. “Three HCF models for strain fatigue life of welded pipes in austenitic stainless steel”. In: *Procedia Engineering* 101 (2015), pp. 476–484.

[85] G Jiao and T Moan. “Probabilistic analysis of fatigue due to Gaussian load processes”. In: *Probabilistic Engineering Mechanics* 5.2 (1990), pp. 76–83.

[86] TJ Marrow et al. “A quantitative three-dimensional in situ study of a short fatigue crack in a magnesium alloy”. In: *International Journal of Fatigue* 66 (2014), pp. 183–193.

[87] K M Holford et al. “A new methodology for automating acoustic emission detection of metallic fatigue fractures in highly demanding aerospace environments: An overview”. In: *Progress in Aerospace Sciences* 90 (2017), pp. 1–11.

[88] M Mokhtarishirazabad, P Lopez-Crespo, and M Zanganeh. “Stress intensity factor monitoring under cyclic loading by digital image correlation”. In: *Fatigue & Fracture of Engineering Materials & Structures* 41.10 (2018), pp. 2162–2171.

[89] TH Becker et al. “An approach to calculate the J-integral by digital image correlation displacement field measurement”. In: *Fatigue & Fracture of Engineering Materials & Structures* 35.10 (2012), pp. 971–984.

[90] B K Bay et al. “Digital volume correlation: three-dimensional strain mapping using X-ray tomography”. In: *Experimental mechanics* 39.3 (1999), pp. 217–226.

[91] F Gillard et al. “The application of digital volume correlation (DVC) to study the microstructural behaviour of trabecular bone during compression”. In: *Journal of the mechanical behavior of biomedical materials* 29 (2014), pp. 480–499.

[92] M Mostafavi et al. “Yield behavior beneath hardness indentations in ductile metals, measured by three-dimensional computed X-ray tomography and digital volume correlation”. In: *Acta Materialia* 82 (2015), pp. 468–482.

[93] N Limodin et al. “Influence of closure on the 3D propagation of fatigue cracks in a nodular cast iron investigated by X-ray tomography and 3D volume correlation”. In: *Acta Materialia* 58.8 (2010), pp. 2957–2967.

[94] TJ Marrow et al. “In situ measurement of the strains within a mechanically loaded polygranular graphite”. In: *Carbon* 96 (2016), pp. 285–302.

[95] F Forsberg et al. “3D micro-scale deformations of wood in bending: synchrotron radiation μCT data analyzed with digital volume correlation”. In: *Journal of structural biology* 164.3 (2008), pp. 255–262.

[96] A King et al. “Three-dimensional in situ observations of short fatigue crack growth in magnesium”. In: *Acta Materialia* 59.17 (2011), pp. 6761–6771.

[97] D Takamatsu et al. “Quantitative visualization of salt concentration distributions in lithium-ion battery electrolytes during battery operation using X-ray Phase Imaging”. In: *Journal of the American Chemical Society* 140.5 (2018), pp. 1608–1611.

[98] B Wang et al. “Ultrafast synchrotron X-ray imaging studies of microstructure fragmentation in solidification under ultrasound”. In: *Acta Materialia* 144 (2018), pp. 505–515.

[99] C L A Leung et al. “In situ X-ray imaging of defect and molten pool dynamics in laser additive manufacturing”. In: *Nature communications* 9.1 (2018), p. 1355.

[100] H K Gaikwad et al. “Molecular imaging of cancer using X-ray computed tomography with protease targeted iodinated activity-based probes”. In: *Nano letters* 18.3 (2018), pp. 1582–1591.

[101] P Vontobel, E Lehmann, and W D Carlson. “Comparison of X-ray and neutron tomography investigations of geological materials”. In: *IEEE transactions on nuclear science* 52.1 (2005), pp. 338–341.

[102] W Kockelmann et al. “IMAT–a new imaging and diffraction instrument at ISIS”. In: *Physics Procedia* 43 (2013), pp. 100–110.

[103] W Kockelmann et al. “Time-of-Flight Neutron Imaging on IMAT@ ISIS: A New User Facility for Materials Science”. In: *Journal of Imaging* 4.3 (2018), p. 47.

[104] J Johansson. “Residual stresses and fatigue in a duplex stainless steel”. In: (1999).

[105] J Polak. “Cyclic plastic response and fatigue life of duplex and superduplex stainless steels”. In: *Kovove Materialy* 43.4 (2005), pp. 280–289.

[106] G Chai, R L Peng, and S Johansson. “Fatigue behaviors in duplex stainless steel studied using in-situ SEM/EBSD method”. In: *Procedia materials science* 3 (2014), pp. 1748–1753.

[107] U Krupp et al. “The significance of microstructural barriers during fatigue of a duplex steel in the high-and very-high-cycle-fatigue (HCF/VHCF) regime”. In: *International Journal of Fatigue* 32.6 (2010), pp. 914–920.

[108] G Chai. “The formation of subsurface non-defect fatigue crack origins”. In: *International Journal of Fatigue* 28.11 (2006), pp. 1533–1539.

[109] M Nyström and B Karlsson. “Fatigue of duplex stainless steel influence of discontinuous, spinodally decomposed ferrite”. In: *Materials Science and Engineering: A* 215.1-2 (1996), pp. 26–38.

[110] N Akdut. “Phase morphology and fatigue lives of nitrogen alloyed duplex stainless steels”. In: *International Journal of Fatigue* 21 (1999), S97–S103.

[111] TJ Marrow and JE King. “Fatigue crack propagation mechanisms in a thermally aged duplex stainless steel”. In: *Materials Science and Engineering: A* 183.1-2 (1994), pp. 91–101.

[112] A S Tremsin et al. “Investigation of microstructure in additive manufactured Inconel 625 by spatially resolved neutron transmission spectroscopy”. In: *Science and Technology of advanced MaTerialS* 17.1 (2016), pp. 324–336.

[113] R Ramadhan et al. “Mapping residual strain induced by cold working and by laser shock peening using neutron transmission spectroscopy”. In: *Materials & Design* 143 (2018), pp. 56–64.

[114] M Connolly et al. “In situ neutron transmission Bragg edge measurements of strain fields near fatigue cracks grown in air and in hydrogen”. In: *International Hydrogen Conference (IHC 2016): Materials Performance in Hydrogen Environments.* ASME Press. 2017.

[115] PJ Withers. “Fracture mechanics by three-dimensional crack-tip synchrotron X-ray microscopy”. In: *Philosophical Transactions of the Royal Society A: Mathematical, Physical and Engineering Sciences* 373.2036 (2015), p. 20130157.

[116] K Van Tittelboom et al. “Use of neutron radiography and tomography to visualize the autonomous crack sealing efficiency in cementitious materials”. In: *Materials and structures* 46.1-2 (2013), pp. 105–121.

[117] K Iwase et al. “Bragg-edge transmission imaging of strain and microstructure using a pulsed neutron source”. In: *Nuclear Instruments and Methods in Physics Research Section A: Accelerators, Spectrometers, Detectors and Associated Equipment* 605.1-2 (2009), pp. 1–4.

[118] E. Fermi, W. J. Sturm, and R. G. Sachs. “The Transmission of Slow Neutrons through Microcrystalline Materials”. In: *Phys. Rev.* 71 (9 1947), pp. 589–594.

[119] W Kockelmann et al. “Energy-selective neutron transmission imaging at a pulsed source”. In: *Nuclear Instruments and Methods in Physics Research Section A: Accelerators, Spectrometers, Detectors and Associated Equipment* 578.2 (2007), pp. 421–434.

[120] JR Santisteban et al. “Time-of-flight neutron transmission diffraction”. In: *Journal of applied crystallography* 34.3 (2001), pp. 289–297.

[121] R Woracek et al. “Neutron Bragg-edge-imaging for strain mapping under in situ tensile loading”. In: *Journal of Applied Physics* 109.9 (2011), p. 093506.

[122] P Vontobel et al. “Neutron tomography: Method and applications”. In: *Physica B: Condensed Matter* 385 (2006), pp. 475–480.

[123] F Natterer and F Wübbeling. *Mathematical methods in image reconstruction.* Vol. 5. Siam, 2001.

[124] G Burca et al. “Modelling of an imaging beamline at the ISIS pulsed neutron source”. In: *Journal of Instrumentation* 8.10 (2013), P10001.

[125] C T Chantler. “Detailed tabulation of atomic form factors, photoelectric absorption and scattering cross section, and mass attenuation coefficients in the vicinity of absorption edges in the soft X-ray (Z= 30–36, Z= 60–89, E= 0.1 keV–10 keV), addressing convergence issues of earlier work”. In: *Journal of Physical and Chemical Reference Data* 29.4 (2000), pp. 597–1056.

[126] T Minniti et al. “Characterization of the new neutron imaging and materials science facility IMAT”. In: *Nuclear Instruments and Methods in Physics Research Section A: Accelerators, Spectrometers, Detectors and Associated Equipment* 888 (2018), pp. 184–195.

[127] EH Lehmann et al. “The micro-setup for neutron imaging: A major step forward to improve the spatial resolution”. In: *Nuclear Instruments and Methods in Physics Research Section A: Accelerators, Spectrometers, Detectors and Associated Equipment* 576.2-3 (2007), pp. 389–396.

[128] A Griesche et al. “Three-dimensional imaging of hydrogen blister in iron with neutron tomography”. In: *Acta Materialia* 78 (2014), pp. 14–22.

[129] Y-S Chen et al. “Direct observation of individual hydrogen atoms at trapping sites in a ferritic steel”. In: *Science* 355.6330 (2017), pp. 1196–1199.

[130] Sandymeyer Steel Company. *Duplex Stainless Steel Plate Alloy 2205*. URL: `https://www.sandmeyersteel.com/2205.html` (visited on 06/21/2019).

[131] B Abbey et al. “Feasibility study of neutron strain tomography”. In: *Procedia Engineering* 1.1 (2009), pp. 185–188.

[132] B Abbey et al. “Reconstruction of axisymmetric strain distributions via neutron strain tomography”. In: *Nuclear Instruments and Methods in Physics Research Section B: Beam Interactions with Materials and Atoms* 270 (2012), pp. 28–35.

[133] D Taylor. “The theory of critical distances”. In: *Engineering Fracture Mechanics* 75.7 (2008), pp. 1696–1705.

[134] TC Lindley, CE Richards, and RO Ritchie. “The mechanics and mechanisms of fatigue crack growth in metals (a review)”. In: *Metall. Met. Form.* 43.9 (1974), pp. 268–280.

[135] S Erjian. “Stress intensity factors for surface cracks emanating from the circumferential notch root in notched round bars”. In: *Engineering fracture mechanics* 37.4 (1990), pp. 813–816.

[136] T Minniti et al. “Materials analysis opportunities on the new neutron imaging facility IMAT@ ISIS”. In: *Journal of Instrumentation* 11.03 (2016), p. C03014.

[137] A S Tremsin et al. “High Resolution Photon Counting With MCP-Timepix Quad Parallel Readout Operating at 1KHz Frame Rates”. In: *IEEE Transactions on Nuclear Science* 60.2 (2012), pp. 578–585.

[138] AS Tremsin et al. “Improved efficiency of high resolution thermal and cold neutron imaging”. In: *Nuclear Instruments and Methods in Physics Research Section A: Accelerators, Spectrometers, Detectors and Associated Equipment* 628.1 (2011), pp. 415–418.

[139] A S Tremsin, W B Feller, and R G Downing. “Efficiency optimization of microchannel plate (MCP) neutron imaging detectors. I. Square channels with 10B doping”. In: *Nuclear Instruments and Methods in Physics Research Section A: Accelerators, Spectrometers, Detectors and Associated Equipment* 539.1-2 (2005), pp. 278–311.

[140] A S Tremsin et al. “Energy-resolving neutron transmission radiography at the ISIS pulsed spallation source with a high-resolution neutron counting detector”. In: *2008 IEEE Nuclear Science Symposium Conference Record*. IEEE. 2008, pp. 2902–2908.

[141] A Reid et al. “Mapping of axial plastic zone for roller bearing overloads using neutron transmission imaging”. In: *Materials & Design* 156 (2018), pp. 103–112.

[142] W Treimer. “Neutron tomography”. In: *Neutron Imaging and Applications*. Springer, 2009, pp. 81–108.

[143] A C Kak, M Slaney, and G Wang. “Principles of computerized tomographic imaging”. In: *Medical Physics* 29.1 (2002), pp. 107–107.

[144] D Micieli et al. “A comparative study of reconstruction methods applied to Neutron Tomography”. In: *Journal of Instrumentation* 13.06 (2018), p. C06006.

[145] F Marone and M Stampanoni. “Regridding reconstruction algorithm for real-time tomographic imaging”. In: *Journal of synchrotron radiation* 19.6 (2012), pp. 1029–1037.

[146] DSS (Dassault Systèmes Simulia Corp). “ABAQUS Analysis user’s manual 6.14-2”. In: (2014).

[147] S C Roy. “Modeling and analysis of material behavior during cavitation erosion”. PhD thesis. Université Grenoble Alpes, 2015.

[148] W Woo et al. “Effect of wavelength-dependent attenuation on neutron diffraction stress measurements at depth in steels”. In: *Journal of Applied Crystallography* 44.4 (2011), pp. 747–754.

[149] Y Kim et al. “Evaluation of single crystal elastic constants and stacking fault energy in high-nitrogen duplex stainless steel by in-situ neutron diffraction”. In: *Scripta Materialia* 119 (2016), pp. 1–4.

[150] N Jia et al. “Tensile deformation behavior of duplex stainless steel studied by in-situ time-of-flight neutron diffraction”. In: *Metallurgical and Materials Transactions A* 39.13 (2008), p. 3134.

[151] R Badji, B Bacroix, and M Bouabdallah. “Texture, microstructure and anisotropic properties in annealed 2205 duplex stainless steel welds”. In: *Materials characterization* 62.9 (2011), pp. 833–843.

[152] TM Holden, CN Tomé, and RA Holt. “Experimental and theoretical studies of the superposition of intergranular and macroscopic strains in Ni-based industrial alloys”. In: *Metallurgical and Materials Transactions A* 29.12 (1998), pp. 2967–2973.

[153] M Welvaert and Y Rosseel. “On the definition of signal-to-noise ratio and contrast-to-noise ratio for fMRI data”. In: *PloS one* 8.11 (2013), e77089.

[154] FEI Visualization Sciences Group. “Thermo Scientific Avizo Software 9”. In: (2016).

[155] M Knyazeva and M Pohl. “Duplex steels. Part II: carbides and nitrides”. In: *Metallography, Microstructure, and Analysis* 2.5 (2013), pp. 343–351.

[156] H Toda et al. “Damage micromechanisms in dual-phase steel investigated with combined phase-and absorption-contrast tomography”. In: *Acta Materialia* 126 (2017), pp. 401–412.

[157] M Mostafavi et al. “Three-dimensional crack observation, quantification and simulation in a quasi-brittle material”. In: *Acta Materialia* 61.16 (2013), pp. 6276–6289.

[158] IEC IEC. *IEC 61400-4: Wind turbines-Part 4: Design requirements for wind turbine gearboxes.* 2012.

[159] W Musial, S Butterfield, and B McNiff. *Improving wind turbine gearbox reliability.* Tech. rep. National Renewable Energy Lab.(NREL), Golden, CO (United States), 2007.

[160] A Warhadpande et al. “Effects of plasticity on subsurface initiated spalling in rolling contact fatigue”. In: *International Journal of Fatigue* 36.1 (2012), pp. 80–95.

[161] A Bhattacharyya, G Subhash, and N Arakere. “Evolution of subsurface plastic zone due to rolling contact fatigue of M-50 NiL case hardened bearing steel”. In: *International Journal of Fatigue* 59 (2014), pp. 102–113.

[162] A S Pandkar, N Arakere, and G Subhash. “Microstructure-sensitive accumulation of plastic strain due to ratcheting in bearing steels subject to rolling contact fatigue”. In: *International Journal of Fatigue* 63 (2014), pp. 191–202.

[163] N Weinzapfel, F Sadeghi, and V Bakolas. "An approach for modeling material grain structure in investigations of Hertzian subsurface stresses and rolling contact fatigue". In: *Journal of Tribology* 132.4 (2010), p. 041404.

[164] A Grabulov, R Petrov, and HW Zandbergen. "EBSD investigation of the crack initiation and TEM/FIB analyses of the microstructural changes around the cracks formed under rolling contact fatigue (RCF)". In: *International Journal of Fatigue* 32.3 (2010), pp. 576–583.

[165] MH Evans. "White structure flaking (WSF) in wind turbine gearbox bearings: effects of butterflies and white etching cracks (WECs)". In: *Materials Science and Technology* 28.1 (2012), pp. 3–22.

[166] A-F Gourgues. "Electron backscatter diffraction and cracking". In: *Materials Science and technology* 18.2 (2002), pp. 119–133.

[167] M Kamaya, A J Wilkinson, and J M Titchmarsh. "Measurement of plastic strain of polycrystalline material by electron backscatter diffraction". In: *Nuclear engineering and design* 235.6 (2005), pp. 713–725.

[168] M M Nowell, R A Witt, and B W True. "EBSD sample preparation: Techniques, tips, and tricks". In: *Microscopy Today* 13.4 (2005), pp. 44–49.

[169] A M Korsunsky et al. "Fast residual stress mapping using energy-dispersive synchrotron X-ray diffraction on station 16.3 at the SRS". In: *Journal of synchrotron radiation* 9.2 (2002), pp. 77–81.

[170] A Steuwer et al. "High-resolution strain mapping in bulk samples using full-profile analysis of energy dispersive synchrotron X-ray diffraction data". In: *Nuclear Instruments and Methods in Physics Research Section B: Beam Interactions with Materials and Atoms* 238.1-4 (2005), pp. 200–204.

[171] M Mostafavi et al. "Dynamic contact strain measurement by time-resolved stroboscopic energy dispersive synchrotron X-ray diffraction". In: *Strain* 53.2 (2017), e12221.

[172] Z Budrovic et al. "Plastic deformation with reversible peak broadening in nanocrystalline nickel". In: *Science* 304.5668 (2004), pp. 273–276.

[173] I Nikitin and M Besel. "Residual stress relaxation of deep-rolled austenitic steel". In: *Scripta Materialia* 58.3 (2008), pp. 239–242.

[174] T Ungár et al. "Crystallite size distribution and dislocation structure determined by diffraction profile analysis: principles and practical application to cubic and hexagonal crystals". In: *Journal of applied crystallography* 34.3 (2001), pp. 298–310.

[175] D Balzar and H Ledbetter. "Voigt-function modeling in Fourier analysis of size-and strain-broadened X-ray diffraction peaks". In: *Journal of Applied Crystallography* 26.1 (1993), pp. 97–103.

[176] AJ Allen et al. "Neutron diffraction methods for the study of residual stress fields". In: *Advances in Physics* 34.4 (1985), pp. 445–473.

[177] AJ Allen et al. "The analysis of internal strains measured by neutron diffraction in Al/SiC metal matrix composites". In: *Acta metallurgica et materialia* 40.9 (1992), pp. 2361–2373.

[178] Y Sun et al. "Neutron diffraction studies on lattice strain evolution around a crack-tip during tensile loading and unloading cycles". In: *Scripta materialia* 53.8 (2005), pp. 971–975.

[179] E-W Huang et al. “Plastic behavior of a nickel-based alloy under monotonic-tension and low-cycle-fatigue loading”. In: *International Journal of Plasticity* 24.8 (2008), pp. 1440–1456.

[180] SR Agnew, DW Brown, and CN Tomé. “Validating a polycrystal model for the elastoplastic response of magnesium alloy AZ31 using in situ neutron diffraction”. In: *Acta materialia* 54.18 (2006), pp. 4841–4852.

[181] YB Guo and CR Liu. “Mechanical properties of hardened AISI 52100 steel in hard machining processes”. In: *Journal of manufacturing science and engineering* 124.1 (2002), pp. 1–9.

[182] HKDH Bhadeshia. “Steels for bearings”. In: *Progress in materials Science* 57.2 (2012), pp. 268–435.

[183] I Hutchings and P Shipway. *Tribology: friction and wear of engineering materials*. Butterworth-Heinemann, 2017.

[184] TA Harris and RM Barnsby. “Life ratings for ball and roller bearings”. In: *Proceedings of the Institution of Mechanical Engineers, Part J: Journal of Engineering Tribology* 215.6 (2001), pp. 577–595.

[185] NTN Americas. *Cylindrical and Tapered Roller Bearings*. Tech. rep. Catalog A-1500-III, 2009.

[186] ASM International. “Atlas of stress-strain curves”. In: *ASM International* (2002), p. 375.

[187] T Minniti. “Bragg Edge Analysis for Transmission Imaging Experiments software tool: BEATRIX”. In: *Journal of Applied Crystallography* 52.4 (2019).

[188] AS Tremsin et al. “Optimization of Timepix count rate capabilities for the applications with a periodic input signal”. In: *Journal of Instrumentation* 9.05 (2014), p. C05026.

[189] MR Daymond and HG Priesmeyer. “Elastoplastic deformation of ferritic steel and cementite studied by neutron diffraction and self-consistent modelling”. In: *Acta materialia* 50.6 (2002), pp. 1613–1626.

[190] TM Holden, AP Clarke, and RA Holt. “Neutron diffraction measurements of intergranular strains in MONEL-400”. In: *Metallurgical and Materials Transactions A* 28.12 (1997), pp. 2565–2576.

[191] J Helsen et al. “Experimental investigation of bearing slip in a wind turbine gearbox during a transient grid loss event”. In: *Wind Energy* 19.12 (2016), pp. 2255–2269.

[192] F Spinato et al. “Reliability of wind turbine subassemblies”. In: *IET Renewable Power Generation* 3.4 (2009), pp. 387–401.

[193] H Chengbing, F Xinxin, et al. “Institutions function and failure statistic and analysis of wind turbine”. In: *Physics procedia* 24 (2012), pp. 25–30.

[194] H D M de Azevedo, A M Araújo, and N Bouchonneau. “A review of wind turbine bearing condition monitoring: State of the art and challenges”. In: *Renewable and Sustainable Energy Reviews* 56 (2016), pp. 368–379.

[195] Y Guo, J Keller, and W LaCava. “Planetary gear load sharing of wind turbine drivetrains subjected to non-torque loads”. In: *Wind Energy* 18.4 (2015), pp. 757–768.

[196] F Sadeghi et al. “A review of rolling contact fatigue”. In: *Journal of tribology* 131.4 (2009), p. 041403.

[197] S Turteltaub and ASJ Suiker. “Transformation-induced plasticity in ferrous alloys”. In: *Journal of the Mechanics and Physics of Solids* 53.8 (2005), pp. 1747–1788.

[198] AP Voskamp. “Material response to rolling contact loading”. In: *Journal of tribology* 107.3 (1985), pp. 359–364.

[199] AP Voskamp and EJ Mittemeijer. “State of residual stress induced by cyclic rolling contact loading”. In: *Materials science and technology* 13.5 (1997), pp. 430–438.

[200] A Warhadpande, F Sadeghi, and R D Evans. “Microstructural alterations in bearing steels under rolling contact fatigue part 1historical overview”. In: *Tribology Transactions* 56.3 (2013), pp. 349–358.

[201] T Slack and F Sadeghi. “Explicit finite element modeling of subsurface initiated spalling in rolling contacts”. In: *Tribology International* 43.9 (2010), pp. 1693–1702.

[202] HA Al-Tameemi, H Long, and RS Dwyer-Joyce. “Initiation of sub-surface micro-cracks and white etching areas from debonding at non-metallic inclusions in wind turbine gearbox bearing”. In: *Wear* 406 (2018), pp. 22–32.

[203] B Gould et al. “An analysis of premature cracking associated with microstructural alterations in an AISI 52100 failed wind turbine bearing using X-ray tomography”. In: *Materials & Design* 117 (2017), pp. 417–429.

[204] H Muro, T Tsushima, and M Nagafuchi. “Initiation and propagation of surface cracks in rolling fatigue of high hardness steel”. In: *Wear* 35.2 (1975), pp. 261–282.

[205] Y Zhou et al. “The effect of contact severity on micropitting: simulation and experiments”. In: *Tribology International* (2019).

[206] H Liu et al. “A review on micropitting studies of steel gears”. In: *Coatings* 9.1 (2019), p. 42.

[207] M El Laithy et al. “Further understanding of rolling contact fatigue in rolling element bearings-a review”. In: *Tribology International* (2019), p. 105849.

[208] K Fischer, F Besnard, and L Bertling. “Reliability-centered maintenance for wind turbines based on statistical analysis and practical experience”. In: *IEEE Transactions on Energy Conversion* 27.1 (2011), pp. 184–195.

[209] E V Zaretsky. “A. Palmgren revisited: A basis for bearing life prediction”. In: *Society of Tribologists and Lubrication Engineers Annual Meeting* (1997).

[210] AM Korsunsky et al. “Measurement of residual elastic strains in a titanium alloy using high energy synchrotron X-ray diffraction”. In: *Experimental mechanics* 46.4 (2006), pp. 519–529.

[211] T Wigger et al. “In situ mapping of normal strains in the field of a growing fatigue crack in a steel weld using digital image correlation and energy dispersive synchrotron X-ray diffraction”. In: *International Journal of Fatigue* 115 (2018), pp. 11–19.

[212] S Sato et al. “Relationship between dislocations and residual stresses in cold-drawn pearlitic steel analyzed by energy-dispersive X-ray diffraction”. In: *Materials Characterization* 83 (2013), pp. 152–160.

[213] P Lopez-Crespo et al. “Characterisation of overloads in fatigue by 2D strain mapping at the surface and in the bulk”. In: *Fatigue & Fracture of Engineering Materials & Structures* 39.8 (2016), pp. 1040–1048.

[214] N Baimpas et al. “A feasibility study of dynamic stress analysis inside a running internal combustion engine using synchrotron X-ray beams”. In: *Journal of synchrotron radiation* 20.2 (2013), pp. 316–323.

[215] M Hammami et al. “Friction torque in rolling bearings lubricated with axle gear oils”. In: *Tribology International* 119 (2018), pp. 419–435.

[216] H Polinder et al. “Basic operation principles and electrical conversion systems of wind turbines”. In: *EPE Journal* 15.4 (2005), pp. 43–50.

[217] S Sheng. *Wind turbine gearbox condition monitoring round robin study-vibration analysis*. Tech. rep. National Renewable Energy Lab.(NREL), Golden, CO (United States), 2012.

[218] C Simpson. “pyXe: XRD Strain Analysis (Version v0.9.1)”. In: (2019).

[219] T A Harris and M N Kotzalas. *Essential concepts of bearing technology*. CRC press, 2006.

[220] W Qiao and D Lu. “A survey on wind turbine condition monitoring and fault diagnosisPart I: Components and subsystems”. In: *IEEE Transactions on Industrial Electronics* 62.10 (2015), pp. 6536–6545.

[221] J S Nam et al. “Development of a gearbox test rig with non-torque loading capacity”. In: *Journal of Mechanical Science and Technology* 30.4 (2016), pp. 1713–1722.

[222] AD Richardson et al. “The effect of over-based calcium sulfonate detergent additives on white etching crack (WEC) formation in rolling contact fatigue tested 100Cr6 steel”. In: *Tribology International* 133 (2019), pp. 246–262.

[223] B Gould et al. “Figure the impact of steel microstructure and heat treatment on the formation of white etching cracks”. In: *Tribology International* 134 (2019), pp. 232–239.

[224] T Bruce et al. “Characterisation of white etching crack damage in wind turbine gearbox bearings”. In: *Wear* 338 (2015), pp. 164–177.

[225] HKDH Bhadeshia and W Solano-Alvarez. “Critical assessment 13: elimination of white etching matter in bearing steels”. In: *Materials Science and Technology* 31.9 (2015), pp. 1011–1015.

[226] B Gould and A Greco. “The influence of sliding and contact severity on the generation of white etching cracks”. In: *Tribology Letters* 60.2 (2015), p. 29.

[227] L Xie et al. “Effect of surface hardening technique and case depth on rolling contact fatigue behavior of alloy steels”. In: *Tribology Transactions* 58.2 (2015), pp. 215–224.

[228] M W Johnson and M R Daymond. “An optimum design for a time-of-flight neutron diffractometer for measuring engineering stresses”. In: *Journal of applied crystallography* 35.1 (2002), pp. 49–57.

[229] LB McCusker et al. “Rietveld refinement guidelines”. In: *Journal of Applied Crystallography* 32.1 (1999), pp. 36–50.

[230] G Salerno et al. “On the interaction between welding residual stresses: a numerical and experimental investigation”. In: *International Journal of Mechanical Sciences* 144 (2018), pp. 654–667.

[231] C Bühr et al. “Prediction of residual stress within linear friction welds using a computationally efficient modelling approach”. In: *Materials & Design* 139 (2018), pp. 222–233.

[232] A Narayanan et al. “Residual stress in laser cladded rail”. In: *Tribology International* 140 (2019), p. 105844.

[233] W Woo et al. “In-situ neutron diffraction studies on high-temperature deformation behavior in a CoCrFeMnNi high entropy alloy”. In: *Intermetallics* 62 (2015), pp. 1–6.

[234] S Van Petegem et al. “In-situ neutron diffraction during biaxial deformation”. In: *Acta Materialia* 105 (2016), pp. 404–416.

[235] Z Wang et al. “Stress relaxation in a nickel-base superalloy at elevated temperatures with in situ neutron diffraction characterization: Application to additive manufacturing”. In: *Materials Science and Engineering: A* 714 (2018), pp. 75–83.

[236] H Wang et al. “Correlation of localized residual stresses with ductile fracture toughness using in situ neutron diffraction and finite element modelling”. In: *International Journal of Mechanical Sciences* (2019).

[237] MR Daymond and PJ Withers. “A new stroboscopic neutron diffraction method for monitoring materials subjected to cyclic loads: thermal cycling of metal matrix composites”. In: *Scripta materialia* 35.6 (1996).

[238] J Feuchtwanger et al. “Rearrangement of twin variants in ferromagnetic shape memory alloy–polyurethane composites studied by stroboscopic neutron diffraction”. In: *Journal of Physics: Condensed Matter* 20.10 (2008), p. 104247.

[239] T Kawasaki et al. “Stroboscopic time-of-flight neutron diffraction during cyclic testing using the event data recording system at J-PARC”. In: *Journal of Applied Crystallography* 51.3 (2018).

[240] A Reid et al. “Measurement of strain evolution in overloaded roller bearings using energy dispersive X-ray diffraction”. In: *Tribology International* 140 (2019), p. 105893.

[241] I Martinez et al. “Acoustic Emission Localisation on Roller Bearing Defects using Time-Delay and Sum Beamforming Technique”. In: *UNPUBLISHED* ().

[242] MS Patil et al. “A theoretical model to predict the effect of localized defect on vibrations associated with ball bearing”. In: *International Journal of Mechanical Sciences* 52.9 (2010), pp. 1193–1201.

[243] O Arnold et al. “MantidData analysis and visualization package for neutron scattering and μ SR experiments”. In: *Nuclear Instruments and Methods in Physics Research Section A: Accelerators, Spectrometers, Detectors and Associated Equipment* 764 (2014), pp. 156–166.

[244] B H Toby and R B Von Dreele. “GSAS-II: the genesis of a modern open-source all purpose crystallography software package”. In: *Journal of Applied Crystallography* 46.2 (2013), pp. 544–549.

[245] J W Cooley and J W Tukey. “An algorithm for the machine calculation of complex Fourier series”. In: *Mathematics of computation* 19.90 (1965), pp. 297–301.

[246] J F James et al. “A student’s guide to Fourier transforms with applications in physics and engineering”. In: *Computers in Physics* 10.1 (1996), pp. 47–47.

[247] PSR Diniz, EAB Da Silva, and SL Netto. *Digital signal processing: system analysis and design.* Cambridge University Press, 2010.

[248] S De Ridder et al. “Comparison between EEMD, wavelet and FIR denoising: Influence on event detection in impedance cardiography”. In: *2011 Annual International Conference of the IEEE Engineering in Medicine and Biology Society*. IEEE. 2011, pp. 806–809.

[249] V Šmeļova et al. “Microstructural changes in white etching cracks (WECs) and their relationship with those in dark etching region (DER) and white etching bands (WEBs) due to rolling contact fatigue (RCF)”. In: *International Journal of Fatigue* 100 (2017), pp. 148–158.

[250] G Nicholas et al. “Direct load measurement of a wind turbine high speed shaft bearing in the field”. In: *1st World Congress on Condition Monitoring 2017 (WCCM 2017)*. British Institute of Non-Destructive Testing. 2017, pp. 879–886.

[251] F Fiori et al. “Crack detection in Al alloy using phase-contrast neutron radiography and tomography”. In: *Measurement Science and Technology* 17.9 (2006), p. 2479.